

Inferring the Evolutionary Histories of Stars and Their Planets

David Paul Fleming

A dissertation
submitted in partial fulfillment of the
requirements for the degree of

Doctor of Philosophy

University of Washington

2020

Reading Committee:

Rory Barnes, Chair

Tom Quinn

Victoria Meadows

Jacob VanderPlas

Michael Johnson (GSR)

Program Authorized to Offer Degree:
Astronomy

©Copyright 2020

David Paul Fleming

University of Washington

Abstract

Inferring the Evolutionary Histories of Stars and Their Planets

David Paul Fleming

Chair of the Supervisory Committee:
Professor Rory Barnes
Astronomy

Modern astronomical surveys like NASA's *Kepler* mission have collected a wealth of data in the search for Earth-like exoplanets. This vast quantity of data has enabled novel statistical investigations of the physical processes that shape the observed populations of stars and their planets. Theoretical models are a critical component of such studies and are required to explain how and why observed planetary systems have evolved over time. By comparing model predictions with observed data and its uncertainties, a process mathematically formalized by Bayesian inference, we can infer the long-term evolution of planetary systems and come to understand what processes have shaped their present state.

In this dissertation, I develop theoretical and probabilistic models to understand and infer the long-term evolution of single and binary stars. Although my modeling efforts focus on the dynamical evolution of such systems, e.g. how and why a binary's orbit evolves over time, I consider what impact stellar and binary evolutionary processes have on planets orbiting the stars. I employ my models to examine different aspects of the lifetime of planetary systems, including early stellar interactions with a protoplanetary disk and the evolving high-energy radiation environment experienced by terrestrial planets orbiting late M-dwarfs throughout the stellar pre-main sequence. I confront my model predictions with observational data from missions like *Kepler* to constrain unobserved model parameters and develop testable hypotheses for unexplained features in the data. Through my novel theories and inference methods, I help determine how the past evolution of stars

in planetary systems shape what we observe today.

To study the dynamics of the birth environment of exoplanets, I ran an ensemble of smooth particle hydrodynamic (SPH) N-body simulations of circumbinary protoplanetary disks. My work demonstrates that these dynamically-rich disks coevolve with their central host binary stars, exchanging angular momentum through gravitational resonances, ultimately driving the orbital evolution of both the binary and the inner-edge of the disk where planets can form and migrate. I extend my work with circumbinary planetary systems and develop a model to explain the anomalous lack of observed circumbinary planets (CBPs) orbiting short-period binary stars in the *Kepler* field. By constructing a theoretical model for the coupled stellar-tidal evolution of binary stars, I show that the expanding orbits of young binaries can efficiently destabilize CBPs that preferentially orbit just exterior to the dynamical stability limit, explaining their observed dearth.

I continue my work with binary stars to explore how the competition between tidal torques and magnetic braking in binaries can shape the observed rotation period distribution of low-mass main sequence stars in the *Kepler* field. I show how my model reproduces previously-unexplained stellar populations in the *Kepler* field, such as subsynchronous binary stars identified by Lurie et al. (2017). I then explain how my model impacts the stellar age determination method of gyrochronology and explore how predictions from my theory could be used to distinguish between which model best describes tidal interactions in main sequence low-mass binary stars.

Finally, I turn my modeling efforts to infer the long-term high-energy radiation environment experienced by the TRAPPIST-1 planetary system, the current best target for the detection and characterization of terrestrial planet atmospheres by the James Webb Space Telescope (JWST). I construct a probabilistic model for TRAPPIST-1's evolving XUV luminosity, conditioning the inference on both observations of TRAPPIST-1 and of late M-dwarfs. From this inference, I find that TRAPPIST-1 likely underwent an extended epoch of enhanced XUV emission, potentially driving extreme volatile loss from its planets, impacting what JWST might observe in future observations. I demonstrate that this Bayesian inference analysis is too computationally-expensive

to scale to either a larger number of stars or a more complex model. To address this concern, I develop a novel open-source machine learning Python package, `approxposterior`. I apply `approxposterior` to the TRAPPIST-1 inference problem and demonstrate that `approxposterior` can accurately repeat the probabilistic analysis, but requiring nearly 3 orders of magnitude less computational resources than `emcee`. I conclude by discussing how my new efficient machine learning method can enable similar Bayesian inference studies for a wider array of research problems concerning the long-term evolution of stars and their planets.

TABLE OF CONTENTS

| | Page |
|--|------|
| List of Figures | v |
| List of Tables | xiii |
| Chapter 1: Introduction | 1 |
| 1.1 What Does the Present Tell Us About the Past? | 1 |
| 1.2 Dissertation Outline | 3 |
| Chapter 2: Dynamics in the Birthplace of Planets: Examining the Resonant Dynamical Interactions Between Binary Stars and Circumbinary Disks | 4 |
| 2.1 Introduction | 4 |
| 2.2 Simulations | 8 |
| 2.2.1 Methods | 8 |
| 2.2.2 Model Parameters | 9 |
| 2.2.3 Initial Conditions | 10 |
| 2.3 Results and Analysis | 11 |
| 2.3.1 Gap Clearing | 11 |
| 2.3.2 Disk Evolution | 13 |
| 2.3.3 Binary Evolution | 25 |
| 2.4 Effects of Varying Disk Properties | 32 |
| 2.4.1 Varying Disk Mass | 33 |
| 2.4.2 Varying Disk Resolution | 33 |
| 2.4.3 Varying Disk Aspect Ratio | 34 |
| 2.5 Discussion | 35 |
| 2.5.1 Implications for Long-term Binary Evolution | 37 |
| 2.5.2 Implications for Circumbinary Planets | 39 |
| 2.6 Conclusions | 40 |

| | |
|---|-----|
| 2.7 Acknowledgements | 41 |
| Chapter 3: The Dynamical Death of Circumbinary Planets: Coupled Stellar-Tidal Evolution Ejection of Circumbinary Exoplanets | 43 |
| 3.1 Introduction | 43 |
| 3.2 Methods | 49 |
| 3.2.1 VP _L anet | 49 |
| 3.2.2 Stellar Evolution | 50 |
| 3.2.3 Tidal Evolution | 54 |
| 3.2.4 Coupled Stellar-Tidal Evolution | 57 |
| 3.2.5 Energy and Angular Momentum Conservation | 61 |
| 3.2.6 N-body Simulations of Circumbinary Planetary Systems | 62 |
| 3.3 Simulations | 63 |
| 3.3.1 Coupled Stellar-Tidal Initial Conditions | 63 |
| 3.3.2 N-body Simulations | 66 |
| 3.3.3 Tying It All Together | 69 |
| 3.4 Results: Coupled Stellar-Tidal Evolution Simulations | 70 |
| 3.4.1 Fiducial Simulation | 70 |
| 3.4.2 Varying Tidal Q | 71 |
| 3.4.3 Varying Radius of Gyration | 74 |
| 3.4.4 Varying Magnetic Braking Law | 76 |
| 3.4.5 Varying Rotation Periods | 78 |
| 3.4.6 Monte Carlo Simulations | 78 |
| 3.4.7 3:2 Spin-Orbit Resonance | 81 |
| 3.4.8 Long-term a_{crit} Evolution | 83 |
| 3.4.9 Relaxed Assumptions | 86 |
| 3.5 Results: N-body Simulations | 88 |
| 3.5.1 Dynamical Stability | 88 |
| 3.5.2 Mock Transit Observations | 92 |
| 3.6 Application to Kepler-47 | 95 |
| 3.7 Discussion | 98 |
| 3.7.1 Future Prospects | 100 |
| 3.8 Acknowledgments | 101 |

| | |
|---|-----|
| Chapter 4: The Competition between Magnetic Braking and Tidal Torques in Binary Stars: Application to the <i>Kepler</i> Field | 103 |
| 4.1 Introduction | 103 |
| 4.2 Methods | 106 |
| 4.2.1 Stellar Evolution | 106 |
| 4.2.2 Tidal Evolution | 108 |
| 4.2.3 Coupled Stellar-Tidal Evolution For tidally locked Systems | 116 |
| 4.3 Simulations | 116 |
| 4.4 Results | 119 |
| 4.4.1 Interaction Between Magnetic and Tidal Braking: Subynchronous Rotation | 119 |
| 4.4.2 Influence of P_{orb} , Q and τ | 123 |
| 4.4.3 P_{rot} Distribution of a Synthetic Population of Stellar Binaries | 128 |
| 4.4.4 Deviations From Single Star P_{rot} Evolution: Implications for Gyrochronology | 133 |
| 4.4.5 Comparison to <i>Kepler</i> | 139 |
| 4.4.6 CPL or CTL? | 141 |
| 4.5 Discussion | 143 |
| 4.6 Acknowledgments | 145 |
| 4.7 Analytic Torque Balance | 145 |
| Chapter 5: Bayesian Inference with Slow Models using <code>approxposterior</code> | 147 |
| 5.1 Bayesian Inference with Computationally-Expensive Models | 147 |
| 5.1.1 Fast and Accurate Approximate Bayesian Inference with <code>approxposterior</code> | 149 |
| 5.2 <code>approxposterior</code> Algorithm | 151 |
| 5.3 <code>approxposterior</code> : Theory and Practical Usage | 153 |
| 5.3.1 Augmenting the Training Set | 153 |
| 5.3.2 Convergence | 156 |
| 5.3.3 A Simple Example | 157 |
| 5.3.4 Online Documentation | 162 |
| 5.4 Applying <code>approxposterior</code> to Terrestrial Exoplanet Atmospheric Retrieval . . | 162 |
| 5.5 Conclusions | 164 |
| Chapter 6: Inferring the XUV History of the TRAPPIST-1 Planetary System | 167 |
| 6.1 Introduction | 167 |

| | | |
|--------------|--|-----|
| 6.2 | Methods | 169 |
| 6.2.1 | Simulating XUV Evolution with VP _L anet | 169 |
| 6.2.2 | Markov Chain Monte Carlo Analysis | 170 |
| 6.2.3 | Prior Probability Distributions | 171 |
| 6.2.4 | Likelihood Function and Convergence | 172 |
| 6.2.5 | Inference with approxposterior | 174 |
| 6.3 | Results | 175 |
| 6.3.1 | The Evolution of TRAPPIST-1 | 175 |
| 6.3.2 | Comparison with approxposterior | 178 |
| 6.3.3 | TRAPPIST-1’s Evolutionary History and Its Planets’ XUV Environment . . | 180 |
| 6.4 | Discussion and Conclusions | 184 |
| 6.5 | Acknowledgments | 186 |
| Chapter 7: | Conclusions | 188 |
| Bibliography | | 191 |

LIST OF FIGURES

| Figure Number | Page |
|---|------|
| 2.1 Azimuthally averaged surface density profiles for Simulations 1-5 after 200 years of evolution. Overplotted are the 1:3 EOLR (dashed black line) and the 1:2 corotation resonance (dashed orange line). | 12 |
| 2.2 Disk eccentricity versus simulation time in units of binary orbits as a function of initial binary eccentricity. | 14 |
| 2.3 Disk eccentricity versus radius after about 520 years of evolution. | 17 |
| 2.4 Change in binary eccentricity versus simulation time in units of binary orbits for several initial binary eccentricities. For an initially circular and nearly circular binary, effectively no eccentricity growth occurs whereas for higher initial eccentricities, significant growth occurs. | 19 |
| 2.5 Two dimensional histogram of disk gas particles binned by semi-major axis and longitude of periastron, ϖ , (the sum of the longitude of ascending node, Ω , and argument of periastron, ω) relative to ϖ of the binary. Each bin is colored by the log of the number of gas particles it contains. We note that figure displays the disk in orbital element space and not in configuration space. The left and right panels display the histograms for two simulations with binaries having initial eccentricities of 0 and 0.1032, respectively, both after 200 years of evolution. The right panel clearly displays a $m = 1$ spiral wave launched from near the 1:3 EOLR within the disk. | 21 |
| 2.6 Two dimensional histogram of disk gas particles binned by semi-major axis and longitude of periastron, ϖ of the form of that shown in Fig. 2.5 for a binary with $e_i = 0.05$. We stress that the plot is shown in orbital element space and not configuration space. As the binary eccentricity increases through interactions with the surrounding disk, a single weak spiral arm begins to form. Once $e \approx 0.08$, the spiral arm becomes slightly more apparent, resembling a fainter version of the arm shown in Figure 2.5 for the $e_i = 0.1032$ case. | 23 |
| 2.7 Change in binary semi-major axis versus simulation time in units of binary periods for several initial binary eccentricities. For all cases, the binary's semi-major axis secularly decreases. | 26 |

| | | |
|-----|--|----|
| 2.8 | Evolution of e_{bin} as a function of a_{bin} from simulations with initial e_{bin} of 0.05, 0.1032, and 0.25 over-plotted with the analytic fit of equation 2.9 with $\alpha_{eff} = 0.006$. As the system evolves, time advances towards the left in this depiction. | 28 |
| 2.9 | The results of simulations about a binary with initial $e_{bin} = 0.1032$ and $a_{bin} = 0.1469$ AU with various disk properties. The control case corresponds to Simulation 4. The top left panel gives the change in binary eccentricity as a function of time. The top right panel shows the change in binary semi-major axis vs time. The bottom left panel displays disk eccentricity vs time and the bottom right panel displays the figure legend. | 36 |
| 3.1 | Semi-major axes of confirmed <i>Kepler</i> CBPs relative to the host binary's critical semi-major axis (a_{CBP}/a_{crit}) as a function of binary orbital period. Each point is annotated with the planet's name. The red-shaded region highlights the observational finding that, to date, no CBPs have been discovered orbiting binaries with binary orbital periods less than 7.45 days. (Welsh et al., 2014; Winn and Fabrycky, 2015). We neglect Kepler-47d as its orbital parameters are not well constrained. <i>Inset:</i> Histogram of observed <i>Kepler</i> CBPs' a_{CBP}/a_{crit} . The histogram demonstrates that most CBPs' semi-major axes cluster near the dynamical stability limit, a_{crit} | 47 |
| 3.2 | Stellar radius and rotation period evolution as computed by our stellar evolution model, STELLAR, for a $1 M_\odot$ (blue), $0.75 M_\odot$ (orange), and $0.25 M_\odot$ (green) star both with solar metallicity. The dots in both panels indicate the approximate time each star reaches the Zero Age Main Sequence. <i>Left:</i> Stellar radius as a function of time according to a cubic spline interpolation of the Baraffe et al. (2015) stellar models. <i>Right:</i> Stellar rotation period as a function of time computed via stellar radius evolution and both magnetic braking models under conservation of angular momentum (see Eq. (3.7)). The solid lines correspond to simulations using the Reiners and Mohanty (2012) magnetic braking law while the dashed lines use the Repetto and Nelemans (2014) magnetic braking law. | 53 |
| 3.3 | Tidal evolution of a binary star system with no stellar evolution under the CPL model (Ferraz-Mello et al., 2008; Heller et al., 2011) as computed by our tidal evolution model, EQTIDE. See the text for the system properties. <i>Left:</i> Binary orbital and stellar rotational period versus time. Tides transport angular momentum from the stellar rotations into the orbit until the binary becomes tidally locked and synchronous (denoted by the black dashed line). <i>Right:</i> Binary orbital eccentricity versus time. After the orbit synchronizes, the eccentricity decreases until the binary circularizes (denoted by the dash-dotted line). | 58 |

| | | |
|-----|---|----|
| 3.4 | <i>Left Panel:</i> Absolute relative difference between the total system energy and initial total system energy as a function of time. <i>Right Panel:</i> Absolute relative difference of the total system angular momentum and initial total system angular momentum as a function of time. Both total energy and angular momentum are approximately conserved at the 10^{-4} level with high frequency oscillations caused by limitations of Runge-Kutta integrations. | 61 |
| 3.5 | Evolution of a binary system using our default parameters from Table 3.1. <i>Top:</i> a_{crit} vs. time. The grey arrows demarcate both the ratio of the maximum critical semi-major axis to the initial and final values, $a_{crit,max}/a_{crit,init} = 1.16$ and $a_{crit,max}/a_{crit,final} = 1.58$ for this system, respectively. <i>Middle:</i> Orbital and stellar rotation period vs. time. The black dashed line indicates that the binary tidally locks after about 1 Myr. <i>Bottom:</i> e vs. time. The dot-dashed line indicates when the binary circularizes at about 1 Gyr, well after tidally locking. | 72 |
| 3.6 | The role of tidal dissipation in binary star evolution. <i>Top Left:</i> a_{crit} vs. time. <i>Top Right:</i> Binary orbital period vs. time. <i>Bottom Left:</i> e vs. time. <i>Bottom Right:</i> $a_{crit,max}/a_{crit,init}$ vs. tidal Q. The blue and orange lines correspond to a $1 M_\odot - 1 M_\odot$ and a $1 M_\odot - 0.5 M_\odot$ binary, respectively. The solid, dashed, and dot-dashed lines correspond to tidal Qs of 10^5 , 10^6 , and 10^7 , respectively. Smaller tidal Qs drive large a_{crit} expansion. | 75 |
| 3.7 | The role of the radius of gyration in binary star evolution. <i>Top Left:</i> a_{crit} vs. time. <i>Top Right:</i> Binary orbital period vs. time. <i>Bottom Left:</i> e vs. time. <i>Bottom Right:</i> $a_{crit,max}/a_{crit,init}$ vs. r_g . The blue and orange lines correspond to a $1 M_\odot - 1 M_\odot$ and a $1 M_\odot - 0.5 M_\odot$ binary, respectively. The solid, dashed, and dot-dashed lines correspond to an r_g of 0.15, 0.3, and 0.45, respectively. Larger r_g lead to increased a_{crit} growth. | 77 |
| 3.8 | The role of the magnetic braking law and initial stellar P_{rot} in binary star evolution. <i>Top Left:</i> a_{crit} vs. time. <i>Top Right:</i> Binary orbital period vs. time. <i>Bottom Left:</i> e vs. time. <i>Bottom Right:</i> $a_{crit,max}/a_{crit,init}$ vs. initial stellar P_{rot} . The blue and orange lines correspond to simulations that use the stellar magnetic braking relation from Reiners and Mohanty (2012) and Repetto and Nelemans (2014), respectively. The solid, dashed, and dot-dashed lines correspond to a binary with stellar initial spin periods of 0.5 d, 1 d, and 2 d, respectively. We find that the Repetto and Nelemans (2014) relation leads to larger $a_{crit,max}/a_{crit,init}$ and stars with shorter initial spin periods lead to larger $a_{crit,max}/a_{crit,init}$ as well. | 79 |
| 3.9 | $a_{crit,max}/a_{crit,init}$ as a function of the initial stellar P_{rot} for a $1 M_\odot - 1 M_\odot$ binary for $e = 0.05$ (<i>Left</i>) and $e = 0.15$ (<i>Right</i>). The white lines are contours in $a_{crit,max}/a_{crit,init}$. When the stars start with $P_{rot} \lesssim 1$ days, $a_{crit,max}/a_{crit,init}$ readily grows to $\gtrsim 1.1$, large enough to destabilize some CBPs near the dynamical stability boundary. | 80 |

| | | |
|------|--|----|
| 3.10 | Scatter plot of the initial orbital angular momentum J_{orb} , versus the ratio of total initial stellar rotational angular momentum to the initial orbital angular momentum, $J_{rot,tot}/J_{orb}$. Each point is colored by the $a_{crit,max}/a_{crit,init}$ achieved in that simulation. Simulations with an initial angular momentum ratio of $\gtrsim 0.1$ tend to produce a large enough $a_{crit,max}/a_{crit,init}$ to destabilize a CBP. | 82 |
| 3.11 | Full evolution of binary systems using our default parameters from Table 3.1, except with initial eccentricities of $e = 0.15$ (blue) and $e = 0.3$ (orange). <i>Top:</i> a_{crit} vs. time. The systems attain $a_{crit,max}/a_{crit,init} = 1.16, 1.19$ for binaries with initial eccentricities of $e = 0.15$ and $e = 0.3$, respectively. <i>Middle:</i> Orbital and stellar rotation period vs. time. Both systems tidally lock after ~ 1 Myr into 1:1 (blue) and 3:2 (orange) spin-orbit resonances. <i>Bottom:</i> e vs. time. The dotted line demarcates binaries that tidally locked into a 3:2 (above the line) and 1:1 (below the line) spin-orbit resonance. | 84 |
| 3.12 | <i>Left:</i> a_{crit} as a function of time. The black horizontal line indicates when stellar radii overlap and the stars merge, halting the simulation. <i>Right:</i> Maximum critical semi-major axis divided by the critical semi-major axis observed at time t , $a_{crit,max}/a_{crit,t}$. Depending on the magnetic braking physics, the observed a_{crit} can differ from its maximum by an order of magnitude. | 85 |
| 3.13 | Histograms of the maximum a_{crit} divided by the critical semi-major axis observed at time t , $a_{crit,max}/a_{crit,t}$ for the binary systems simulated in § 3.4.6 observed at 100, 500, 1000, and 2000 Myr (blue, orange, red, and grey histograms, respectively). In general for older systems, $a_{crit,max}/a_{crit,t}$ increases as a_{crit} recedes due to angular momentum loss via magnetic braking in tidally locked systems. The distribution of $a_{crit,max}/a_{crit,t}$ smears out and develops an extended tail for older systems due to the different tidal and rotational properties of the binary systems. | 87 |
| 3.14 | Binary orbital evolution for several plausible sets of initial conditions. <i>Top Left:</i> a_{crit} vs. time. <i>Top Right:</i> Binary orbital period vs. time. <i>Bottom Left:</i> e vs. time. <i>Bottom Right:</i> $a_{crit,max}/a_{crit,init}$ for the five cases. The blue, orange, green, red, and purple curves correspond to cases A, B, C, D, and E, respectively. In agreement with previously discussed simulations, we find that initial fast rotators with smaller tidal Qs achieve large $a_{crit,max}/a_{crit,init}$ up to of order 2 for plausible initial conditions. | 89 |
| 3.15 | Histogram of planet c's fraction of time spent transiting one of the binary stars for Neptune- (<i>Left:</i>), Saturn- (<i>Middle:</i>), and Jupiter-mass (<i>Right:</i>) exoplanets. The orange histograms correspond to when c remains stable while b goes unstable and the blue curve corresponds to when both b and c remain stable. The solid and dashed histograms correspond to cases where both planets' initial inclinations are uniformly sampled from $[0^\circ, 1^\circ]$ and $[0^\circ, 3^\circ]$, respectively. Generally, the larger the mutual inclination, the less time c spends transiting. | 94 |

| | | |
|------|---|-----|
| 4.5 | Median P_{orb}/P_{rot} at the end of the simulation according to the CPL (left) and CTL (right) models binned by $\log_{10}(Q)$ and $\log_{10}(\tau)$, respectively, and P_{orb} . For $P_{orb} < 10$ d, the CPL model predicts that most systems will tidally lock into synchronous rotation, whereas the CTL model requires $\tau \geq 0.1$ s to tidally lock. For large $Q (> 10^7)$ and small $\tau (\tau < 0.1$ s), weak tidal torques cannot prevent magnetic braking from spinning down stars past the tidally locked state, producing a population of subsynchronous rotators (red regions, $P_{rot} > P_{orb}$). | 124 |
| 4.6 | Median $\log_{10}(Q)$ of primary stars binned by P_{orb} and P_{orb}/P_{rot} evolved using the CPL model. | 125 |
| 4.7 | Same format as Fig. 4.6, but for $\log_{10}(\tau[s])$ under the CTL model. | 127 |
| 4.8 | Evolution of stellar P_{rot} , normalized by P_{eq} (see Eqn. (4.20) and Eqn. (4.22)), for initial circular binary orbits with initial $P_{orb} = 7.5$ d according to the CPL (solid) and CTL (dashed) models for several values of Q and τ , respectively, using the Matt et al. (2015) magnetic braking model. Systems with strong tidal torques tidally lock, whereas in systems with weaker tidal torques (larger Q and smaller τ , respectively), magnetic braking initially overpowers tidal torques, spinning down the stars past the tidally locked state, resulting in subsynchronous rotation. | 129 |
| 4.9 | Rotation state for tidally locked (blue, $P_{rot} = P_{eq}$), interacting (green, P_{rot} within 10% of P_{eq} and not locked), and not locked (orange, remainder of binaries) stellar binaries. Left: P_{rot} as a function of stellar mass and age according to our CPL simulations integrated to system ages uniformly sampled over 1 – 7 Gyr. Right: Marginalized P_{rot} distribution for each case. Top: Marginalized mass distributions. | 131 |
| 4.10 | Same format as Fig. 4.9, but for the CTL simulations. | 132 |
| 4.11 | P_{rot} distribution for tidally locked (blue) and interacting (green, P_{rot} within 10% of P_{eq} and not locked) binaries according to the CPL (solid line) and CTL (dashed line) models. | 134 |
| 4.12 | P_{rot} as a function of stellar mass and age according to our CPL (left), CTL (left center), and single star (right center) simulations integrated to system ages uniformly sampled over 1 – 7 Gyr using the Matt et al. (2015) magnetic braking model. For each case, we only plot 2,500 systems for clarity but account for all systems when computing the marginalized distributions. Right: The P_{rot} distribution for each case, marginalized over stellar mass. | 135 |
| 4.13 | Relative age error between single and binary stars for both the CPL (left) and CTL (right) tidal models. The error is computed as the percent difference between the mean ages of single and tidally interacting binary stars in mass and P_{rot} bins. | 136 |

| | |
|---|-----|
| 4.14 Histogram of rapidly-rotating ($P_{rot} < 20$ d) star ages for single and primary stars in binaries from Fig. 4.12. Rapidly-rotating single stars must be young (ages $\lesssim 2$ Gyr), while tidally locked rapidly-rotating binaries exhibit a wide range of ages. . . | 138 |
| 4.15 P_{orb}/P_{rot} as a function of P_{orb} according to the CPL model (left) and the CTL model (middle), and Lurie et al. (2017) <i>Kepler</i> EB observations (right). All points are colored by e . In the right panel, the <i>Kepler</i> EBs at low P_{orb} and low P_{orb}/P_{rot} are likely either brown dwarfs or exoplanets (Lurie et al., 2017), and hence are not modeled by our simulations, so we do not consider them, but we display them for completeness. | 140 |
| 5.1 Same as Fig. 6.2, but overplotted with the training set for <code>approxposterior</code> 's GP. The orange points display the initial training points whereas the blue points display the points iteratively selected by maximizing the Kandasamy et al. (2017) utility function, Eqn. (5.2). By design, <code>approxposterior</code> selected points to expand its training set in regions of high posterior density, improving its GP's predictive accuracy in the most relevant regions of parameter space while seldom wasting computational resources in the low likelihood regions. | 155 |
| 5.2 The <code>approxposterior</code> convergence diagnostic, z_t , as a function of iteration for the run presented in the Chapter 6. Note that in <code>approxposterior</code> , the initial iteration is iteration 0. The black dashed line indicates the adopted convergence threshold of $\epsilon = 0.1$. <code>approxposterior</code> quickly converges to a consistent and accurate result. | 158 |
| 5.3 The posterior probability distribution for the 2D Rosenbrock example from Wang and Li (2018) estimated by <code>approxposterior</code> . The red points denote points selected by <code>approxposterior</code> 's training set augmentation scheme using the BAPE algorithm. As explained above, <code>approxposterior</code> preferentially selects points in regions of high posterior density. The posterior distribution estimated by <code>approxposterior</code> is in good agreement with the results of Wang and Li (2018), their Figures 1 and 3. | 161 |
| 5.4 Joint and marginal posterior probability distributions derived by <code>emcee</code> (purple) and <code>approxposterior</code> (orange) from an atmospheric retrieval of a simulated noised JWST transmission spectrum of TRAPPIST-1e (used with permission from Lustig-Yaeger et al., in prep). This retrieval experiment attempts to infer the isothermal atmospheric temperature, T , and the mixing ratios of H ₂ O and CO ₂ . <code>approxposterior</code> accurately recovers both the nontrivial correlations between model parameters and marginal parameter constraints as did <code>emcee</code> , within Monte Carlo error, but requiring about 800 times fewer computational resources. | 165 |

| | | |
|-----|--|-----|
| 6.1 | Joint and marginal posterior probability distributions for the TRAPPIST-1 stellar parameters given in Eqn. (6.2) made using <code>corner</code> (Foreman-Mackey, 2016). The black vertical dashed lines on the marginal distributions indicate the median values and lower and upper uncertainties from the 16th and 84th percentiles, respectively. The blue curves superimposed on the marginal distributions display the adopted prior probability distribution for each parameter. From the posterior, we infer that there is a 40% chance that TRAPPIST-1 is still in the saturated phase today. ¹⁷⁷ | 177 |
| 6.2 | Same format as Fig. 6.1, but derived by <code>approxposterior</code> . <code>approxposterior</code> recovered constraints and parameter correlations that are in good agreement with the <code>emcee</code> MCMC, but requiring $980 \times$ less computational resources. | 179 |
| 6.3 | Same format as Fig. 6.1, but with the fiducial posterior distribution in black and the <code>approxposterior</code> -derived posterior distribution in blue. The joint and marginal posterior distributions estimated by <code>approxposterior</code> are in excellent agreement with our fiducial <code>emcee</code> -derived results. | 181 |
| 6.4 | Plausible evolutionary histories of TRAPPIST-1's L_{bol} (left), L_{XUV} (center), and radius (right) using 100 samples drawn from the posterior distribution and simulated with <code>VPLanet</code> . In each panel, the blue shaded regions display the 1, 2, and 3 σ uncertainties. The insets display the marginal distributions (black) evaluated at the age of the system, with the blue dashed lines indicating the observed value and $\pm 1 \sigma$ uncertainties. The radius, L_{bol} , and L_{XUV} constraints are adopted from Van Grootel et al. (2018) and Wheatley et al. (2017), respectively, by convolving the Van Grootel et al. (2018) L_{bol} measurement with the L_{XUV}/L_{bol} constraints from Wheatley et al. (2017). | 182 |
| 6.5 | $F_{XUV}/F_{XUV,\oplus}$ for each TRAPPIST-1 planet derived from samples drawn from the posterior distribution and simulated using <code>VPLanet</code> when the system was 0.01, 0.1, and 1 Gyr old. The latter age corresponds to the approximate age at which TRAPPIST-1 entered the main sequence. The TRAPPIST-1 planetary system has likely endured a long-lasting extreme XUV environment. | 185 |

LIST OF TABLES

| Table Number | Page |
|--|------|
| 2.1 Kepler 38 parameters adapted from Orosz et al. (2012) | 8 |
| 2.2 Simulation parameters. | 11 |
| 3.1 Parameter Ranges | 63 |
| 3.2 N-body Simulation Initial Condition Ranges | 68 |
| 3.3 Single Planet System Outcome Fraction | 90 |
| 3.4 Circumbinary planetary system N-body simulation outcome fractions. | 92 |
| 6.1 Prior Distributions | 173 |
| 6.2 Parameter Constraints and Errors | 182 |

ACKNOWLEDGMENTS

I would like to acknowledge that we are on the traditional land of the first people of Seattle, the Duwamish People past and present and honor with gratitude the land itself and the Duwamish Tribe.

DEDICATION

To my wife, Anya

Chapter 1

INTRODUCTION

1.1 What Does the Present Tell Us About the Past?

Planets are inextricably linked to their host stars through their common birth environment. Numerous intertwined astrophysical processes, ranging from tidal forces to stellar high-energy emission, shape the long-term evolution of planetary systems. Modern astronomical surveys have produced a wealth of information to both discover planet-hosting stars and help elucidate the processes that govern their evolution. Notably, completed missions such as *Kepler* and *K2*, and the in-progress Transiting Exoplanet Survey Satellite (TESS), monitor the long-term bright variation of thousands of stars to detect transiting exoplanets and eclipsing binary stars, massively increasing the known population of such systems. Furthermore, future missions such as the James Webb Space Telescope (JWST) will attempt to detect and characterize the first terrestrial planetary atmospheres, likely the inner-most planets of the nearby TRAPPIST-1 system (Lustig-Yaeger et al., 2019). With such large amounts of data comes an unprecedented opportunity for both population-level statistical studies and individual target characterization to infer the fundamental properties of the populations of stars and their planets.

An unavoidable problem for astronomy, however, is that the timescales over which astrophysical processes operate are often much, much longer than the lifetime of a single astronomer, or even the duration of recorded human history. For example, the lifetime of Sun-like stars is of order 10 billion years, a factor of 10^7 longer than an optimistic estimate for the lifetime of a person. How can we hope to learn about the long-term evolution of such objects? Astronomers are therefore reduced to observing brief snapshots of the cosmos over time, dramatically complicating the challenge of teasing out what processes govern what we observe. The fundamental problem of astronomy therefore becomes, given what we observe, how can we infer what processes produced

what we see, and what does this information tell us about the past and future evolution of this celestial object?

Interpreting and understanding observations of astrophysical systems requires a theoretical model. In the case where observations have not yet been made, e.g. the detection of a terrestrial exoplanetary atmosphere, theoretical models can be used to make predictions that will aid in the interpretation of such observations. For potentially habitable terrestrial exoplanets, for example, Luger and Barnes (2015) showed how large pre-main sequence luminosities of low-mass stars drive water photolysis during an extended runaway greenhouse phase, potentially causing extreme amounts of O₂ to build up in their atmospheres, significantly impacting the exoplanets' observed spectra. When observations are available, model predictions can be conditioned on the observations to derive constraints on model parameters, that is, astronomers can attempt to match their model outputs with the observations within the uncertainties. Typically, model parameters represent physically meaningful quantities, like an exoplanet's radius or an atmospheric chemical abundance, that we hope to infer to understand the underlying astrophysical processes at work.

When future facilities, like JWST, go online and attempt to characterize terrestrial exoplanetary atmospheres in the search for biosignatures, astronomers will use complex radiative transfer codes to derive atmospheric compositions (e.g. SMART; Meadows and Crisp, 1996; Crisp, 1997). Critical to understanding and interpreting these results is determining how the exoplanet and its atmosphere evolved to its present state. To answer this question, one must use theoretical models, conditioned on the observations, to simulate the system's long-term evolution. These problems are not limited to observations of exoplanets, however, as observations of stellar systems, e.g. *Kepler* eclipsing binary orbital and rotation synchronization measurements (Lurie et al., 2017), also require theoretical modeling of their long-term evolution to interpret observations.

Many theoretical studies examine the long-term evolution of systems to interpret observations and constrain parameters, i.e. exoplanetary rotation rates, stellar tidal Qs, etc, do so in the form of "best fit models" by finding the set of model parameters that best reproduce the observations. Another common technique is performing a grid search through parameter space to examine how model predictions vary as a function of model parameters. For example, Ribas et al. (2016) and

Barnes et al. (2016) both employed the aforementioned techniques when examining the long-term dynamical and atmospheric evolution of Proxima Centauri b to estimate its present-day potential habitability. These techniques are useful and informative, but ultimately insufficient, however, as a robust analysis used to interpret observations must be based in a probabilistic framework in which model predictions are conditioned on the observations and the associated uncertainties, e.g. by using a statistical technique like Bayesian inference. Any constrained parameter requires an uncertainty estimation to put the interpretation in context and permit a robust, credible interpretation of the results. For example, if a forward model yields a best fit prediction of 1 Earth ocean of liquid surface water remaining on an exoplanet, uncertainties are required to interpret this result. If instead, in this example, one propagated uncertainties through the forward model to find that the remaining surface water content is 1^{+10}_{-1} Earth oceans, the planet's current state ranges from desiccated to water-rich, with both cases entirely consistent with the observations, yet indicative of significantly different evolutionary histories.

1.2 *Dissertation Outline*

Here I sketch the outline for my entire dissertation, chapter-by-chapter.

Finally, I summarize my findings and discuss prospects for related future research.

Chapter 2

DYNAMICS IN THE BIRTHPLACE OF PLANETS: EXAMINING THE RESONANT DYNAMICAL INTERACTIONS BETWEEN BINARY STARS AND CIRCUMBINARY DISKS

Portions of this chapter were originally published in collaboration with Thomas R. Quinn in the January 2017 edition of the Monthly Notices of the Royal Astronomical Society (Fleming and Quinn 2017, MNRAS, Vol. 464, 3; p.3343-3356, 2017 © Monthly Notices of the Royal Astronomical Society, DOI: 10.1093/mnras/stw2624), and are reproduced below with permission of the Monthly Notices of the Royal Astronomical Society.

2.1 Introduction

All planets form, accrete, and evolve in protoplanetary disks (e.g. Lin et al., 1996; Nelson et al., 2000; Papaloizou and Terquem, 2006; Rogers et al., 2011; Bodenheimer and Lissauer, 2014), so any study the observed properties and evolutionary histories of exoplanets must include a discussion of their birth environment. Protoplanetary disks are dynamically active environments, with the potential for planetary migration and scattering events that can shape the resultant exoplanetary system. Circumbinary protoplanetary disks are particularly dynamically hot environments as all the aforementioned phenomenon can occur (e.g. Pierens and Nelson, 2013), with the added complication of dynamical coupling between the binary and disk (Papaloizou et al., 2001). This coupling influences both the binary orbital elements and the disk dynamics, constituting a complex interplay that influences the birth location of circumbinary planets (CBPs). Moreover, while binary stars are embedded in their natal circumbinary disks, the stars contract along the pre-main sequence and tides shape the binary's orbit, producing complex, dynamically active evolutionary histories for binary star systems and any exoplanets they may host. In this Chapter, I examine the

dynamical coupling of binaries and their gaseous protoplanetary circumbinary disks to characterize their coevolution.

Observations by *Kepler* of binary systems have so far yielded 11 transiting circumbinary planets. Until recently, all discovered circumbinary planets have resided near to or outside the dynamical stability limit characterized by Dvorak (1986); Holman and Wiegert (1999). This finding has prompted many to study how planets form in such systems and why they seem biased towards lying at the brink of dynamical instability (Welsh et al., 2014; Pierens and Nelson, 2013). Simulations and theoretical arguments by Pelupessy and Portegies Zwart (2013) and Bromley and Kenyon (2015) rule out in situ formation in the inner edge of the disc near where several circumbinary planets have been observed. Currently, one of the most successful models in explaining the circumbinary planet population is planetary migration. In this model, a planet, having formed farther out in the disc, migrates inward through viscous interactions with a gaseous disc, potentially undergoing planet-planet scattering, until it reaches near its observed location. Several previous studies applied migration to observed circumbinary planetary systems and have been able to show that for certain disc and viscous drag models, the observed planet orbits are nearly recovered (e.g. Kley and Haghighipour, 2014, 2015; Pierens and Nelson, 2007, 2013).

However, the recent discovery by Kostov et al. (2016) of the first long-period transiting circumbinary planet complicates this picture. The newly discovered planet candidate, KOI-2939b, is a Jupiter-sized exoplanet on a roughly 3 year orbit that suggestively lies in the conservative habitable zone of two short-period G dwarfs (Kostov et al., 2016). The existence of a such a system shows that not all circumbinary planets are driven, either through migration or other mechanisms, inward towards the dynamical stability limit. This has important consequences for not only how planets migrate and evolve in a viscous circumbinary disc, but also for how and where these planets form within the protoplanetary disc.

Clearly, characterizing the influence exerted on the planet by the protoplanetary disc is important for understanding how such systems form. Additionally, the influence of the central binary on the external disc causes the disc to evolve and potentially undergo large scale changes. Previous studies of both protoplanetary disks and accretion disks around binary supermassive black holes

(SMBHs) found that circumbinary disks can become eccentric, precess, and have density waves excited from resonances (Dunhill et al., 2015; MacFadyen and Milosavljević, 2008; Papaloizou et al., 2001; Pierens and Nelson, 2007, 2013; Roedig et al., 2012). Specifically in the context of planetary systems, a hydrodynamic theory presented by Lubow (1991) showed that nonlinear coupling mediated by density waves launched at eccentric Lindblad resonances causes disc eccentricity growth.

Much theoretical work in this area has focused on how planetesimals can grow and evolve in circumbinary disks. Paardekooper et al. (2012) found that for planetesimals on circumbinary orbits, *in situ* formation proves quite difficult, suggesting that planets form far out in the disc and subsequently migrate inward. More recently, Bromley and Kenyon (2015) showed that planetesimals on the most circular orbit about the central binary can attain small relative velocities, facilitating their growth. With a model that considers both the gravity and gas drag of a precessing, eccentric circumbinary disc, Silsbee and Rafikov (2015) found that the inner radius for 10 – 100m planetesimal growth depends on the disc eccentricity, density and precession rate. The binary’s influence on the disc is not without a cost, however, as the disc also drives changes in the binary orbital elements, which as they evolve, can change how the binary influences the disc.

Early work on how binary systems interact with accretion disks by Goldreich and Tremaine (1980) studied Jupiter’s interaction with the Sun’s protoplanetary disk. This study showed that a satellite’s orbital eccentricity could be increased through energy and momentum transfers with the disk at Lindblad resonances, causing significant changes over a few thousand years. The case of accretion disks around two objects was explored by Pringle (1991) and later by Papaloizou et al. (2001). Pringle (1991) found that a central binary’s interaction with an external accretion disk can decrease binary separation and change binary eccentricity, depending on disk structure. In the context of a Jupiter to brown dwarf mass companion orbiting a central star, Papaloizou et al. (2001) found that for sufficiently massive companions, a coupling between small initial disk eccentricity and the companion’s tidal potential excited an $m = 2$ wave from the 1:3 EOLR causing further disk eccentricity growth. Wave excitation at the 1:3 EOLR can also couple with the interaction between the eccentric disk and the companion to induce orbital eccentricity growth of the companion.

Many recent and past works explored the more general case of binary stars evolving under the influence of a gaseous circumbinary disk. Simulations of unequal mass binaries embedded in a protoplanetary disk by Artymowicz et al. (1991) show rapid binary eccentricity growth and semi-major axis decay due to interactions with the 1:3 EOLR and the viscous disk. Subsequent theoretical work by Lubow and Artymowicz (1996) and Lubow and Artymowicz (2000) derived relations to show how resonant and viscous interactions drive \dot{e}_{bin} and \dot{a}_{bin} . Binary orbital element and disk evolution has also been explored in systems with circumbinary gaseous disks containing migrating planets in simulations by Pierens and Nelson (2007) who also found binary and disk eccentricity growth.

Characterizing disk-binary interactions are important on much larger scales, as well. Simulations by Mayer et al. (2007) show that eccentric supermassive black hole binaries can rapidly form from the merger between two spiral galaxies. An external disk forms exterior to the SMBH binary as interactions with the disk and external gas clouds can cause the black hole separation to decrease (Roškar et al., 2015). Numerous studies have been conducted to explore how binary SMBH-disk interactions cause binary SMBH eccentricity growth and semi-major axis decay, possibly explaining the “last parsec” problem allowing SMBH binaries to coalesce (e.g. Armitage and Natarajan, 2005; Escala et al., 2005; Cuadra et al., 2009; Roedig et al., 2012; Aly et al., 2015). Extensive work has also been made to explore accretion onto binary SMBHs, how it varies with both the binary and disk properties and what impact accretion has on the dynamical properties of the system (e.g. Shi et al., 2012; D’Orazio et al., 2013; Nixon et al., 2013; Farris et al., 2014).

For circumbinary systems, the binary and its disk are intertwined in non-trivial ways. The coevolution of such systems depends strongly on resonant interactions that can impart significant changes on both the binary and disk. Previous simulations focused on studying either disk evolution or binary evolution, often making approximations such as holding the binary orbital elements fixed. In this work we seek to explore how the coevolution of the disk and binary proceeds by allowing all particles to gravitationally interact. Using the Kepler 38 binary as our model system, we present the results of N-body SPH simulations of unequal mass binaries of variable initial eccentricity that probe the dynamical coupling of binary stars and a circumbinary disk. We show

| $m_1 [M_\odot]$ | $m_2 [M_\odot]$ | $a_{bin} [\text{AU}]$ | e_{bin} |
|-----------------|-----------------|-----------------------|-----------|
| 0.949 | 0.249 | 0.1469 | 0.1032 |

Table 2.1: Kepler 38 parameters adapted from Orosz et al. (2012).

that the initial eccentricity of the binary dictates how strongly the disk-binary system resonantly couples. The strength of this coupling in turn dictates how eccentricity grows in either the disk, the binary or both and how structure forms within the disk.

2.2 Simulations

2.2.1 Methods

The simulations described in this paper were performed in 3D using the massively parallel N-body and Smooth Particle Hydrodynamics (SPH) code, ChaNGa (Menon et al., 2015).¹ ChaNGa, implemented in Charm++ (Kale and Krishnan, 1996), uses a modified version of the Barnes-Hut tree algorithm with hexadecapole order multiples and a node opening criterion of $\theta_{BH} = 0.7$ for fast and accurate calculation of gravitational forces. The Euler equations which describe the gas dynamics of the simulated circumbinary disk were solved using an SPH implementation based on Wadsley et al. (2004). ChaNGa uses a multisteping algorithm that gives each particle its own timestep to ensure sufficient dynamical resolution (Quinn et al., 1997). Artificial viscosity was implemented using Monaghan viscosity (Monaghan and Gingold, 1983). The viscosity α_{SPH} and β_{SPH} parameters were set to 1 and 2, respectively. The Balsara switch was used to limit shear viscosity (Balsara, 1995). For additional information about the implementation and performance of ChaNGa see Jetley et al. (2008).

The orbits of both the binary and all the disk particles are computed using ChaNGa’s implementation of the symplectic leapfrog integrator. Each particle feels the force of gravity due to every other particle, including the two stars. Since the orbits of the stars are not integrated using a higher order technique, we employed conservative time stepping. We ran simulations shrinking time step-

¹A public version of ChaNGa is available from <http://www-hpcc.astro.washington.edu/tools/changa.html>.

ping parameters to ensure that the binary orbit was accurately resolved such that any evolution in the orbital parameters is due to gravitational interactions with the disk and not any numerical effects. The timestep picking criterion used was bGravStep where $\Delta t = \eta / \sqrt{r/a}$ where a is the acceleration of the particle, r is the distance to the particle or node that causes the largest acceleration and η is an accuracy parameter. We used this timestep criterion as its form is particularly suited for Keplerian orbits, and in the absence of collisions, it has the desirable property of giving the particle a fixed number of timesteps per orbital period ($n = 2\pi/\eta$) (Richardson et al., 2000). We found that $\eta = 0.005$ yielded sufficiently small timesteps to properly resolve the dynamics of the binary. In addition, we used a Courant number of 0.4 for enforcing the Courant condition.

All simulations were ran on the University of Washington’s Hyak supercomputer cluster. Each simulation was ran on either a 12 or 16 core node for about a month each with roughly 8,000 core hours used per simulation on average. In total, over 100,000 core hours were used for the entire suite of simulations.

2.2.2 Model Parameters

The model system studied in this paper is Kepler 38, a binary composed of a G and an M dwarf. The physical parameters for this system were adapted from Orosz et al. (2012) and are given in Table 2.1. We ran eight simulations of Kepler 38 embedded in a circumbinary disk for 10^4 binary orbits, about 520 years. The simulations considered in this paper were ran primarily to examine how the surrounding circumbinary disk impacts the dynamics of the central binary as a function of the eccentricity of the binary, e_{bin} , and how the disk in turn evolves. The disk masses are also varied in Simulations 6, 7, and 8 to explore its role in the evolution of the binary’s orbital parameters. We study the sensitivity of our results on disk resolution and aspect ratio in Simulations 9, 10, and 11 with discussion in Section 2.4. A summary of the relevant simulation parameters used in this study are given in Table 2.2.

2.2.3 Initial Conditions

Initial conditions for the circumbinary disk were computed using the Python package *diskpy*². Given the stellar and disk parameters, *diskpy* calculates the positions and velocities for gas particles for a protoplanetary disk in equilibrium. Each gas particle is placed on a circular orbit about the the binary’s barycenter assuming a central mass equal to the total binary mass. The gas particles’ orbits also feel the force of radial pressure gradients within the disk. Great care was taken to ensure that the disk was as close to equilibrium as possible in both the radial and vertical directions to avoid any influence from an initial disequilibrium state. For a more in-depth description of the initial conditions generated by *diskpy*, see Backus and Quinn (2016).

The disk, composed of 10^5 SPH particles unless stated otherwise, has initial inner and outer boundaries of 0.25 and 4.0 AU, respectively. The initial surface density profile of the disk is set to

$$\Sigma(r) = \Sigma_0 r^{-1/2} \quad (2.1)$$

where Σ_0 is assigned such that if the disk extended to 10 AU, it would have a total mass of about $0.01 M_\odot$, similar to the models of Pierens and Nelson (2007) and Kley and Haghighipour (2014). To prevent numerical artefacts, the disk inner and outer edges of the surface density profiles are smoothed. For the inner edge, a smooth polynomial spline approximation to a step function is used while the outer edge of the disk is given by an exponential cutoff.

An open boundary condition is applied at the inner disk edge such that inflowing particles are allowed to be accreted by the central binary. The stars, modeled as “sink” particles, accrete a gas particle if it enters the Roche lobe of a star. This process is modeled by adding the mass of the accreted gas particles to the star’s mass and conserving linear momentum throughout the accretion process. Unless stated otherwise, the sink radius was set to 0.066 AU. A simulation was ran with a sink radius a factor of 5 smaller than the typical value and we found that our results were not affected.

²*diskpy* GitHub repository: <https://github.com/ibackus/diskpy>

| Simulation Number | e_{bin} | $M_{disk} [\text{M}_\odot]$ | N_{gas} | H/R |
|-------------------|-----------|-----------------------------|-----------------|------|
| 1 | 0 | 0.00383 | 10^5 | 0.06 |
| 2 | 0.001 | 0.00383 | 10^5 | 0.06 |
| 3 | 0.05 | 0.00383 | 10^5 | 0.06 |
| 4 | 0.1032 | 0.00383 | 10^5 | 0.06 |
| 5 | 0.25 | 0.00383 | 10^5 | 0.06 |
| 6 | 0.1032 | 0.00766 | 10^5 | 0.06 |
| 7 | 0.1032 | 0.00192 | 10^5 | 0.06 |
| 8 | 0.1032 | 0.00574 | 10^5 | 0.06 |
| 9 | 0.1032 | 0.00383 | 5×10^4 | 0.06 |
| 10 | 0.1032 | 0.00383 | 2×10^5 | 0.06 |
| 11 | 0.1032 | 0.00383 | 10^5 | 0.12 |

Table 2.2: Simulation parameters.

The disk has a locally isothermal temperature profile following

$$T(r) = T_0(r_0/r) \quad (2.2)$$

where at 1 AU from the barycenter, T_0 is 750 K. Unless otherwise specified, the circumbinary disks are initialized to be stable against axisymmetric perturbations with $Q_{min} > 1.5$ (Toomre, 1964). The vertical scale height of the disk, H , was on average resolved by 2.5 resolution lengths, h , where $2h$ is the distance to the nearest 32 neighboring SPH particles.

2.3 Results and Analysis

2.3.1 Gap Clearing

As the simulation evolves, the time varying gravitational force of the binary truncates the inner edge of the circumbinary disk and excites various Lindblad resonances within the disk. The gap, cleared quickly in about 100 binary orbits, is preserved by a balance of resonant and viscous torques within the disk (Artymowicz and Lubow, 1994). For larger gaps, corotation and Lindblad resonances can fall within the evacuated region removing their influence from the system. These resonances, especially those closest to the inner edge of the disk, can drive evolution in the binary's

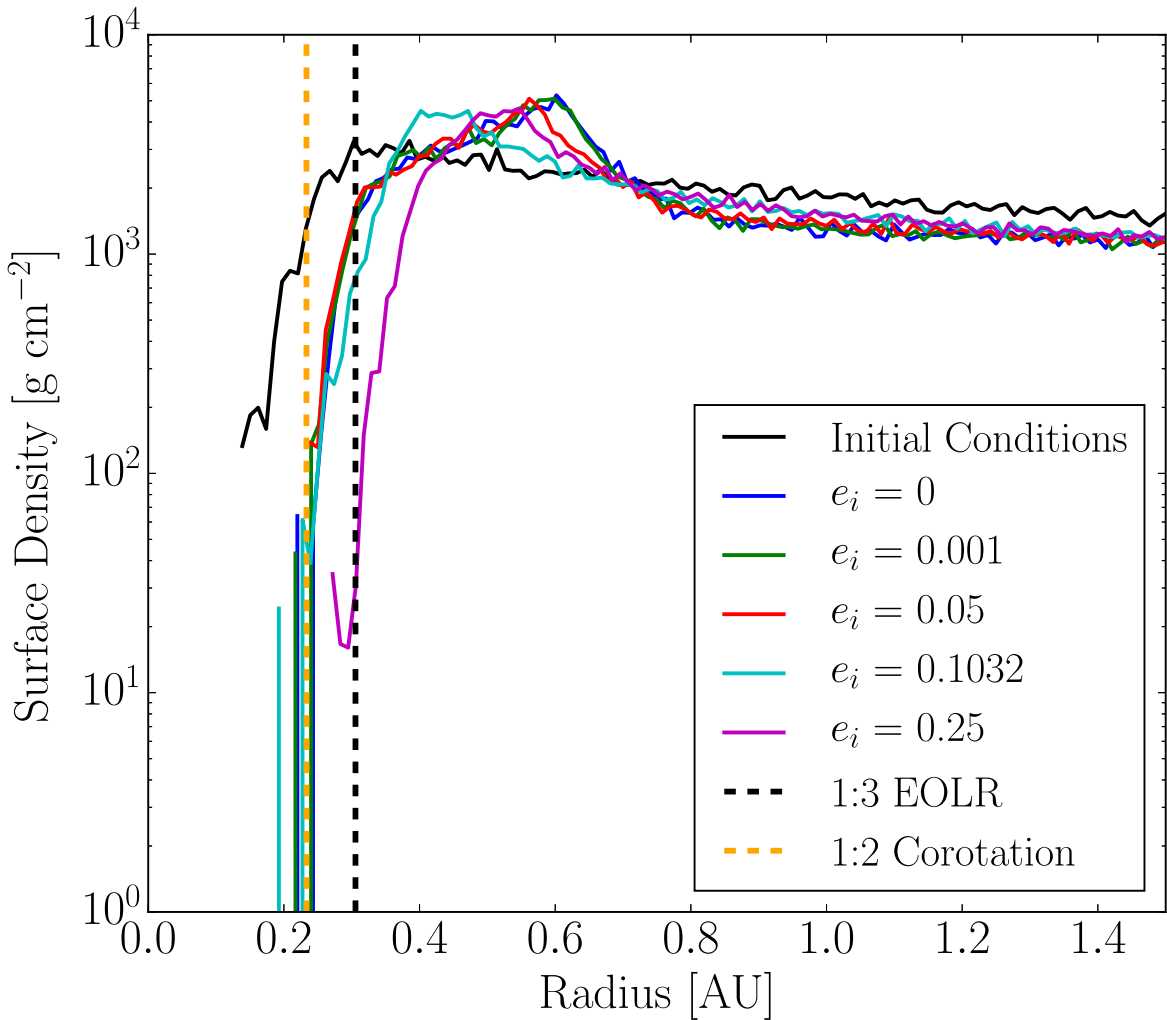


Figure 2.1: Azimuthally averaged surface density profiles for Simulations 1-5 after 200 years of evolution. Overplotted are the 1:3 EOLR (dashed black line) and the 1:2 corotation resonance (dashed orange line).

orbital elements (Goldreich and Tremaine, 1980; Artymowicz et al., 1991) and pump eccentricity in the disk (Papaloizou et al., 2001). Therefore, in order to understand the subsequent dynamical evolution of both the binary and the disk, the inner disk edge structure must be understood to see which resonances may play a role. The approximate size of the gaps found in these simulations is $r \approx 2a_{bin}$ with more eccentric binaries producing larger gaps, in good agreement with the results of Artymowicz and Lubow (1994). Our results are also consistent with the findings of D’Orazio et al. (2016) who show that for binary mass ratios above $q = 0.04$ as is the case for our simulations, a hollow central cavity forms around the secondary within the circumbinary disk. Gaps of this size tend to remove the eccentricity-damping 1:2 corotation resonance while leaving the 1:3 EOLR as the closest to the inner disk edge at a radius of $2.08a_{bin}$ suggesting that this resonance dominates the evolution of the binary’s eccentricity and semi-major axis (Artymowicz et al., 1991; Artymowicz, 1992; Papaloizou et al., 2001).

To verify the absence of the 1:2 corotation resonance and prominence of the 1:3 EOLR, the surface density profiles for Simulations 1 – 5 are shown in Fig. 2.1 after 200 years of evolution. For all e_{bin} , the surface density at the 1:3 EOLR is at least an order of magnitude larger than at the 1:2 corotation resonance when it is present within the disk. Since the gap opens rather quickly, in of order 5 years for the Kepler 38 binary, this finding supports the hypothesis that the 1:3 EOLR will be the dominant resonance within the disk that will drive subsequent evolution within the system.

2.3.2 Disk Evolution

The structure and eccentricity of the protoplanetary disk was examined over 10^4 binary periods in over 230 snapshots for each simulation to track how it evolves with the central binary.

Disk Eccentricity Growth

A central binary excites eccentricity in the surrounding circumbinary disk via resonant gravitational interactions (Papaloizou et al., 2001; Artymowicz and Lubow, 1996). Previous simulations of circumbinary disks (Kley et al., 2008; Papaloizou et al., 2001; Pierens and Nelson, 2007, 2013)

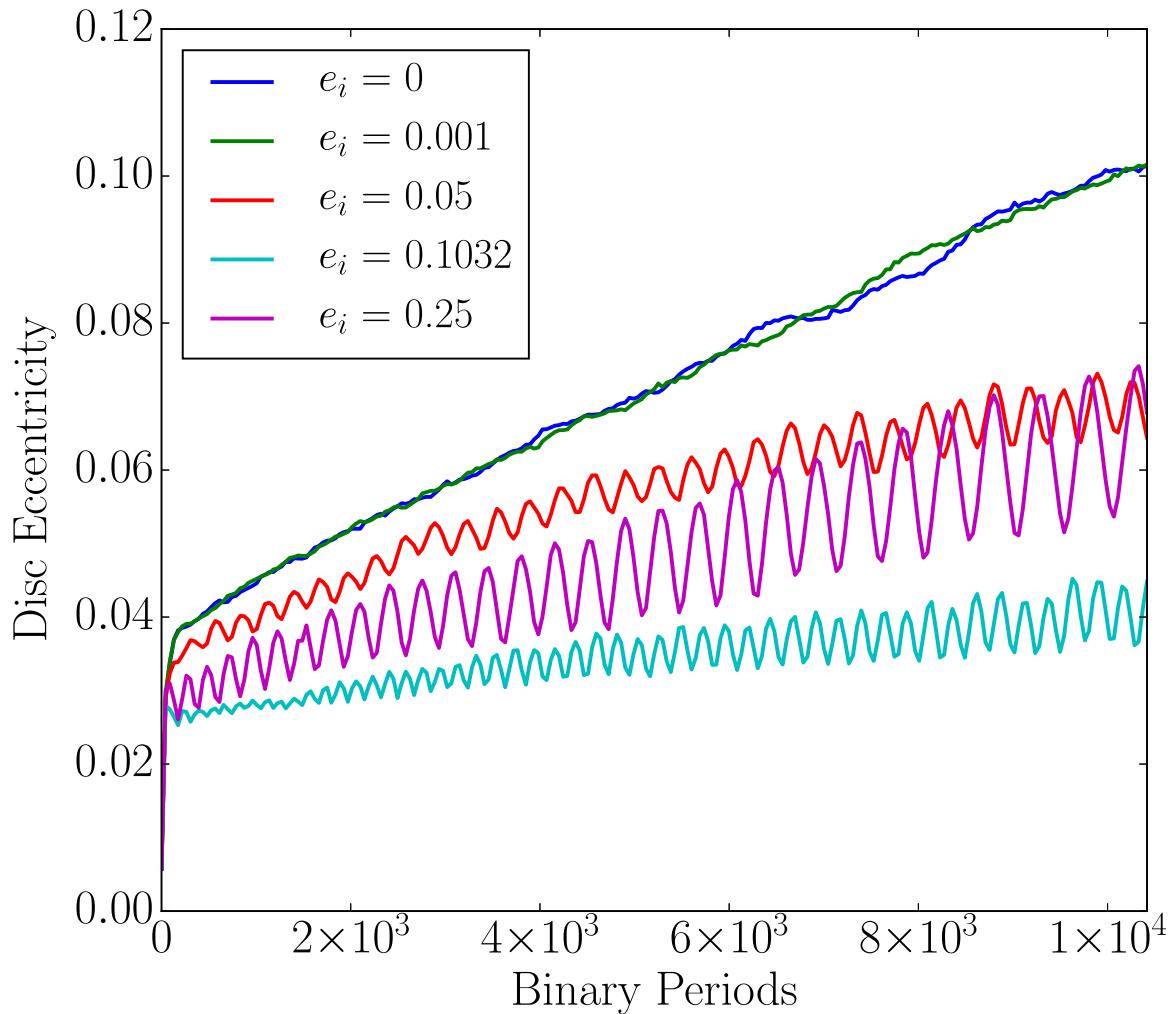


Figure 2.2: Disk eccentricity versus simulation time in units of binary orbits as a function of initial binary eccentricity.

found that disk eccentricity increases due to interactions that occur at the 1:3 EOLR. To explain why the disk becomes eccentric, Papaloizou et al. (2001) showed that disk eccentricity growth occurs via a parametric instability driven by coupling between the binary's tidal potential and a disk $m = 1$ mode due to a small initial disk eccentricity. This coupling excites an $m = 2$ spiral wave from the 1:3 EOLR that removes angular momentum from the disk at constant energy making the gas orbits eccentric. The material at the 1:3 EOLR rotates more slowly than the orbital pattern speed allowing the resonant torques to grow eccentricity in the system through the $m = 2$ wave. We therefore expect our circumbinary disks to become eccentric as well. To explore this effect in our simulations, we computed the disk eccentricity via a mass average following the prescription of Pierens and Nelson (2007)

$$\bar{e}_d = \frac{\int_0^{2\pi} \int_{R_{in}}^{R_{out}} e \Sigma r dr d\phi}{\int_0^{2\pi} \int_{R_{in}}^{R_{out}} \Sigma r dr d\phi}, \quad (2.3)$$

where Σ is the local surface density and the integral was evaluated out to a radius of 3 AU over 50 radial bins. The disk eccentricity in each radial bin was taken to be the mass-weighted average of the eccentricity of all gas particles within the bin assuming the particles orbit the system's barycenter. We neglected the influence of gas pressure in this calculation.

For all simulations, disk eccentricity growth is observed and consistent with the results of the similar gaseous circumbinary disk simulations of Kley et al. (2008), Pierens and Nelson (2007, 2013) and Farris et al. (2014). The disk eccentricity change over time for each simulation is shown in Fig. 2.2. For $e_{bin} \approx 0$, significant disk eccentricity growth occurs. After about 500 years, the disk reaches eccentricities of about 0.1 while continuing to grow linearly. For larger initial e_{bin} up to $e_{bin} \approx 0.1$, less eccentricity growth occurs indicating that more eccentric binaries tend to produce less eccentric disks.

For non-zero e_{bin} , the disk eccentricity grows linearly with a periodic modulation. The period of this disk eccentricity oscillation is similar to the inner disk edge clump precession timescale discussed in Section 2.3.2 below suggesting that the clump impacts the disc's eccentricity modulation, but only when the binary is sufficiently eccentric. This finding is consistent with the work

of Lubow and Artymowicz (2000) who explain that the inner disk edge precesses with a period of $10^2 - 10^3$ binary periods when $e_{disk}/e_{bin} \sim 0.2 - 0.7$.

We find that the global disk eccentricity growth is predominantly due to the inner edge of the disk becoming eccentric. Fig. 2.3 shows the disk eccentricity versus radius for Simulations 1-5 after about 520 years of evolution. For binaries with $e_{bin} \approx 0$, disk inner edge eccentricities are of order 0.4 while more eccentric binaries tend to produce less eccentric inner edges.

To understand the eccentricity growth of our circumbinary disks, specifically why less eccentric binaries tend to produce more eccentric disks, we turn to the theory of Papaloizou et al. (2001). Papaloizou et al. (2001) explains that a nonlinear coupling between the binary and a small initial disk eccentricity excites an $m = 2$ wave from the 1:3 EOLR within the disk with a resonant forcing pattern speed $\omega/2$ for binary orbital frequency ω . This wave transports angular momentum outwards, driving eccentricity growth in the system. We confirmed the presence of the $m = 2$ spiral wave originating from the 1:3 EOLR in our simulations via a Fourier transform over azimuthal angle of the disk surface density. This wave removes angular momentum from the disk, accounting for the increase in disk eccentricity.

Disc eccentricity growth as a function of e_{bin} depends on how strongly the binary couples to the disk. When strong coupling occurs, both the binary and inner disk edge grow to similar eccentricities while weak coupling results in the less massive of the binary or the disk inner edge developing appreciable eccentricity. For initially circular binaries, Papaloizou et al. (2001) described strong coupling as occurring when the disk mass within the gap radius is comparable to the mass of the secondary. For our simulations, the mass of the secondary is roughly an order of magnitude larger than the mass of the entire disk, so we expect the binary to be weakly coupled to the disk resulting in significant disk eccentricity growth as is observed in our simulations (see Fig. 2.2 and Fig. 2.3). For initially eccentric binaries, the Papaloizou et al. (2001) strong coupling criterion does not apply. Instead, we note that the time-averaged orbit of an eccentric binary corresponds to an azimuthal $m = 1$ mode perturbation to a circular orbit. This $m = 1$ mode couples to the $m = 1$ mode of the eccentric inner disk edge, placing the system in the strong coupling regime causing the disk eccentricity and e_{bin} to grow to similar magnitudes, as is observed in our simulations (see

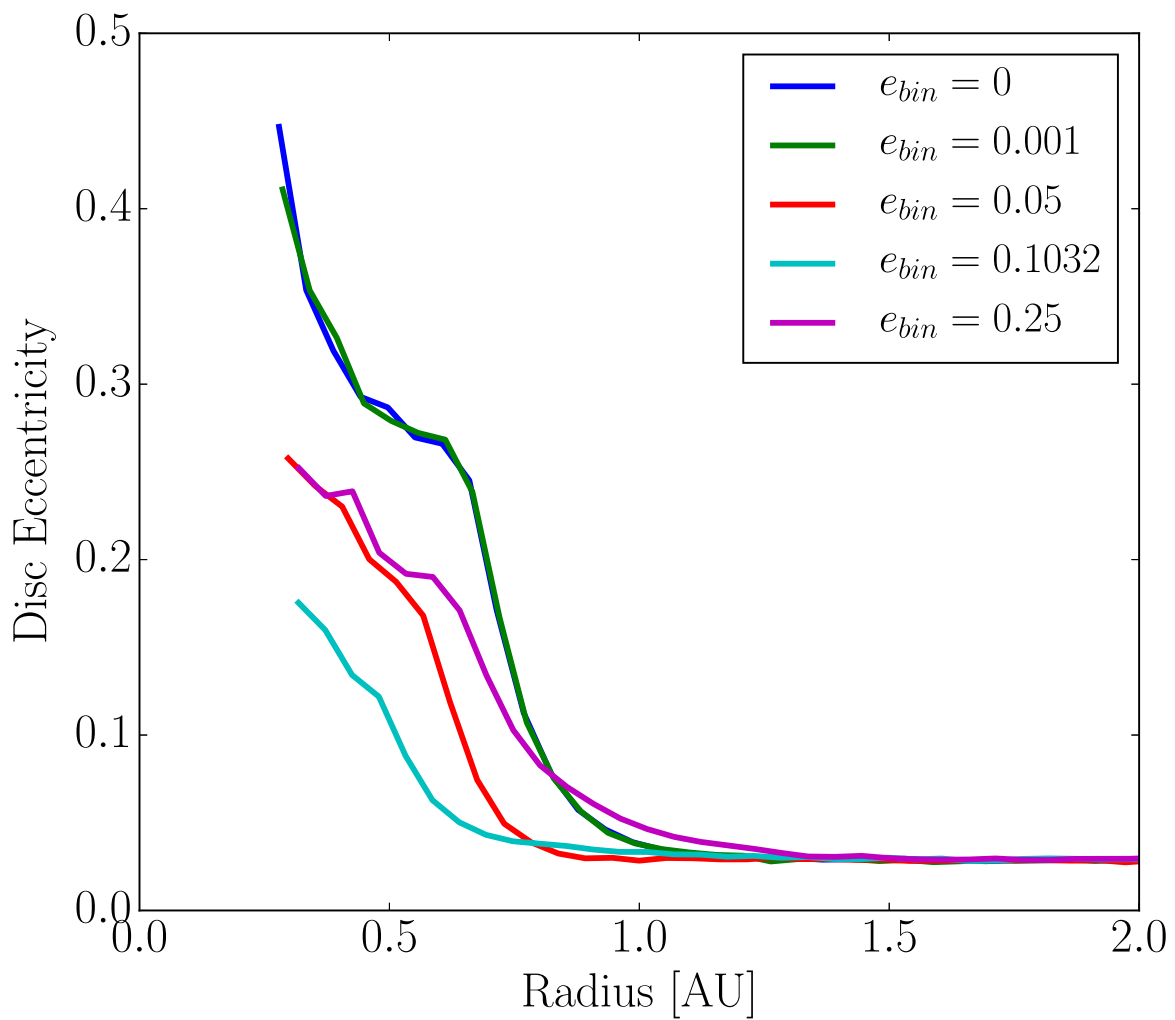


Figure 2.3: Disk eccentricity versus radius after about 520 years of evolution.

Fig. 2.2 and Fig. 2.4). We discuss these coupling mechanisms and their implications in more detail in Sections 2.3.2 and 2.3.3.

The $e_{bin} = 0.25$ and $e_{bin} = 0.05$ simulations show larger disk eccentricity than the $e_{bin} = 0.1032$ case in contrast to expected behavior. For $e_{bin} = 0.05$, this can be understood as intermediate coupling. The initial binary eccentricity is not low enough to conform exactly to the Papaloizou et al. (2001) criterion and is not large enough to couple strongly to the disk inner edge resulting in an intermediate coupling with larger disk eccentricity growth than the $e_{bin} = 0.1032$ case and also appreciable e_{bin} growth that is still less than the $e_{bin} = 0.1032$ case (see Section 2.3.3). For the $e_{bin} = 0.25$ case, the binary eccentricity may be large enough that higher order resonances in the disk begin to impact the evolution (Artymowicz, 1992), potentially accounting for the system's departure from expected behavior.

DisK Structure

The gravitational influence of the binary forces several major changes within the structure of the circumbinary disk. To explore how the structure of the disk changes with time and e_{bin} , we examined the orbits of gas particles and how they vary with distance from the binary. To accomplish this, two-dimensional histograms of all gas particles within a radial distance of 3 AU from the barycenter were made for each snapshot. We computed the histograms over semi-major axis, a , and the longitude of periastron, ϖ , defined in this work as the sum of the argument of periastron, ω , and the longitude of the ascending node, Ω , relative to that of the binary, ϖ_{bin} , for each gas particle. Fig. 2.5 and Fig. 2.6 shows these histograms for all particles in the disk out to 3 AU for several of our simulations.

In all simulations, a precessing overdense knot was found just outside inner edge of the disk. The knot corresponds to a coherent precession of eccentric gas particle orbits at the inner disk edge. The knot depicted in Fig. 2.5 precesses relative to the binary in the prograde sense with a period of about 20 years, or 400 binary periods, for $e_{bin} \approx 0$. Fig. 2.5 shows the $a - \varpi$ histogram for two simulations with initial e_{bin} of 0 and 0.1032, respectively after 200 years of evolution. Precession of orbits near the binary at the inner disk edge are expected due to the binary's time-varying potential

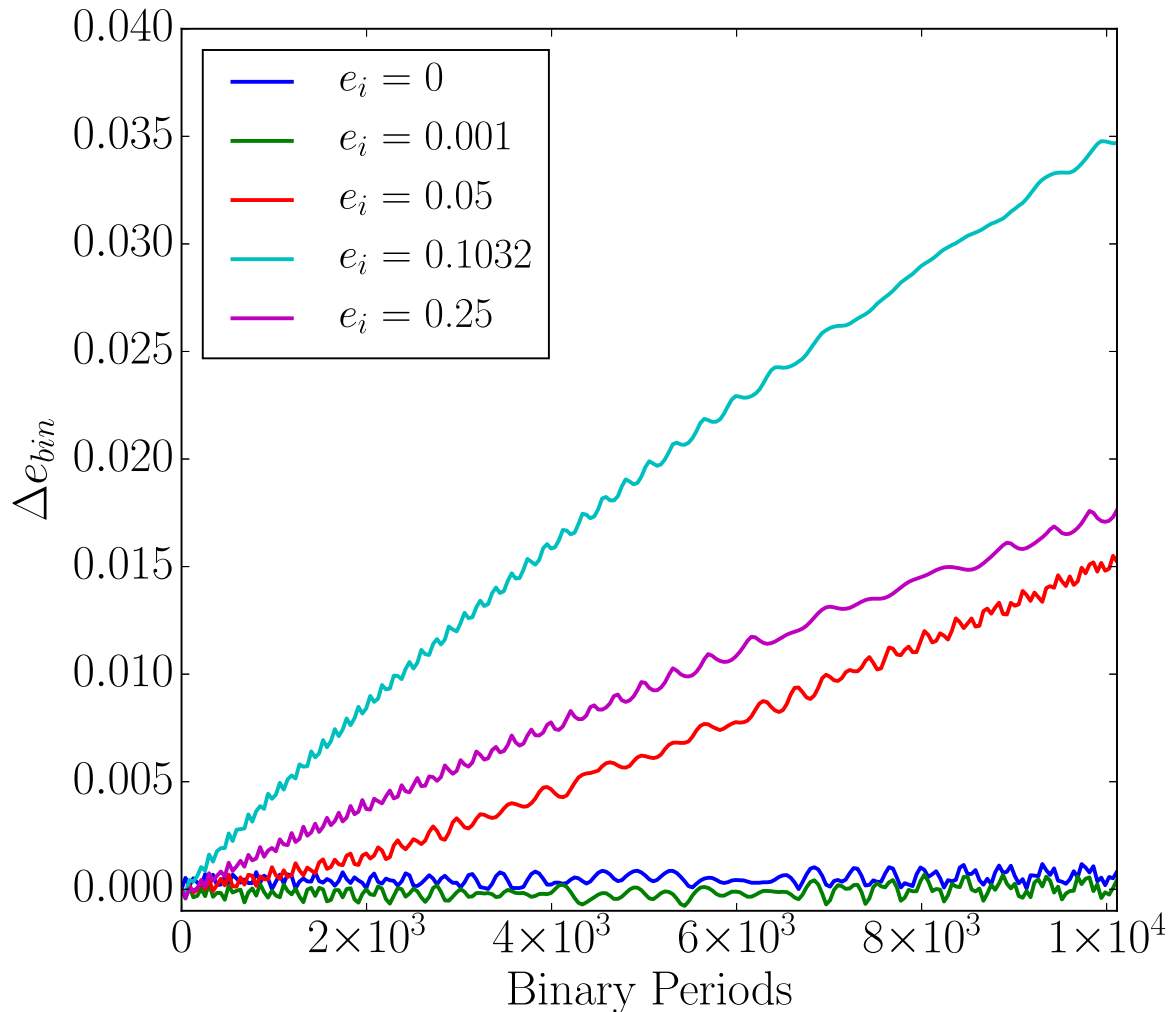


Figure 2.4: Change in binary eccentricity versus simulation time in units of binary orbits for several initial binary eccentricities. For an initially circular and nearly circular binary, effectively no eccentricity growth occurs whereas for higher initial eccentricities, significant growth occurs.

as shown in the simulations and analytic theory of Lubow and Artymowicz (2000). The existence of this knot is consistent with the identification of a similar overdense lump located at the inner edge of gaseous circumbinary accretion disks about binary black holes from 2D simulations by Farris et al. (2014).

An additional structure identified in the disk is a single arm ($m = 1$) spiral wave launched from near the inner edge of the disk as shown in Fig. 2.5. The spiral wave is an alignment of gas particle longitude of periastrons relative to the binary's. For the initial $e_{bin} = 0.1032$ simulation, the wave develops rapidly within the first 50 years, or about 10^3 binary periods. Recent N-body simulations of circumbinary planetesimal disks by Lines et al. (2016) confirmed the presence of an $m = 1$ wave disks about eccentric binaries. When under the influence of an asymmetric gaseous disk potential, Lines et al. (2016) identified the wave as a preferential alignment of planetesimal longitude of periastrons as a function of orbital radius around the eccentric binary of the Kepler 16 system, similar to the spiral wave found in this work.

In our simulations, the spiral wave's orientation remains locked to the binary's slow prograde ϖ_{bin} precession throughout the entire simulation, although a slight drift of a degree or so does occur. The wave's fixed orientation relative to the binary is an important effect whose consequences will be examined more carefully in Section 2.3.3. Simply put, if the wave did circulate relative to the binary, its long term effect on the system, if any, would average out to zero, so the fixed orientation could indeed dynamically impact the system.

Note that in the simulation with an initial $e_{bin} = 0$ (left panel), no spiral $m = 1$ arm exists in contrast to the $e_{bin} = 0.1032$ simulation (right panel) which shows a prominent spiral arm. The arm is also observed in the simulation with initial $e_{bin} = 0.25$ but not with initial $e_{bin} = 0.001$. Since the spiral arm is only observed when the binary has an appreciable eccentricity, we can infer that a coupling between binary eccentricity and the inner disk edge impacts its formation.

To investigate the role of binary eccentricity in exciting the wave, Simulation 3 was ran with initial $e_{bin} = 0.05$ to see if the spiral wave could be excited with an intermediate e_{bin} between the two regimes identified above. In the intermediate regime as explained in Section 2.3.2, e_{bin} is not large enough to be strongly coupled to the disk while also not low enough to weakly couple

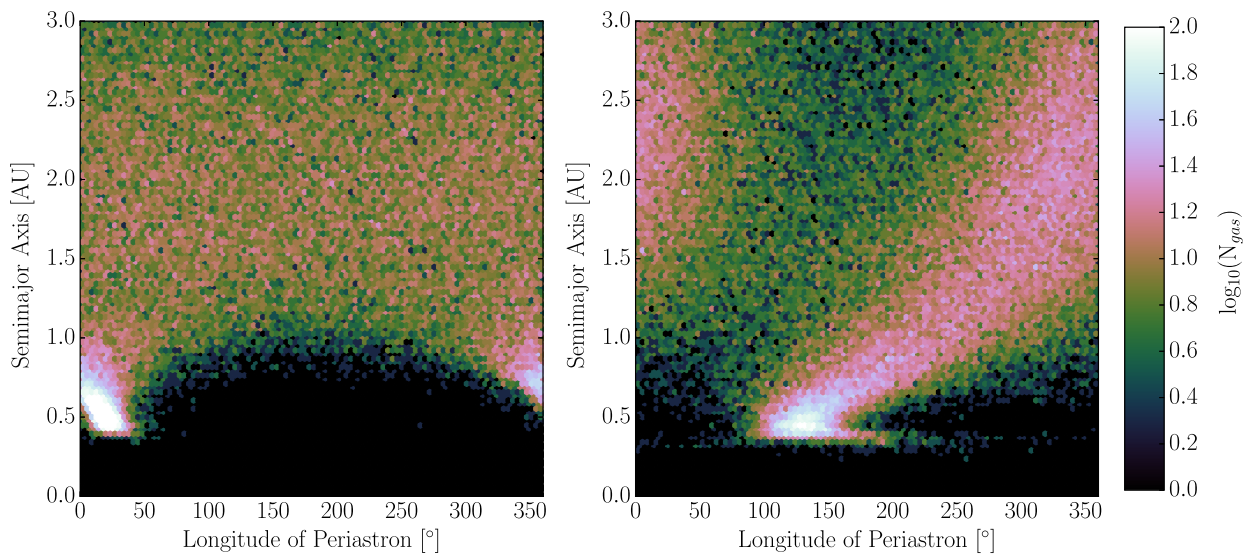


Figure 2.5: Two dimensional histogram of disk gas particles binned by semi-major axis and longitude of periastron, ϖ , (the sum of the longitude of ascending node, Ω , and argument of periastron, ω) relative to ϖ of the binary. Each bin is colored by the log of the number of gas particles it contains. We note that figure displays the disk in orbital element space and not in configuration space. The left and right panels display the histograms for two simulations with binaries having initial eccentricities of 0 and 0.1032, respectively, both after 200 years of evolution. The right panel clearly displays a $m = 1$ spiral wave launched from near the 1:3 EOLR within the disk.

to the disk to drive disk eccentricity. From the onset of the initial $e_{bin} = 0.05$ simulation, a faint $m = 1$ spiral wave appeared and gradually strengthened as shown in Fig. 2.6. The wave, initially weak, became more apparent after about 900 years. The $m = 1$ spiral arm in this simulation does not become as pronounced as the one seen in the initial $e_{bin} = 0.1032$ simulation, suggesting that the strength of the arm depends on e_{bin} and supporting the notion that this disk-binary system undergoes an intermediate coupling.

We again apply the theory of Papaloizou et al. (2001) to understand the origin and behavior of the spiral wave. We know from Section 2.3.2 that a nonlinear coupling between non-zero disk eccentricity and the binary’s tidal potential excites an $m = 2$ spiral density wave from the 1:3 EOLR that mediates angular momentum transfer in the system. Also, we have shown that the strength of the coupling between the binary and disk, which depends on e_{bin} , determines the magnitude of the disk inner edge eccentricity. Additional structural changes within the disk proceed via a higher order coupling.

In Papaloizou et al. (2001), the authors show that the $m = 2$ density wave emitted at the 1:3 EOLR can couple back through the binary tidal potential. This additional coupling produces a time independent $m = 1$ wave and an associated potential. The extra potential from the $m = 1$ wave can allow for the removal of angular momentum from the system via resonant torques. The $m = 1$ wave produced via the recoupling mechanism is precisely the $m = 1$ spiral wave identified in this work. The presence of the $m = 1$ wave was reconfirmed via a Fourier decomposition of the disk surface density. Since we only observe the $m = 1$ spiral wave in disks around eccentric binaries, we infer that this recoupling mechanism only occurs when the disk and binary are strongly coupled. Lines et al. (2016)’s observation of a $m = 1$ spiral wave present in their simulation of a planetesimal disk surrounding the eccentric Kepler 16 binary support this argument.

Since the orientation of the $m = 1$ wave in our simulations remains locked to that of the binary’s, it does not circulate and hence is independent of time. Also, as we will explore in Section 2.3.3, the additional potential from the $m = 1$ resonantly torques on the binary causing evolution in its orbital eccentricity.

Next we examine why the orientation of the spiral wave remains fixed relative to the binary.

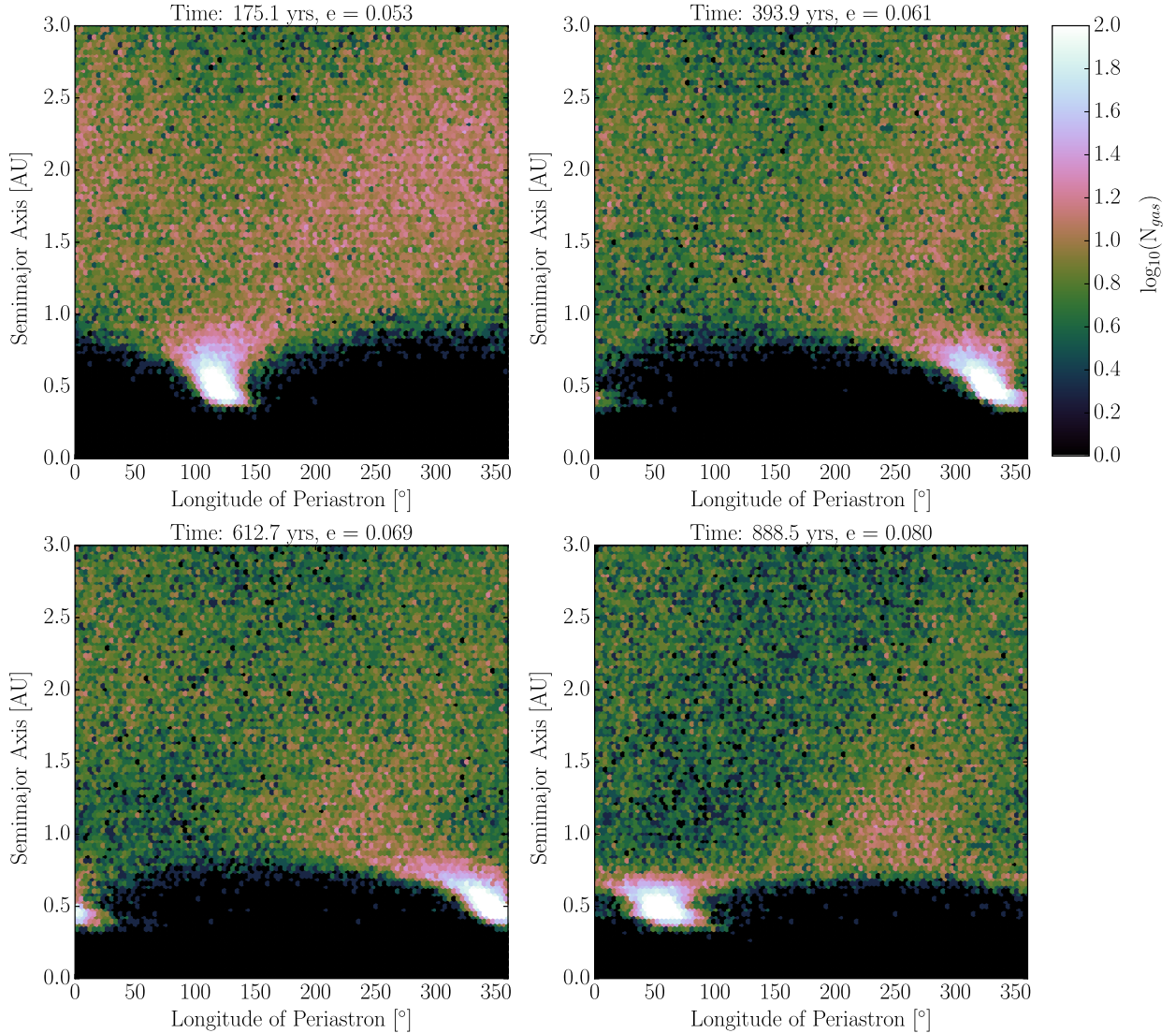


Figure 2.6: Two dimensional histogram of disk gas particles binned by semi-major axis and longitude of periastron, ϖ of the form of that shown in Fig. 2.5 for a binary with $e_i = 0.05$. We stress that the plot is shown in orbital element space and not configuration space. As the binary eccentricity increases through interactions with the surrounding disk, a single weak spiral arm begins to form. Once $e \approx 0.08$, the spiral arm becomes slightly more apparent, resembling a fainter version of the arm shown in Figure 2.5 for the $e_i = 0.1032$ case.

We apply the analytic theory for circumbinary orbits of Leung and Lee (2013) to partially explain this effect. The theory, accurate to first order in e_{bin} , decomposes the orbit of a test particle about two stars into a superposition of the circular motion of a guiding center and the radial and vertical epicyclic motion due to the non-axisymmetric components of the binary's potential. Leung and Lee (2013) give the equations for the precession rate of the argument of periastron, ω , and the longitude of the ascending node, Ω , respectfully, to be

$$\dot{\omega} \approx \frac{3}{4} \frac{m_a m_b}{(m_a + m_b)^2} \left(\frac{a_{bin}}{r} \right)^2 \quad (2.4)$$

$$\dot{\Omega} \approx -\frac{3}{4} \frac{m_a m_b}{(m_a + m_b)^2} \left(\frac{a_{bin}}{r} \right)^2 \quad (2.5)$$

where m_a and m_b are the masses of the primary and secondary stars, respectively, a_{bin} is the binary semi-major axis and r is the radial distance from the barycenter.

Since these rates are approximately equal and opposite, one expects a gas particle's longitude of periastron, as defined earlier, to remain fixed, as is observed for the spiral waves in our simulations about sufficiently eccentric binaries. In the context of gaseous circumbinary disks, this interpretation has a few potential shortcomings. First, a given gas particle does not live in isolation since it feels the effects of disk self gravity and pressure gradients within the disk that can impact its orbit. Also since this theory is only linear in e_{bin} , its applicability could lessen as the binary becomes more eccentric due to interactions with the disk. However, the binaries considered have low to moderate eccentricities and the disks are rather low-mass such that disk self gravity is negligible so the gravitational influence of the binary should dominate. Therefore, we expect this theory to still provide a decent approximate explanation for why the spiral arm remains fixed relative to the binary.

2.3.3 Binary Evolution

Secular theory (Goldreich and Tremaine, 1979, 1980; Pringle, 1991; Papaloizou et al., 2001) and previous simulations (Artymowicz et al., 1991; Cuadra et al., 2009; Roedig et al., 2012; Dermine et al., 2013) show that angular momentum losses to a disk change the central binary's orbital elements. Angular momentum loss occurs mainly through resonant gravitational torques at the Lindblad and corotation resonances. In the case of binary stars embedded in an external disk, loss of angular momentum can result in changes to the binary eccentricity and semi-major axis. For unequal mass binary stars with low to moderate eccentricity, the majority of eccentricity growth is due to resonant torques at the 1:3 EOLR. This resonance dominates since these systems tend to open a gap in the disk such that the 1:3 EOLR resides nearest to the inner edge of the disk while the eccentricity damping 1:2 corotation resonance lies within the evacuated region (Artymowicz et al., 1991; Artymowicz, 1992). Simulations of binaries embedded in circumbinary disks by Roedig et al. (2012) agree with this interpretation as they identified gravitational torque density peaks responsible for binary eccentricity evolution located at the 1:3 EOLR in the disk. For the simulations presented in this work, we expect a secular increase in binary eccentricity and decrease in semi-major axis as the binary loses angular momentum to circumbinary disk.

As shown in Fig. 2.4, binary eccentricity for initially eccentric binaries grows over the duration of the simulation. The eccentricity growth rate, \dot{e}_{bin} , seems to scale with initial e_{bin} . In the simulation with initial $e_{bin} = 0.25$, however, e_{bin} increases more slowly than the initial $e_{bin} = 0.1032$ case. When the initial $e_{bin} \approx 0$, no binary eccentricity growth occurs in contrast to the results of similar simulations of binaries embedded in an external disk by Papaloizou et al. (2001); Pierens and Nelson (2007); Cuadra et al. (2009) who find significant eccentricity growth with an initial $e_{bin} \approx 0$, a discrepancy we will address later. In all cases, e_{bin} oscillates as the simulations progress. This oscillation is due to forcing by the $m = 1$ potential of the eccentric external disk (Lubow and Artymowicz, 2000).

For all simulations, the binary semi-major axis secularly decreases where the rate of decline is lower for increasingly eccentric binaries as shown in Fig. 2.7. As before, the initial $e_{bin} = 0.25$ case

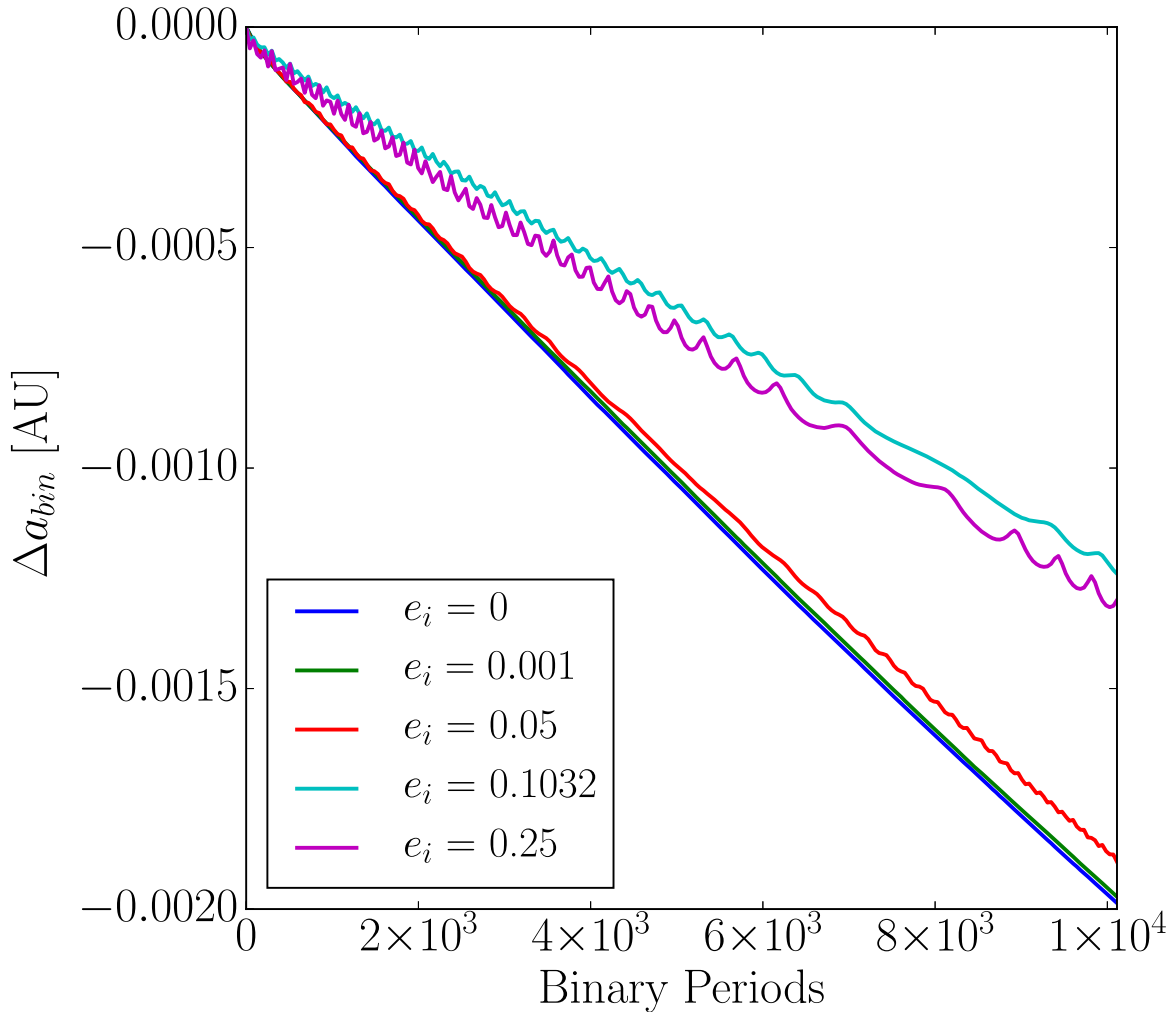


Figure 2.7: Change in binary semi-major axis versus simulation time in units of binary periods for several initial binary eccentricities. For all cases, the binary's semi-major axis secularly decreases.

defies this trend as it shows a greater semi-major axis decline than the initial $e_{bin} = 0.1032$ case instead of the expected lesser decline. Additionally, the binary's longitude of periastron slowly precesses in the prograde sense less than 1°yr^{-1} over the duration of the simulation similar to the results of comparable simulations by Kley and Haghighipour (2015).

Modeling Binary Evolution

Any changes in the binary orbital elements will depend on the details of the binary's interactions with the disk. As discussed in Section 2.3.2, we applied the secular theory of Papaloizou et al. (2001) to show that the strength of the disk-binary coupling dictates how eccentricity grows within the system. We apply the same arguments used above to understand disk eccentricity growth to binary eccentricity evolution. For circular binaries, we argued that the binary and disk are weakly coupled since the mass of the secondary is much greater than the mass of the entire circumbinary disk. In this weak coupling regime, the eccentricity of the less massive of the binary-disk system grows, which in this case is the disk. As expected, the disk develops appreciable eccentricity. From these arguments, we expect the binary to develop very little, if any, eccentricity. This behavior is exactly what we observe in our simulations (see Fig. 2.4).

For simulations of disks around eccentric binaries, we argued that the disk and binary are strongly coupled through the $m = 1$ modes of the eccentric binary orbit and inner disk edge orbits. In this regime, both the binary and disk eccentricities grow together and further coupling between the disk and binary can occur. Additional disk-binary coupling discussed at length in Section 2.3.2 lead to the excitation of a time-independent $m = 1$ spiral wave and associated potential from the 1:3 EOLR whose orientation remains locked to that of the binary's orbit (see Fig. 2.5). Since this wave remains fixed relative to the binary, it resonantly torques the binary through the 1:3 EOLR, removing angular momentum from the binary's orbit, increasing e_{bin} . If the wave instead circulated over time, its potential would time-average to zero and have no effect on the binary orbital elements. The presence of the $m = 1$ spiral wave leads to the qualitatively different binary eccentricity evolution for the $e_{bin} = 0.1032$ case relative to the $e_{bin} \approx 0$ case displayed in Fig. 2.4. In all simulations, the binary semi-major axis decreases due to energy dissipation from the viscous

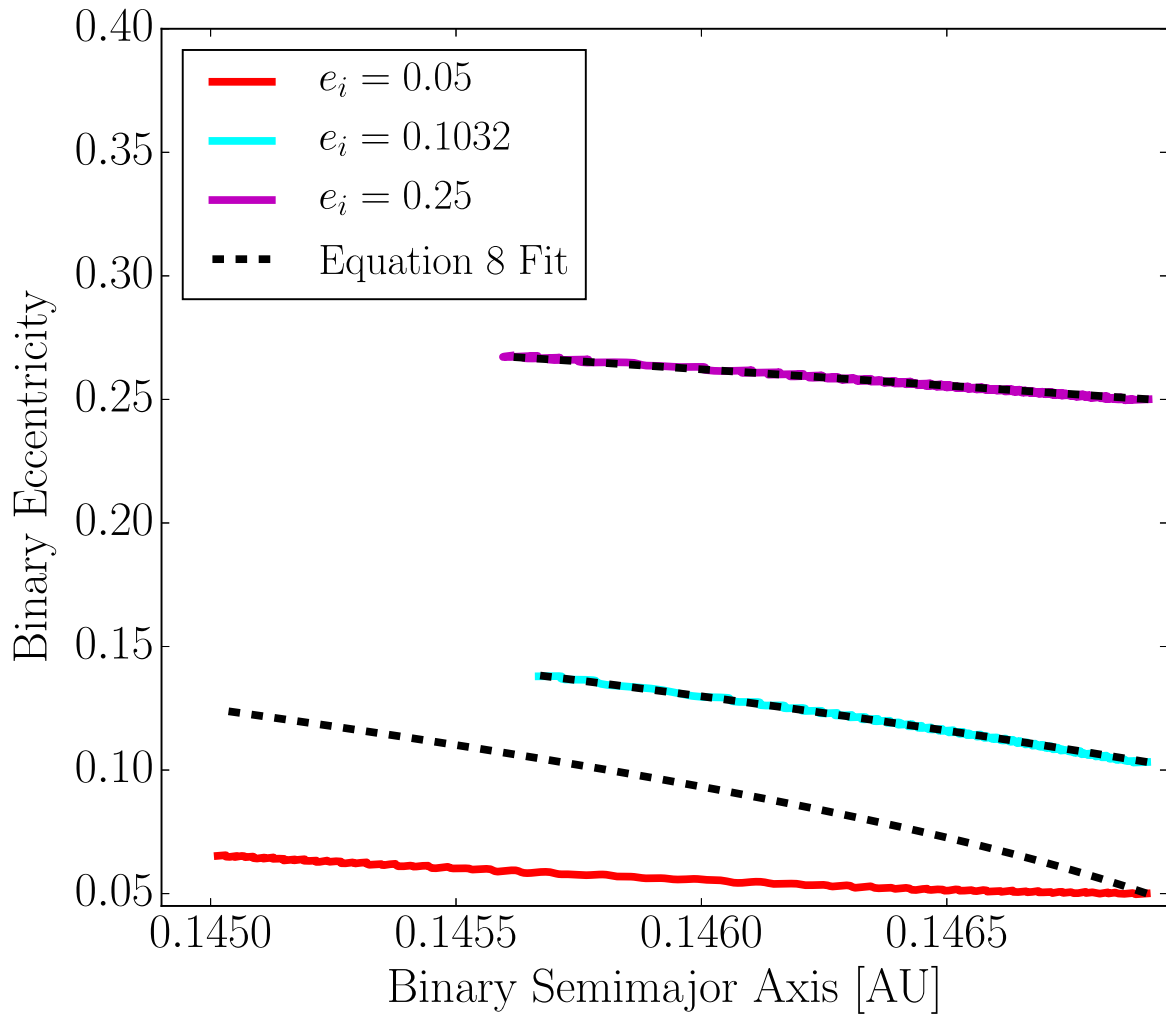


Figure 2.8: Evolution of e_{bin} as a function of a_{bin} from simulations with initial e_{bin} of 0.05, 0.1032, and 0.25 over-plotted with the analytic fit of equation 2.9 with $\alpha_{eff} = 0.006$. As the system evolves, time advances towards the left in this depiction.

disk.

Similar N-body SPH simulations of binaries embedded in a circumbinary disk by Artymowicz et al. (1991) showed that for binaries with mass ratio $\mu = m_2/m_1 = 0.3$ and $e_{bin} \approx 0.1$ similar to the systems examined in this paper, resonant interactions with the surrounding disk at the 1:3 EOLR drive eccentricity growth and semi-major axis decay. In this regime, we expect the binary eccentricity growth observed by Artymowicz et al. (1991) since the binary and disk are strongly coupled.

With the origin of binary eccentricity evolution understood using the theory of Papaloizou et al. (2001), we seek to quantify binary orbital evolution. Following the analysis of Dermine et al. (2013), we applied the theory of Lubow and Artymowicz (1996, 2000) to quantify the eccentricity and semi-major axis evolution of a binary with initial $e_{bin} \approx 0.1$ embedded in an external gaseous disk due to resonant interactions with the 1:3 EOLR using the following relation

$$\dot{e} = \frac{1-e^2}{e} \left(\frac{l}{m} - \frac{1}{\sqrt{1-e^2}} \right) \frac{\dot{a}}{a}. \quad (2.6)$$

where $(l, m) = (1, 2)$ is the potential component corresponding to the 1:3 EOLR (Artymowicz et al., 1991; Lubow and Artymowicz, 2000) and e and a are the binary eccentricity and semi-major axis, respectively.

For less eccentric binaries, the semi-major axis and eccentricity evolution is well-described by

$$\dot{e} = -\frac{50e}{\alpha_{eff}} \frac{\dot{a}}{a} \quad (2.7)$$

where α_{eff} is the effective standard viscosity parameter (Lubow and Artymowicz, 1996; Dermine et al., 2013).

Note that α_{eff} in equation 2.7 is not in general the same as the α_{SPH} viscosity parameter discussed in Section 2.2.1. To relate α_{eff} and α_{SPH} , we use the following relation from Lodato and Price (2010) and Meru and Bate (2012)

$$\alpha_{eff} = \frac{k_{BSW}}{20} \alpha_{SPH} \frac{h}{H} \quad (2.8)$$

where h is the smoothing length, H is the disk aspect ratio and the factor of 1/20 comes from the Meru and Bate (2012) derivation of the coefficient for the Monaghan and Gingold (1983) viscosity implementation used in ChaNGa (Murray, 1996). The k_{BSW} factor arises from our use of the Balsara switch which limits shear viscosity by scaling both α_{SPH} and β_{SPH} (Balsara, 1995). The range of k_{BSW} is [0,1]. Since both h and k_{BSW} can vary between gas particles and H can vary radially as the disk evolves, we average over the disk to get $k_{BSW} = 0.3$ and $h/H = 0.4$. Given these values, we set $\alpha_{eff} = 0.006$ as the approximate value for our simulations with $N_{gas} = 10^5$.

Equations 2.6 and 2.7, derived by Lubow and Artymowicz (1996) via examining the balance between viscous and resonant interactions at the inner disk edge, apply in separate regimes that depend sensitively on e_{bin} . Lubow and Artymowicz (1996) estimate that once $e_{bin} \gtrsim 0.1\alpha_{eff}^{1/2}$, the 1:3 EOLR dominates binary eccentricity growth while below this threshold for circular binaries, no eccentricity growth occurs. These separate regimes correspond to the weak and strong disk-binary coupling for circular and eccentric binaries, respectively, discussed in previous sections. For nearly circular binaries, $e_{bin} < 0.1\alpha_{eff}^{1/2}$ and $\dot{e}_{bin} \approx 0$ as expected for weak disk-binary coupling. Conversely for eccentric binaries, $e_{bin} \gtrsim 0.1\alpha_{eff}^{1/2}$ and $\dot{e}_{bin} > 0$ as demonstrated above for strong disk-binary coupling. We combine equations 2.7 and 2.6 to model how e_{bin} and a_{bin} should evolve under the influence of an external disk following the models of Lubow and Artymowicz (1996, 2000) and Dermine et al. (2013)

$$de/da = \begin{cases} -\frac{50e}{\alpha_{eff}} \frac{1}{a} & \text{if } e_{bin} \lesssim 0.1\alpha_{eff}^{1/2} \\ \frac{1-e^2}{ea} \left(\frac{l}{m} - \frac{1}{\sqrt{1-e^2}} \right) & \text{if } e_{bin} \gtrsim 0.1\alpha_{eff}^{1/2}. \end{cases} \quad (2.9)$$

Hence, eccentricity increases while the semi-major axis decreases.

To verify that equation 2.9 is a proper model for our simulations, the observed evolution of e_{bin} and a_{bin} for simulations with initial $e_{bin} = 0.05, 0.1032$, and 0.25 were compared with the theoretical result of equation 2.9 assuming $\alpha_{eff} = 0.006$. The comparison is shown in Fig. 2.8.

The results of both the simulations with initial $e_{bin} = 0.1032$ and $e_{bin} = 0.25$ are in good agreement with the theoretical expectations of equation 2.6 and also in accordance with the simulation of a similar system with initial $e_{bin} = 0.1$ by Artymowicz et al. (1991). Equation 2.9 can also be applied to the initial $e_{bin} \approx 0$ cases. For these simulations, the binary semi-major axis decreases via energy dissipation through the viscous disk while no eccentricity growth occurs as seen in Fig. 2.4 and Fig. 2.7. Our results are consistent with the prediction of equation 2.9. These findings indicate that equation 2.9 successfully quantifies how the binary evolves in the different disk-binary coupling regimes.

The initial $e_{bin} = 0.05$ case proves troublesome. Equation 2.9 does a poor job fitting the binary eccentricity and semi-major axis evolution. The poor fit can be understood in the context of how the disk and binary undergo an intermediate coupling in between the strong and weak regimes. As discussed in Sections 2.3.2 and 2.3.2, the binary eccentricity is not large enough to launch a prominent $m = 1$ spiral wave and drive the eccentricity growth for more eccentric binaries. In between regimes, we expect the binary eccentricity to grow weakly as we observe in our simulations. Equation 2.9 succeeds for systems firmly in the weakly or strongly coupled regime but does not perform well for intermediate coupling.

This behavior has interesting consequences for the subsequent evolution of a system. For the intermediate case as the binary eccentricity grows with time, it will eventually reach $e_{bin} \approx 0.1$ and will then begin to strongly couple to the gaseous disk. As discussed previously, strong coupling launches a $m = 1$ spiral wave in the disk and increases the growth rate of binary eccentricity. Also in the strongly coupled regime, we expect the disk eccentricity to decrease from higher values and be similar in magnitude to the binary eccentricity.

In a similar vein for nearly circular binaries, we expect them to remain circular. Other simulations of binaries embedded in circumbinary disks such as those by Pierens and Nelson (2007) and Cuadra et al. (2009) have found that initially circular binaries eventually develop appreciable non-zero eccentricities. This behavior can be understood by examining equation 2.9. If the binary is perturbed and some non-zero eccentricity develops, we would expect the binary eccentricity to grow very slowly, gradually strengthening the coupling between the disk and binary until interme-

diate coupling is reached and the system progresses as described above. This picture is consistent with the results of Pierens and Nelson (2007) who found the binary eccentricity began to grow on timescales longer than those explored in this work. Therefore over timescales much longer than simulated here, we would expect our initial $e_{bin} = 0.01$ case to become appreciably eccentric. We extrapolate the results of our simulations to longer timescales and consider the consequences below.

We ran additional simulations to ensure that the 1:3 EOLR did indeed dominate binary evolution and no other effect played a major role. To do this, a shorter simulation with an initial binary eccentricity of 0.1032 was performed with the initial disk gap radius located outside of the 1:3 EOLR. Minimal binary eccentricity growth and effectively no binary semi-major axis decay occurred until the disk viscously spread inward. Additionally, the $m = 1$ spiral wave observed in other simulations of sufficiently eccentric binaries also did not exist until mass was able to drift inward and accumulate at the 1:3 EOLR at which point the e_{bin} and a_{bin} began to evolve. These findings support the supposition that interactions with the 1:3 EOLR drives the binary evolution as anticipated.

To study what effect, if any, accretion has on the how the binary stars' orbital elements vary, a procedure similar to that used by Roedig et al. (2012) was performed. For a given simulation each accretion event was tracked such that the accreted gas particle's mass and velocity components were outputted. Using these events, e_{bin} and a_{bin} were evolved by adding each accreted particle to the binary imposing linear momentum and mass conservation as is done natively in ChaNGa for sink particles. This test demonstrated that accretion had a negligible effect on e_{bin} and a_{bin} . Therefore, it is safe to assume that the evolution of the binary orbital elements is primarily driven by interactions with the external disk, in particular at the 1:3 EOLR for the systems considered in this work.

2.4 Effects of Varying Disk Properties

Previous studies have examined how varying disk properties can change how a circumbinary disk evolves. For example, Lines et al. (2015) showed that disk eccentricity is sensitive to the initial

disk surface density gradient and aspect ratio. Here, we analyze the results of simulations that vary disk mass, gas resolution, and aspect ratio in order to examine how disk properties impact the disk - binary coevolution.

2.4.1 Varying Disk Mass

To study how our results vary with disk mass, three additional simulations were run with $e_{bin} = 0.1032$ to see if varying disk mass changes binary evolution. Simulation 6 with $2 \times M_{disk}$, Simulation 7 with $0.5 \times M_{disk}$, and Simulation 8 with $1.5 \times M_{disk}$ were run. For these additional simulations, we expect the disk to be strongly coupled to the eccentric binary since the coupling only depends on the magnitude of binary eccentricity. We do expect, however, that eccentricity growth to occur more quickly for systems with more massive disks since torque scales with the disk mass. The results of the simulations are shown in Fig. 2.9.

The disk eccentricity of Simulation 7 was similar to that of Simulation 4 while Simulation 6 showed larger disk eccentricity values. As expected, more massive disks became more eccentric. Not depicted is the spiral arm development. Similar to the standard initial $e_{bin} = 0.1032$ case, a prominent $m = 1$ spiral wave quickly forms in Simulations 6, 7, and 8 consistent with the picture that binary eccentricity determines how strongly the disk and binary couple. In all three simulations, the wave has the same shape and remains fixed relative to the binary except for Simulation 6 which showed slight prograde precession of the spiral arm.

For more massive disks, binary eccentricity grew more quickly and the binary underwent more semi-major axis decay. Although not plotted, both Simulations 6, 7 and 8 are still well-described by equation 2.9 and hence correspond to either faster or slower binary evolution timescales.

2.4.2 Varying Disk Resolution

To ensure that our simulations were sufficiently resolved, we ran two additional simulations, Simulations 9 and 10, which has decreased and increased the initial number of gas particles by a factor of 2 to 5×10^4 and 2×10^5 , respectively. The results of these simulations are shown in Fig. 2.9.

In both simulations, we find the general trend of eccentricity growth and semi-major axis decay holds. The lower resolution Simulation 9 eccentricity growth is less than the fiducial Simulation 4. In addition, the disk eccentricity does not oscillate as seen in other simulations. This suggests that the clump which dominates the disk eccentricity does not form into a coherent structure, indicating that $N_{gas} = 5 \times 10^4$ might not be large enough to properly resolve all the physics at the disk inner edge. We find that the $m = 1$ spiral wave appears in the disk indicating that the binary strongly couples to the disk as we expect from our previous simulations.

The higher resolution Simulation 10 exhibits both binary and disk eccentricity evolution that is in good agreement with the fiducial Simulation 4. Additionally, we again observed a prominent $m = 1$ spiral wave within the disk that behaved identically to its Simulation 4 counterpart. One disagreement between Simulation 10 and Simulation 4 is that the higher resolution simulation displayed less binary semi-major axis decay. This result is expected, however, since higher resolution N-body SPH simulations will have smaller gas softening lengths, h . As shown in equation 2.8, the effective standard viscosity parameter $\alpha_{eff} \propto h$. The theoretical work of Lubow and Artymowicz (1996, 2000) estimate that $\dot{a}/a \propto -\alpha_{eff}$. We therefore expect a higher resolution run with smaller h and hence smaller α_{eff} to exhibit less binary semi-major axis decay due to dissipation from the viscous disk.

Since the main effects explored in this work, the binary eccentricity evolution and the accompanying development of disk eccentricity and structure, are in good agreement between the standard and higher resolution runs, we find that our nominal resolution of $N_{gas} = 10^5$ is sufficient.

2.4.3 Varying Disk Aspect Ratio

Simulations of accretion disks around binary black holes have examined the effects of larger aspect ratio disks, mainly focusing on accretion rates. Two dimensional SPH simulations of gas accretion onto binaries embedded in a circumbinary disk by Young and Clarke (2015) found that increasing gas temperature leads to increased accretion rates onto the primary star and growth in the binary mass ratio. Simulations of disks about black hole binaries by Ragusa et al. (2016) showed that disks with aspect ratios $H/R \gtrsim 0.1$ have enhanced accretion rates as the inspiralling gas is not suppressed

by the binary's gravitational torque. To examine disk aspect ratio's effect on disk-binary evolution in our simulations, we ran Simulation 11 with a disk aspect ratio of $H/R = 0.12$. To initialize the disk with a larger aspect ratio, we increased the disk temperature by setting T_0 in equation 2.2 to 2500 K giving us about a factor of 2 larger aspect ratio relative to the fiducial Simulation 4.

The result of Simulation 11 is presented in Fig. 2.9. We found that the thicker disk resulted in greater binary semi-major axis decay and eccentricity growth compared to the fiducial Simulation 4. The increased binary semi-major axis decay agrees with the theoretical expectation of Lubow and Artymowicz (1996, 2000) who estimate that $\dot{a}/a \propto -(H/R)^2$. The enhanced binary eccentricity growth follows as a consequence of equation 2.6.

In Simulation 11, the binary accretion rate was enhanced by about a factor of 4 relative to the fiducial Simulation 4 in agreement with the general findings of both Young and Clarke (2015) and Ragusa et al. (2016). We found that accretion had little impact on the binary orbital element evolution. As expected from arguments presented in Section 2.3.2, the disk and binary were strongly coupled, producing a prominent $m = 1$ spiral wave similar to the one seen in Fig. 2.5. The disk also displayed larger eccentricity initially but it did not grow appreciably over the course of the simulation.

2.5 Discussion

The coevolution of a binary with a gaseous circumbinary disk, primarily driven by resonant interactions at the 1:3 EOLR, has several important consequences for the subsequent dynamical evolution of the system. As shown above, an eccentric binary system tends to gain eccentricity and experience a secular decay in semi-major axis due to viscous and resonant interactions with the disk. This evolution not only changes due to additional feedback with the disk, but also impacts regions in the disk where planets form and migrate.

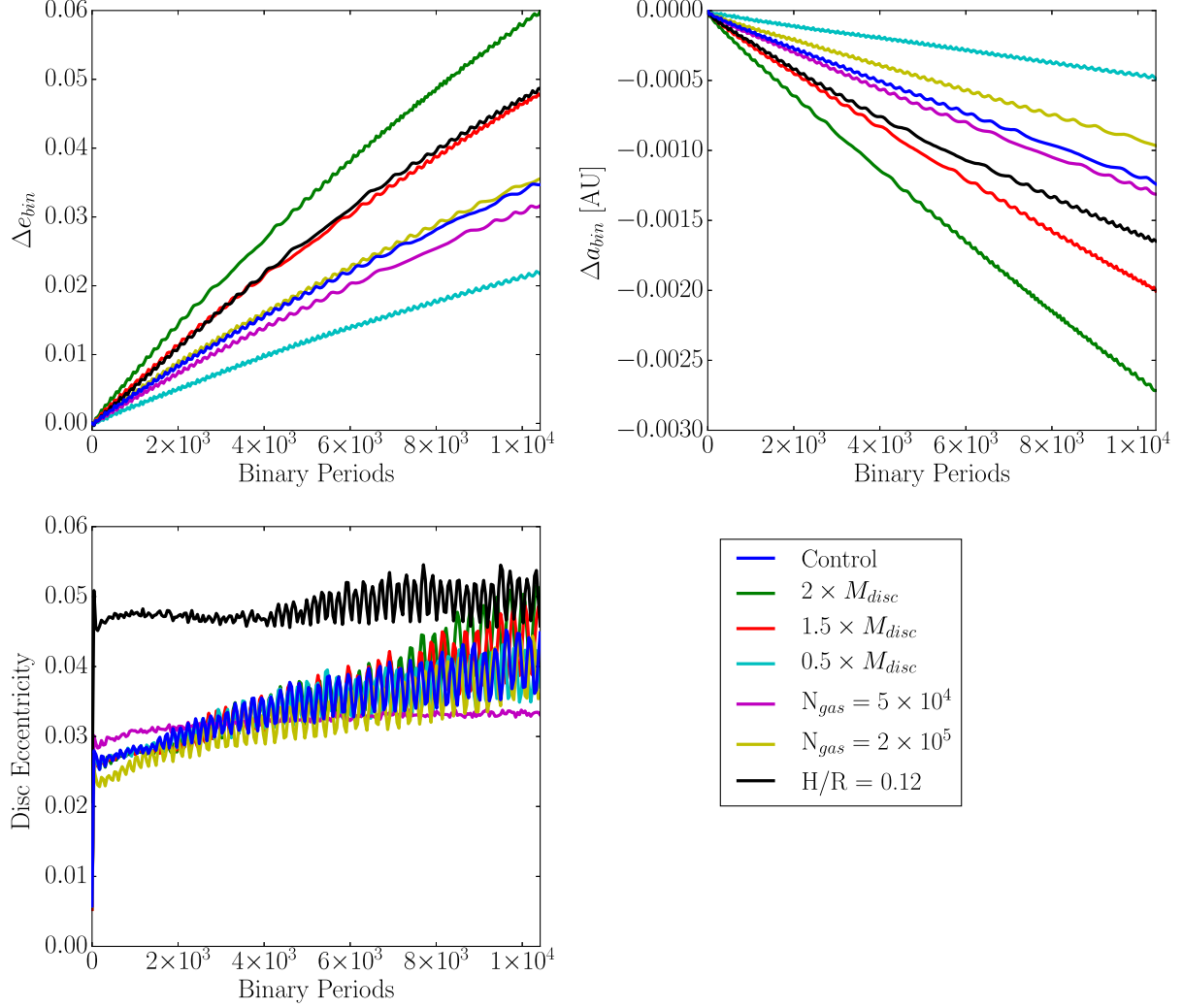


Figure 2.9: The results of simulations about a binary with initial $e_{bin} = 0.1032$ and $a_{bin} = 0.1469$ AU with various disk properties. The control case corresponds to Simulation 4. The top left panel gives the change in binary eccentricity as a function of time. The top right panel shows the change in binary semi-major axis vs time. The bottom left panel displays disk eccentricity vs time and the bottom right panel displays the figure legend.

2.5.1 Implications for Long-term Binary Evolution

N-body simulations of an unequal mass binary embedded in a protoplanetary disk by Artymowicz et al. (1991) found rapid semi-major axis decay leading the authors to suggest that the binary separation may become small enough that tidal effects or even stellar coalescence may occur for such systems. Tides between stellar companions tend to circularize the orbit over long timescales once the stellar separation becomes sufficiently small. Detailed studies of companions to Sun-like stars by Raghavan et al. (2010) and measurements of solar-type spectroscopic binaries in M35 by Meibom and Mathieu (2005) both found that binaries from these populations with periods less than about 10 days tend to be circularized. Theoretical work on the premain-sequence evolution of $0.5 - 1.25 M_{\odot}$ binaries by Zahn and Bouchet (1989) demonstrate that binaries with orbital periods of about 8 days or less are tidally circularized with effectively all of the circularization occurring before the stars reach the main-sequence. For binaries with an initial period slightly greater than the ~ 10 day tidal circularization boundary embedded in a circumbinary disk, binary-disk interactions could potentially decrease a_{bin} enough to make tidal effects important for subsequent evolution given that the lifetimes of protoplanetary disks are of order 1 Myr (Haisch et al., 2001).

In addition, we would expect some longer period binaries to develop appreciable eccentricity through this mechanism. Observations of spectroscopic binaries discussed by Mazeh (2008) show that a large number of such binaries have large eccentricities, some up to $e_{bin} \approx 1$, suggesting that disk-binary interactions may in fact be an important mechanism in pumping binary eccentricity. Ideally, additional observations of binaries with circumbinary planets, systems guaranteed to have had protoplanetary disks, will allow us to better constrain and model this effect.

The extent to which disk-binary interactions impact astrophysical systems over the disc's lifetime is difficult to measure. Over the course of the disc's lifetime, what may occur is some process that removes the 1:3 EOLR from the disk. As a_{bin} decays through disk-binary interactions, the location of the 1:3 EOLR shifts inwards. Also as e_{bin} grows, the central gap size increases (Artymowicz and Lubow, 1994). The combined a_{bin} and e_{bin} evolution could result in the 1:3 EOLR moving into the evacuated disk gap, removing its influence from the system, leaving higher order

resonances to influence the binary. For binaries with large e_{bin} , Artymowicz et al. (1991) speculates that the combination of higher order inner and outer Lindblad resonances and corotation resonances should combine to reduce the magnitude of \dot{e}_{bin} and \dot{a}_{bin} , potentially preventing subsequent evolution. This picture is not so simple, however, as simulations of binary SMBHs embedded in gaseous disks by Cuadra et al. (2009) and Roedig et al. (2011) both find that binary eccentricity growth continues to $e_{bin} > 0.35$ where this growth did not slow until $e_{bin} \approx 0.6 - 0.8$. We note that the simulations of Roedig et al. (2011) assumed a fixed a_{bin} which neglects the inward motion of the resonances as a_{bin} decays, potentially leaving them in the evacuated region, removing their effects from the system. The impact of higher order resonances on binary evolution is a complicated matter that requires proper treatment in which both the binary and disk are allowed to coevolve together and likely depends on disk structure and artificial viscosity implementation. Additionally, findings by Pringle (1991) show that in principle, there is no limit to the amount of angular momentum that can be lost by a central binary to an external disk suggesting that binary coalescence is not as unrealistic as it sounds. We caution that when performing simulations of binaries embedded in a gaseous disk that explore the role of semi-major axis decay, one should ensure that their observed semi-major axis decay has converged as both resolution and non-trivial effects such as accretion (e.g. Roedig et al., 2012) can have a substantial impact.

One effect not explored in this work is the possibility of Kozai-Lidov (KL) oscillations for the general case of a misalign disks in binary systems. For an inclined test particle orbiting one component of a binary, periodic KL oscillations allow for the particle's eccentricity to grow at the expense of its inclination Kozai (1962); Lidov (1962). For the case of an inclined circumstellar disk about one component of the binary, Martin et al. (2014) found that the disk can exhibit KL cycles with the periodic disk eccentricity maxima approaching ~ 0.6 . A later study of similar systems by Lubow et al. (2015) demonstrated that misaligned disks can become much more extended than coplanar disks and potentially could overflow the Roche lobe of the star. Simulations of misaligned circumbinary disks by Nixon et al. (2013) showed that disks of almost all inclinations can tear leading to massive accretion and potentially a merger of the central binary.

Given these results in the general case of systems with misaligned circumbinary disks, the bi-

nary eccentricity evolution is likely significantly impacted by the disk evolution and depart from the results presented here for thin, coplanar disks. The disk, if misaligned, could reach large eccentricities due to KL oscillations and via interactions with the binary if it does not tear. If the disk does in fact tear, the binary would likely not couple with the disk at all but could in fact coalesce as demonstrated by Nixon et al. (2013). The general case of a binary coupling with an inclined circumbinary disk is greatly complicated by KL oscillations, torque scaling with inclination and the potential for tearing and warrants a more robust future study.

2.5.2 Implications for Circumbinary Planets

The observed orbital elements of binary stars that host a circumbinary planet are the product of a complex evolutionary history. From Fig. 2.4 and Fig. 2.7, we see that for systems similar to the ones considered in this work, appreciable changes can occur on order 10^4 binary orbits.

As shown in Section 2.4.1, the mass of the disk strongly influences the binary evolution. More massive disks, for example, drive much faster e_{bin} growth and a_{bin} decay. Faster dynamical binary evolution due to massive disks could be particularly relevant for *Kepler* circumbinary planets as the work of Dunhill and Alexander (2013) suggests that these circumbinary planets formed and migrated in massive disks. Additionally, disk-binary interactions can make planet formation more difficult. Simulations by Lines et al. (2016) identified an $m = 1$ spiral wave in the circumbinary disk that corresponds to an alignment of planetesimal longitudes of periastron. This wave, whose origin was explained in this work, caused an increase in erosive planetesimal collisions making in-situ formation difficult in circumbinary protoplanetary disks.

The decay of a_{bin} via disk-binary interactions also causes the inward shift of mean motion and Lindblad resonances. These resonances can significantly impact the orbital stability of local objects in the disk in several important ways. For the restricted three body problem, resonance overlapping can lead to stochastic orbital evolution as shown from the criterion derived by Wisdom (1980). For the case of binary orbital evolution driven by tides, Bromley and Kenyon (2015) point out that evolving binary eccentricity and semi-major axis changes the location of critical resonances and hence where they overlap, potentially making stable systems unstable over time. The location

of mean motion resonances also dictate where circumbinary planets may reside. The numerical integrations of both Popova and Shevchenko (2013) and Chavez et al. (2015) show that many circumbinary planets lie in a stable region shepherded by unstable mean motion resonances. If a_{bin} evolves significantly on short enough timescales, so too do the locations of the resonances, sweeping inward and potentially destabilizing orbits. We note, however, that a_{bin} evolution appears to be a resolution dependent effect which future work should address.

This behavior is of particular importance for studies of planetary migration in circumbinary disks. Studies of circumbinary planetary migration in a viscous, eccentric disk find that planets tend to migrate inwards until they are trapped in or near the 4:1 mean motion resonance in the region of stability identified by Holman and Wiegert (1999) (Nelson and Papaloizou, 2003; Kley and Haghjipour, 2014). Since the resonances and the region of stability move as binary eccentricity and semi-major axis evolve, the final location and stability of migrating planets in circumbinary disks is sensitive to binary evolution. Simulations of circumbinary systems, especially those using N-body SPH methods like the ones presented in this work, must ensure that they properly account for the disk-binary interactions.

2.6 Conclusions

In this work, we showed that unequal mass binary stars embedded in a circumbinary gaseous disk carved out a gap in the disk and caused structural changes within the disk. Resonant interactions with the binary at the 1:3 EOLR excited disk eccentricity. Sufficiently eccentric binaries excited a $m = 1$ spiral wave within the disk. This wave corresponded to an alignment of gas particle longitude of periastrons that varied with radius. The spiral wave formed within 50 years for disks about sufficiently eccentric binaries but took longer to strengthen for less eccentric binaries (see Fig. 2.5). Eccentric binary stars became more eccentric and experienced a secular decrease in semi-major axis while initially nearly circular binaries underwent no eccentricity growth over the timescales considered.

Eccentricity growth within the system was understood in the context of the theory of Papaloizou et al. (2001) in which nonlinear coupling between non-zero disk eccentricity and the binary's tidal

potential excites an $m = 2$ spiral density wave from the 1:3 EOLR that mediates angular momentum transfer in the system. Nearly circular binaries weakly couple to the external disk and drive the inner disk edge to become very eccentric. Eccentric binaries, however, strongly couple to the disk leading to eccentricity growth for both the disk and binary. The origin of the $m = 1$ wave within the disk is understood as a recoupling of the $m = 2$ spiral density wave with the binary tidal potential.

This model does have limited applicability as disk gap size scales with e_{bin} , so the 1:3 EOLR could fall within the evacuated region removing its effect from the system, potentially slowing down binary evolution. For simulations of gaseous circumbinary disks, we caution that the disk-binary interaction must be sufficiently accounted for to properly model the system. We leave the characterization of the long-term impact of disk-binary interactions to future work.

Limitations of this work include the difficulty in integrating the binary orbit. Since the binary feels the force of every other SPH particle in our simulations and is integrated using ChaNGa’s native leapfrog integrator, very conservative timestepping was employed to ensure that the binary orbit was well-resolved and physically accurate. The conservative timestepping scheme significantly slowed our simulations. In light of this limitation, potential future work could include running a long-term higher resolution simulation over at least 10^5 binary orbits for small yet non-zero e_{bin} in order to better characterize how the disk and binary coevolve. Additional future work could involve examining equal mass binaries or binaries with larger eccentricities than those explored in this work. Since binaries with large eccentricities excite higher order resonances within the disk (e.g. Artymowicz, 1992; Lubow and Artymowicz, 2000) and carve out gaps that could remove the 1:3 EOLR from the disk (Artymowicz and Lubow, 1994), it would be interesting to examine how these other resonances can impact binary evolution. A study on how different numerical viscosity implementations impact binary evolution would also prove fruitful to examine its influence on disk-binary coevolution, specifically binary semi-major axis decay.

2.7 Acknowledgements

We thank the anonymous referee for helpful comments and suggestions that improved the quality of the manuscript. We would also like to thank Isaac Backus for a careful reading of the manuscript

and Jacob Lustig-Yaeger for helpful feedback. This work was facilitated through the use of advanced computational, storage, and networking infrastructure provided by the Hyak supercomputer system at the University of Washington. We made use of *pynbody* (<https://github.com/pynbody/pynbody>) in our analysis for this paper. This work was performed as part of the NASA Astrobiology Institute's Virtual Planetary Laboratory, supported by the National Aeronautics and Space Administration through the NASA Astrobiology Institute under solicitation NNH12ZDA002C and Cooperative Agreement Number NNA13AA93A. David Fleming is supported by an NSF IGERT DGE-1258485 fellowship. Thomas Quinn is supported by NASA grant NNX15AE18G.

Chapter 3

THE DYNAMICAL DEATH OF CIRCUMBINARY PLANETS: COUPLED STELLAR-TIDAL EVOLUTION EJECTION OF CIRCUMBINARY EXOPLANETS

Portions of this chapter were originally published in collaboration with Rory Barnes, David E. Graham, Rodrigo Luger, and Thomas R. Quinn in the May 2018 edition of the Astrophysical Journal (Fleming et al., 2018, ApJ, Vol. 858, 2; 2018 © American Astronomical Society, DOI: 10.3847/1538-4357/aabd38), and are reproduced below with permission of the American Astronomical Society.

3.1 Introduction

To date, 11 transiting circumbinary planets (CBPs) have been discovered by *Kepler*. The shortest period binary star system around which a CBP has been discovered is Kepler-47, with a binary period of 7.45 days (Orosz et al., 2012). The lack of CBPs around shorter period binaries is probably real given the thousands of short-period ($P_{bin} \lesssim 10$ days) eclipsing binaries discovered by the *Kepler* mission (Kirk et al., 2016) and observational biases that favor their detection (Muñoz and Lai, 2015). From a planet formation standpoint, there should not be a severe lack of CBPs: both Alexander (2012) and Vartanyan et al. (2016) show that circumbinary disks around binaries with semi-major axes $a \lesssim 1$ AU provide favorable conditions for planet formation. Bromley and Kenyon (2015) demonstrated that outside the inner region of the circumbinary disk, planet formation should occur similarly to planet formation in disks around single stars. From these results, Bromley and Kenyon (2015) concluded that circumbinary and single star planet occurrence rates should be similar, a claim bolstered by both Martin and Triaud (2014) and Armstrong et al. (2014) who find that the minimum CBP occurrence rate derived from *Kepler* data is of order 10% and increases

with CBP inclination relative to the plane of the binary.

Although detecting CBPs via the transit method is more difficult than in the single star case (Welsh et al., 2014; Winn and Fabrycky, 2015), especially since many CBPs spend less than 50% of the time in a transiting configuration (Martin, 2017), CBPs have in general a higher transit probability than their single star counterparts (Martin and Triaud, 2015) making their detection feasible. Martin (2017) showed that the time-dependent chance of observing the transit of CBPs implies that continued future observations of the *Kepler* field could find up to 30 new CBPs, so where are the planets orbiting short-period binaries?

One explanation for the lack of transiting CBPs could simply be that most CBPs are not in a transiting configuration, perhaps due to dynamical interactions with the central binary. However, Foucart and Lai (2013) show that natal circumbinary disks, and hence the planets themselves, should be nearly coplanar with the binary due to gravitational torques from the central binary on the disk, an effect that is especially pronounced for short-period binaries. Furthermore, in an analysis of the observed population of *Kepler* CBPs, Li et al. (2016) find that the observed coplanarity of CBPs and their host binaries is not due to a selection bias. From both theoretical arguments and analysis of *Kepler* data, it seems that an additional physical mechanism is required to explain the lack of discovered transiting CBPs in the *Kepler* field around short-period binaries.

Several recent studies have invoked the presence of a stellar tertiary companion to explain not only how short-period binaries could form but also to explain the lack of CBPs around short-period binaries. Fabrycky and Tremaine (2007) showed that secular interactions with a tertiary companion can drive Kozai-like oscillations that cause large eccentricity oscillations in the inner binary. The increased binary eccentricity leads to efficient tidal dissipation in the inner binary, shrinking the orbital period to of order a day from much longer periods. The comprehensive population synthesis study by Moe and Kratter (2018) support this finding and show that the combination of tidal dissipation and Kozai-like oscillations due to a tertiary companion can account for $\sim 40\%$ of binaries with periods $\lesssim 10$ days. Muñoz and Lai (2015), Martin et al. (2015), and Hamers et al. (2016) all show that these binary-tertiary interactions, in addition to shrinking the inner binary orbit, can lead to rich dynamical interactions that can drive many CBPs towards eccentric and inclined or-

bits, making detection more difficult and potentially leading to orbital instability. This mechanism provides a particularly compelling explanation for the lack of CBPs around short-period binaries given that in a survey of solar-type binaries, Tokovinin et al. (2006) find that 96% of binaries with periods $\lesssim 3$ days have a tertiary companion. However, no study to date has examined the lack of CBPs around isolated binaries, i.e., binaries without a tertiary companion. Not all close binaries have a companion, as Tokovinin et al. (2006) find that the tertiary companion fraction decreases to 34% for binaries with periods $\gtrsim 12$ days after correcting for observational biases, indicating that binaries with orbital periods $\gtrsim 3$ days are less likely to have a tertiary companion, and therefore the Kozai-like oscillations model cannot solely account for their lack of observed CBPs.

Short-period isolated binaries can form through a combination of fragmentation and dynamical processing. Bonnell and Bate (1994) found that very low mass ($\lesssim 0.01 M_{\odot}$) binaries with separations $\lesssim 1$ AU can form either in a protoplanetary disk orbiting an unstable protostellar core or from the unstable core itself, and must accrete mass to become a stellar binary. When close binaries do form, simulations by Bate (2000) find that they are likely to host circumbinary disks, necessary for CBP formation. Circumbinary disks play a major role in hardening the central binary and increasing its mass; Bate (2000) shows that accretion from a circumbinary disk is likely to shrink the binary separation, sometimes by up to 2 orders of magnitude. Simulations by Artymowicz and Lubow (1996) find that binaries can efficiently accrete mass from a circumbinary disk, indicating that shrinking the binary semi-major axis via accretion can readily occur. With the inclusion of a realistic treatment of magnetic fields in MHD simulations of protobinary stars, Zhao and Li (2013) find that binary orbital decay via accretion is significantly enhanced relative to simulations without magnetic fields. Additionally, gravitational torques between a circumbinary disk and the central binary shrink the binary semi-major axis (e.g. Artymowicz et al., 1991; Bate et al., 2002; Armitage and Natarajan, 2005; Fleming and Quinn, 2017), which, when coupled with accretion, can produce short-period, isolated binaries.

In this paper, we focus on isolated binaries with binary orbital periods in the regime $3 \leq P_{bin} \leq 7.45$ days, as these binaries are less likely to have a tertiary companion than binaries with $P_{orb} \leq 3$ days (Tokovinin et al., 2006). The upper limit of this range corresponds to the orbital period of

Kepler-47, the shortest period CBP-hosting binary system. We also consider the full population of *Kepler* CBPs. As previously mentioned, in the *Kepler* sample there are no known CBPs orbiting the ~ 2000 eclipsing binaries with $P_{orb} \lesssim 7.45$ days (Kirk et al., 2016), highlighted in the red-shaded region in Fig. 3.1. Note that CBPs have been discovered by other means, such as microlensing (e.g. Bennett et al., 2016).

One intriguing characteristic of the observed population of *Kepler* CBPs is their tendency to orbit just exterior to the dynamical stability limit (Welsh et al., 2014; Winn and Fabrycky, 2015). The dynamical stability limit, referred to as the “critical semi-major axis” (a_{crit}), is the minimum semi-major axis for a CBP to remain dynamically stable (Dvorak et al., 1989; Holman and Wiegert, 1999). Holman and Wiegert (1999) derived an empirical formula for a_{crit} from an ensemble of N-body simulations given by

$$a_{crit} = (1.60 + 5.1e - 2.22e^2 + 4.21\mu - 4.27e\mu - 5.09\mu^2 + 4.61e^2\mu^2)a \quad (3.1)$$

where a is the binary semi-major axis, e the binary eccentricity and $\mu = m_2/(m_1 + m_2)$ is the binary mass ratio. We note that the a_{crit} derived by Holman and Wiegert (1999) is not a hard limit as Eq. (3.1) has an error of about 3% - 6%. We plot the semi-major axis of observed *Kepler* CBPs normalized by a_{crit} (a_{CBP}/a_{crit}) as a function of host binary orbital period in Fig. 3.1 to demonstrate CBPs’ tendency to orbit just exterior to a_{crit} . Using Nbody simulations, Quarles et al. (2018) found that some *Kepler* circumbinary systems could host an additional planet interior to the observed one. Clearly, however, the observed CBPs cluster near the stability limit as the distribution of the ratio of a_{CBP} to their host binary’s a_{crit} has a minimum of $a_{cbp}/a_{crit} \approx 1.1$ and a median of $a_{cbp}/a_{crit} \approx 1.26$. Analyses by Martin and Triaud (2014) and Li et al. (2016) show that this clustering does not solely stem from an observational bias, suggesting a physical origin.

CBP migration in a protoplanetary disk provides a compelling physical explanation for the observed pile-up of planets near the dynamical stability limit around binary stars. Numerous studies of planet formation in circumbinary disks show that CBPs likely did not form *in situ* (e.g.

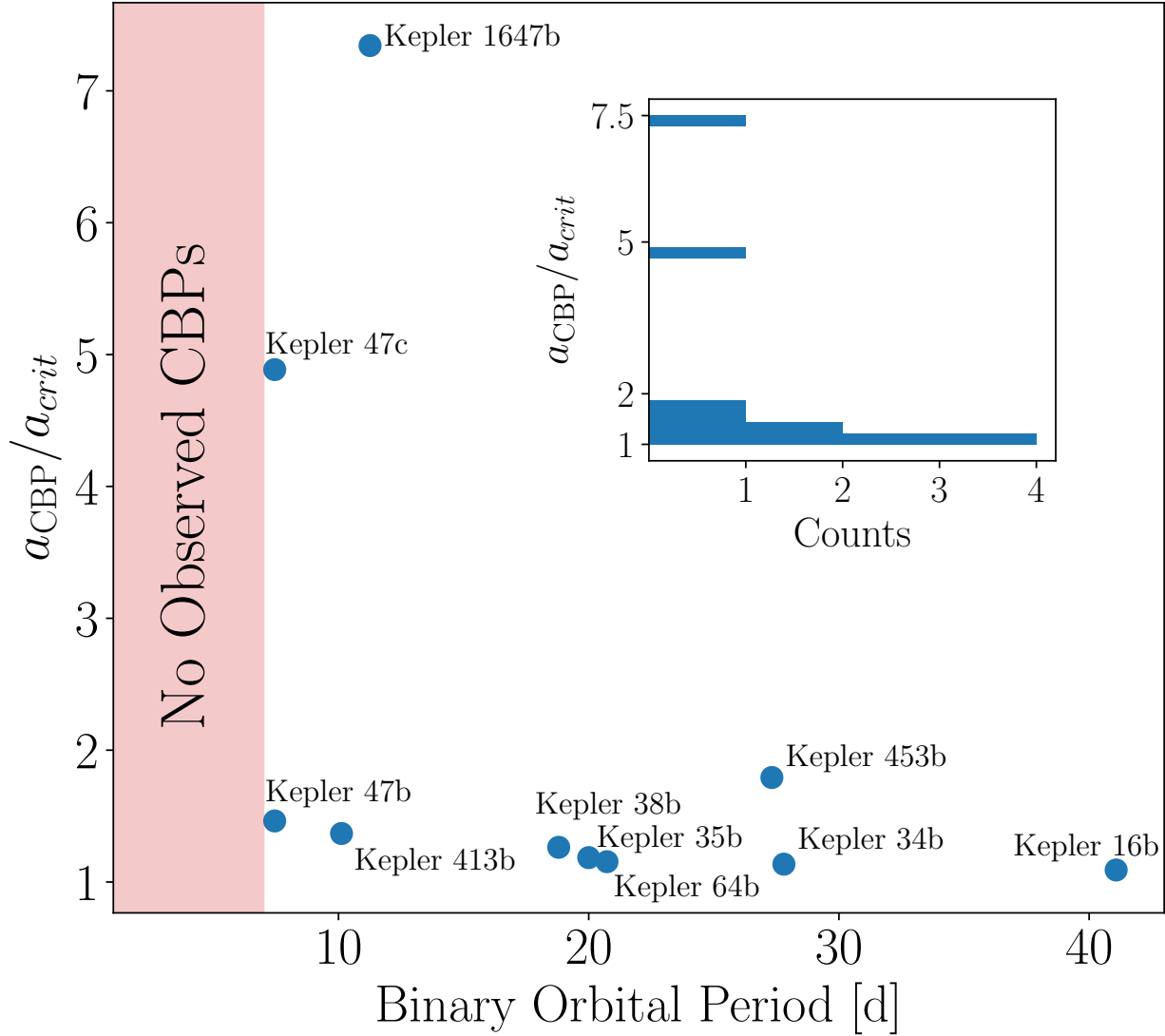


Figure 3.1: Semi-major axes of confirmed *Kepler* CBPs relative to the host binary's critical semi-major axis ($a_{\text{CBP}}/a_{\text{crit}}$) as a function of binary orbital period. Each point is annotated with the planet's name. The red-shaded region highlights the observational finding that, to date, no CBPs have been discovered orbiting binaries with binary orbital periods less than 7.45 days. (Welsh et al., 2014; Winn and Fabrycky, 2015). We neglect Kepler-47d as its orbital parameters are not well constrained. *Inset:* Histogram of observed *Kepler* CBPs' $a_{\text{CBP}}/a_{\text{crit}}$. The histogram demonstrates that most CBPs' semi-major axes cluster near the dynamical stability limit, a_{crit} .

Paardekooper et al., 2012; Meschiari, 2012a,b; Pelupessy and Portegies Zwart, 2013) and instead migrated to their present location. Simulations of CBPs embedded in a natal protoplanetary disk by Pierens and Nelson (2007) show that the planets migrate inward, halting in the region of stability just outside of the central disk cavity that is formed from binary gravitational truncation (Artymowicz and Lubow, 1994). Dunhill and Alexander (2013), Pierens and Nelson (2013), and Kley and Haghighipour (2014) all find that CBP migration can explain the observed properties of CBPs discovered by *Kepler*, depending on the precise mass and structure of the disk, suggesting that the pile-up of CBPs near the dynamical stability limit is indeed a real and expected effect. If these planets did in fact form farther out in the disk and migrate inward, they must have formed in the first few Myrs of the system’s existence before the disk dispersed, given typical lifetimes of protoplanetary disks (e.g. Haisch et al., 2001).

Whether due to migration or uncharacterized circumbinary disk physics, the pile-up of CBPs near a_{crit} seems to have a physical origin. The other important characteristic of the observed *Kepler* CBP population, the binary orbital period below which no CBPs are observed, 7.45 days (see Fig. 3.1), likely has a physical origin, as well. Curiously, this cutoff is within the range of binary orbital periods Zahn and Bouchet (1989) found that separates eccentric from circular binary systems, 7.2 – 8.5 days. The theoretical cutoff identified by Zahn and Bouchet (1989) in their study of coupled stellar-tidal physics effectively characterizes the approximate binary orbital period at which the influence of tides becomes important to the system’s evolution. In this case, it seems that in addition to stellar evolution, tidal processes in binary star systems may impact the observed circumbinary planet distribution.

In this work, we propose that the lack of CBPs around short-period binary stars is a natural outcome of coupled stellar-tidal binary evolution that we describe as follows: In young binary systems, tidal forces synchronize the stellar rotations to match the orbital period, transferring rotational angular momentum to the orbit, increasing the orbital semi-major axis, and finally, expanding the region of dynamical instability around the binary and engulfing CBPs. CBPs located just exterior to the initial dynamical stability limit enter the expanding instability region, become destabilized, and can be ejected from the system. We refer to this proposed mechanism, the Stellar-Tidal Evo-

lution Ejection of Planets, as the STEEP process for notational convenience.

In § 3.2, we detail our computational methods and outline the mathematics of our theory. We outline our experimental scheme in § 3.3 and discuss the results of our simulations in § 3.4 and § 3.5. We apply our theory to the Kepler-47 system in § 3.6 and explore the implications our results and future prospects in § 3.7.

3.2 Methods

In this section, we outline how we simulate coupled stellar-tidal evolution using the code `VPLanet` (Barnes et al., 2016, Barnes *et al.*, *in prep*) and perform N-body simulations using the code `REBOUND` (Rein and Liu, 2012) to probe the stability of circumbinary planetary systems in which the inner-most planet falls within a_{crit} as a result of coupled stellar-tidal evolution.

3.2.1 `VPLanet`

We simulate coupled stellar-tidal binary star evolution using the code `VPLanet`, a modular code that allows the user to specify which physical processes impact a given variable. Each physical process, here referred to as a module, is given by a set of nonlinear ordinary differential equations or explicit functions of time (see § 3.2.2 for the `STELLAR` module, § 3.2.3 for the `EQTIDE` module, and § 3.2.4 for additional coupling of `STELLAR` and `EQTIDE` for an in-depth description and their respective equations). `VPLanet` provides a framework in which equations from different modules are coupled such that different physical processes impact the evolution of a given variable by summing the time derivatives from each relevant module. For n modules impacting the evolution of the variable x , at each timestep `VPLanet` computes the time derivative of x as

$$\left(\frac{dx}{dt} \right)_{tot} = \left(\frac{dx}{dt} \right)_1 + \left(\frac{dx}{dt} \right)_2 + \dots + \left(\frac{dx}{dt} \right)_n. \quad (3.2)$$

This numerical setup allows `VPLanet` to simultaneously integrate an arbitrary number of coupled nonlinear ODEs to rapidly simulate a system in which numerous physical processes impact the system, such as tidally interacting pre-main sequence binaries.

`VPLanet` numerically integrates the equations using a fourth-order Runge-Kutta scheme with adaptive time-stepping. Our time-stepping algorithm chooses the timestep to resolve the evolution of the fastest changing variable for each simulation step in order to ensure that we completely resolve the evolution of the system. The timescale over which a given variable x changes is estimated by computing $|x|/|dx/dt|$ where dx/dt is the instantaneous derivative of the variable x computed by `VPLanet` via Eq. (3.2). Each simulation step, we calculate the timestep by computing, for each variable, its evolutionary timescale under each module and multiply the minimum value by a scale factor, η . We find that our simulations converge and approximately conserve both energy and angular momentum to $\sim 10^{-4}$ when $\eta \lesssim 10^{-3}$ (see § 3.2.5 and § 3.4.1).

3.2.2 Stellar Evolution

In our simulations, we track how a star’s rotation rate and radius change over time due to stellar evolution using a module called `STELLAR`. The two main stellar evolution processes that impact a star’s radius and rotation rate are stellar contraction/expansion and magnetic braking. In general, a star’s radius will contract during the pre-main sequence phase and expand slowly during the main sequence. Conservation of angular momentum dictates that as a star contracts, its rotation rate increases (and vice-versa). We model a star’s radius as a function of time using a cubic spline interpolation of the radius tracks for a star of a given mass from the stellar evolution models of Baraffe et al. (2015) for solar metallicity stars.

We derive the time derivative of a star’s rotation rate due to both magnetic braking and radius evolution under conservation of angular momentum. For simplicity, we model a star as a solid body with a given density profile parameterized by the radius of gyration, r_g , where the moment of inertia is given by $I = mr_g^2R^2$ for mass m and radius R . We assume solid body rotation for stars as the surface rotation evolution of low-mass ($\lesssim 1M_\odot$) stars can be reasonably approximated by assuming stellar solid-body rotation (Bouvier et al., 1997) and since adopting stellar solid-body rotation is common amongst studies examining stellar-tidal interactions (e.g. Dobbs-Dixon et al., 2004; Heller et al., 2011; Barnes et al., 2013; Repetto and Nelemans, 2014; Bolmont and Mathis, 2016; Bolmont et al., 2017). We neglect effects such as differential rotation and changes in r_g but

perform sensitivity tests on r_g in § 3.4.3.

The rotational angular momentum for a star is simply $J = I\omega$, where ω is the rotational frequency. By conservation of angular momentum, the star's rotation rate changes due to stellar radius evolution according to

$$\dot{\omega}_{\text{contraction}} = \frac{-2\dot{R}\omega}{R}. \quad (3.3)$$

A star loses angular momentum due to magnetic braking, decreasing ω . Magnetic braking is caused by the corotation of the stellar wind with the star's magnetic field lines (see Parker, 1958; Mestel, 1968). The poloidal magnetic field of the star carries the corotating mass far away from the star, effectively removing angular momentum from the star. Even though mass loss rates for sun-like stars are small (e.g., $\dot{M} \sim 10^{-14} \text{ M}_\odot/\text{yr}$; Tarduno et al., 2014), a star's rotation rate can slow appreciably with time due to this effect (see Fig. 3.2).

Numerous models for stellar magnetic braking have been examined in the literature and here we consider two models. The first is from Reiners and Mohanty (2012), who derived their model in the context of relating stellar rotation to stellar magnetic field strength. The model is calibrated to reproduce observations of the Sun's current rotation period and the rotation-mass distribution of field stars that are a few Gyr-old. Reiners and Mohanty (2012) give the change in stellar angular momentum due to magnetic braking as

$$\begin{aligned} \frac{dJ_*}{dt} &= -C \left[\omega \left(\frac{R^{16}}{m^2} \right)^{1/3} \right] \text{ for } \omega \geq \omega_{\text{crit}} \\ \frac{dJ_*}{dt} &= -C \left[\left(\frac{\omega}{\omega_{\text{crit}}} \right)^4 \omega \left(\frac{R^{16}}{m^2} \right)^{1/3} \right] \text{ for } \omega < \omega_{\text{crit}}, \end{aligned} \quad (3.4)$$

where the authors find a best fit of $C = 2.66 \times 10^3 (\text{gm}^5 \text{ cm}^{-10} \text{ s}^3)^{1/3}$, $\omega_{\text{crit}} = 8.56 \times 10^{-6} \text{ s}^{-1}$ for $m > 0.35 \text{ M}_\odot$, and $\omega_{\text{crit}} = 1.82 \times 10^{-6} \text{ s}^{-1}$ for $m \leq 0.35 \text{ M}_\odot$.

The second magnetic braking model we consider is presented in Repetto and Nelemans (2014) and is derived from the empirical relation for stellar spin-down of Sun-like stars empirically derived

by Skumanich (1972). The change in angular momentum due to this spin-down law is given by

$$\frac{dJ_\star}{dt} = -\gamma mr_g^2 R^4 \omega^3 \quad (3.5)$$

where $\gamma = 5 \times 10^{-25}$ s m $^{-2}$ (Repetto and Nelemans, 2014). Assuming one of the magnetic braking laws for \dot{J}_\star , the change in stellar rotation rate due to magnetic braking is

$$\dot{\omega}_{MB} = \frac{\dot{J}_\star}{I} \quad (3.6)$$

for a fixed stellar radius under conservation of angular momentum assuming negligible mass loss.

Both magnetic braking laws presented above are derived for spin-down rates of single stars, while in this work, we apply them to the evolution of short-period stellar binaries. These magnetic braking laws, however, have successfully been used to model the evolution of short-period binary systems ranging from compact object-stellar binaries (e.g. Verbunt and Zwaan, 1981; Repetto and Nelemans, 2014), the formation of main sequence stellar contact binaries (e.g. Stepień, 1995; Andronov et al., 2006), and cataclysmic variable evolution (e.g. Ivanova and Taam, 2003). Therefore, our usage of magnetic braking laws derived for single stars is valid in this context.

We combine Eq. (3.3) and Eq. (3.6) to get the net change in stellar rotation rate due to magnetic braking and stellar radius evolution under conservation of angular momentum:

$$\dot{\omega} = \dot{\omega}_{contraction} + \dot{\omega}_{MB} = \frac{\dot{J}_\star}{I} - \frac{2\dot{R}\omega}{R}. \quad (3.7)$$

and \dot{J} is given by either Eq. (3.4) or Eq. (3.5).

In Fig. 3.2, we plot the stellar radius and rotation period evolution for solar metallicity low-mass stars assuming $r_g = 0.27$ using both magnetic braking laws to demonstrate the qualitative behavior of our stellar evolution model, STELLAR. In general, the stellar radii contract along the pre-main sequence and slowly expand on the main sequence, while the stellar rotations slow over time due to magnetic braking.

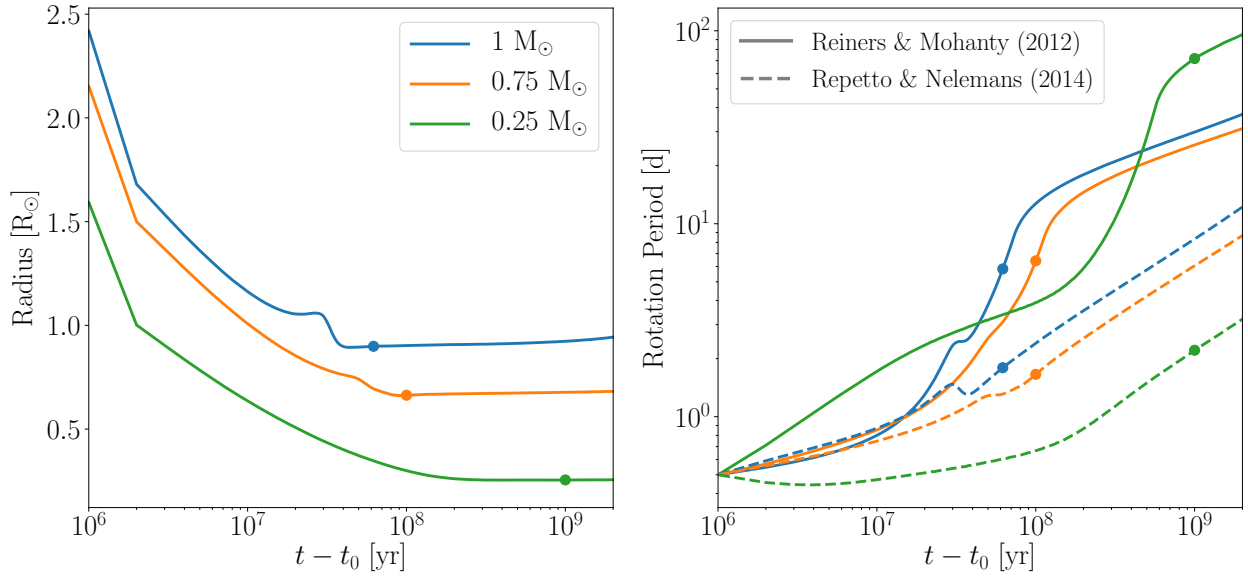


Figure 3.2: Stellar radius and rotation period evolution as computed by our stellar evolution model, STELLAR, for a $1 M_{\odot}$ (blue), $0.75 M_{\odot}$ (orange), and $0.25 M_{\odot}$ (green) star both with solar metallicity. The dots in both panels indicate the approximate time each star reaches the Zero Age Main Sequence. *Left:* Stellar radius as a function of time according to a cubic spline interpolation of the Baraffe et al. (2015) stellar models. *Right:* Stellar rotation period as a function of time computed via stellar radius evolution and both magnetic braking models under conservation of angular momentum (see Eq. (3.7)). The solid lines correspond to simulations using the Reiners and Mohanty (2012) magnetic braking law while the dashed lines use the Repetto and Nelemans (2014) magnetic braking law.

3.2.3 Tidal Evolution

For our tidal physics, we use a variant of the equilibrium tidal theory first introduced by Darwin (1880), the “Constant Phase Lag” (CPL) equilibrium tide theory as derived in Ferraz-Mello et al. (2008) in our module, EQTIDE. Equilibrium tidal theories predict that gravitational torques between the bodies and their respective tidal bulges drive a secular evolution in the eccentricity (e), semi-major axis (a) and the bodies’ spins (ω) and obliquities (ψ). The CPL model assumes the tidally-interacting bodies raise tidal bulges on each other that maintain a fixed phase with respect to the line connecting the bodies’ centers of mass. A tidal bulge is composed of a linear sum of discrete tidal lags each with their own respective frequency. Each tidal lag’s frequency is independent of any orbital or rotational forcing frequency and there is no coupling between tidal lags. In this formalism, the CPL model is akin to a driven, damped harmonic oscillator (Greenberg, 2009). This theory, accurate up to second order in e , has been used extensively in many previous studies (e.g. Leconte et al., 2010; Heller et al., 2011; Barnes et al., 2013) and has successfully reproduced the qualitative tidal evolution of Solar System bodies (e.g. Goldreich and Soter, 1966). Given the physical complexity of tidally interacting astrophysical bodies, linear equilibrium tidal models, such as the CPL model, are likely not valid at large e or inclinations as the linearity assumption breaks down (Ferraz-Mello et al., 2008; Greenberg, 2009). To maintain qualitative accuracy in our tidal evolution, we restrict the binary eccentricity to $e \lesssim 0.2$. We note that other equilibrium tidal theories exist, such as the “Constant Time Lag” (CTL) model (e.g. Hut, 1981), but we do not consider them here since in our adopted eccentricity regime, Leconte et al. (2010) showed that both the CPL and CTL model yield similar results.

Below we present a form of the CPL model tidal evolution given by Heller et al. (2011) with a modification for synchronous rotators from Ferraz-Mello et al. (2008). Note that in this work we set all obliquities to 0 and do not consider their evolution, however we include it in our model for completeness. The CPL equations for e and a evolution are:

$$\frac{de}{dt} = -\frac{ae}{8Gm_1m_2} \sum_{i=1}^2 Z'_i \left(2\varepsilon_{0,i} - \frac{49}{2}\varepsilon_{1,i} + \frac{1}{2}\varepsilon_{2,i} + 3\varepsilon_{5,i} \right) \quad (3.8)$$

$$\frac{da}{dt} = \sum_{i=1}^2 \frac{da_i}{dt} \quad (3.9)$$

where if the i^{th} body is tidally locked in a synchronous orbit,

$$\frac{da_{i,sync}}{dt} = -\frac{a^2}{Gm_1m_2} Z'_i (7e^2 + \sin^2(\psi_i)) \varepsilon_{2,i}, \quad (3.10)$$

otherwise

$$\begin{aligned} \frac{da_i}{dt} = & \frac{a^2}{4Gm_1m_2} Z'_i \left(4\varepsilon_{0,i} + e^2 \left[-20\varepsilon_{0,i} + \frac{147}{2}\varepsilon_{1,i} \right. \right. \\ & \left. \left. + \frac{1}{2}\varepsilon_{2,i} - 3\varepsilon_{5,i} \right] - 4\sin^2(\psi_i) [\varepsilon_{0,i} - \varepsilon_{8,i}] \right). \end{aligned} \quad (3.11)$$

The CPL equations for ψ and ω evolution are

$$\frac{d\psi_i}{dt} = \frac{Z'_i \sin(\psi_i)}{4m_i r_{g,i}^2 R_i^2 n \omega_i} ([1 - \xi_i] \varepsilon_{0,i} + [1 + \xi_i] (\varepsilon_{8,i} - \varepsilon_{9,i})) \quad (3.12)$$

$$\begin{aligned} \frac{d\omega_i}{dt} = & -\frac{Z'_i}{8m_i r_{g,i}^2 R_i^2 n} (4\varepsilon_{0,i} + e^2 [-20\varepsilon_{0,i} + 49\varepsilon_{1,i} + \varepsilon_{2,i}] \\ & + 2\sin^2(\psi_i) [-2\varepsilon_{0,i} + \varepsilon_{8,i} + \varepsilon_{9,i}]) \end{aligned} \quad (3.13)$$

for the i^{th} body where G is Newton's gravitational constant, n is the binary's mean motion , and ε denote the signs of the tidal phase lags.

The intermediate variables Z'_i and ξ_i are given by

$$Z'_i = 3G^2 k_{2,i} m_j^2 (m_1 + m_2) \frac{R_i^5}{a^9} \frac{1}{nQ_i} \quad (3.14)$$

$$\xi_i = \frac{r_{g,i}^2 R_i^2 \omega_i a n}{Gm_j} \quad (3.15)$$

where the j^{th} body is the i^{th} body's companion in the binary, $k_{2,i}$ is the i^{th} body's Love number of degree 2, and Q is the tidal quality factor (also referred to as the “tidal Q”). For all stars in all

simulations, we assume $k_2 = 0.5$. This choice of k_2 does not impact our results as it is degenerate with the choice of tidal Q via the k_2/Q scaling in Eq. (3.14). We choose to vary stellar tidal Qs to probe how different tidal dissipation rates impact our results (see § 3.4.2).

The signs of the tidal phase lags for the i^{th} body are given by

$$\begin{aligned}\varepsilon_{0,i} &= \Sigma(2\omega_i - 2n) \\ \varepsilon_{1,i} &= \Sigma(2\omega_i - 3n) \\ \varepsilon_{2,i} &= \Sigma(2\omega_i - n) \\ \varepsilon_{5,i} &= \Sigma(n) \\ \varepsilon_{8,i} &= \Sigma(\omega_i - 2n) \\ \varepsilon_{9,i} &= \Sigma(\omega_i)\end{aligned}\tag{3.16}$$

where $\Sigma(x)$ gives returns 1 for positive x , -1 for negative x , or 0 otherwise.

As a system approaches a tidally locked state, the numerical integration of our tidal equations can become unstable due to the discrete nature of the CPL model and of the integration scheme itself. For example, if a simulation approaches a tidally locked and synchronous state, $\omega \approx n$, then the derivatives of the tidal equations become discontinuous. Numerical integration is inherently a discrete scheme, so solutions for systems near such a state will oscillate around a 1:1 spin-orbit resonance, causing $\varepsilon_{0,i}$ to rapidly switch signs and hence change how the systems evolve, leading to unstable, unphysical behavior. To rectify this issue, once a body's spin period is within 1% of the orbital period, we force the system into a tidally locked, synchronous state by setting $\omega = n$, following Barnes et al. (2013). In § 3.2.4, we derive equations that account for the coupled stellar-tidal evolution for tidally locked star(s) to conserve both energy and angular momentum and ensure that our model results in a physically realistic evolution.

Stars on eccentric orbits can enter a pseudo-synchronous rotation state or become trapped in a higher order spin orbit resonance when the system tidally locks, with a familiar example being Mercury's 3:2 spin-orbit resonance (Goldreich and Peale, 1966). Note that here the use of “spin-orbit resonance” does not mean this system is trapped in a dynamical resonance in the traditional sense,

but instead enters into a spin-orbit commensurability in which the spin and rotational frequencies are integer multiples of each other; we use “spin-orbit resonance” for notational convenience. If a body tidally locks into a pseudo-synchronous rotation state, the rotational period is a continuous function of both the orbital eccentricity and period (see Goldreich, 1966; Wisdom, 2008). The CPL model, however, only permits 2 rotation states for tidally locked bodies, a 1:1 and 3:2 spin-orbit resonance (Barnes, 2017). In the CPL model an orbit is trapped in a 3:2 spin-orbit resonance when the binary tidally locks with $e \geq \sqrt{1/19} \approx 0.229$ (Ferraz-Mello et al., 2008) and locks into synchronous rotation otherwise. In our adopted eccentricity regime, $e \lesssim 0.2$, stars tidally lock into a synchronous state with $\omega = n$ but in § 3.4.7 we probe how capture into a 3:2 spin-orbit-resonance for more eccentric binary star systems impacts our results.

In Fig. 3.3, we plot the tidal evolution of a $1 M_{\odot}$ – $1 M_{\odot}$ binary star system using the fiducial parameters given in Table 3.1 to demonstrate the qualitative behavior of our tidal evolution model, EQTIDE. For details of the numerical intergration of the simulation, see § 3.2.1. In general, tides transfer angular momentum from the stellar rotations into the orbit until the binary reaches a tidally locked, synchronous orbit after $\sim 10^6$ yr. The binary orbit circularizes after $\sim 5 \times 10^8$ yr.

3.2.4 Coupled Stellar-Tidal Evolution

The coupled stellar-tidal orbital evolution of binary systems has been extensively studied in the literature for systems ranging from star-star binaries (e.g. Huang, 1966; Mestel, 1968; van’t Veer and Maceroni, 1988; Zahn and Bouchet, 1989; Li and Wickramasinghe, 1998; Khaliullin and Khaliullina, 2011) to star-planet binaries (e.g. Dobbs-Dixon et al., 2004; Barker and Ogilvie, 2009; Lanza and Mathis, 2016) to even star-compact object binaries (e.g. Verbunt and Zwaan, 1981; Repetto and Nelemans, 2014). In particular, the pioneering theoretical study of Zahn and Bouchet (1989) tracked the coupled stellar-tidal evolution of low-mass stellar binaries with a focus on the pre-main sequence evolution and outlined the general qualitative behavior that arises from this coupling. Although their study mainly focused on orbital circularization during the pre-main sequence, Zahn and Bouchet (1989) also showed that as the binary approached synchronization, the binary orbital period increases as tides transfer rotational angular momentum from the stellar rotations to the

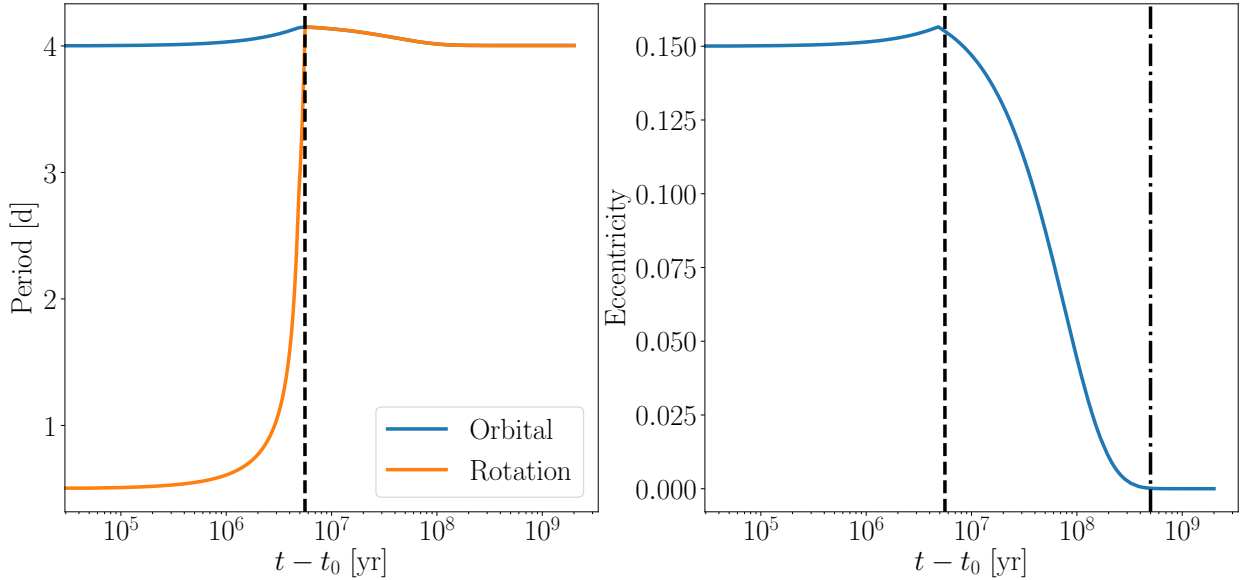


Figure 3.3: Tidal evolution of a binary star system with no stellar evolution under the CPL model (Ferraz-Mello et al., 2008; Heller et al., 2011) as computed by our tidal evolution model, EQTIDE. See the text for the system properties. *Left:* Binary orbital and stellar rotational period versus time. Tides transport angular momentum from the stellar rotations into the orbit until the binary becomes tidally locked and synchronous (denoted by the black dashed line). *Right:* Binary orbital eccentricity versus time. After the orbit synchronizes, the eccentricity decreases until the binary circularizes (denoted by the dash-dotted line).

orbit. We reproduce this phenomenon in our simulations (see § 3.4).

Common to many of the aforementioned studies of coupled stellar-tidal evolution is that for tidally locked systems, any angular momentum lost from the star(s) is lost at the expense of the orbit. For tidally locked synchronous rotators, for example, as magnetic braking slows the stellar rotations, tides speed up the stellar rotations to force the stars' spin periods to be equal to the orbital period. Tidal speed-up of stellar rotations to maintain synchronization removes angular momentum from the orbit, causing orbital semi-major axis decay and faster stellar rotations. A similar spin-orbit coupling occurs for stellar radius contraction and expansion for tidally locked stars. In this section, we derive equations for how the binary semi-major axis, a , changes due to both magnetic braking and stellar radius evolution when either one or both stars are in a tidally locked orbit. We assume constant mass, as mass loss is negligible for low-mass main sequence stars. These equations provide an additional change in the binary semi-major axis, denoted $\dot{a}_{coupled}$, such that the net change in the binary semi-major axis is $\dot{a}_{net} = \dot{a}_{tides} + \dot{a}_{coupled}$ where the \dot{a}_{tides} term comes from EQTIDE Eq. 3.9. We explore the dynamical and observational consequences for magnetic braking-driven semi-major axis decay in § 3.4.1 and § 3.4.8.

Case 1: One Tidally Locked Star

In the case of one tidally locked star, the angular momentum of the orbit and star are explicitly coupled as any angular momentum change in the star imparts a change in the orbit as mediated by tidal forces. In this case, we consider the following quantity

$$J = \mu_{tot} \sqrt{GMa(1 - e^2)} + m_1 r_{g,1}^2 R_1^2 \omega + J_{mb}, \quad (3.17)$$

where J is the total angular momentum, J_{mb} is the reservoir of angular momentum lost to space via magnetic braking, $\mu_{tot} = m_1 m_2 / (m_1 + m_2)$, $M = m_1 + m_2$ and the rotation rate ω is set by the star's tidally locked state, e.g. synchronous or a 3:2 spin-orbit-resonance. This net angular momentum quantity only includes the contributions from both the orbit and the tidally locked star as these are explicitly coupled by tides in this case. We assume $\dot{J} = 0$ as the total angular momentum is

conserved. By taking the time derivative of Eq. (3.17) and rearranging, we obtain

$$\dot{a}_{coupled}^{(1)} = \frac{-\dot{J}_{mb} - 2m_1 r_{g,1}^2 \omega R_1 \dot{R}_1 + \frac{\mu^2 G M a e}{J} \dot{e}}{\frac{\mu^2 G M (1-e^2)}{2J} - \frac{3\omega}{2a} m_1 r_{g,1}^2 R_1^2} \quad (3.18)$$

for the binary semi-major axis change due to the magnetic braking and stellar radius evolution for one tidally locked rotating star. Note that $\dot{J}_{mb} > 0$ as this term tracks the amount of angular momentum lost from the system and hence gains the amount lost from stars due to magnetic braking. Eq. (3.18) is given for the case when the primary star is tidally locked and is trivially altered for the case when the secondary star is tidally locked by exchanging indices.

Following the lead of previous works (e.g. Verbunt and Zwaan, 1981; Repetto and Nelemans, 2014), we assume magnetic braking and stellar radius evolution do not torque the orbit and hence cannot change e , only a . We leave the \dot{e} term in Eq. (3.18) and Eq. (3.20) for completeness.

Case 2: Two Tidally Locked Stars

When both stars are tidally locked, the angular momentum of the orbit and both stars is coupled. Just as in the one-tidally-locked-star case, the total angular momentum of the system

$$J = \mu_{tot} \sqrt{G M a (1 - e^2)} + m_1 r_{g,1}^2 R_1^2 \omega + m_2 r_{g,2}^2 R_2^2 \omega + J_{mb}, \quad (3.19)$$

where 1 and 2 denote the primary and secondary star, respectively, and $J = 0$. As before, we take the time derivative of Eq. (3.19), rearrange, and obtain

$$\dot{a}_{coupled}^{(2)} = \frac{-\dot{J}_{mb} - 2\omega \left(m_1 r_{g,1}^2 R_1 \dot{R}_1 + m_2 r_{g,2}^2 R_2 \dot{R}_2 \right) + \frac{\mu^2 G M a e}{J} \dot{e}}{\frac{\mu^2 G M (1-e^2)}{2J} - \frac{3\omega}{2a} \left(m_1 r_{g,1}^2 R_1^2 + m_2 r_{g,2}^2 R_2^2 \right)} \quad (3.20)$$

for the binary semi-major axis change due to the magnetic braking and stellar radius evolution.

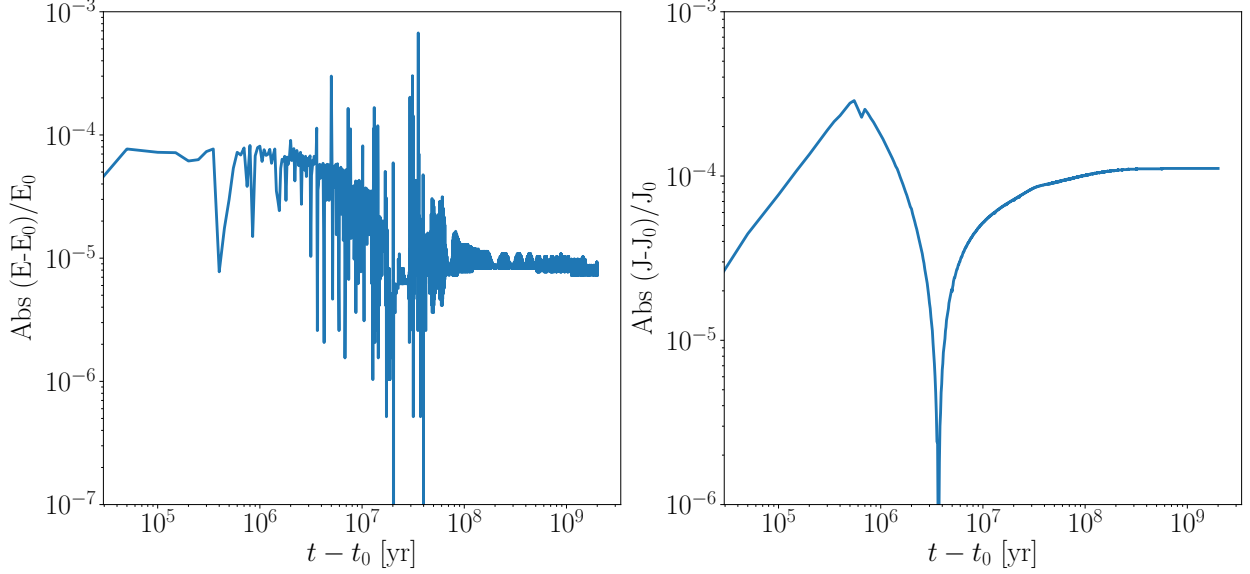


Figure 3.4: *Left Panel:* Absolute relative difference between the total system energy and initial total system energy as a function of time. *Right Panel:* Absolute relative difference of the total system angular momentum and initial total system angular momentum as a function of time. Both total energy and angular momentum are approximately conserved at the 10^{-4} level with high frequency oscillations caused by limitations of Runge-Kutta integrations.

Case 3: Free Rotators

We include either Eq. (3.18) or Eq. (3.20) in our numerical integration only when either one or both stars become tidally locked in our simulations. When neither star is tidally locked, the aforementioned mechanism does not apply, and hence we set $\dot{a}_{\text{coupled}} = 0$.

3.2.5 Energy and Angular Momentum Conservation

In Fig. 3.4, we plot the relative absolute change in both the total system energy and angular momentum as a function of time for our fiducial simulation (see Table 3.1, § 3.4.1) to demonstrate that both energy and angular momentum are approximately conserved in our VPLanet simulations. The secular drifts in total angular momentum stem from our usage of the CPL tidal model that extends to only second order in e and hence cannot not exactly conserve angular momentum. We conclude our methodology satisfies the conservation laws to sufficient accuracy.

3.2.6 *N*-body Simulations of Circumbinary Planetary Systems

Here, we complement our VPLanet simulations of coupled stellar-tidal evolution with several suites of N-body simulations that probe the dynamical and observational impact of single and two-planet circumbinary planetary systems in which the inner-most planet falls within the a_{crit} . We simulate such systems using the N-body code REBOUND (Rein and Liu, 2012). We use REBOUND’s high-order, adaptive timestepping IAS15 integration scheme to integrate the gravitational forces in our simulations as it is accurate and flexible enough to handle close encounters and scattering events while conserving energy to a high precision (Rein and Spiegel, 2015). We outline the simulation setup and our choice of initial conditions in § 3.3.2.

We show that due to coupled stellar-tidal evolution, a CBP that initially resides near the dynamical stability limit can fall within the a_{crit} and go unstable, potentially disrupting the entire circumbinary planetary system. For single-planet circumbinary systems, the planet will likely be ejected, potentially leaving no observational signature that the binary ever hosted a planet. Multi-planet circumbinary systems in which the inner planet falls within a_{crit} , however, can potentially undergo richer dynamical evolution in which binary-planet scattering and planet-planet scattering can reshape the system resulting in multiple planetary ejections, but also leave one or more planets bound to the stars. Several previous studies have examined the impact of binary-planet and/or planet-planet scattering in circumbinary systems (e.g. Kratter and Shannon, 2014; Smullen et al., 2016; Sutherland and Fabrycky, 2016; Gong and Ji, 2017; Gong, 2017). No study yet has examined the case we consider in this paper in which the inner planet of a two-planet circumbinary planetary system initially resides interior to the dynamical stability limit. This calculation is important as it not only allows us to estimate how many planets are actually ejected from these systems but also to estimate how ejection and scattering events can impact the detectability of any surviving CBPs.

Note that in our simulations, we do not model planet-planet or star-planet collisions for computational speed and simplicity. This approach is justified as previous studies of planet-planet scattering and instabilities in circumbinary planetary systems all find that planetary ejection occurs far more often than collisions when a planet is lost from the system (see Smullen et al., 2016;

Table 3.1. Parameter Ranges

| Parameter | Range | Fiducial |
|---------------------|---------------|----------|
| $M_\star [M_\odot]$ | $0.5 - 1$ | 1 |
| e | 0.0 - 0.2 | 0.15 |
| $P_{bin,init}$ [d] | $3 - 7.5$ | 4 |
| $P_{rot,init}$ [d] | $0.1 - 2$ | 0.5 |
| Q | $10^5 - 10^7$ | 10^6 |
| r_g | $0.15 - 0.45$ | 0.27 |

Sutherland and Fabrycky, 2016). Also note we do not consider the coupled stellar-tidal-N-body evolution.

3.3 Simulations

Here we outline the details of both our VPLanet and REBOUND N-body simulations and justify our assumed initial conditions.

3.3.1 Coupled Stellar-Tidal Initial Conditions

We probe how model parameters and the underlying assumptions impact the ability for coupled stellar-tidal evolution to destabilize CBPs by running several sets of simulations varying just one parameter at a time and several suites of many simulations varying multiple parameters over the adopted ranges. Using VPLanet, we simulated coupled stellar-tidal evolution by simultaneously integrating the equations presented in § 3.2.2-3.2.4 for 2 Gyr for each simulation as described in § 3.2. In Table 3.1, we give the default values and range for our simulation initial conditions. Below, we justify our choice of parameter ranges and fiducial values and discuss the qualitative results of a simulation initialized with the fiducial values to elucidate how coupled stellar-tidal evolution drives changes in a_{crit} .

Stellar Tidal Qs

Binary stars' tidal Qs strongly determine the extent to which a short-period binary tidally evolves. Currently, the value of Q for low-mass stars is uncertain. From observations of tidally circularized binaries in clusters, tidal Qs for sun-like stars have been estimated to be of order $Q \sim 10^6$ (e.g. Meibom and Mathieu, 2005). Observations of orbital decay of hot Jupiters find tidal Qs for the host stars are of order $\sim 10^5 - 10^6$ (Jackson et al., 2009; Essick and Weinberg, 2016; Patra et al., 2017; Wilkins et al., 2017). Given these observations, we adopt $Q = 10^6$ as our fiducial value. Detailed studies of tidal dissipation in sun-like stars by Ogilvie and Lin (2007), however, have shown that a star's tidal Q has complicated dependencies on the viscous and hydrodynamical processes operating within the star and can strongly vary depending on the star's spin frequency and the orbital frequency of its companion. Additionally, Barker and Ogilvie (2009) find that the tidal Q likely varies even among stars in the same spectral class. In the case of pre-main sequence stars, Bolmont and Mathis (2016) find that efficient tidal dissipation yields tidal Qs of order $10^4 - 10^6$. Since our simple model uses a constant tidal Q and cannot capture more complex tidal Q evolution, in § 3.4.2 we vary the tidal Q amongst our simulations by two orders of magnitude to probe our model's sensitivity to various tidal Qs.

Stellar Rotations

The STEEP process requires that short-period binary stars form with rotation periods (P_{rot}) shorter than the orbital period. For short stellar rotational periods, $P_{rot} \lesssim 1$ day, the rotational angular momentum can be of order the orbital angular momentum, allowing for a significant increase in a_{crit} via tidal transfer of angular momentum. Here, we review observations of young single stars and binaries in open clusters to justify our stellar rotation assumptions.

In a study of about 250 stars in the ~ 1 Myr old Orion OB1c/d association, Stassun et al. (1999) find a flat distribution for $P_{rot} > 0.5$ days. Interestingly, Stassun et al. (1999) find several stars rotating near the break-up velocity, a rotational period of $P_{rot} \sim 0.25$ days, indicating that young stars can indeed be very rapid rotators. Given this finding, we set the lower limit for initial P_{rot}

in our study to be $0.1 - 0.2$ days. Rebull et al. (2006) examined the P_{rot} of about 900 stars in the roughly 1 Myr old Orion Molecular Cloud, finding most stars with $1 < P_{rot} < 10$ days, and a minority with $P_{rot} \lesssim 1$ day. A study of P_{rot} of young weak T Tauri star candidates in the Orion star forming region by Marilli et al. (2007) found a roughly flat distribution with a peak near $P_{rot} = 1.5$ days, similar to the aforementioned findings. Studies of older open clusters with ages $\sim 100 - 200$ Myr consistently find stellar rotation distributions with P_{rot} often as low as $P_{rot} = 0.5$ days and many stars with $P_{rot} = \lesssim 1$ day, although there is an appreciable spread in P_{rot} with some reaching up to $P_{rot} \sim 10$ days (see Marilli et al., 2007; Meibom et al., 2009, 2011). Young stars can readily have $P_{rot} \lesssim 1$ day.

For the P_{rot} of binary stars, Meibom et al. (2007) observed the ~ 150 Myr old open cluster M35 and measured the P_{rot} distributions of primary stars of close binaries and single stars. Meibom et al. (2007) found that the primary stars in binaries tended to have shorter P_{rot} than single stars with statistically significant differences in the means and medians of the two P_{rot} distributions of at least the 99.9% level after controlling for tidal effects. Stauffer et al. (2016) derive a similar result from observations of P_{rot} in young, low-mass binaries in the Pleiades. We conclude that a significant number of young binary stars form with $P_{rot} \lesssim 1$ days.

Stellar Radius of Gyration

Measuring the stellar r_g is, in general, quite a difficult task so here we rely on theoretical stellar evolution models to inform our choices. From the Baraffe et al. (2015) stellar evolution models for sun-like stars, $r_g \approx 0.45$ on the pre-main sequence, decreasing to $r_g \approx 0.27$, our fiducial value, on the main sequence. Our model utilizes a constant r_g , so we vary it in a series of simulations to gauge how strongly it impacts the evolution of a_{crit} over time in § 3.4.3. We consider our fiducial value of $r_g = 0.27$ to be a conservative estimate as we show in § 3.4 most of the a_{crit} evolution occurs while the stars reside on the pre-main sequence.

3.3.2 *N-body Simulations*

Each N-body simulation is comprised of two segments. First, we run long-term integration probing the dynamical stability of a one- or two-planet circumbinary system comprised of planets “b” and “c”, when applicable, to determine if any planets are ejected from the system. Once that run finishes, we run a short-term integration initialized with the final state of the long-term dynamical stability integration to perform a series of mock transit observations that explore how dynamical instabilities in such systems impact the detectability of the remaining planets. Splitting a given simulation into two segments allows us to both characterize the dynamics of circumbinary systems in which the inner planet falls within a_{crit} and to probe the resulting observational consequences. We outline the procedures for each part of the simulation below. We summarize and examine the results of these simulations in § 3.5.

N-body Simulations Initial Conditions

For each simulation, we initialize the binary with two $1 M_\odot$ stars with an orbital period of 7 days and e randomly uniformly sampled from $[0, 0.2]$ orbiting in the $x - y$ plane. This choice simplifies the system geometry such that the binary is always in a transiting configuration ($i_{bin} = 90^\circ$). The binary longitude of the ascending node (Ω), argument of pericenter (ω), and mean anomaly (M) are all randomly uniformly sampled from $[0, 2\pi]$.

With the binary parameters set, b’s semi-major axis is randomly uniformly sampled from $[0.94, 1]$ times a_{crit} . i.e. just within the a_{crit} (recall that the errors on Eq. (3.1) are at worst 6% (Holman and Wiegert, 1999)). In multi-planet simulations, planet c’s semi-major axis is constructed such that it is randomly uniformly sampled from $[5, 10]$ mutual Hill radii from b, where a mutual Hill radius is

$$R_{hill,mutual} = \left(\frac{m_b + m_c}{3M_{bin}} \right)^{\frac{1}{3}} \frac{a_b + a_c}{2}, \quad (3.21)$$

where m_b and m_c are the masses of planet b and c, respectively, M_{bin} is the total mass of the binary, and a_b and a_c are the semi-major axes of planets b and c, respectively (Chambers et al., 1996). CBP eccentricities are randomly uniformly sampled from $[0, 0.1]$ and Ω , ω and M are all randomly

uniformly sampled from $[0, 2\pi)$. We summarize the randomized orbital elements for both the binary and the planets in Table 3.2. All CBP orbital elements are initialized in Jacobi coordinates.

In single planet simulations, we examined three cases varying the mass of planet b, while in multi-planet simulations, we examined six cases in which we varied both the mass of planets b and c and their initial inclination relative to the plane of the binary to examine their impact on our results. For the planet masses, we consider three cases: Neptune-, Saturn-, and Jupiter-mass CBPs as these roughly span the observed masses for transiting CBPs. Both planet masses are randomly sampled from the same normal distributions with mean m_p and standard deviation $0.1m_p$, where m_p is equal to the mass of Neptune, Saturn, or Jupiter depending on the simulation suite. We chose to sample both planet masses from the same distribution for a given simulation to keep the planet mass ratio $m_b/m_c \sim 1$, which simplifies our results because varying CBP mass ratios can strongly impact the scattering process in such systems (Gong and Ji, 2017). For the planet inclinations relative to the binary, we randomly uniformly sample from $[0^\circ, 1^\circ]$ (the “low inclination” case) or $[0^\circ, 3^\circ]$ (the “high inclination” case). Both of these initial inclination distributions are broadly consistent with the observed trend of transiting circumbinary exoplanets to be nearly coplanar with their host binary (e.g. Li et al., 2016), but we stress that the true inclination distribution of transiting circumbinary exoplanets is unknown. We adopt these two simple distributions given our ignorance of the true underlying distribution and since the inclination distribution can significantly impact the observed transitability of circumbinary exoplanets (see Armstrong et al., 2014; Martin and Triaud, 2015). We run 1,000 simulations for each of the aforementioned cases for a total of 9,000 N-body simulations.

Dynamical Stability Integration

In the first part of a simulation, we integrate a one or two-planet circumbinary system for 10^5 binary orbital periods. This timescale, about an order of magnitude longer than the CBP dynamical stability simulations of Holman and Wiegert (1999) in terms of binary orbital periods, and is sufficiently long for the majority of dynamically unstable systems to go unstable. We classify a system as unstable when one or both of the planets is ejected from the system. A planet is considered

Table 3.2. N-body Simulation Initial Condition Ranges

| Parameter | Distribution |
|--------------------|--------------------------------|
| e_{bin} | $U(0, 0.2)$ |
| $e_{b,c}$ | $U(0, 0.1)$ |
| a_b [AU] | $U(0.94, 1.0) \times a_{crit}$ |
| $nR_{hill,mutual}$ | $U(5, 10)$ |
| $\Omega_{bin,b,c}$ | $U(0, 2\pi)$ |
| $\omega_{bin,b,c}$ | $U(0, 2\pi)$ |
| $M_{bin,b,c}$ | $U(0, 2\pi)$ |

ejected when its semi-major axis exceeds 50 AU from the system barycenter, a distance that is over an order of magnitude larger than any of the CBP’s initial semi-major axes. When a planet gets ejected, it is removed from the N-body simulation. At the end of the integration, we record the final architecture of the simulation, namely the remaining planet’s Cartesian positions and orbital elements relative to the binary barycenter.

Mock Transit Observation Integration

In the second part of a simulation, we integrate the remaining bodies in the system for 4 years, the approximate lifetime of the *Kepler* mission, and perform mock transit observations to estimate if any remaining CBPs transit and, if so, how frequently they transit. The geometry of our simulations is set up such that the binary orbits in the $x - y$ plane and the observer looks down the $+x$ axis towards the origin. In this simplified configuration, the binary is always in a transiting configuration and almost all of the CBPs are initially in a transiting configuration. A more realistic treatment would allow the binary to have an arbitrary inclination on the sky with respect to the observer and include more physically-motivated binary and CBP orbital parameter priors. For our purposes, however, this simple case permits a first order analysis of the dynamics of these unstable systems and their observational consequences. We leave a more robust treatment for future work and refer

the reader to Martin and Triaud (2014) for a detailed examination of the detectability of CBPs orbiting non-transiting binaries.

To perform mock transit observations, every ~ 2 simulation minutes we record if any of the remaining planets are transiting either of the two host stars. A planet is transiting if

$$d < r_{planet} + r_{star} \text{ and } x_{planet} > x_{star} \quad (3.22)$$

where r_i is the radius of the i^{th} body, d is the projected distance between the centers of mass of the planet and star under consideration, and x_i is the x Cartesian coordinate of the i^{th} body. We require $x_{planet} > x_{star}$ since in our simplified geometry, the observer lies along the $+x$ axis and looks towards the origin. This frequent sampling over the course of the *Kepler* timescale integration not only checks if any remaining planet transits, but also facilitates the calculation of the fraction of time transiting either or both of the binary stars (henceforth referred to as FTT). Given the inherent difficulty in detecting transiting CBPs (e.g. Welsh et al., 2014; Winn and Fabrycky, 2015), FTT is a useful quantity as CBPs that have larger FTTs spend more time transiting and should be more detectable. We discuss the results of this analysis in § 3.5.

3.3.3 Tying It All Together

In summary, we first run an expansive set of VPLanet simulations to examine how coupled-stellar tidal evolution affects a_{crit} . Our simulations not only probe how this evolution depends on parameters such as the stellar tidal Q, but also examine thousands of different initial states for diverse binary systems. These simulations reveal how the STEEP process forces CBPs within a_{crit} . We present the results of these simulations in § 3.4. To complete the theoretical picture given by the STEEP process, we then run an ensemble of N-body simulations with REBOUND to characterize how CBP systems evolve when one planet is interior to the stability limit. Finally, we follow up these simulations with mock transit observations to gain a crude understanding of how the STEEP process impacts the observability of any surviving CBPs. We present the results of these simulations in § 3.5.

3.4 Results: Coupled Stellar-Tidal Evolution Simulations

Here we present the results of simulations of coupled stellar-tidal evolution of binary star systems. In § 3.4.1 through § 3.4.9 we simulate coupled stellar-tidal evolution for binary star systems using VPLanet to quantify how the initial binary orbit, the initial stellar rotations, and the details of the tidal interactions impact the evolution of $a_{crit,init}$.

3.4.1 Fiducial Simulation

To demonstrate how binary star systems evolve due to coupled stellar-tidal physics, we present the full evolution of a $1 M_\odot - 1 M_\odot$ binary system using the fiducial parameter values given in Table 3.1 for the initial conditions (compare to Fig. 3.3). We present the results of this simulation in terms of a_{crit} , the orbital and rotation periods, and the e in Fig. 3.5, annotated with key simulation results and evolutionary regimes.

Initially, the rotation rate, ω , slows as tides transfer rotational angular momentum into the orbit causing the orbital period to grow. During this time, stellar contraction supplies additional rotational angular momentum, slowing the ω decay, while magnetic braking removes some rotational angular momentum from the system entirely. The system tidally locks after about 1 Myr as tides efficiently transport stellar rotational angular momentum into the orbit.

The early growth in the binary orbital period drives most of the a_{crit} growth with the small increases in e providing the rest. a_{crit} reaches its largest value just before tidal locking occurs due to the slight e growth. For $e = 0$, the binary would reach the peak a_{crit} precisely once the binary tidally locks. In the top panel of Fig. 3.5, we show in grey the difference between the maximum and initial critical semi-major axis, $a_{crit,max}/a_{crit,init} = 1.16$, a value likely large enough to destabilize some CBPs, see Fig. 3.1.

In all our simulations, we find that a binary reaches the maximum semi-major axis at about the time it becomes tidally locked. This occurs for two reasons. First, once both stars are tidally locked and synchronized, tides have already transferred as much angular momentum from the stellar rotations into the orbit as possible - any remaining tidal coupling will work to maintain

the tidal locking and will not further expand the binary orbit. Second, for these systems, we find that tidal locking occurs well in advance of orbital circularization via tides. Larger non-zero eccentricities maintain larger a_{crit} according to Eq. (3.1).

After tidal locking, the binary rotation and orbital periods perfectly mirror each other as tides keep the binary synchronous (see § 3.2.3 and § 3.4.7 for higher-order spin-orbit resonances at larger e). In this regime, e decreases until the orbit is circularized after about 1 Gyr, well after the stars are tidally locked, further decreasing a_{crit} .

Once the system is tidally locked, magnetic braking cannot slow stellar rotations, so instead it removes angular momentum from the orbit causing the orbital period and a_{crit} to decay dramatically with the orbital period dropping by almost 1 day per Gyr. This substantial orbital decay causes a_{crit} to drop by about a factor of 1.6 relative to its maximum value. The combination of orbital circularization and magnetic braking for tidally locked binaries causes significant observational consequences for short-period binaries: the orbit, and hence a_{crit} , observed today is likely much different than what it was in the past. For example if this system was observed at the end of the simulation, we might expect to find CBPs near a_{crit} based on the *Kepler* CBP discoveries. Coupled stellar-tidal evolution could have destabilized CBPs near a_{crit} early on in the system’s lifetime such that there would be no CBPs to detect. a_{crit} decay implies that the dynamical instability region around the binary was much larger in the past such that any surviving CBPs would necessarily have to be located at larger a_{CBP} relative to the central binary’s a and hence be harder to detect. We examine this effect further in § 3.4.8 with a particular focus on the impact of the initial binary orbital period and the details of the magnetic braking physics.

3.4.2 Varying Tidal Q

The value of the stellar tidal Q s is of primary importance to the STEEP process as it controls the timescale of tidal evolution and the rate of angular momentum transfer from stellar rotations to the orbit. In Fig. 3.6, we present the evolution of a $1 M_\odot - 1 M_\odot$ and a $1 M_\odot - 0.5 M_\odot$ binary with stellar tidal Q s ranging from 10^5 - 10^7 . For simplicity, we set both stars’ Q to the same value.

For each simulation, the binary orbital period increases by upwards of one day for smaller tidal

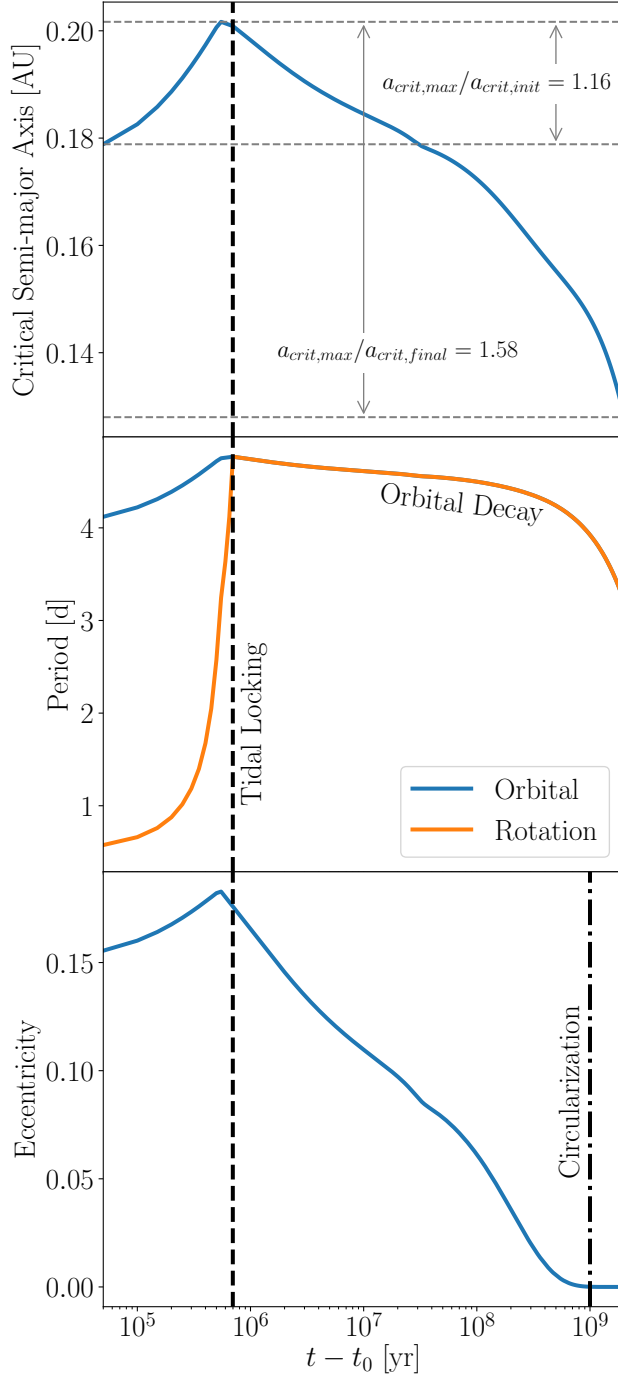


Figure 3.5: Evolution of a binary system using our default parameters from Table 3.1. *Top:* a_{crit} vs. time. The grey arrows demarcate both the ratio of the maximum critical semi-major axis to the initial and final values, $a_{crit,max}/a_{crit,init} = 1.16$ and $a_{crit,max}/a_{crit,final} = 1.58$ for this system, respectively. *Middle:* Orbital and stellar rotation period vs. time. The black dashed line indicates that the binary tidally locks after about 1 Myr. *Bottom:* e vs. time. The dot-dashed line indicates when the binary circularizes at about 1 Gyr, well after tidally locking.

Q_s as angular momentum is tidally transferred to the orbit. Stellar contraction during the pre-main sequence phase speeds up the stellar rotations, providing additional angular momentum for transfer into the orbit. The increasing orbital period is accompanied by a modest increase in e from 0.15 to upwards of 0.18. The orbital period increases until the system tidally locks at which point the tidal transfer of rotational angular momentum to the orbit is complete. Tidal locking occurs at around 10^5 years for $Q = 10^5$ and 1 Myr and 10 Myr for $Q = 10^6$ and $Q = 10^7$, respectively. The increasing orbital period primarily drives the increase in a_{crit} , which peaks approximately at the same time as the orbital period. Once the system tidally locks, the orbital period decays as magnetic braking siphons angular momentum from the orbit. As seen in Fig. 3.6, magnetic braking drains a large amount of angular momentum from the orbit, often causing the orbital period to decrease by a little over a day in 100 Myr, a decrease of 25%.

We find that binary stars with lower tidal Q_s tend to reach larger $a_{crit,max}/a_{crit,init}$. Lower tidal Q_s lead to faster tidal evolution since the equations in our CPL model all have a $1/Q$ dependence (see § 3.2.3). When the tidal evolution proceeds more quickly, there is less time for magnetic braking to siphon rotational angular momentum away from the stars, allowing for tides to transport a larger amount of the rotational angular momentum into the orbit, increasing the period and $a_{crit,max}/a_{crit,init}$. Binary stars with $Q \lesssim 10^6$ readily reach $a_{crit,max}/a_{crit,init} \gtrsim 1.1$, a value large enough to destabilize some CBPs that form near the dynamical stability limit.

Orbital circularization via tides proceeds more quickly for binary stars with lower stellar tidal Q due to the $1/Q$ scaling in the CPL model equations (see § 3.2.3). The orbits of binary stars with $Q = 10^5$ circularize in around 10 Myr while those with $Q = 10^7$ can take longer than 2 Gyr to full circularize. In general, the tidal circularization timescale also depends on the binary orbital period as tighter binaries will circularize more rapidly. Binary star orbits with orbital periods $\gtrsim 10$ days are not likely to circularize (e.g. Zahn and Bouchet, 1989; Meibom and Mathieu, 2005; Raghavan et al., 2010; Lurie et al., 2017).

The unequal-mass binaries tend to have lower $a_{crit,max}/a_{crit,init}$ than their equal-mass counterparts because the lower-mass star tidally locks earlier than the more massive primary. At this point, magnetic braking cannot slow down the lower-mass star's rotation rate as tidal locking fixes

it to the mean motion, i.e. magnetic braking siphons angular momentum from the orbit, slowing the growth of the binary period (see § 3.2.4).

3.4.3 Varying Radius of Gyration

The parameter r_g strongly influences how this transfer occurs due to both tidal evolution, see Eq. (3.13), and stellar evolution for magnetic braking (Eq. (3.7)). In this subsection, we present the full evolution of simulations in which we vary r_g holding all other parameters constant, see Fig. 3.7.

As shown in Fig. 3.7, simulations with large r_g can reach orbital periods over 2 days larger than the initial value primarily due to the stars' rotational angular momentum scaling as r_g^2 . With more rotational angular momentum to transfer to the orbit, tidal locking occurs later, at around 10-100 Myr for stars with $r_g = 0.45$ as compared to around 10⁵ years for stars with $r_g = 0.15$. Interestingly, all systems in this set of simulations circularize after about 1 Gyr. Systems with larger r_g circularize much more rapidly once e begins to decrease. As before, the orbital period growth leads to a_{crit} growth with a peak when the binary tidally locks. Once tidal locking occurs for both stars, magnetic braking saps angular momentum from the orbit, rapidly decreasing the orbital period by over 1 day over 100 Myr.

Systems with unequal mass binaries tend to reach lower $a_{crit,max}/a_{crit,init}$ at a given r_g than their equal mass counterparts because the lower mass star tidally locks more quickly than the more massive primary. Once tidally locked, the secondary star cannot spin down via magnetic braking so angular momentum instead comes from the orbit, reducing the amount by which the orbital period can grow before the primary star tidally locks.

In general, we find that stars with larger r_g tend to reach larger $a_{crit,max}/a_{crit,init}$. At larger values of r_g for a given rotation rate, a star possesses more rotational angular momentum available for transfer into the orbit via tides allowing for larger $a_{crit,max}/a_{crit,init}$. For binary stars with $r_g \gtrsim 0.27$, the binaries attain $a_{crit,max}/a_{crit,init} \gtrsim 1.1$, large enough to destabilize and eject some CBPs.

For sun-like stars, the pre-main sequence lasts for ~ 50 Myr and up to 1 Gyr for lower-mass late M-dwarfs. As shown above, a significant portion of a_{crit} growth occurs while the stars reside

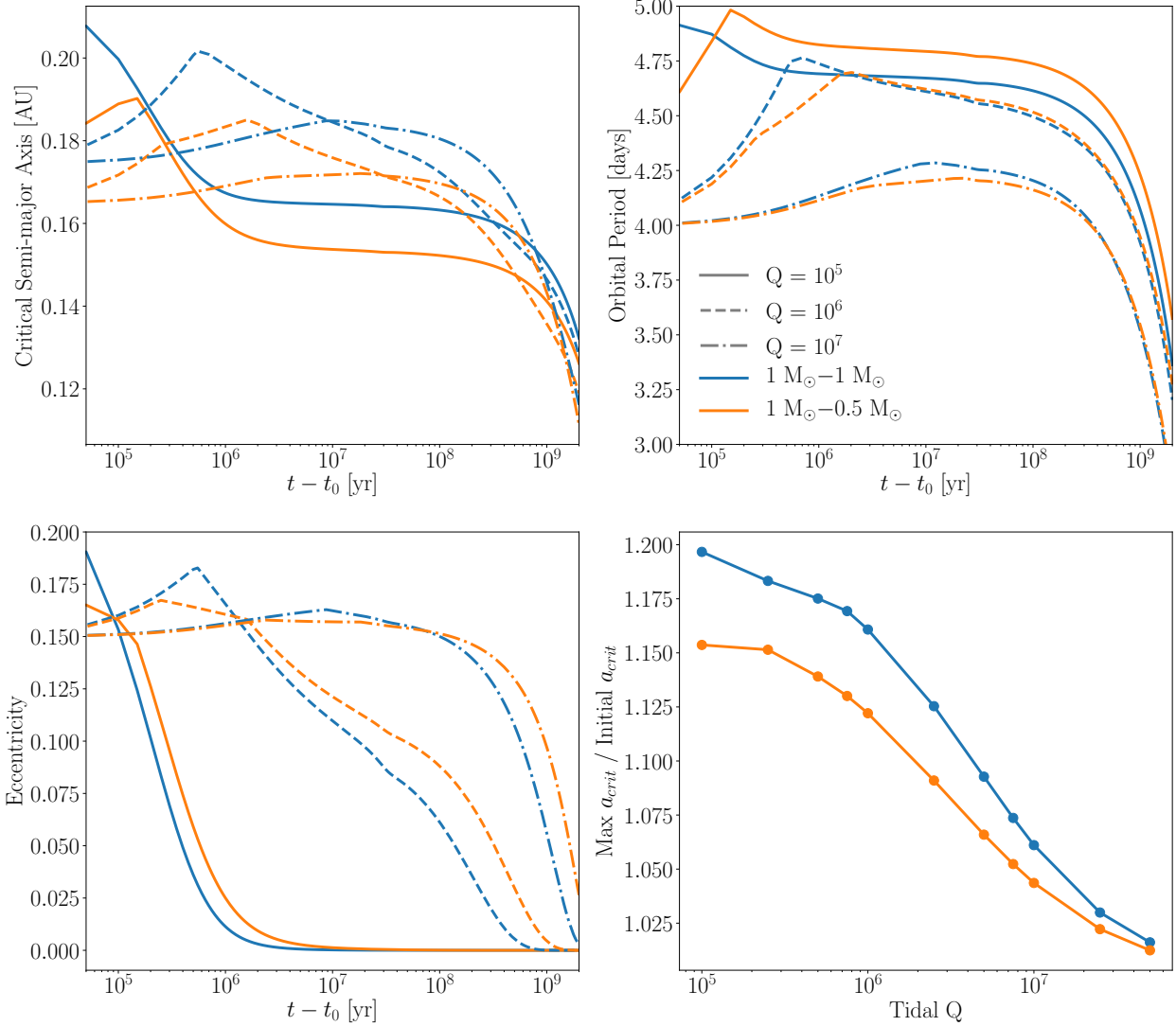


Figure 3.6: The role of tidal dissipation in binary star evolution. *Top Left:* a_{crit} vs. time. *Top Right:* Binary orbital period vs. time. *Bottom Left:* e vs. time. *Bottom Right:* $a_{\text{crit},\text{max}}/a_{\text{crit},\text{init}}$ vs. tidal Q . The blue and orange lines correspond to a $1 M_\odot - 1 M_\odot$ and a $1 M_\odot - 0.5 M_\odot$ binary, respectively. The solid, dashed, and dot-dashed lines correspond to tidal Q s of 10^5 , 10^6 , and 10^7 , respectively. Smaller tidal Q s drive large a_{crit} expansion.

on the pre-main sequence as radius contraction provides a substantial angular momentum reservoir for transfer into the orbit via tides. On the pre-main sequence, Baraffe et al. (2015) predicts that low mass stars have $r_g \sim 0.45$. Therefore during the pre-main sequence when a_{crit} tends to increase the most, the stellar radius of gyration is large allowing a_{crit} to grow significantly as seen in Fig. 3.7 yielding ratios upwards of $a_{crit,max}/a_{crit,init} \sim 1.4$. Once the stars reach the main sequence, r_g drops to ~ 0.27 slowing the a_{crit} evolution. Given that we adopted $r_g \sim 0.27$ as our fiducial value when it is likely much larger during the major period of a_{crit} growth, we consider our $a_{crit,max}/a_{crit,init}$ estimates to be conservative lower limits.

3.4.4 Varying Magnetic Braking Law

Magnetic braking removes angular momentum from stars, slowing their rotation rates. For the short-period binaries considered here, magnetic braking depletes the stellar rotational angular momentum reservoir that is available for tidal transfer in the orbit before tidal locking, reducing $a_{crit,max}/a_{crit,init}$. To probe the sensitivity of our results to our choice of magnetic braking law, we test run identical sets of simulations using the Reiners and Mohanty (2012) and Repetto and Nelemans (2014) magnetic braking models (see § 3.2.2) for binaries stars with various initial P_{rot} . Again for simplicity, in each simulation both stars start with the same given P_{rot} . The results of these simulations are shown in Fig. 3.8. Note that we examine the long-term evolutionary differences between these two magnetic braking models in § 3.4.8.

In terms of $a_{crit,max}/a_{crit,init}$, the differences between the two models are modest with the Repetto and Nelemans (2014) magnetic braking model yielding slightly larger values of $a_{crit,max}/a_{crit,init}$. In general, the Repetto and Nelemans (2014) model tends to remove less rotational angular momentum than the model of Reiners and Mohanty (2012). The differences between the two models in terms of $a_{crit,max}/a_{crit,init}$ decrease with increasing initial stellar P_{rot} as for longer P_{rot} there is less stellar angular momentum for magnetic braking to remove. The difference between the two models becomes more drastic in the late evolution of the binaries once both stars are tidally locked. In that case, the slow angular momentum depletion of the Repetto and Nelemans (2014) model causes a slight decay in the orbital period of about a quarter of a day while the Reiners and Mo-

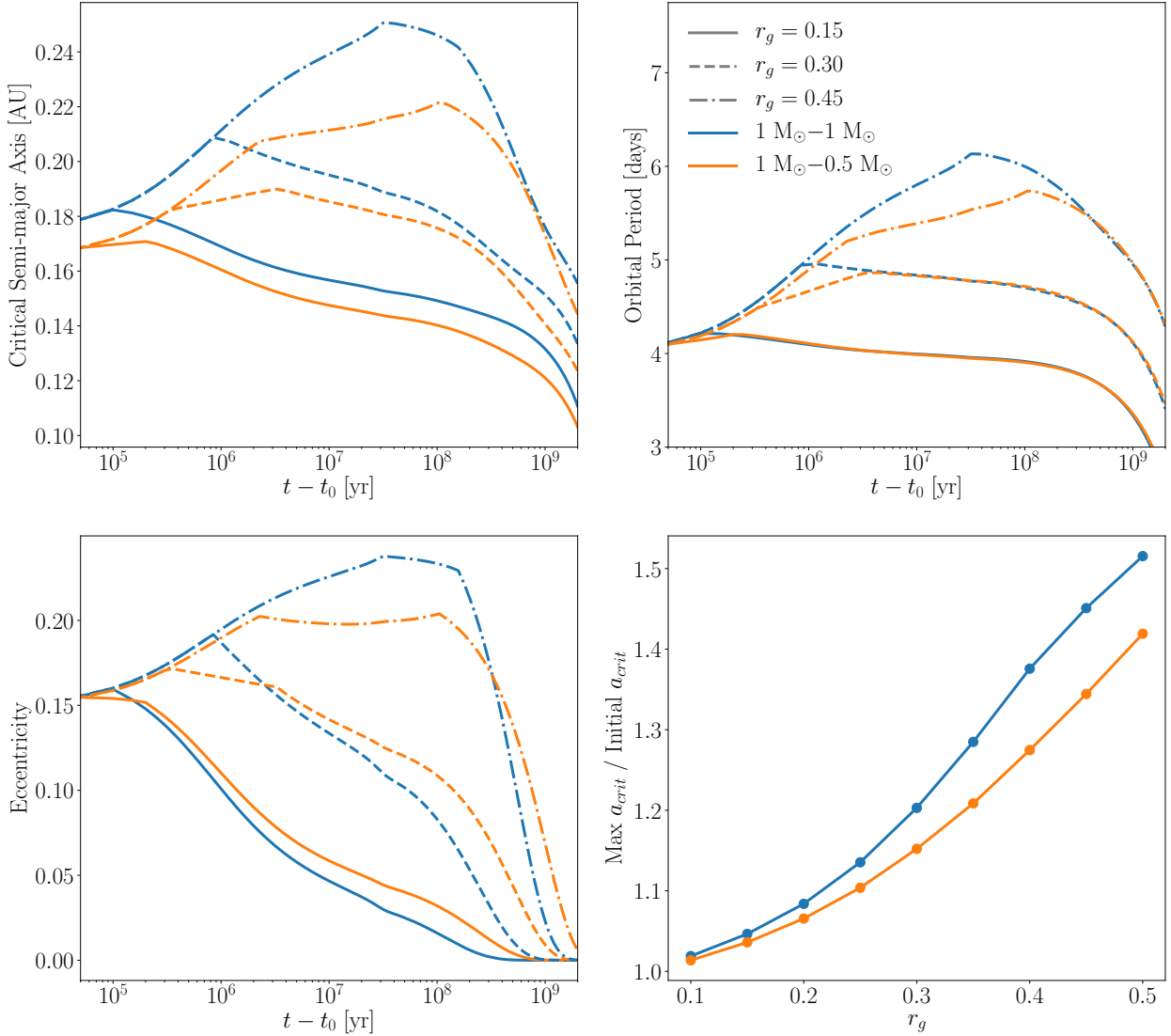


Figure 3.7: The role of the radius of gyration in binary star evolution. *Top Left:* a_{crit} vs. time. *Top Right:* Binary orbital period vs. time. *Bottom Left:* e vs. time. *Bottom Right:* $a_{crit,max}/a_{crit,init}$ vs. r_g . The blue and orange lines correspond to a $1 M_{\odot} - 1 M_{\odot}$ and a $1 M_{\odot} - 0.5 M_{\odot}$ binary, respectively. The solid, dashed, and dot-dashed lines correspond to an r_g of 0.15, 0.3, and 0.45, respectively. Larger r_g lead to increased a_{crit} growth.

hanty (2012) model produces a decay of 1-1.5 days. Overall, our results are moderately sensitive to the choice of magnetic braking model and we choose to use the Reiners and Mohanty (2012) model as our fiducial model as it tends to produce a more conservative estimate of $a_{crit,max}/a_{crit,init}$. For both magnetic braking models when the stars have initial $P_{rot} \sim 1$ day, the binary reaches $a_{crit,max}/a_{crit,init} \gtrsim 1.1$, large enough to destabilize CBPs.

3.4.5 Varying Rotation Periods

Previously, we posited that an initial $P_{rot} \lesssim 1$ day, a value consistent with observations of young stars (see § 3.3.1), should be sufficient for the STEEP process to operate. Here, we demonstrate that initial $P_{rot} \lesssim 1$ days do indeed lead to appreciable growth in a_{crit} through an expansive suite of simulations.

In Fig. 3.9, we present the results of 20,000 simulations in which we varied the initial P_{rot} for both stars over a grid of 0.2-1.5 days for a $1M_\odot - 1M_\odot$ binary for $e = 0.05$ and $e = 0.15$. For the other initial conditions, we adopt the default values given in Table 3.1. For both eccentricities, binaries in which both stars begin with $P_{rot} \lesssim 1$ days achieve $a_{crit,max}/a_{crit,init} \gtrsim 1.1$. When the stars have initial $P_{rot} \lesssim 0.5$ days $a_{crit,max}/a_{crit,init}$ can reach 1.3 – 1.4, large enough to potentially destabilize many *Kepler* CBPs as they typically reside at $a_{planet}/a_{crit} \lesssim 1.4$. The initial P_{rot} that lead to appreciable a_{crit} growth are entirely consistent with observations of young sun-like stars, demonstrating that the STEEP process can effectively destabilize some CBPs near the dynamical stability boundary.

3.4.6 Monte Carlo Simulations

In the previous sections, we ran simulations varying one or two parameters at a time to explore the sensitivity of the STEEP process to the initial conditions. We found that simulations with parameters roughly consistent with observations, such as initial stellar P_{rot} and parameters broadly consistent with theoretical expectations result in binaries whose coupled stellar and tidal evolution can effectively destabilize CBPs. However, the coupled nature of our model necessitates a broader

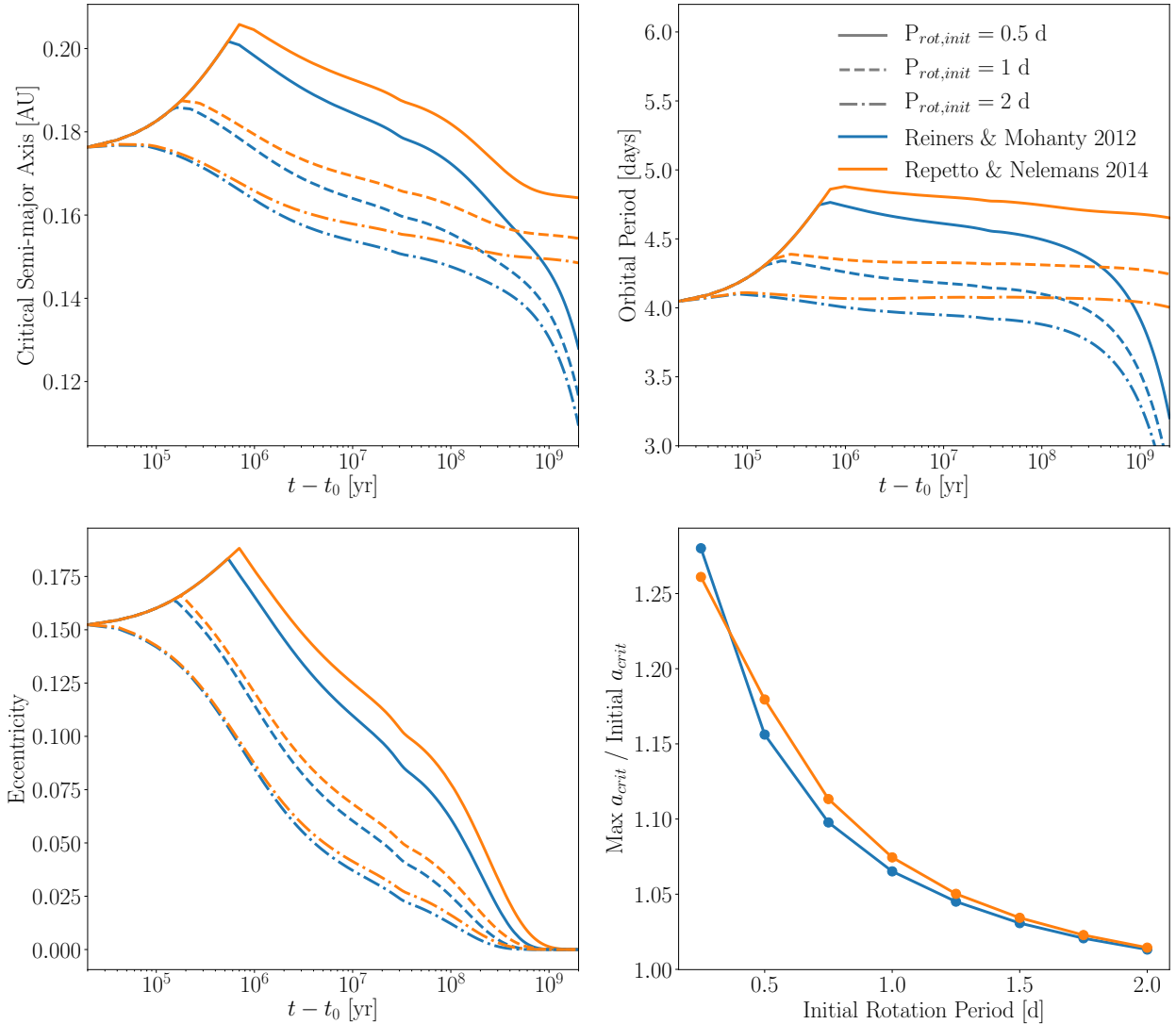


Figure 3.8: The role of the magnetic braking law and initial stellar P_{rot} in binary star evolution. *Top Left:* a_{crit} vs. time. *Top Right:* Binary orbital period vs. time. *Bottom Left:* e vs. time. *Bottom Right:* $a_{crit,max}/a_{crit,init}$ vs. initial stellar P_{rot} . The blue and orange lines correspond to simulations that use the stellar magnetic braking relation from Reiners and Mohanty (2012) and Repetto and Nelemans (2014), respectively. The solid, dashed, and dot-dashed lines correspond to a binary with stellar initial spin periods of 0.5 d, 1 d, and 2 d, respectively. We find that the Repetto and Nelemans (2014) relation leads to larger $a_{crit,max}/a_{crit,init}$ and stars with shorter initial spin periods lead to larger $a_{crit,max}/a_{crit,init}$ as well.

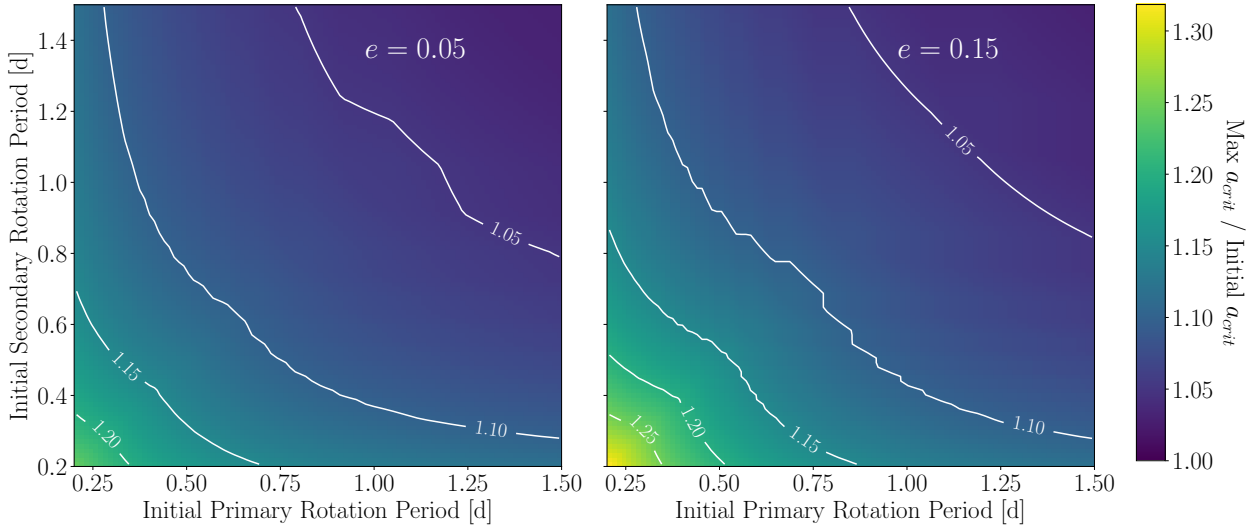


Figure 3.9: $a_{crit,max}/a_{crit,init}$ as a function of the initial stellar P_{rot} for a $1 M_\odot - 1 M_\odot$ binary for $e = 0.05$ (Left) and $e = 0.15$ (Right). The white lines are contours in $a_{crit,max}/a_{crit,init}$. When the stars start with $P_{rot} \lesssim 1$ days, $a_{crit,max}/a_{crit,init}$ readily grows to $\gtrsim 1.1$, large enough to destabilize some CBPs near the dynamical stability boundary.

study to test the STEEP process's robustness to combinations of the parameters.

We therefore perform a Monte Carlo study to identify regions in parameter space where large $a_{crit,max}/a_{crit,init}$ occur. We run 10,000 simulations where each star's mass, r_g , initial P_{rot} , initial binary orbital period and e are randomly sampled from uniform distributions from the ranges listed in Table 3.1. Each star's tidal Q was sampled randomly from a log-uniform distribution from the listed range. For each simulation, we compute $a_{crit,max}/a_{crit,init}$ from the full evolution of the system over 2 Gyr. The results of the simulations are displayed in Fig. 3.10 as a two-dimensional projection in terms of the initial orbital angular momentum, J_{orb} , and ratio of total initial stellar rotational angular momentum to the initial orbital angular momentum, $J_{rot,tot}/J_{orb}$.

A clear gradient emerges in $J_{rot,tot}/J_{orb}$ space. As $J_{rot,tot}/J_{orb}$ increases, on average so does $a_{crit,max}/a_{crit,init}$. This result is expected since when the initial rotational angular momentum content is comparable to the orbital angular momentum, tidal transfer to the orbit will on average increase a_{crit} more. We find that simulations with initial $J_{rot,tot}/J_{orb} \gtrsim 0.1$ yield $a_{crit,max}/a_{crit,init} \gtrsim 1.1$, large enough to destabilize CBPs near the dynamical stability boundary. Simulations with initial

$J_{rot,tot}/J_{orb} \approx 1$ can result in simulations with large $a_{crit,max}/a_{crit,init} \approx 1.4$, some upwards of $2 - 3$ for initial stellar rotation rates near the break-up velocity, a value that is almost certain to destabilize and eject any nascent circumbinary planetary system.

There is considerable scatter in $a_{crit,max}/a_{crit,init}$, however, as simulations with $J_{rot,tot}/J_{orb} \approx 1$ can result in little evolution in a_{crit} . We find that these cases correspond to simulations where one or both stars have tidal $Q_s \sim 10^7$. As discussed in § 3.4.2, large tidal Q_s result in much slower tidal evolution. When the tidal evolution proceeds more slowly, so too does the angular momentum transfer into the orbit (see Fig. 3.6). In this case, the slow tidal evolution allows for magnetic braking to efficiently siphon large amounts of angular momentum from the system, resulting in negligible a_{crit} evolution.

For tidal Q_s low enough to prevent significant angular momentum loss due to magnetic braking, i.e. $Q < 10^7$, young binary systems with short initial $P_{rot} \lesssim 1$ day can attain $J_{rot,tot}/J_{orb} \gtrsim 0.1$, resulting in large enough growth in a_{crit} to destabilize CBPs found near the dynamical stability boundary.

3.4.7 3:2 Spin-Orbit Resonance

To probe the impact of large e and capture into higher order spin-orbit resonances, we run two simulations using the default parameters in Table 3.1 but with $e = 0.15$ and $e = 0.3$. The results of the simulations are given in Fig. 3.11. The initially more eccentric binary tidally locks into a 3:2 spin-orbit resonance after about 1 Myr since $e > \sqrt{1/19}$ (see § 3.2.3), while the less eccentric binary tidally locks into and remains in a synchronous 1:1 spin-orbit state. Once e decays to $e < \sqrt{1/19}$ after about 100 Myr for the more eccentric binary, the system becomes trapped in the synchronous state, the only other allowed spin-orbit resonance for tidally locked systems under the CPL model.

The binary that tidally locks into a 3:2 spin-orbit resonance reaches a larger $a_{crit,max}/a_{crit,init}$ than the other synchronously rotating binary system. This result is surprising given that in a 3:2 spin-orbit resonance, $P_{rot} = 2/3P_{orb}$, so relative to the synchronous case, less stellar rotational angular momentum is transported into the orbit, reducing the increase in orbital period and hence a_{crit} .

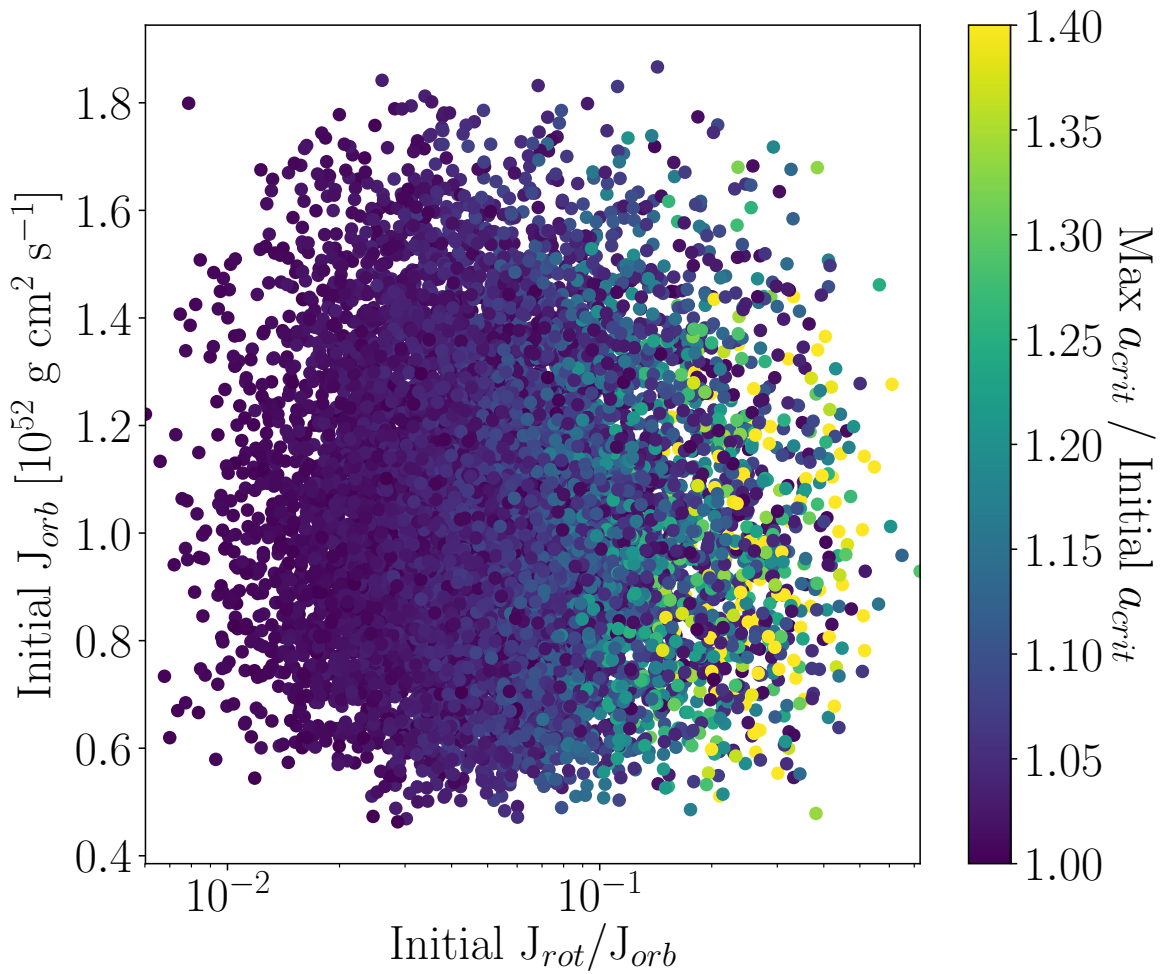


Figure 3.10: Scatter plot of the initial orbital angular momentum J_{orb} , versus the ratio of total initial stellar rotational angular momentum to the initial orbital angular momentum, $J_{rot,tot}/J_{orb}$. Each point is colored by the $a_{crit,max}/a_{crit,init}$ achieved in that simulation. Simulations with an initial angular momentum ratio of $\gtrsim 0.1$ tend to produce a large enough $a_{crit,max}/a_{crit,init}$ to destabilize a CBP.

However, larger e correspond to lower orbital angular momentum which scales as $\sqrt{1 - e^2}$. The more eccentric binary system has less orbital angular momentum than the other system so transfer of angular momentum from the stellar rotation to the orbit yields proportionally larger increases in a_{crit} , explaining the larger $a_{crit,max}/a_{crit,init}$. Therefore we anticipate that the STEEP process is effective for eccentric binary systems that tidally lock into higher order spin-orbit resonances.

3.4.8 Long-term a_{crit} Evolution

As shown in the above simulations, a_{crit} changes over time such that a binary's observed a_{crit} can differ significantly from past values. This effect is especially relevant for observed *Kepler* circumbinary systems as the orbit, and hence a_{crit} , observed today is much different than in the past and the magnitude of the difference depends on the age of the system. Most notably, the post-tidal locking a_{crit} decay implies that the dynamical instability region around the binary was likely larger in the past. Any CBPs that survived initial a_{crit} increases would necessarily appear to orbit on much larger a_{CBP} relative to the a_{crit} about the central binary and would therefore be harder to detect.

Specific Cases

To illustrate this effect and the observational consequences, we simulate 4 binary systems for 8 Gyr of evolution using the default parameters in Table 3.1 for binary orbital periods of 3, 4, 5, and 6 days using the magnetic braking formalisms of Reiners and Mohanty (2012) and Repetto and Nelemans (2014). The results of the simulations are shown in Fig. 3.12.

In left panel of Fig. 3.12, we see the full evolution of these systems and there is a stark difference between the two cases: the Reiners and Mohanty (2012) magnetic braking law causes significant orbital decay relative to the modest decay induced by the Repetto and Nelemans (2014) magnetic braking relation. The Reiners and Mohanty (2012) magnetic braking law removes a significant amount of angular momentum from the orbits driving orbital period decays of about 1 day per Gyr such that the binaries actually merge after a few Gyr as the stellar radii overlap. The or-

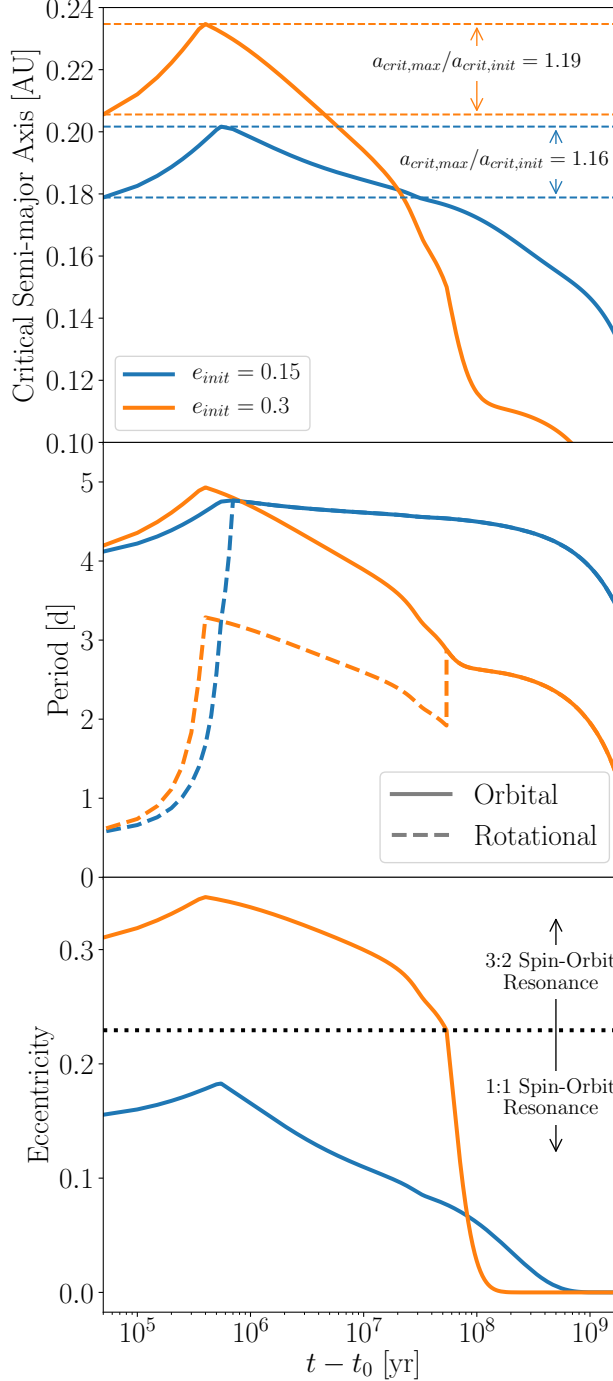


Figure 3.11: Full evolution of binary systems using our default parameters from Table 3.1, except with initial eccentricities of $e = 0.15$ (blue) and $e = 0.3$ (orange). *Top:* a_{crit} vs. time. The systems attain $a_{crit,max}/a_{crit,init} = 1.16, 1.19$ for binaries with initial eccentricities of $e = 0.15$ and $e = 0.3$, respectively. *Middle:* Orbital and stellar rotation period vs. time. Both systems tidally lock after ~ 1 Myr into 1:1 (blue) and 3:2 (orange) spin-orbit resonances. *Bottom:* e vs. time. The dotted line demarcates binaries that tidally locked into a 3:2 (above the line) and 1:1 (below the line) spin-orbit resonance.

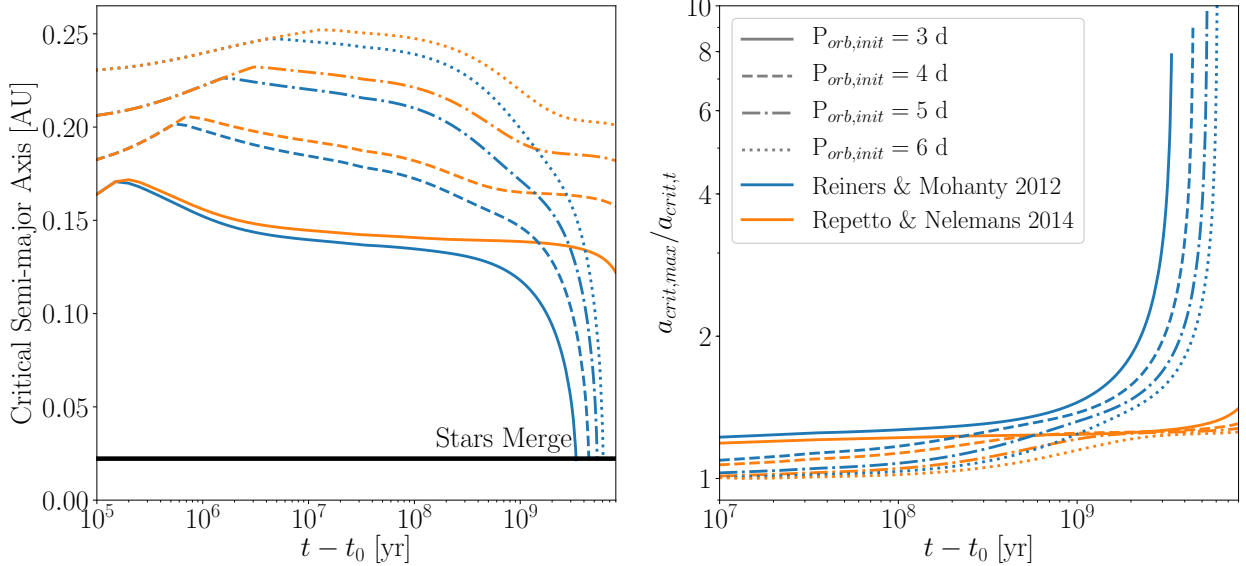


Figure 3.12: *Left:* a_{crit} as a function of time. The black horizontal line indicates when stellar radii overlap and the stars merge, halting the simulation. *Right:* Maximum critical semi-major axis divided by the critical semi-major axis observed at time t , $a_{crit,max}/a_{crit,t}$. Depending on the magnetic braking physics, the observed a_{crit} can differ from its maximum by an order of magnitude.

bital period decay is more modest for the Repetto and Nelemans (2014) magnetic braking law. The different outcomes predicted by these models could be used as an observational test to constrain which magnetic braking model is more suitable, however, we leave that analysis for future work.

In the right panel of Fig. 3.12, we plot $a_{crit,max}/a_{crit}$ over time. For the simulations using the Reiners and Mohanty (2012) magnetic braking law, a_{crit} can vary by a factor of 2 – 10 from its maximum value depending on the age of the system, while the simulations using the Repetto and Nelemans (2014) law vary by factors of order unity. This implies that the region of dynamical instability can appreciably shrink for tidally locked short orbital period binaries over time. Therefore when one observes these systems, the fact that the dynamical instability region was likely much larger in the past precludes any CBPs from orbiting near the observed a_{crit} . Any CBPs that survived the a_{crit} increase would then be orbiting at much larger a_{CBP}/a_{crit} ratios than what is observed for *Kepler* CBPs. If a CBP is discovered around a tidally locked binary in the future, its current state must be considered in the context of the host binary’s past coupled stellar-tidal evolution.

Monte Carlo Simulations

Here we examine how distributions of $a_{crit,max}/a_{crit,t}$ from our simulations from § 3.4.6 evolve as a function of time to examine the impact of different initial conditions. We plot the distribution of $a_{crit,max}/a_{crit,t}$ at four different times in Fig. 3.13. As the systems age, the distributions tend to shift towards larger $a_{crit,max}/a_{crit,t}$ values, indicating that for most initial states a , and hence a_{crit} , decays relative to its peak due to magnetic braking. At later times, the $a_{crit,max}/a_{crit,t}$ distributions tend to smear out and develop heavy tail indicating that even though $a_{crit,max}/a_{crit,t}$ tends to grow, the properties of the individual system, e.g. the stellar mass or tidal Qs, play an important role in determining how much a_{crit} evolves. For example, lower mass stars contract for longer periods of time, which for tidally locked stars, injects additional angular momentum in the orbit, slowing a_{crit} decay due to magnetic braking.

3.4.9 Relaxed Assumptions

In previously-discussed simulations, we have taken a rather conservative approach in selecting our initial conditions. Here we relax those assumptions and run five simulations with progressively more extreme-yet-plausible initial conditions to see how a_{crit} evolves. Case A has the same initial conditions as our fiducial simulation (see § 3.4.1) but with an initial orbital period of 5 days and an initial e of 0.1. Case B is the same as Case A but with both stellar tidal Qs set to 10^5 . Case C is the same as Case B but with both stellar radii of gyration set to $r_g = 0.45$. In Case D, the initial conditions are the same as Case C but with the initial stellar P_{rot} set to 0.25 days. Finally in Case E, we set the initial $e = 0.2$ and adopt the initial conditions of Case D for all other parameters.

For each individual simulations, see Fig. 3.14, the results proceed as expected: simulations with larger r_g and lower initial P_{rot} , e.g. Case C and Case D, respectively, result in larger $a_{crit,max}/a_{crit,init}$ with the ratios approaching 2. In all simulations, the a_{crit} growth peaks early on in the system at $\lesssim 100$ Myr. For binaries with $e > 0.3$, the model tends to break down and yield unrealistic results and merits further exploration with the CTL tidal model, which may be applicable at large e . Nevertheless, these simulations demonstrate that a_{crit} can grow up to twice the initial value

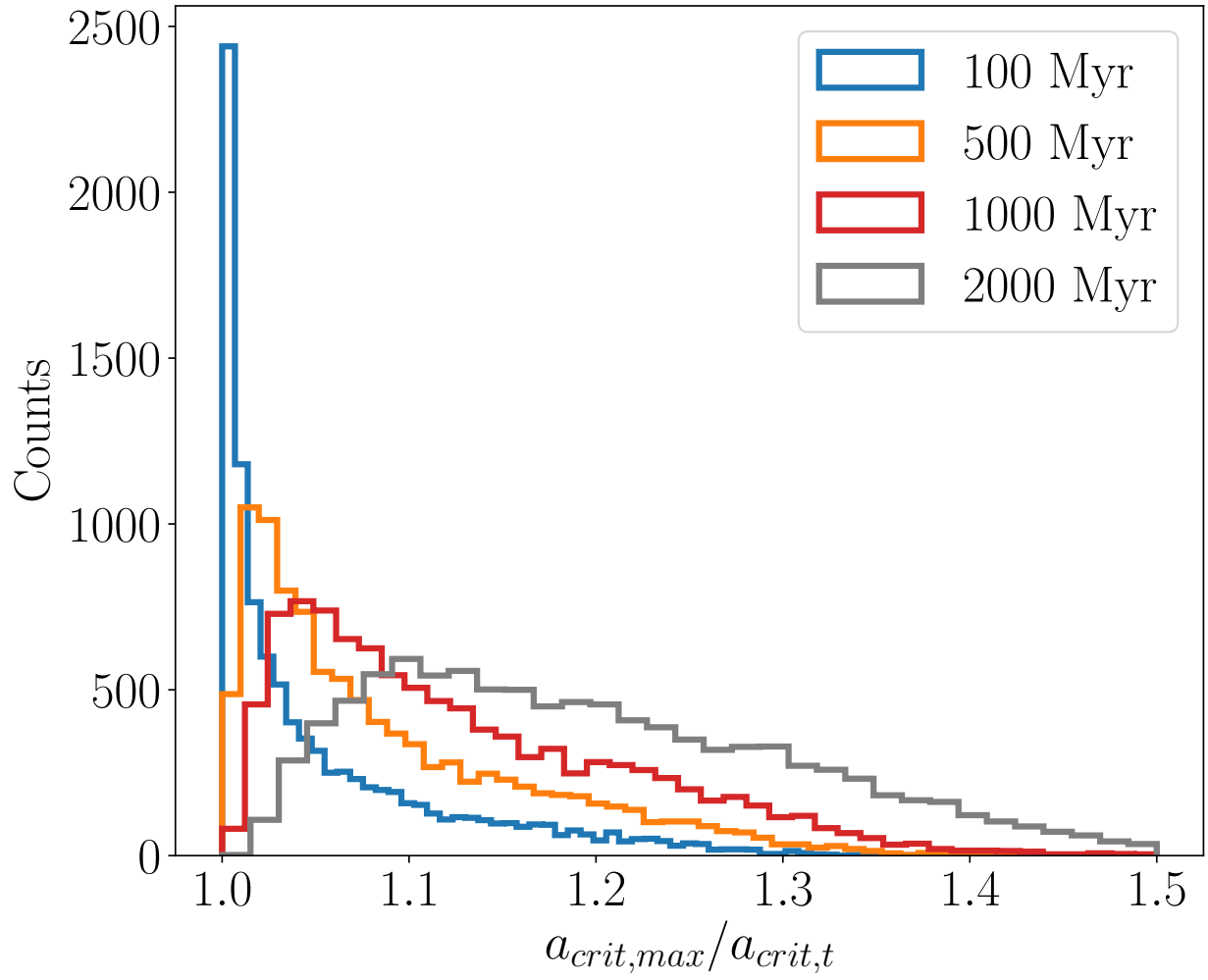


Figure 3.13: Histograms of the maximum a_{crit} divided by the critical semi-major axis observed at time t , $a_{crit,max}/a_{crit,t}$ for the binary systems simulated in § 3.4.6 observed at 100, 500, 1000, and 2000 Myr (blue, orange, red, and grey histograms, respectively). In general for older systems, $a_{crit,max}/a_{crit,t}$ increases as a_{crit} recedes due to angular momentum loss via magnetic braking in tidally locked systems. The distribution of $a_{crit,max}/a_{crit,t}$ smears out and develops an extended tail for older systems due to the different tidal and rotational properties of the binary systems.

depending on the initial conditions.

3.5 Results: N-body Simulations

Here we present the results of N-body simulations of circumbinary planetary systems using the N-body code REBOUND (Rein and Liu, 2012; Rein and Spiegel, 2015). The initial conditions and set-up are described in § 3.3.2. In § 3.5.1, we examine how orbital instabilities in circumbinary planetary systems stemming from the inner-most planet residing within a_{crit} affect the system architecture and lead to planetary ejections while in § 3.5.2, we examine the observational consequences of CBP ejections.

3.5.1 Dynamical Stability

Single Planet Circumbinary System

In Table 3.3, we display the fraction of simulations of a single planet circumbinary system that result in a stable or unstable planet for Neptune-, Saturn-, and Jupiter-mass planets. In our simulations, planet b, which initially resided within a_{crit} , is ejected 70% - 75% of the time confirming that the majority of CBPs that drift interior to a_{crit} are ejected from the system (c.f. Holman and Wiegert, 1999). From the definition of a_{crit} from Eq. (3.1), however, one expects *every* CBP that drifts interior to a_{crit} to go unstable and get ejected whereas only 70% - 75% of such planets are ejected in our simulations. The difference can be rectified by examining precisely how Holman and Wiegert (1999) computed a_{crit} . For each given a_{CBP} , Holman and Wiegert (1999) initialized 8 test particles on circular orbits that are equally spaced in mean anomaly. After the integration, Holman and Wiegert (1999) deemed the minimum semi-major axis in which all 8 test particles survive a_{crit} . Therefore a test particle, and hence a planet, within a_{crit} is likely, but not guaranteed, to go dynamically unstable and be ejected from the system, explaining our results.

We find that on average, the deeper within the region of dynamical instability a CBP is and the more eccentric its orbit, the more likely it is to be ejected from the system. There appears to be a weak dependence on ejection probability with planet mass with Neptune-mass CBPs getting

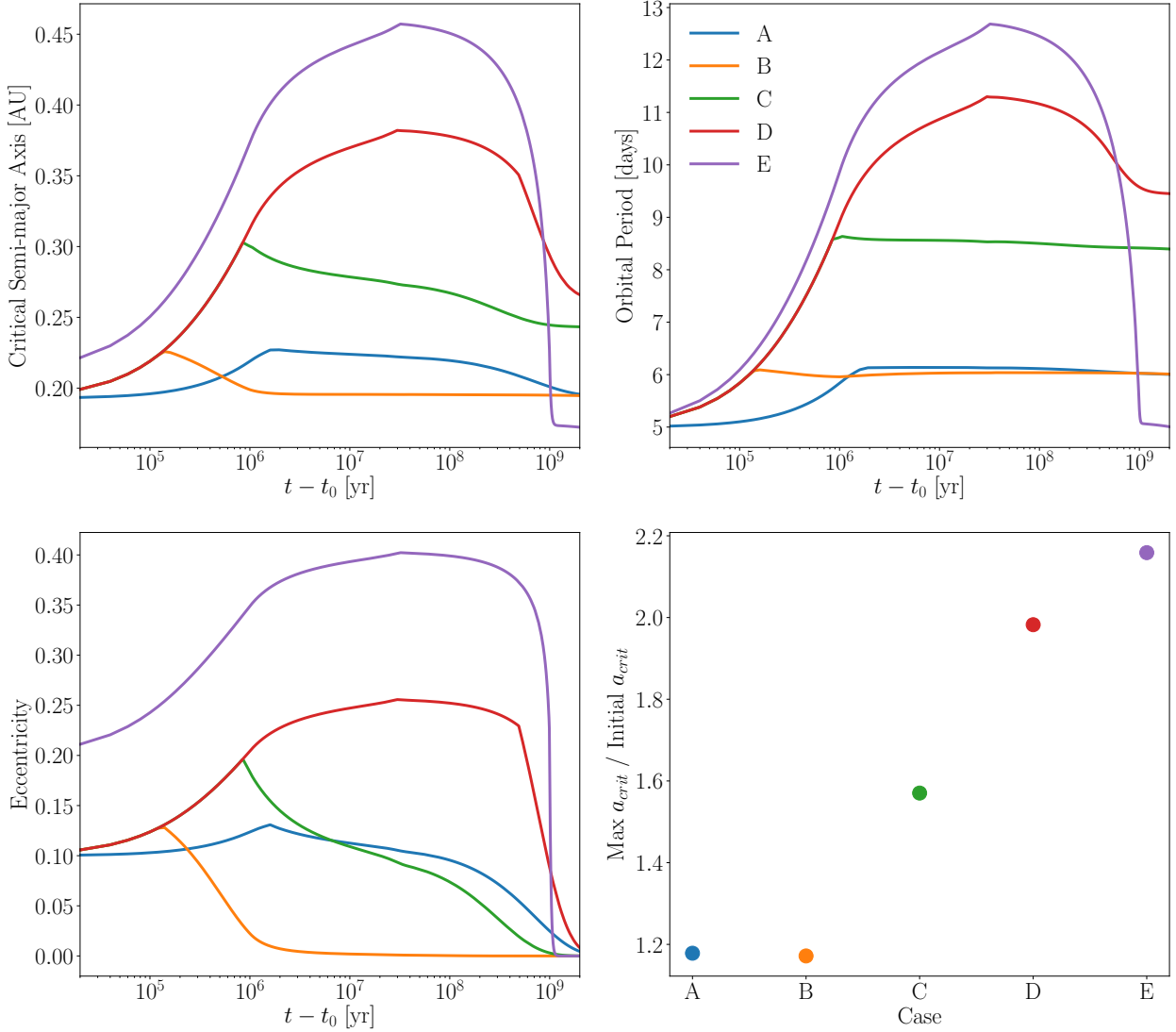


Figure 3.14: Binary orbital evolution for several plausible sets of initial conditions. *Top Left:* a_{crit} vs. time. *Top Right:* Binary orbital period vs. time. *Bottom Left:* e vs. time. *Bottom Right:* $a_{crit,max}/a_{crit,init}$ for the five cases. The blue, orange, green, red, and purple curves correspond to cases A, B, C, D, and E, respectively. In agreement with previously discussed simulations, we find that initial fast rotators with smaller tidal Qs achieve large $a_{crit,max}/a_{crit,init}$ up to of order 2 for plausible initial conditions.

Table 3.3. Single Planet System Outcome Fraction

| Case | Stable | Unstable |
|--------------|--------|----------|
| Neptune Mass | 0.253 | 0.747 |
| Saturn Mass | 0.282 | 0.718 |
| Jupiter Mass | 0.3 | 0.7 |

ejected $\sim 75\%$ of the time while more massive planets were slightly less likely to be ejected. We re-ran these simulations for 10^6 binary orbital periods, an order of magnitude longer, and found that our results did not significantly change.

Multiplanet Circumbinary System

In Table 3.5.1, we display the fraction of simulations of a two-planet circumbinary system that result in a stable or unstable planet as a function of initial planet orbital inclination distribution and planet mass. A clear result of our multi-planet circumbinary system dynamical stability simulations is that at least one planet is ejected from the system with this result occurring in 87% - 95% of simulations, a value broadly consistent with the results of previous studies of planet-planet scattering in circumbinary systems (e.g. Sutherland and Fabrycky, 2016; Smullen et al., 2016; Gong and Ji, 2017; Gong, 2017).

In simulations in which a planet is ejected, the typical result is planet c remaining stable while planet b is ejected from the system. This outcome occurs in 78% - 88% of simulations. Planet b remains stable 7% - 18% of the time where most instances in which b remains stable correspond to simulations in which both planets remain stable. Simulations in which both b and c remain stable typically correspond to initial conditions in which b and c are more widely separated with inter-planet separations near $10R_{Hill,mutual}$ and when b resides near to a_{crit} . The few simulations in which b remains stable while c is ejected correspond to scattering events where b scatters exterior to c while c scatters into the region of dynamical instability and is ejected from the system

soon thereafter. Planet b remains stable at the expense of c’s ejection in 2% - 6% of simulations. The spread in simulation outcomes stems from the planet(s)’ and binaries’ random initial orbital parameters (see Table 3.2).

The most infrequent result that occurs in 1% - 5% of simulations is when both b and c are ejected from the system, a value roughly consistent with Gong (2017) who find $\sim 10\%$ systems are destabilized due to planet-planet scattering near a_{crit} . Simulations in which both b and c are ejected tend to occur when b is initialized deeper within the region of dynamical instability and when b and c are more closely separated with separations near $5R_{Hill,mutual}$ in good agreement with the simulations of Kratter and Shannon (2014). Given that planet c survives in 89% - 97% of simulations, we anticipate that in systems with higher multiplicity, the farther out planets would likely remain stable.

Our results show clear dependences on both CBP orbital inclination relative to the binary’s and planet’s mass. Systems with more massive planets tend to remain stable. For a given planet mass, however, simulations with planets initialized using the “high inclination” distribution more frequently result in planet b going unstable as the larger mutual inclinations tend to result in more violent scattering events. This behavior is reflected in a depletion in the fraction of simulations in which b remains stable and an appreciable enhancement in the fraction of simulations in which planet c remains stable after b is ejected.

Our results indicate that systems in which the inner-most CBP falls within the region of dynamical instability, *e.g.* due to a_{crit} expansion resulting from coupled stellar-tidal evolution, likely lose at least one planet. Therefore for short-period binary systems where we expect coupled stellar-tidal evolution to increase a_{crit} and envelope CBPs that preferentially lie near the limit, at least one CBP is likely to be ejected from the system, potentially accounting for the lack of observed CBPs in such systems.

We note that our results are conservative given our assumptions that the inner-most CBP orbits just interior to a_{crit} to simulate the time right after the planet falls within a_{crit} due to the STEEP process. In practice, a CBP that falls within a_{crit} and is not promptly ejected will fall deeper into the dynamical instability region as coupled stellar-tidal evolution expands a_{crit} . As discussed above,

Table 3.4. Circumbinary planetary system N-body simulation outcome fractions.

| Case | Low Inclination | | | High Inclination | | |
|----------------------|-----------------|-------------|--------------|------------------|-------------|--------------|
| | Neptune Mass | Saturn Mass | Jupiter Mass | Neptune Mass | Saturn Mass | Jupiter Mass |
| b, c stable | 0.064 | 0.088 | 0.132 | 0.053 | 0.09 | 0.106 |
| b stable, c unstable | 0.063 | 0.047 | 0.052 | 0.027 | 0.017 | 0.023 |
| c stable, b unstable | 0.825 | 0.843 | 0.784 | 0.881 | 0.879 | 0.849 |
| b, c unstable | 0.048 | 0.022 | 0.032 | 0.039 | 0.014 | 0.022 |

Note. — In “low inclination” simulations, both planet b and c’s inclination with respect to the binary orbital plane is sampled from $U(0^\circ, 1^\circ)$ while in “high inclination” simulations, both planet b and c’s inclination is sampled from $U(0^\circ, 3^\circ)$. The fractions are normalized such that each column sums to 1.

the deeper a CBP is within the dynamical instability region, the more likely it is to be ejected. Therefore if we relaxed our conservative assumptions and initialized CBPs more interior to a_{crit} , we would expect more ejections. Additionally it is possible that CBPs form with large mutual inclinations although the observed CBP population has low mutual inclinations with respect to the host binaries (Li et al., 2016). If we allowed for more inclined orbits, based off of our previous results we would anticipate more ejections based on the results of Chatterjee et al. (2008) and more CBPs scattered away from a transiting configuration.

3.5.2 Mock Transit Observations

Next we present the results of our mock transit observation simulations. In the single CBP system case, the result is trivial: if the planet is ejected, it does not transit while if it remains in the system, it most likely transits as each planet was initialized in a transiting configuration and interactions with the host binary tend to not excite large inclinations given the small initial mutual inclination. For the two-planet circumbinary system case, we focus on the detectability of planet c as we have shown that the dominant outcome of our dynamical stability N-body simulations is that planet b

is ejected while planet c remains in the system on a perturbed-yet-stable orbit. We summarize the results of our mock transit observations in Fig. 3.15 which depicts a histogram of the fraction of time transiting (FTT) for planet c for various initial masses and inclinations for the case in which both planets b and c remain stable (blue lines) and the case in which planet b gets ejected while planet c remains (orange lines). For reference, a Jupiter-sized exoplanet with $i = 90^\circ$ on a 30 day circular orbit, a typical orbital period for planets in our simulations, orbiting a Sun-like star spends about 1% of the time transiting for a FTT of 10^{-2} . Almost all of the CBPs in our simulations are initialized in a transiting configuration and typically have an initial FTT of order 10^{-2} .

We find that in most cases in which planet b is ejected while planet c remains stable, planet b's ejection does little to impact the "transitability" of the remaining planet. In the case of Neptune-mass planets in Fig. 3.15, the histograms for b unstable, c stable and b, c stable have similar shapes indicating that planet b's ejection does little to change planet c's FTT. For Saturn-mass planets, specifically those with an initially larger inclination, there is a small extended tail in the FTT distribution for the case when planet b is ejected while planet c remains stable indicating that more inclined, massive planets are scattered to slightly larger inclinations and eccentricities, reducing their FTT.

From Fig. 3.15, clear trends in both mass and initial inclination can be seen. After an instability event occurs in which planet b is ejected, the more massive the CBPs, the less time they spend transiting. For Neptune-mass CBPs after planet b is ejected, planet c's orbit does not appreciably change and retains a large FTT, see the left panel of Fig. 3.15. As the planet mass increases, planet b's chaotic evolution significantly perturbs planet c's orbit, scattering it to larger inclinations, reducing FTT. This effect is most notable in the extended tail and large peak at FTT near 0 for the orange lines in the right panel of Fig. 3.15 for Jupiter-mass planets. This demonstrates that planet b's ejection can readily scatter planet c away from a transiting configuration for massive planets, preventing its detection via the transit method. This effect is less pronounced for less massive CBPs.

The initial inclination significantly impacts the subsequent CBP transitability. The more inclined planet c initially is, the lower the FTT as planet c in general has a larger initial impact

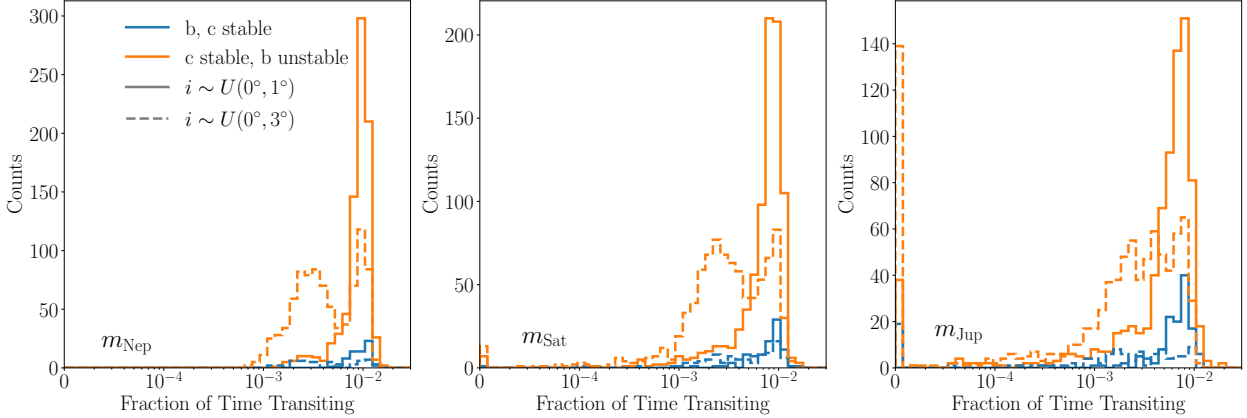


Figure 3.15: Histogram of planet c’s fraction of time spent transiting one of the binary stars for Neptune- (Left:), Saturn- (Middle:), and Jupiter-mass (Right:) exoplanets. The orange histograms correspond to when c remains stable while b goes unstable and the blue curve corresponds to when both b and c remain stable. The solid and dashed histograms correspond to cases where both planets’ initial inclinations are uniformly sampled from $[0^\circ, 1^\circ]$ and $[0^\circ, 3^\circ]$, respectively. Generally, the larger the mutual inclination, the less time c spends transiting.

parameter and can scatter more violently to higher inclinations when planet b is ejected from the system. This effect is most clearly seen in the right panel of Fig. 3.15 for Jupiter-mass CBPs as there is a prominent peak near FTT = 0 for the “high inclination” case (dashed line) that is much larger than the FTT = 0 peak for the “low inclination” case (solid line). This difference indicates that more highly-inclined Jupiter-mass CBPs are preferentially scattered away from a transiting configuration compared to less-inclined planets. In addition to the slight increase in inclination for some surviving planets reducing their FTT, we find that a_c also increases slightly after planet b’s ejection, reducing its FTT. This finding is in good agreement with Gong and Ji (2017).

Our results indicate that when the inner-most planet in a multi-planet circumbinary system is ejected after falling within a_{crit} , it is likely that there will be little impact on the remaining planet’s detectability. In the case of massive planets and/or large initial inclinations, however, the inner-most planet’s ejection can more readily scatter the remaining planet away from and potentially out of a transiting configuration. Even in this case, however, there is likely little to no change in the surviving planet’s FTT. Of course, more distant planets are in general less likely to transit, so the

STEEP process still reduces the total number of transiting CBPs.

One complicating factor is that we make our mock transit observations right after the dynamical stability integrations. From our coupled stellar-tidal VPLanet simulations, we showed that the maximum a_{crit} value is typically achieved well within 1 Gyr (see § 3.4) indicating that if a CBP will be enveloped by a_{crit} and fall within the region of dynamical instability, it will happen early on in the system’s lifetime. Our mock transit observations implicitly assume that we observe the system soon after a_{crit} has enveloped the inner-most planet in a given system, a time that likely occurs well within the 1st Gyr of the system’s lifetime. In real transit survey’s like the *Kepler* mission, the observed stars are not likely to have ages ≤ 1 Gyr like the systems in our mock observations. As shown in § 3.4.8 for tidally locked binary star systems, the older a system is, the more the binary semi-major axis and hence a_{crit} has decayed leaving the surviving CBPs to orbit at larger a_{CBP}/a_{crit} than they did in the past. This effect complicates the detection of CBPs via the transit method and requires that any CBPs discovered around short-period binaries must be understood in the context of the host binary’s past coupled stellar-tidal evolution.

3.6 Application to Kepler-47

We apply the STEEP process to Kepler-47, the shortest period planet-hosting binary system (Orosz et al., 2012). Kepler-47 is a nearly circular G and M dwarf binary with an orbital period of about 7.45 days. Kepler-47 is the only known multi-planet hosting binary with three CBPs, all with nearly co-planar, low-eccentricity orbits (Orosz et al., 2012; Welsh et al., 2015). Kepler-47 appears to have undergone appreciable tidal evolution as the primary star’s P_{rot} is about 4% longer than the orbital period, an indication that the binary is near tidal synchronization (Orosz et al., 2012). Kepler-47 is a suitable candidate for the STEEP process so we seek to examine how its planets could have survived a potential destabilization from the coupled stellar-tidal evolution of the binary.

The planets in the Kepler-47 system are all of order Neptune mass or less, so we can draw comparisons with our two-planet CBP system N-body simulations of Neptune mass planets in § 3.5 (see also Fig. 3.15). As shown previously, the ejection of the inner-most planet in a low-mass CBP system typically results in little or no change in the orbits and hence transitability of the surviving

exterior planets. Although rarely the inner-most planet’s ejection can destabilize the entire system, the dominant result that the rest of the system remains stable and effectively unchanged. If the Kepler-47 system did previously have a planet interior to Kepler-47b that was ejected after falling into the region of dynamical instability, it could have been ejected from the system without any noticeable observational impact on the surviving planetary system. With three planets on nearly co-planar and low-eccentricity orbits, the Kepler-47 planetary system seems relatively dynamically cold, supporting this picture and making its current state compatible with the STEEP process.

If Kepler-47 did not previously have an additional close-in planet, we examine Kepler-47b, the innermost planet in the Kepler-47 system, which resides at a semi-major axis that is about $1.46a_{crit}$ for the Kepler-47 binary. As shown in § 3.4.6 and § 3.4.9, it is plausible for a binary to attain a_{crit} ratios near 1.4 depending on the initial stellar P_{rot} and stellar tidal Qs. With Kepler-47’s relatively longer orbital period, there was likely an initially larger angular momentum reservoir in the orbit relative to that in the stellar rotations so any transfer would probably not increase the orbital period significantly. We display such a case of Kepler-47’s potential past a_{crit} evolution in Fig. 3.16. For this simulation, we used the observed stellar masses (Orosz et al., 2012), initial stellar tidal Qs of 5×10^5 , $r_g = 0.45$, an initial $e = 0.22$, and an initial orbital period of 7.5 days. Note that this case does not represent the precise past evolution of Kepler-47, but instead shows one possible past evolution that is consistent with observations. In this simulation, given Kepler-47’s longer initial orbital period, the binary orbital period and hence a_{crit} grows less via tidal transfer making it less likely to potentially destabilize Kepler-47b. Under this scenario, Kepler-47b likely formed or migrated to a location far enough away from the central binary to insulate it from the central binary’s coupled stellar-tidal evolution, preventing a destabilizing event and making this system compatible with the STEEP process. Note that accurately modeling Kepler-47’s past evolution to assess how the STEEP process could have impacted the circumbinary planetary system requires running a large number of simulations of coupled stellar-tidal evolution and comparing their results with observations. The results of such a simulation suite could potentially constrain parameters, such as tidal Qs, but that analysis is beyond the scope of this work.

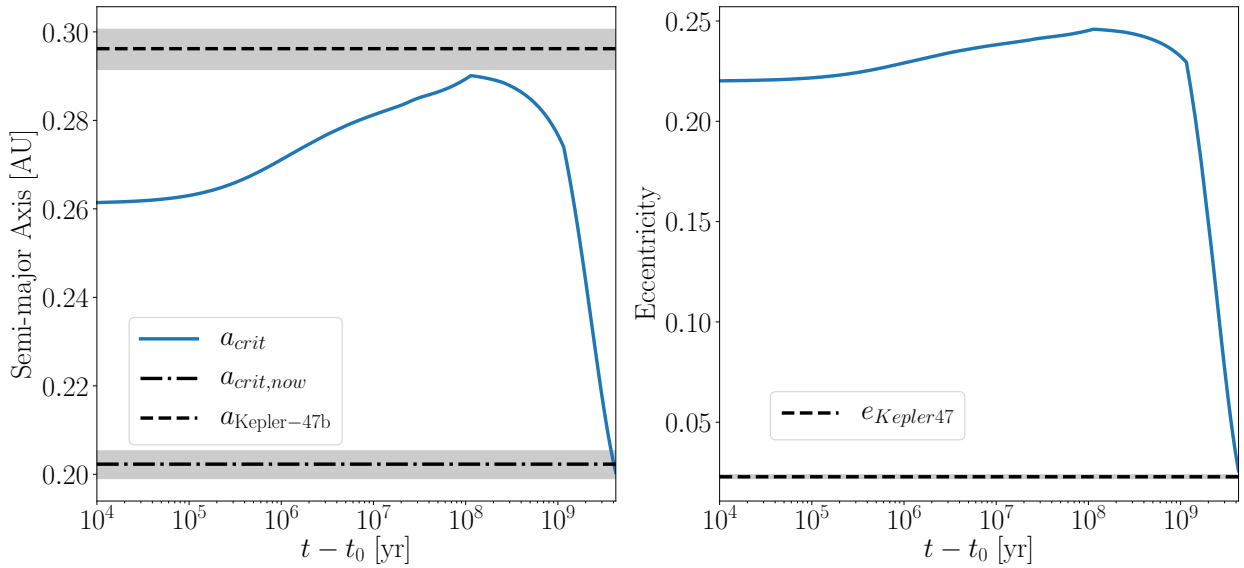


Figure 3.16: One potential coupled stellar-tidal evolutionary history of Kepler-47. *Left:* a_{crit} evolution. The blue curve shows a potential past evolution of Kepler-47's a_{crit} . The dashed line represents Kepler-47b's current semi-major axis while the dot-dashed line indicates Kepler-47's observed a_{crit} . The grey regions display the uncertainties on Kepler-47b's semi-major axis and on Kepler-47's a_{crit} from Orosz et al. (2012). *Right:* Eccentricity evolution. The blue curve displays a potential past evolution of Kepler-47's e . The dashed line and grey regions denote Kepler-47's observed e and the associated uncertainties, respectively. This potential past evolution of the Kepler-47 achieves an a_{crit} nearly large enough to potentially eject Kepler-47b while also reaching an a_{crit} and e consistent with the observed values (Orosz et al., 2012). A more rigorous statistical examination of this system is required to constrain its actual past coupled stellar-tidal evolution.

3.7 Discussion

In this work, we proposed an explanation for the apparent lack of CBPs around isolated binary stars that arises as a natural consequence of short-period binary star evolution. We showed that binary stars that start with P_{rot} faster than the orbital period transfer angular momentum into the orbit as tides drive the system to a tidally locked state. The addition of angular momentum to the orbit increases a , expanding a_{crit} . Since CBPs tend to preferentially exist near a_{crit} , they are then enveloped by the expanding dynamical stability limit and expelled from the system, explaining their observed lack. We referred to this Stellar Tidal Evolution Ejection of Planets as the STEEP process. Binary star systems are a product of complex coupled stellar-tidal evolution and their current observed state likely differs appreciably from its past. Any CBPs that exist around short-period isolated binaries must orbit at large a_{CBP} relative to the binary's a as the past larger region of dynamical stability precludes stable orbits closer to the binary and since the binary's a decays with time post tidal locking due to magnetic braking. If any future surveys discover new CBPs around short-period isolated binaries, their current state must be understood in the context of the binary's previous evolution.

We examined the dynamical stability of circumbinary planetary systems in which the innermost planet falls within the region of dynamical instability by running a series of N-body simulations and found that in most cases, at least one planet is ejected. We performed mock transit observations of such systems after the dynamical stability integration to examine how a potential planetary ejection can impact the detectability any remaining planets. Most surviving planets' orbits exterior to the ejected planet did not appreciably change after a planet ejection, allowing them to remain detectable via the transit method, although more massive planets tended to scatter away from transiting configurations. Given the sizable population of short-period binary systems (Kirk et al., 2016) around which there are no discovered CBPs, destabilization and subsequent ejection via the STEEP process could have ejected many CBPs contributing to the population of free-floating planets (Veras and Raymond, 2012). This population could be examined by microlensing surveys (e.g. Sumi et al., 2011) and compared with expected free-floating planet population pro-

duced by other mechanisms such as planet-planet scattering in single-star systems to gauge its significance.

Our treatment of stellar evolution has its limitations as well, even though we used modern stellar evolution models (Baraffe et al., 2015) and magnetic braking laws (Reiners and Mohanty, 2012; Repetto and Nelemans, 2014). Future examinations of coupled stellar-tidal evolution should model realistic evolving stellar radii of gyration, stellar metallicity effects (e.g. Bolmont et al., 2017), differential rotation (e.g. Lanza and Mathis, 2016), and the effect of binarity on stellar-tidal evolution in order to produce more quantitatively accurate models. Additionally, future studies should consider directly coupling an N-body code with a coupled stellar-tidal evolution model to robustly model the STEEP process, but we note that such simulations would be quite computationally expensive given the \sim Gyr timescales of coupled stellar-tidal evolution.

Future examinations of the STEEP process should focus on how coupled stellar-tidal evolution proceeds at large e . If a binary star system tidally locks at $e \gtrsim 0.2$, it can get captured into a pseudo-synchronous rotation state or a higher order spin-orbit resonance. We examined the case of an eccentric binary tidally locking into a 3:2 spin-orbit resonance in § 3.4.7. We found that at larger e , the orbit has less angular momentum so, for given initial stellar P_{rot} , tidal transfer of angular momentum to the orbit leads to larger increases in a_{crit} than the synchronous rotation case. Our model tends to break down at $e \gtrsim 0.3$ as the CPL model is derived to second order in e and does not resolve tidal locking into pseudo-synchronous rotation like the CTL model does, so future work could examine coupled stellar-tidal evolution using the CTL model. The precise details of tidal evolution at large e , however, is speculative and likely poorly constrained by linear equilibrium tidal models like the CPL and CTL models (e.g. Ferraz-Mello et al., 2008; Greenberg, 2009).

One effect not modeled by the STEEP process is the impact of mean motion resonances (MMRs) between the CBP and inner binary on the stability of CBP orbits. Holman and Wiegert (1999) found that the inner-most $n : 1$ MMR exterior to a_{crit} produced “islands” of instability such that CBPs orbiting exterior to a_{crit} near the MMR could still go unstable and be ejected from the system, a finding confirmed by the recent study of Lam and Kipping (2018). Similar to how a_{crit}

expands as the binary orbital period increases, the location of the inner-most $n : 1$ MMR will extend outward, potentially destabilizing CBPs still residing exterior to a_{crit} . This phenomenon can potentially make the STEEP process more effective at ejecting close-in CBPs and should be examined in future studies.

3.7.1 Future Prospects

The prospect for detecting additional CBPs appears bright as future surveys and algorithmic improvements can potentially increase the known population of CBPs. Newly discovered CBPs will help characterize the true underlying distribution of a_{CBP} relative to a_{crit} and provide a direct observational test of the destabilization of CBPs via coupled stellar-tidal evolution. Refined detection algorithms could uncover previously undetected CBPs in both *Kepler* and *K2* observations. Future *TESS* observations are expected to find approximately 1,100 eclipsing binaries (Sullivan et al., 2015) that could host additional CBPs, improving population statistics and helping to settle this remaining issue. Coupled with the previously-discovered *Kepler* eclipsing binaries (Kirk et al., 2016), the eclipsing binaries *TESS* will discover will provide a rich dataset that could be used to constrain how coupled stellar-tidal evolution proceeds and could potentially allow for constraints on parameters such as stellar tidal Qs. Launching between 2022-2024, the *ESA*-led *PLATO* mission will monitor nearly 1,000,000 stars searching for transits with a focus on low-mass terrestrial planets, potentially discovering new CBPs (Rauer et al., 2014). Additionally, the *Gaia* mission can potentially probe the population of gaseous CBPs and the CBP-binary mutual inclination distribution allowing for comparison with the *Kepler* circumbinary population (Sahlmann et al., 2015).

A key component required to understand the observed CBP population is CBP planet formation. Although numerous studies have examined planet formation in circumbinary systems (e.g. Alexander, 2012; Paardekooper et al., 2012; Meschiari, 2012a,b; Pelupessy and Portegies Zwart, 2013; Bromley and Kenyon, 2015; Vartanyan et al., 2016), no previous study has examined the impact of coupled stellar-tidal evolution on young binary stars embedded in a circumbinary disk. Given that complex disk-binary interactions can lead to significant changes in both the orbit of the binary and the structure of the circumbinary disk (e.g. Fleming and Quinn, 2017), coupled

stellar-tidal evolution would necessarily play an important role in that feedback especially since appreciable tidal orbital evolution can occur over the ~ 1 Myr disk lifetime (Haisch et al., 2001). Although likely computationally non-trivial, accounting for coupled stellar-tidal evolution in simulations of binaries embedded in protoplanetary circumbinary disks could yield new insights into how CBPs form and migrate in circumbinary disks.

In recent years, numerous theoretical modeling efforts have sought to characterize how the presence of two stars impacts the potential habitability of CBPs (e.g. Kane and Hinkel, 2013; Forgan, 2014; Popp and Eggl, 2017). As future studies look to characterize and detect potentially habitable CBPs, we suggest that such efforts should focus on longer-period binaries, those with $P_{orb} \gtrsim 7.5$ days, as in this regime, the STEEP process is less likely to result in the ejection of close-in CBPs.

As future observations discover and characterize new CBPs, probing the true underlying CBP population, the evolution of the binary stars that host these planets must be well known. Understanding coupled stellar-tidal evolution in young, short-period binary star systems can provide critical insights into how binaries form and host circumbinary planetary systems and hence provide insights into the observed CBP population. In this work, we outlined a theoretical framework, the STEEP process, for the long-term evolution of short-period binary stars that provides an explanation for the lack of CBPs around such binary systems. Future detections or non-detections of CBPs around short-period binaries will provide the best indirect observational test of the STEEP process.

3.8 Acknowledgments

The authors wish to thank the anonymous referee for their careful reading of the manuscript and their insightful suggestions that improved the quality of the manuscript. We also would like to thank Russell Deitrick and Jacob Lustig-Yaeger for constructive conversations that improved the quality of this work. This work was facilitated through the use of advanced computational, storage, and networking infrastructure provided by the Hyak supercomputer system and funded by the STF at the University of Washington. DPF is supported by an NSF IGERT DGE-1258485 fellowship. This work was supported by NASA Headquarters under the NASA Earth and Space

Science Fellowship Program - Grant 80NSSC17K0482. DPF, RB, RL, and TRQ acknowledge that this work was supported by the NASA Astrobiology Institute's Virtual Planetary Laboratory under Cooperative Agreement number NNA13AA93A. R.L. acknowledges support from NASA grant NNX14AK26G. Software: matplotlib: Hunter (2007), numpy: van der Walt et al. (2011), pandas: McKinney (2010)

Chapter 4

THE COMPETITION BETWEEN MAGNETIC BRAKING AND TIDAL TORQUES IN BINARY STARS: APPLICATION TO THE *Kepler* FIELD

Portions of this chapter were originally published in collaboration with Rory Barnes, James R. A. Davenport, and Rodrigo Luger in the August 2019 edition of the Astrophysical Journal (Fleming et al., 2019, ApJ, Vol. 881, 2; 2019 © American Astronomical Society, DOI: 10.3847/1538-4357/ab2ed2), and are reproduced below with permission of the American Astronomical Society.

4.1 Introduction

The long-term angular momentum evolution of low-mass ($M \lesssim 1 M_{\odot}$) stars is controlled by magnetic braking, the torque exerted on stars due to the coupling of stellar winds to the surface magnetic field (Mestel, 1968). Early in stellar lifetimes, stars spin-up as they contract along the pre-main sequence. Once stars reach the main sequence, stellar radii remain mostly constant while magnetic braking removes angular momentum from the stars, gradually spinning them down over time (Skumanich, 1972). Although the precise details of how magnetic braking operates are not fully known, models of magnetic braking have been used to successfully model the bulk trends of P_{rot} distributions in clusters (e.g. Praesepe, Reiners and Mohanty, 2012; Matt et al., 2015; Douglas et al., 2017) and field stars (e.g. the *Kepler* field, Matt et al., 2015; van Saders et al., 2018). Furthermore, the magnetic braking-driven long-term spin-down of stars has been used to estimate stellar ages, a method known as gyrochronology (Skumanich, 1972; Barnes, 2003, 2007; Mamajek and Hillenbrand, 2008; Barnes, 2010), with older stars assumed to have lost more angular momentum due to magnetic braking and therefore rotate more slowly.

In contrast, the angular momentum evolution in low-mass short-period ($P_{orb} \lesssim 10$ d) stellar binaries is dominated by tides. Tidal torques drive secular changes in the binary orbit and stel-

lar spins, eventually circularizing the orbit and synchronizing the stellar spins in the long-term (Counselman, 1973). Orbital circularization is ubiquitous for short-period binaries, owing to the tidal torque's strong radius and semi-major axis dependence, with both theoretical (e.g. Zahn and Bouchet, 1989; Claret et al., 1995) and observational (e.g. Meibom and Mathieu, 2005; Mazeh, 2008; Lurie et al., 2017) studies finding that most binaries with $P_{orb} \lesssim 10$ d are circularized. For short-period binaries, tidal torques work quickly on ~ 100 Myr timescales, as Zahn and Bouchet (1989) found that the orbit of solar twin binaries circularize during the stellar pre-main sequence. Observations by Meibom and Mathieu (2005) support this picture as they find short-period binaries in the ~ 150 Myr old cluster M35 tend to have circular orbits.

Tides impart a significant signature in the long-term angular momentum evolution for binary stars, especially for stellar spins. Tidal torques drive binaries towards the tidally locked state in which the stellar P_{rot} is equal to the equilibrium rotation period (P_{eq}) predicted by tidal models, with a familiar example of this effect being spin-orbit synchronization where $P_{rot} = P_{eq} = P_{orb}$. Tidal-locking occurs much earlier than orbital circularization with the tidal-locking timescale estimated to be 2 – 3 orders of magnitude less than the circularization timescale (Zahn and Bouchet, 1989; Witte and Savonije, 2002; Mazeh, 2008) as there is typically much less angular momentum in stellar spins than the binary orbit. As a result, tidal-locking is expected for binaries with $P_{orb} \lesssim 20$ d (e.g. Levato, 1974; Meibom et al., 2006; Mazeh, 2008; Zahn, 2008; Meibom et al., 2015).

In low-mass binaries, both magnetic braking and tidal torques compete to shape the stellar P_{rot} evolution. When tides dominate, in particular at close orbital separations, tides can fix $P_{rot} = P_{orb}$, or more generally $P_{rot} = P_{eq}$ for eccentric orbits. In such situations, magnetic braking still operates, removing angular momentum from each star, forcing tides to compensate for each star's loss of angular momentum by spinning up the stars to maintain the tidally locked equilibrium, removing angular momentum from the orbit, hardening the binary (Verbunt and Zwaan, 1981; Repetto and Nelemans, 2014; Fleming et al., 2018). Tides do not win out over magnetic braking in general, however, as magnetic braking can spin-down the stars past the tidally locked state into subsynchronous rotation ($P_{rot} > P_{eq}$, Habets and Zwaan, 1989; Zahn, 1994; Keppens, 1997). This behavior seems to be borne out in nature, as Lurie et al. (2017) discovered a substantial popu-

lation of subsynchronous short-period binaries in the *Kepler* field, clustered near $P_{orb}/P_{rot} \approx 0.9$, in defiance of the expectation of tidal locking at such short orbital separations. The competition between magnetic braking and tidal torques can lead to complex angular momentum evolution in low-mass stellar binaries, and no previous work has conducted a systematic study to examine how this evolution proceeds across a wide range of tidal dissipation parameters and P_{orb} .

Understanding the interaction between tidal torques and magnetic braking is of paramount importance as P_{rot} distributions measured in clusters (e.g. Praesepe, Agüeros et al., 2011; Douglas et al., 2017) and field stars (e.g. *Kepler*, Reinhold et al., 2013; McQuillan et al., 2014) are likely contaminated by unresolved binaries given that roughly half of Sun-like stars are in stellar binaries (Raghavan et al., 2010; Duchêne and Kraus, 2013), and that binaries are difficult to resolve in photometric surveys. In the *Kepler* field, for example, Simonian et al. (2018) recently found that most rapid rotators ($P_{rot} \lesssim 7.5$ d) are likely non-eclipsing, tidally-synchronized short-period photometric binaries, indicating that tidal torques in binaries can significantly impact observed P_{rot} distributions. Tidally-interacting binaries impart a contaminating signal that is not currently accounted for by models. Moreover, any ages inferred from rotation periods of stars in unresolved binaries using gyrochronology could be incorrect owing to the influence of tidal torques. No previous study has quantified this effect.

There is currently a large number of *Kepler* binaries with known P_{rot} and P_{orb} (e.g. Lurie et al., 2017). Both the extended *Kepler* mission (K2, Howell et al., 2014) and the Transiting Exoplanet Survey Satellite (TESS, Ricker et al., 2014; Sullivan et al., 2015) are expected to detect additional low-mass eclipsing binaries, with Gaia parallaxes (Gaia Collaboration et al., 2016) poised to help refine these stellar parameters, potentially creating a rich dataset of the angular momentum budgets of low-mass binaries. Developing a framework for the angular momentum evolution of low-mass binaries can enable the characterization of the nature of tidal torques in binaries by conditioning on datasets of the spin and orbital states of stellar binaries.

Here, we present a model for the angular momentum evolution of low-mass stellar binaries over their full premain and main sequence lifetimes using a realistic treatment of stellar evolution, magnetic braking, and tidal torques. We investigate under what conditions tidal-locking occurs,

and how tidal torques influence rotation in stellar binaries as a function of binary P_{orb} and tidal dissipation parameters for two widely-used equilibrium tidal models. We show how tidal torques can impact stellar rotation in binaries out to $P_{orb} = 100$ d, causing stellar rotation periods to not strongly correlate with age, making the predictions of gyrochronology models fail in such systems. We describe our model in § 4.2 and our simulation procedure in § 4.3. We discuss our results in § 4.4, apply our model to the *Kepler* field in § 4.4.5, and discuss our results’ implications in § 4.5.

4.2 Methods

We simulate coupled stellar-tidal evolution for low-mass binaries using an improved version of the model presented in Fleming et al. (2018). We implement our model in the open-source code VPLanet¹ (Barnes et al., 2019). We integrate all model equations (see § 4.2.1 and § 4.2.2) using the 4th order Runge-Kutta scheme with adaptive timestepping described in Fleming et al. (2018).

4.2.1 Stellar Evolution

We improve upon the interpolation of the Baraffe et al. (2015) stellar evolution models employed by Fleming et al. (2018), STELLAR, by additionally performing a bicubic interpolation of the stellar radius of gyration, r_g , over mass and time of the Baraffe et al. (2015) models. This updated version of STELLAR now tracks the full moment of inertia evolution of low-mass stars according to the Baraffe et al. (2015) stellar evolution models, a critical requirement for modeling the angular momentum evolution of low-mass stars.

We simulate magnetic braking using the model derived by Matt et al. (2015) as this formalism has been shown to successfully model the spin-down of low-mass stars across many ages in both the Praesepe cluster and in the *Kepler* field. This model depends on the stellar Rossby number, $Ro = P_{rot}/\tau_{cz}$, the ratio of the stellar P_{rot} to the stellar convective turnover timescale, τ_{cz} . The Matt et al. (2015) model predicts that below a certain Ro for rapidly-rotating stars, stellar magnetic activity saturates at a constant value, producing a magnetic braking torque that is directly proportional to

¹VPLanet is publicly available at <https://github.com/VirtualPlanetaryLaboratory/vplanet>.

the stellar rotation rate. The angular momentum loss for rapidly-rotating saturated stars is given by

$$\frac{dJ}{dt} = -\left. \frac{dJ}{dt} \right|_0 \chi^2 \left(\frac{\omega}{\omega_\odot} \right) \quad (4.1)$$

while for more slowly-rotating unsaturated stars,

$$\frac{dJ}{dt} = -\left. \frac{dJ}{dt} \right|_0 \left(\frac{\tau_{cz}}{\tau_{cz\odot}} \right)^2 \left(\frac{\omega}{\omega_\odot} \right)^3 \quad (4.2)$$

where

$$\left. \frac{dJ}{dt} \right|_0 = 6.3 \times 10^{30} \text{ erg} \left(\frac{R}{R_\odot} \right)^{3.1} \left(\frac{M}{M_\odot} \right)^{0.5}. \quad (4.3)$$

Saturated magnetic braking occurs for $Ro \leq Ro_\odot/\chi$ for $\chi = 10$ where Matt et al. (2015) defines $\chi = Ro_\odot/Ro_{sat}$. We adopt all model parameters given in Table 1 from Matt et al. (2015), with the correction from Matt et al. (2019), and compute τ_{cz} using Eqn. (36) from Cranmer and Saar (2011).

We model the net change in the stellar rotation rate due to stellar evolution and magnetic braking via the following equation

$$\dot{\omega} = \frac{\dot{J}_{mb}}{I} - \frac{2\dot{R}\omega}{R} - \frac{2\dot{r}_g\omega}{r_g} \quad (4.4)$$

where the moment of inertia $I = Mr_g^2R^2$, J_{mb} is the angular momentum loss due to magnetic braking, and the time derivatives of the stellar R and r_g are computed numerically using our interpolation of the Baraffe et al. (2015) stellar evolution grids.

Core-Envelope Coupling

Our simplified model assumes that stars follow solid body rotation, whereas in real low-mass stars, coupling between the radiative core and convective envelope can impact the surface rotation period evolution (MacGregor and Brenner, 1991; Allain, 1998; Bouvier, 2008; Irwin and Bouvier, 2009). Recent work by Gallet and Bouvier (2013) and Gallet and Bouvier (2015) find that the rapidly-rotating stellar core acts as an angular momentum reservoir for the convective envelope,

potentially transferring angular momentum within the stellar interior and into the envelope for up to 1 Gyr, depending on the adopted magnetic braking model, the initial rotation rate, and the stellar mass. We anticipate that internal angular momentum transport would work against the spin-down caused by tidal torques, increasing tidal locking timescales. Internal angular momentum transport torques could potentially balance both tidal and magnetic braking torques near the tidally locked state, producing slight supersynchronous rotation, analogous to the subsynchronous case examined in § 4.4.1. Modeling core-envelope coupling is beyond the scope of this work, however.

Example Stellar Evolution

In Fig. 4.1, we plot the evolution of R , r_g , and P_{rot} for $0.2 M_\odot$, $0.7 M_\odot$, and $1 M_\odot$ mass stars, representing an M, K, and G dwarf, respectively, computed according to STELLAR and the Matt et al. (2015) magnetic braking model. We assume all stars have an initial $P_{rot} = 1$ d and have an initial age of 5 Myr. All stars’ radii contract along the pre-main sequence, spinning the stars up (right panel). Once the stars reach the main sequence, their structure changes slowly, allowing magnetic braking to dominate the stellar angular momentum evolution, significantly spinning-down the stars over long timescales. The r_g evolution noticeably differs between the stars as the late M dwarf’s (green) r_g varies little as it remains fully convective, while the K and G dwarf grow a radiative core while on the pre-main sequence, decreasing r_g until both reach the main sequence.

4.2.2 Tidal Evolution

Equilibrium tidal models, first introduced by Darwin (1880), track the secular evolution of an orbiter’s semi-major axis, a , eccentricity, e , and the rotation rates, ω_i , and obliquities ψ_i , of both gravitating bodies due to tidal torques. Equilibrium tidal models assume that tidally interacting bodies raise tidal bulges on their companions that remain offset from the line connecting the bodies’ centers of mass due to friction within each body. This assumption is typically referred to as the “weak friction approximation” (Zahn, 2008). The tidal bulges cause torques that permit the exchange of angular momentum between the orbit and both bodies’ spins. Equilibrium tidal mod-

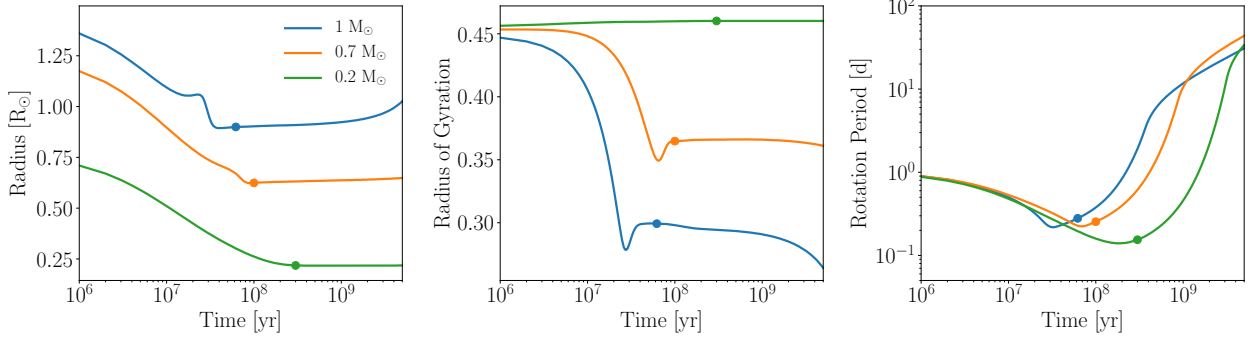


Figure 4.1: Stellar R (left), r_g (middle), and P_{rot} (right) evolution for $0.2 M_\odot$ (M, green), $0.7 M_\odot$ (K, orange), and $1 M_\odot$ (G, blue) mass stars computed according to STELLAR, our interpolation of the Baraffe et al. (2015) stellar evolution models (§ 4.2.1) combined with the Matt et al. (2015) magnetic braking model. Each dot denotes the approximate time when each star reaches the main sequence.

els are linear since they assume that the tidal waves that comprise the tidal bulge raised on a body are uncoupled. Under these assumptions, the tidal evolution is analogous to a driven, damped harmonic oscillator (Greenberg, 2009). For low-mass stars, equilibrium tidal models assume that tidal forces primarily dissipate energy in the outer-convective regions via viscous turbulence (see Zahn, 2008). Although simple, equilibrium tidal models have been used to model the secular orbital and rotation evolution of both Solar System bodies and exoplanets (e.g. Goldreich and Soter, 1966; Jackson et al., 2009; Leconte et al., 2010; Heller et al., 2011; Barnes et al., 2013; Barnes, 2017) and stellar binaries (e.g. Zahn and Bouchet, 1989; Zahn, 2008; Khaliullin and Khaliullina, 2011; Repetto and Nelemans, 2014; Fleming et al., 2018). We refer the reader to Barnes (2017) for an in-depth discussion of the assumptions and limitations of equilibrium tidal models. Here, we consider two common equilibrium tidal models to study the secular spin-orbital evolution of low-mass stellar binaries.

Constant Phase Lag Model

The “Constant Phase Lag” (CPL) (Ferraz-Mello et al., 2008; Heller et al., 2011) equilibrium tidal model assumes that the tidal torque on one body due to its companion arises from a linear com-

bination of several discrete, uncoupled tidal bulges, each with its own associated frequency, that maintain a fixed phase offset with respect to the line connecting the two stars' centers of mass. We use the EQTIDE implementation of the CPL model in VPLanet following the derivation of Ferraz-Mello et al. (2008). The equations that govern the secular change in e and a are as follows:

$$\frac{de}{dt} = -\frac{ae}{8Gm_1m_2} \sum_{i=1}^2 Z_{i,\text{CPL}} \left(2\varepsilon_{0,i} - \frac{49}{2}\varepsilon_{1,i} + \frac{1}{2}\varepsilon_{2,i} + 3\varepsilon_{5,i} \right) \quad (4.5)$$

$$\frac{da}{dt} = \sum_{i=1}^2 \frac{da_i}{dt} \quad (4.6)$$

where if the i^{th} body is tidally locked in a synchronous orbit,

$$\frac{da_{i,\text{sync}}}{dt} = -\frac{a^2}{Gm_1m_2} Z_{i,\text{CPL}} (7e^2 + \sin^2(\psi_i)) \varepsilon_{2,i}, \quad (4.7)$$

otherwise

$$\begin{aligned} \frac{da_i}{dt} = & \frac{a^2}{4Gm_1m_2} Z_{i,\text{CPL}} \left(4\varepsilon_{0,i} + e^2 \left[-20\varepsilon_{0,i} + \frac{147}{2}\varepsilon_{1,i} \right. \right. \\ & \left. \left. + \frac{1}{2}\varepsilon_{2,i} - 3\varepsilon_{5,i} \right] - 4\sin^2(\psi_i) [\varepsilon_{0,i} - \varepsilon_{8,i}] \right). \end{aligned} \quad (4.8)$$

The CPL equations for ψ and ω evolution are

$$\frac{d\psi_i}{dt} = \frac{Z_{i,\text{CPL}} \sin(\psi_i)}{4m_i r_{g,i}^2 R_i^2 n \omega_i} ([1 - \xi_i] \varepsilon_{0,i} + [1 + \xi_i] (\varepsilon_{8,i} - \varepsilon_{9,i})) \quad (4.9)$$

$$\begin{aligned} \frac{d\omega_i}{dt} = & -\frac{Z_{i,\text{CPL}}}{8m_i r_{g,i}^2 R_i^2 n} (4\varepsilon_{0,i} + e^2 [-20\varepsilon_{0,i} + 49\varepsilon_{1,i} + \varepsilon_{2,i}] \\ & + 2\sin^2(\psi_i) [-2\varepsilon_{0,i} + \varepsilon_{8,i} + \varepsilon_{9,i}]) \end{aligned} \quad (4.10)$$

where G is Newton's gravitational constant, n is the binary's mean motion, and the index i denotes that i^{th} body. The tidal phase lags signs, ε , for the i^{th} body are given by

$$\begin{aligned}\varepsilon_{0,i} &= \Sigma(2\omega_i - 2n) \\ \varepsilon_{1,i} &= \Sigma(2\omega_i - 3n) \\ \varepsilon_{2,i} &= \Sigma(2\omega_i - n) \\ \varepsilon_{5,i} &= \Sigma(n) \\ \varepsilon_{8,i} &= \Sigma(\omega_i - 2n) \\ \varepsilon_{9,i} &= \Sigma(\omega_i)\end{aligned}\tag{4.11}$$

where the function $\Sigma(x)$ returns 1 for positive x , -1 for negative x , and 0 otherwise.

The intermediate variable $Z_{\text{CPL},i}$ is given by

$$Z_{i,\text{CPL}} = 3G^2 k_{2,i} M_j^2 (M_i + M_j) \frac{R_i^5}{a^9} \frac{1}{nQ_i} \tag{4.12}$$

where the j^{th} body is the i^{th} body's companion, k_2 is the body's Love number of degree 2, and Q is the tidal quality factor ("tidal Q"). The tidal Q parameterizes the energy dissipation due to tidal evolution, with lower tidal Qs, i.e. larger phase differences between the tidal bulges, driving more rapid tidal evolution.

The other intermediate variable, ξ_i , is defined as

$$\xi_i = \frac{r_{g,i}^2 R_i^2 \omega_i a n}{GM_j}. \tag{4.13}$$

Constant Time Lag Model

The "Constant Time Lag" (CTL) (Hut, 1981; Leconte et al., 2010) equilibrium tidal model assumes a constant time interval between the body's tidal bulge and the passage of the tidally interacting companion. In this formalism, unlike the CPL model, the CTL model is continuous over a range of tidal wave frequencies and applicable for large e . However, if the assumption of linearity is relaxed,

i.e. frequencies associated with tidal bulges are allowed to depend on a spin or orbital forcing frequency, then this model is only valid over a small range of frequencies (Greenberg, 2009). We use the EQTIDE implementation of the CTL model in VPLanet following the derivation of Leconte et al. (2010). The equations that govern the secular changes in e , a , ω , and ψ are as follows:

$$\frac{de}{dt} = \frac{11ae}{2GM_1M_2} \sum_{i=1}^2 Z_{\text{CTL},i} \left(\cos(\psi_i) \frac{f_4(e)}{\beta^{10}(e)} \frac{\omega_i}{n} - \frac{18}{11} \frac{f_3(e)}{\beta^{13}(e)} \right), \quad (4.14)$$

$$\frac{da}{dt} = \frac{2a^2}{GM_1M_2} \sum_{i=1}^2 Z_{\text{CTL},i} \left(\cos(\psi_i) \frac{f_2(e)}{\beta^{12}(e)} \frac{\omega_i}{n} - \frac{f_1(e)}{\beta^{15}(e)} \right), \quad (4.15)$$

$$\frac{d\omega_i}{dt} = \frac{Z_{\text{CTL},i}}{2M_i r_{g,i}^2 R_i^2 n} \left(2\cos(\psi_i) \frac{f_2(e)}{\beta^{12}(e)} - [1 + \cos^2(\psi)] \frac{f_5(e)}{\beta^9(e)} \frac{\omega_i}{n} \right), \quad (4.16)$$

and

$$\frac{d\psi_i}{dt} = \frac{Z_{\text{CTL},i} \sin(\psi_i)}{2M_i r_{g,i}^2 R_i^2 n \omega_i} \left(\left[\cos(\psi_i) - \frac{\xi_i}{\beta} \right] \frac{f_5(e)}{\beta^9(e)} \frac{\omega_i}{n} - 2 \frac{f_2(e)}{\beta^{12}(e)} \right). \quad (4.17)$$

where the intermediate variables are given by

$$Z_{i,\text{CTL}} = 3G^2 k_{2,i} M_j^2 (M_i + M_j) \frac{R_i^5}{a^9} \tau_i, \quad (4.18)$$

and

$$\begin{aligned} \beta(e) &= \sqrt{1 - e^2}, \\ f_1(e) &= 1 + \frac{31}{2}e^2 + \frac{255}{8}e^4 + \frac{185}{16}e^6 + \frac{25}{64}e^8, \\ f_2(e) &= 1 + \frac{15}{2}e^2 + \frac{45}{8}e^4 + \frac{5}{16}e^6, \\ f_3(e) &= 1 + \frac{15}{4}e^2 + \frac{15}{8}e^4 + \frac{5}{64}e^6, \\ f_4(e) &= 1 + \frac{3}{2}e^2 + \frac{1}{8}e^4, \\ f_5(e) &= 1 + 3e^2 + \frac{3}{8}e^4. \end{aligned} \quad (4.19)$$

In both the CPL and CTL model, We assume $k_2 = 0.5$. This choice of k_2 does not impact our results as k_2 is degenerate with Q in the CPL model, e.g. the k_2/Q scaling in Eq. (4.12), and with τ in the CTL model, e.g. $k_2\tau$ scaling in Eq. (4.18), so we instead examine how our results scale with

Q and τ . Any constraints we derive as a function Q or τ can trivially be scaled to other values of k_2 . For example, a common re-parameterization of Q is the reduced tidal quality factor, $Q' = 3Q/2k_2$ (e.g. Leconte et al., 2010). Given our choice of $k_2 = 0.5$, this reduces to $Q' = 3Q$.

Tidal Locking

Tidal torques drive a body's rotation rate towards the tidally locked state. When a body tidally locks, tidal torques fix P_{rot} to the equilibrium P_{rot} , P_{eq} . Typically, tidal locking is understood in the context of a synchronized rotator, e.g. when $P_{rot} = P_{eq} = P_{orb}$. Although spin-orbit synchronization is an expected outcome of tidal evolution (Counselman, 1973), in general for tidally locked bodies on non-circular orbits, both the CPL and CTL model predict pseudosynchronous, or supersynchronous rotation, e.g. Mercury's 3:2 spin-orbit resonance ($P_{rot} = 2/3 P_{orb}$, Goldreich and Peale, 1966).

The CPL model, owing to its assumption of a finite number of discrete tidal lags, only permits a 1:1 and 3:2 spin-orbit state where, following Barnes (2017), the CPL P_{eq} is given by

$$P_{eq}^{\text{CPL}} = \begin{cases} P_{orb} & \text{if } e < \sqrt{1/19} \\ \frac{2}{3}P_{orb} & \text{if } e \geq \sqrt{1/19}. \end{cases} \quad (4.20)$$

Therefore, the CPL model predicts synchronous rotation for $e \lesssim 0.23$, and a supersynchronous 3:2 spin-orbit state otherwise for tidally locked rotators.

We note that two discrete rotation states are not the only permitted ones for tidally locked systems under the CPL formalism. For example, an alternate derivation of P_{eq} for orbiters with rotation axes perpendicular to the orbital plane under the CPL model predicts

$$P_{eq} = \frac{P_{orb}}{1 + 9.5e^2}, \quad (4.21)$$

a continuous function of e (Goldreich, 1966; Murray and Dermott, 1999). Here, we follow the suggestions of both Barnes et al. (2013) and Barnes (2017) and use the discrete P_{eq} version of the

CPL model for self-consistency.

The CTL model is continuous over a range of tidal frequencies and therefore predicts a P_{eq} that is a continuous function of both e and ψ . Following Barnes (2017), we define the CTL P_{eq} by

$$P_{eq}^{\text{CTL}} = P_{orb} \frac{\beta^3 f_5(e)(1 + \cos^2(\psi))}{2f_2(e) \cos(\psi)}. \quad (4.22)$$

The CTL model predicts that bodies on eccentric orbits tidally lock into supersynchronous rotation, and only bodies with aligned spins on circular orbits are synchronous rotators.

In general, a continuous P_{eq} and the discrete 1:1 and 3:2 spin-orbit commensurabilities are not the only equilibrium rotation states for tidally locked rotators predicted by equilibrium tidal models. For example, Rodríguez et al. (2012) show that tidally interacting bodies can get captured into many spin-orbit resonances states, e.g. 2:1, 5:2, 4:3, etc, and below, we search for evidence of them in data of the spin-orbital states of *Kepler* EBs. Note that our model does not resolve capture into such states as the CPL model, owing to its inclusion of only 4 discrete tidal lags, only allows a body to enter into 3:2 and 1:1 spin - orbit commensurabilities. The CTL model predicts a continuous equilibrium period as a function of the P_{orb} , e , and obliquity, for tidally locked bodies, only resolving capture into 1:1 synchronous rotation.

Numerical Details of Tidal Locking

Due to the discontinuities in the equilibrium tidal model equations, for example in Eq. (4.11) when $\omega \approx n$, and due to the inherant discreteness of numerical integrations, numerical solutions for the CPL and CTL models can produce unphysical evolution. We follow Barnes et al. (2013) and Fleming et al. (2018) and fix $P_{rot} = P_{eq}$ according to Eq. (4.20) or Eq. (4.22) for the CPL and CTL models, respectively, when P_{rot} is within 1% of P_{eq} . To ensure that tidal torques dominate over torques due to magnetic braking and stellar evolution when forcing tidal-locking, we additionally require that the P_{rot} derivative points towards P_{eq} on both sides of P_{eq} , i.e. when the gradient of P_{rot} points towards the tidally locked state, before fixing $P_{rot} = P_{eq}$. We find that this scheme produces physically and numerically accurate results.

The Dynamical Tide

An additional mechanism for tidal dissipation in low-mass stellar binaries is the dynamical tide. This effect arises from the turbulent viscous damping of inertial waves that are excited in the stellar convective envelope by a tidal perturber, with Coriolis acceleration serving as the restoring force (Zahn, 1975; Ogilvie and Lin, 2007). Under the dynamical tide formalism, the stellar mass, evolving stellar structure, rotation rate, and tidal forcing frequency can all strongly impact the strength of tidal dissipation, which can span many orders of magnitude (Ogilvie and Lin, 2007; Ogilvie, 2013; Mathis, 2015; Gallet et al., 2017). For example, adopting the tidal frequency-averaged model for tidal dissipation of Ogilvie (2013), both Mathis (2015) and Gallet et al. (2017) show that dynamical tidal dissipation is enhanced during the pre-main sequence due to the expansion of the stellar radiative core and rapid rotation, whereas the magnetic braking-driven spin-down on the main sequence decreases the tidal dissipation. Dissipation due to the dynamical tide could be important for some of the systems considered in this work since, for binary stars on circular orbits, inertial waves are excited in the stellar convective envelopes for $P_{orb} > P_{rot}/2$ and can drive significant spin and orbital evolution (e.g. Witte and Savonije, 2002; Ogilvie and Lin, 2007; Bolmont and Mathis, 2016). Although semi-analytic models for dynamical tidal dissipation that account for the evolving stellar structure and rotation exist (e.g. Mathis, 2015; Bolmont and Mathis, 2016; Gallet et al., 2017), we do not consider them here as they are currently limited to circular orbits. We instead focus on exploring the impact of the equilibrium tide across a wide range of parameter space and leave an examination of how the combination of the dynamical and equilibrium tide impacts the rotation period evolution of low-mass binary stars for future work.

Example Tidal Evolution

We plot the tidal evolution for a , e , and P_{rot} , ignoring stellar evolution, for a solar-twin binary with an initial $P_{orb} = 10$ d, $P_{rot} = 1$ d, $e = 0.2$ for the CPL model and CTL model, assuming $Q = 10^6$ and $\tau = 0.1$ seconds, respectively, in Fig. 4.2. The CPL and CTL model predict the same qualitative evolution: both the binary's e and P_{orb} slightly increase as tides force the spins toward the tidally

locked state, transferring rotational angular momentum into the orbit, increasing the orbital angular momentum by $\sim 1\%$ in the process. At late times, both the CPL and CTL drive the binaries towards orbital circularization, with tidal dissipation decreasing P_{orb} . The predictions of the CPL and CTL model, differ, however, when the binaries tidally lock. Under the CPL model, the binary tidally locks into a synchronous orbit when $e < \sqrt{1/19}$, e.g. Eq. (4.20), while the CTL model predicts supersynchronous rotation due to the CTL model's equilibrium period eccentricity dependence, e.g. Eq. (4.22).

4.2.3 Coupled Stellar-Tidal Evolution For tidally locked Systems

Following Fleming et al. (2018), when one or both binary stars are tidally locked, tidal forces prevent magnetic braking from spinning down the tidally locked star(s), and any angular momentum lost comes at the expense of the binary orbit, decreasing a as a result (Verbunt and Zwaan, 1981). Below in Eq. (4.23) and Eq. (4.24), we modify the a decay equations due to stellar evolution and magnetic braking in tidally locked binaries from Fleming et al. (2018), their Eqs. (18) and (20), to additionally account for r_g evolution when one or both stars tidally lock, respectively, assuming conservation of angular momentum:

$$\dot{a}_{coupled}^{(1)} = \frac{-J_{mb} - 2\omega \left(m_1 r_{g,1}^2 R_1 \dot{R}_1 - m_1 r_{g,1} \dot{r}_{g,1} R_1^2 \right)}{\frac{\mu^2 GM(1-e^2)}{2J_{orb}} - \frac{3\omega}{2a} m_1 r_{g,1}^2 R_1^2} \quad (4.23)$$

and

$$\dot{a}_{coupled}^{(2)} = \frac{-J_{mb} - 2\omega \left(\sum_{i=1}^2 m_i r_{g,i}^2 R_i \dot{R}_i + m_i r_{g,i} \dot{r}_{g,i} R_i^2 \right)}{\frac{\mu^2 GM(1-e^2)}{2J_{orb}} - \frac{3\omega}{2a} \left(m_1 r_{g,1}^2 R_1^2 + m_2 r_{g,2}^2 R_2^2 \right)}, \quad (4.24)$$

where J_{orb} is the orbital angular momentum.

4.3 Simulations

We examine stellar angular momentum evolution in low-mass binaries by simulating two sets of 10,000 stellar binaries, one modeled using the CPL model and the other using the CTL formalism.

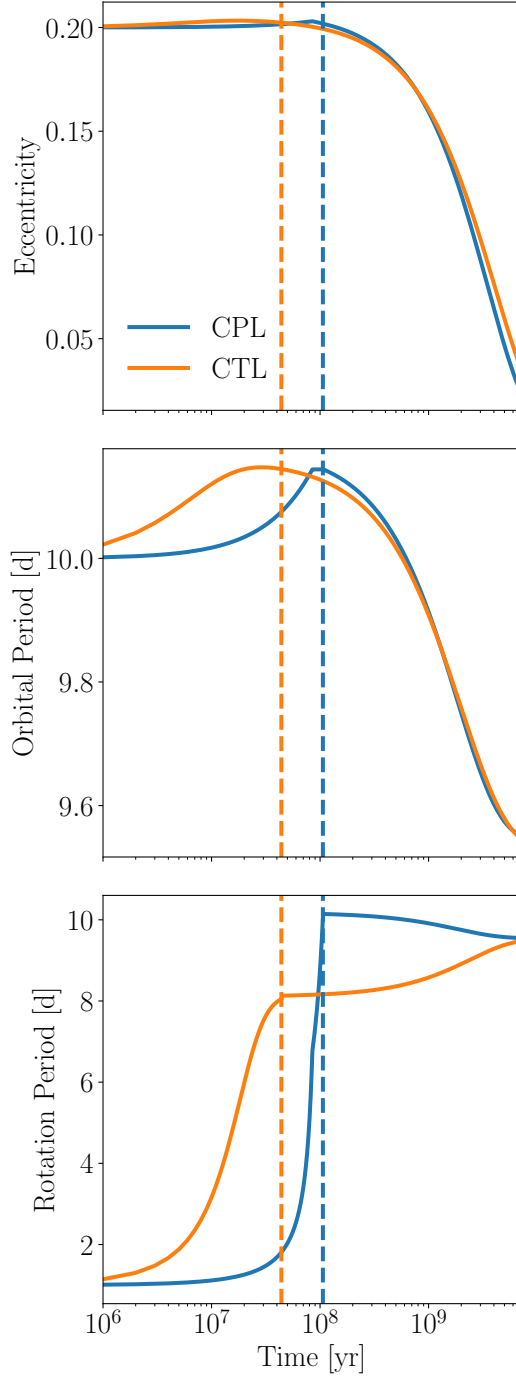


Figure 4.2: Tidal evolution of a $1 M_{\odot} - 1 M_{\odot}$ stellar binary's e (top), P_{orb} (middle), and P_{rot} (bottom) for the CPL (blue) and CTL (orange) model. The blue (CPL) and orange (CTL) vertical dashed lines denote when the stellar binary tidally locks. Both the CPL and CTL model predict the same qualitative evolution. The rotational evolution differs, however, as under the CPL model, the binary tidally locks into a synchronous orbit as $e < \sqrt{1/19}$, e.g. Eq. (4.20), while the CTL model predicts supersynchronous rotation due to the CTL model's equilibrium period eccentricity dependence (see Eq. (4.22)).

We simulate both stars' spin evolution but mainly consider the P_{rot} evolution for the primary, i.e. more massive star in binaries, as it is observationally easier to measure a P_{rot} on the more massive, and hence brighter, star (e.g. Meibom et al., 2006; Lurie et al., 2017). For each simulation, we sample the primary's mass uniformly over $[0.1, 1] M_\odot$. Following Matt et al. (2015), we uniformly sample the \log_{10} of P_{rot} over $[0.8, 15]$ days, a distribution that approximates the P_{rot} distribution of young stars in the ~ 2 Myr old Orion Nebula Cluster (Stassun et al., 1999; Herbst et al., 2001, 2002; Rodríguez-Ledesma et al., 2009). We compute the secondary star's mass by uniformly sampling the mass ratio over $[0.1, 1]$ following observations of mass ratios in low-mass binaries (Raghavan et al., 2010; Moe and Kratter, 2018). Given the inherent uncertainty in and complexity of the formation of short-period binaries (e.g. Bonnell and Bate, 1994; Bate, 2000; Bate et al., 2002; Moe and Kratter, 2018) and the potential for dynamical processing via tides or stellar close encounters (e.g. Mardling and Aarseth, 2001; Hurley et al., 2002; Ivanova et al., 2005; Meibom and Mathieu, 2005), we take an agnostic approach to the initial orbital configuration by uniformly randomly sampling the initial eccentricity (e) over $[0.0, 0.3]$, consistent with eccentricities of field binaries that likely have not been tidally-processed (Raghavan et al., 2010). Although the CTL model is applicable for $e \gtrsim 0.3$, the CPL model is not and can predict qualitatively incorrect evolution in that regime (see Section 4.1 in Leconte et al., 2010), so we restrict $e \leq 0.3$ to allow us to compare both models. We uniformly sample the initial P_{orb} over $[3, 100]$ d and do not consider $P_{orb} < 3$ d as these binaries are likely to have a tertiary companion (Tokovinin et al., 2006) which can significantly impact the inner binary's dynamical evolution (e.g. Fabrycky and Tremaine, 2007; Muñoz and Lai, 2015; Martin et al., 2015; Hamers et al., 2016; Moe and Kratter, 2018).

Values for stellar tidal Q s and τ s for low-mass stars are highly uncertain due to complex viscous evolution within the stars (Ogilvie and Lin, 2007), and can differ for stars of the same spectral class (Barker and Ogilvie, 2009). These parameters can also vary as a function of stellar mass or age (Bolmont and Mathis, 2016; Van Eylen et al., 2016), likely due to low-mass stars' evolving convective regions where the tidal dissipation predominantly occurs (Zahn, 2008). Typical values of Q and τ for Sun-like stars are estimated to be of order $Q \approx 10^6$ and $\tau \approx 0.1$ s, respectively (e.g. Meibom and Mathieu, 2005; Ogilvie and Lin, 2007; Jackson et al., 2008), however a range of

values exist in the literature. Therefore, we consider a wide range of tidal parameters by sampling stellar tidal Q_s log-uniformly over $[10^4, 10^8]$ and τ log-uniformly over $[10^{-2}, 10]$ s. There is no general expression to compute Q as a function of τ , or vice versa, except in some special cases where approximations exist, e.g. Eqn. (2) from Heller et al. (2011). All stars have an initial age of 5 Myr unless stated otherwise as by this time, the gaseous protoplanetary circumbinary disk that can drive significant dynamical evolution in the binary (e.g. Fleming and Quinn, 2017) would likely have dissipated (Haisch et al., 2001). We also perform a smaller subset of simulations to illustrate the behaviour of our coupled model and describe their initial conditions as we introduce them. All code used to run simulations and generate figures is available online.²

4.4 Results

4.4.1 Interaction Between Magnetic and Tidal Braking: Subsynchronous Rotation

Here we focus on binaries in the “weak tides” regime, i.e. long P_{orb} and large Q or small τ , to identify the boundary between evolution dominated by tides or magnetic braking via analytic calculations and simulations.

Analytic Torque Balance

In the weak tides regime, spin-down due to magnetic braking will drive the stellar P_{rot} past P_{eq} , resulting in subsynchronous rotation, $P_{rot} > P_{eq}$. For long P_{orb} , the stars will be slowly-rotating and in the unsaturated regime (Matt et al., 2015). Since magnetic braking scales as P_{rot}^{-3} for unsaturated rotators, e.g. Eqn. (4.2), magnetic braking torques weaken as the stellar rotation slows down, so at some P_{rot} , tidal torques will balance magnetic braking, producing a long-lasting state of subsynchronous rotation. We compute the P_{rot} at which this balance occurs as a function of P_{orb} , k_2 , and τ in § 4.7 by setting the sum of Eqn. (4.16) and Eqn. (4.2) equal to 0, considering tidal torques under the CTL formalism. For simplicity, we assume both stars are solar-mass with 0 obliquity, a circular binary orbit, and that the torque balance occurs while the stars are on the

²<https://github.com/dflemin3/sync>.

main sequence where stellar properties change slowly. Although solar mass stars are the most massive stars we consider in this work, and hence will have the strongest tidal torque for a given tidal dissipation parameter and P_{orb} , they can still exhibit subsynchronous rotation and serve as a useful end member case to examine here and in simulations below. We display the results of this calculation in Fig. 4.3, normalizing P_{rot} by P_{eq} , which for binary stars with 0 obliquity on circular orbits is simply P_{orb} .

Our calculations show that subsynchronous rotation occurs across a wide range of tidal parameters and P_{orb} . In general as tides weaken, i.e. increasing P_{orb} and/or decreasing $\log_{10}(k_2\tau)$, tidal and magnetic braking torques balance at longer P_{rot} . For strong tides, $\log_{10}(k_2\tau) \gtrsim -1$, tidal torques overpower magnetic braking for $P_{orb} \lesssim 40$ d, tidally locking binaries into synchronous rotation. For our fiducial values of $k_2 = 0.5$ and $\tau = 0.1$ s (white dashed line in Fig. 4.3), solar-twin binaries will rotate subsynchronously for $P_{orb} \gtrsim 20$ d, with more severe subsynchronism at longer P_{orb} . This simple calculation, however, does not account for stellar evolution or secular tidal orbital evolution, e.g. tidal friction that will shrink the orbit, gradually strengthening tidal torques, so we turn to simulations to characterize this evolution.

Torque Balance

We simulate the full coupled stellar-tidal evolution of $1 M_\odot - 1 M_\odot$ binaries on initially circular orbits to examine how stellar binaries evolve towards subsynchronous rotation. In Fig. 4.4, we plot P_{rot} , normalized by P_{eq} , and its time derivative for $P_{orb} \in [5, 60]$ d modeled using both the CPL (solid line, $Q = 10^6$) and CTL (dashed line, $\tau = 0.1$ s) models. Both tidal models predict that binaries with $P_{orb} < 10$ d will tidally lock within 100 Myr, in agreement with observations (Meibom and Mathieu, 2005) and previous theoretical work (Zahn and Bouchet, 1989). The CPL model predicts that all binaries tidally lock, even out to $P_{orb} = 60$ d, indicating that tidal locking is not necessarily restricted to short P_{orb} systems. As anticipated by our analytic calculations, the CTL model predicts subsynchronous rotation for $P_{orb} \geq 20$ d as magnetic braking overpowers tidal torques. For $P_{orb} = 20$ d, magnetic braking pushes $P_{rot}/P_{eq} \approx 1.05$, with the maximum value set by the torque balance. As shown in § 4.4.1, the peak P_{rot}/P_{eq} grows for longer P_{orb} since tides

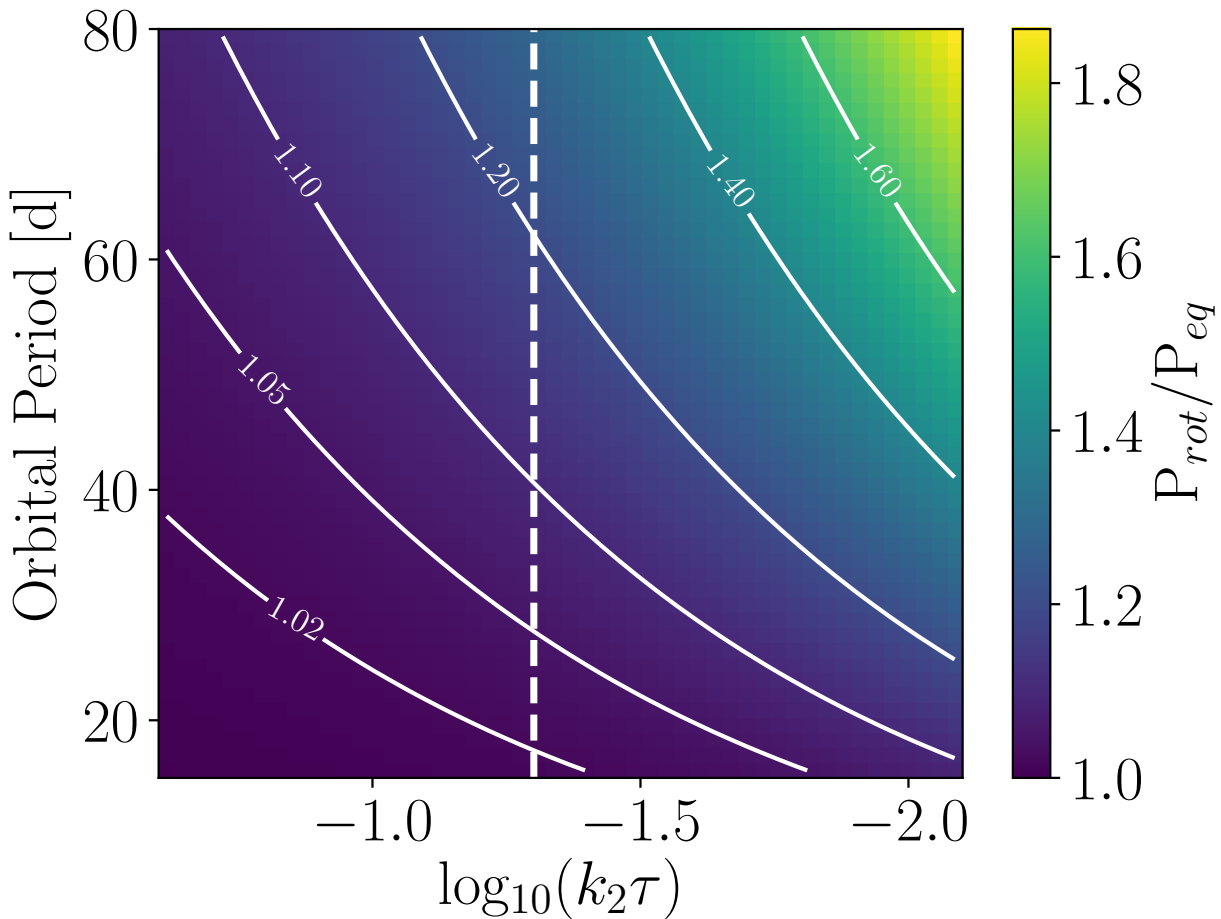
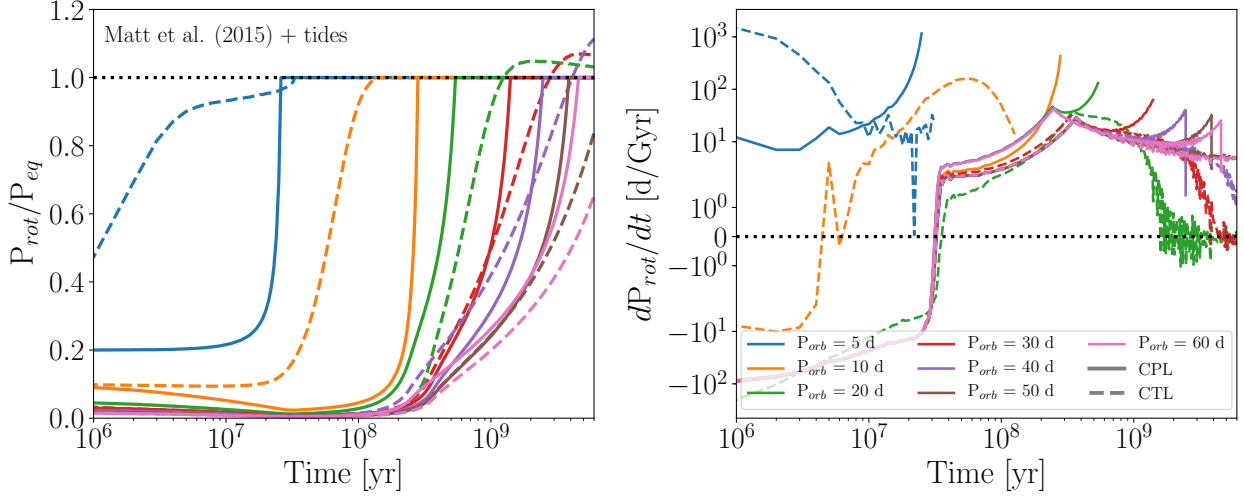


Figure 4.3: The stellar P_{rot} , normalized by P_{eq} , at which the torques due to magnetic braking and tides balance for a $1 M_\odot - 1 M_\odot$ binary on a circular orbit according to Eqn. 4.28. The white dashed line indicates our fiducial values for k_2 and τ , 0.5 and 0.1 s, respectively, that we adopt in the simulations in § 4.4.1.



For $P_{orb} \leq 10$ d, both the CPL and CTL models predict that the binaries lock into synchronous rotation. For all P_{orb} , the CPL models tidally lock whereas the CTL model predicts subsynchronous rotation that persists for Gyrs.

Figure 4.4: Evolution of stellar P_{rot} , normalized by P_{eq} (see Eqn. (4.20) and Eqn. (4.22)), for initial circular binary orbits according to the CPL (solid) and CTL (dashed) models with $Q = 10^6$ and $\tau = 0.1$ s, respectively, using the Matt et al. (2015) magnetic braking model. Left: P_{rot}/P_{eq} for stars with P_{orb} ranging from 5 d to 60 d. The black dotted line indicates the tidally locked state. Right: Net P_{rot} derivative due to stellar evolution, tidal torques, and magnetic braking. We truncate each curve when the binary tidally locks. The legend denotes the initial binary orbital period and we note that the orbital periods do not vary by more than a few percent over the course of the simulations.

weaken with increasing binary separation, e.g. Eqn. (4.18), allowing magnetic braking to dominate the spin evolution.

Subsynchronous rotation does not persist indefinitely, however, as P_{rot} eventually decreases back towards the tidally locked state in the long-term due to a combination of three simultaneous physical effects. First, magnetic braking weakens at long P_{rot} as its torque scales as P_{rot}^{-3} for unsaturated rotators (Matt et al., 2015). Second, as P_{rot} increases further from the tidally locked state, tidal torques strengthen as they try to force P_{rot} back towards P_{eq} (see Eqn. (4.16)). Third, when $P_{rot} > P_{eq}$, tides transfer angular momentum from the orbit into stellar rotations, decreasing P_{orb} , gradually strengthening tidal torques that strongly depend on the binary separation as $a^{-6.5}$. These effects combine to shift the balance of power from magnetic braking-controlled stellar spin down

to tidal torques spinning-up stars, shepherding them towards P_{eq} in the long-term.

We can see this process unfold in the right panel of Fig. 4.4 where we plot the total P_{rot} time derivative due to tidal torques, stellar evolution, and magnetic braking. Early on, $\dot{P}_{rot} < 0$ as stars contract along the pre-main sequence until about 60 Myr when the stars reach the zero age main sequence. Tides and magnetic braking then combine to spin down stars towards the tidally locked state. For the CTL models with $P_{orb} > 10$ d, $\dot{P}_{rot} > 0$ as magnetic braking dominates, driving the stars into subsynchronous rotation. In the long-term, $\ddot{P}_{rot} < 0$, however, as the three processes described above gradually strengthen tidal torques relative to magnetic braking. Tidal torques eventually overpower magnetic braking, seen as a slight negative P_{rot} derivative, slowly driving P_{rot} back towards P_{eq} , producing a population of subsynchronous rotators that can persist for Gyrs. We explore this point further in § 4.4.2.

4.4.2 Influence of P_{orb} , Q and τ

We next examine how P_{rot} evolution in stellar binaries depends on P_{orb} and the strength of tidal dissipation, parameterized by Q and τ for the CPL and CTL models, respectively. In Fig. 4.5, we bin our simulation results after the full 7 Gyr evolution by P_{orb} and Q or τ and compute the median P_{orb}/P_{rot} in each bin, marginalizing over all other parameters.

Spin-orbit synchronization is the typical outcome for binaries with $P_{orb} < 10$ d according to the CPL model for most values of Q . The strong tidal torques predicted by the CPL model can even tidally lock binaries out to $P_{orb} \gtrsim 80$ d for $Q < 10^5$, well beyond the expected limit of 20 d (Meibom et al., 2006). According to the CTL model, binaries with $P_{orb} < 10$ d typically tidally lock for $\tau \gtrsim 0.1$ s, and seldomly tidally lock for $P_{orb} > 20$ d, except for systems with strong tides, $\tau \gtrsim 3$ s. Both models predict a substantial population of subsynchronous rotators (red regions in Fig. 4.5, $P_{rot} > P_{orb}$), consistent with magnetic braking dominating weak tidal torques. The population of supersynchronous rotators (blue regions in Fig. 4.5, $P_{rot} < P_{orb}$) with $P_{orb} > 60$ d does not in general correspond to binaries tidally locking into supersynchronous rotation, but rather, typically arises from the combination of weak tidal torques and magnetic braking not spinning down stars enough for P_{rot} to be close to the tidally locked state. At a given age, longer P_{orb} binaries will

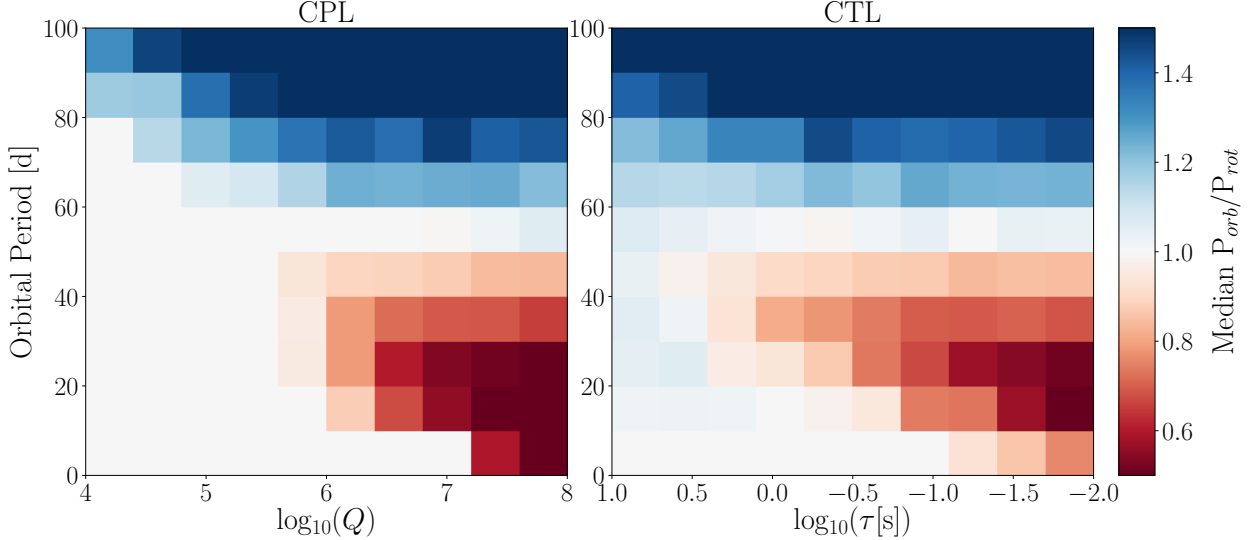


Figure 4.5: Median $P_{\text{orb}}/P_{\text{rot}}$ at the end of the simulation according to the CPL (left) and CTL (right) models binned by $\log_{10}(Q)$ and $\log_{10}(\tau)$, respectively, and P_{orb} . For $P_{\text{orb}} < 10 \text{ d}$, the CPL model predicts that most systems will tidally lock into synchronous rotation, whereas the CTL model requires $\tau \geq 0.1 \text{ s}$ to tidally lock. For large $Q (> 10^7)$ and small $\tau (\tau < 0.1 \text{ s})$, weak tidal torques cannot prevent magnetic braking from spinning down stars past the tidally locked state, producing a population of subsynchronous rotators (red regions, $P_{\text{rot}} > P_{\text{orb}}$).

tend to rotate faster as they experience weaker tidal torques, and hence require longer to spin down towards the tidally locked state.

Both tidal models predict a population of nearly synchronous rotators near $P_{\text{orb}} \approx 60 \text{ d}$. This population corresponds to the evolution described in § 4.4.1 in which magnetic braking initially spins down stars past the tidally locked state, but in the long-term, tidal torques spin up the stars, shepherding them towards the tidally locked state. This process can keep stellar $P_{\text{rot}} \gtrsim P_{\text{eq}}$ for several Gyrs or longer, depending on the P_{orb} and Q or τ (see Fig. 4.4, § 4.4.2).

We isolate the impact of Q and τ on the spin-orbital state of tidally interacting stellar binaries by binning our CPL and CTL simulation results after 7 Gyr of evolution by P_{orb} and $P_{\text{orb}}/P_{\text{rot}}$ in Figures 4.6 and 4.7, respectively. In these figures, we estimate the typical strength of tidal torques, using Q and τ as a proxy, that can produce various spin-orbital states. For the CPL simulations depicted in Fig. 4.6, synchronous and supersynchronous rotators have systematically

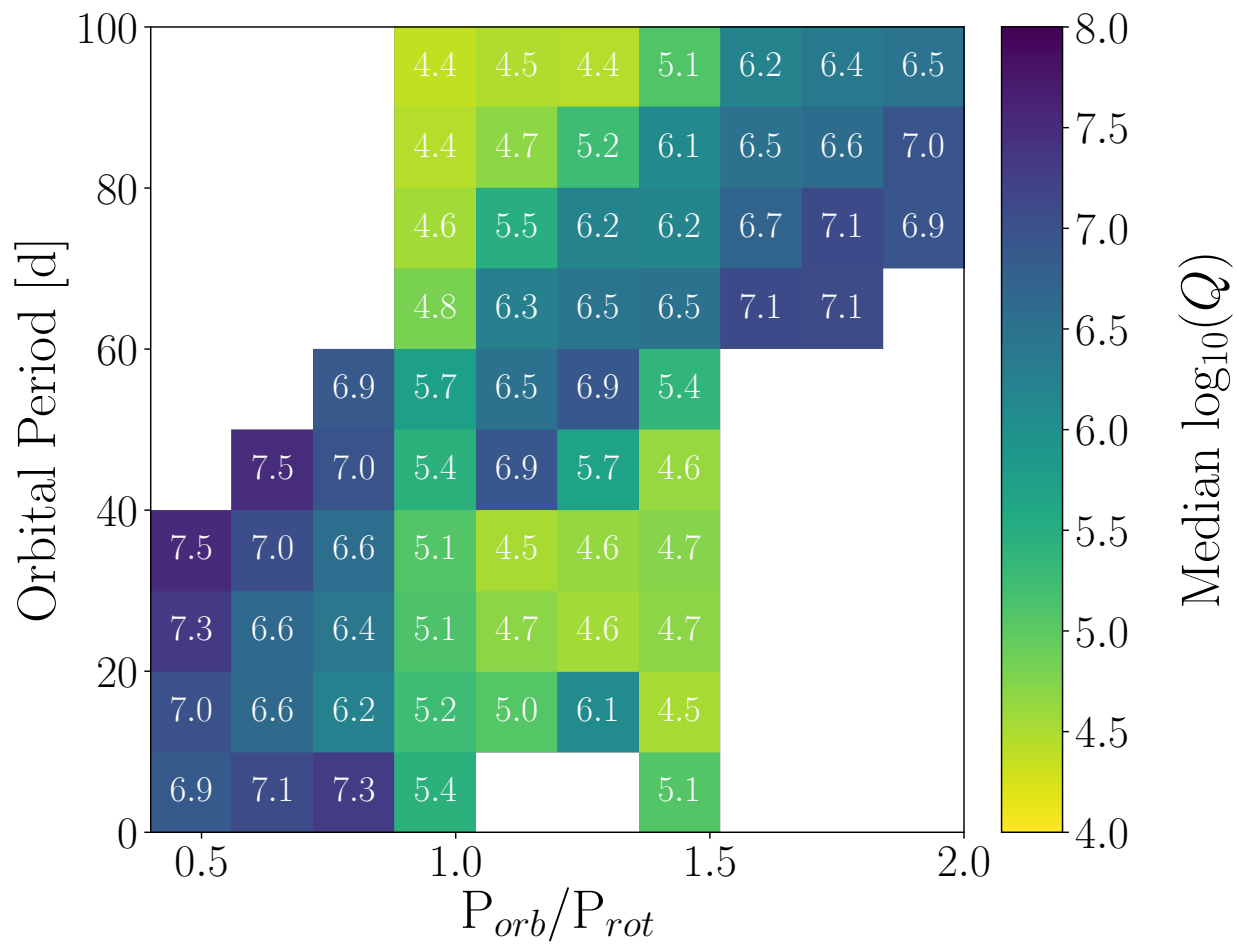


Figure 4.6: Median $\log_{10}(Q)$ of primary stars binned by P_{orb} and P_{orb}/P_{rot} evolved using the CPL model.

low Q s, typically $Q < 10^6$, as strong tidal torques are required to tidally lock these binaries. For $P_{orb} < 10$ d, there are no rotators with $1.0 < P_{orb}/P_{rot} < 1.5$, nor do any stars have $P_{orb}/P_{rot} > 1.5$ for $P_{orb} < 60$ d, as in the CPL model, binaries with eccentric orbits can only tidally lock into a 1:1 or 3:2 spin-orbit commensurability, see Eqn. (4.20).

Subsynchronous rotators have systematically larger Q s, typically $Q > 10^6$, and hence experience weak tidal torques that are dominated by magnetic braking. Subsynchronous rotation can occur under the CPL model for binaries with $P_{orb} < 50$ d. In this regime, the median Q tends to increase with decreasing P_{orb}/P_{rot} , except near the tidally locked state, as magnetic braking dominates weaker tidal torques, yielding longer P_{rot} . This trend reverses at longer $P_{orb} > 60$ d where supersynchronous rotation arises from the inability of tidal torques and magnetic braking to spin-down stars enough to approach the tidally locked state by the end of the simulation. In this case, the more supersynchronous the rotation, the weaker the tidal torques must be, and hence the larger the Q must be.

According to the CTL model simulations, depicted in Fig. 4.7, many binaries tidally lock for $P_{orb} \lesssim 20$ d when $\tau \gtrsim 0.1$ s, with some tidally locking up to $P_{orb} \approx 50$ d when $\tau \gtrsim 1$ s. Subsynchronous rotation typically occurs for stars with $\tau < 0.1$ s. Similar to the behavior depicted in Fig. 4.6, longer P_{rot} are produced by binaries with weaker tidal interactions since P_{orb}/P_{rot} decreases monotonically with τ for $P_{orb} < 40$ d. For $P_{orb} > 50$ d, magnetic braking dominates the evolution seen in the diagonal sequence with a median $\tau \approx 0.1$ s, a value that is typically insufficient for tides to strongly influence the evolution given the wide orbital separations. The shape of this diagonal region arises from the combination of magnetic braking and our flat initial P_{orb} distribution. In this P_{orb} regime, most binaries rotate supersynchronously as tides and magnetic braking fail to sufficiently spin down the stars by the age of the system. At longer P_{orb} , some binaries can strongly tidally-interact, but these systems require extreme tidal $\tau \gtrsim 10$ s. Unlike the CPL simulations depicted in Fig. 4.6, these binaries with $P_{orb} \approx 90$ d are not tidally locked as the tides are still not strong enough to lock the system. We explore this point further in § 4.4.3. We do not often observe $P_{orb}/P_{rot} \gtrsim 1.5$ as we only consider eccentricities up to $e = 0.3$, limiting how rapid supersynchronous systems can rotate according to Eqn. (4.22).

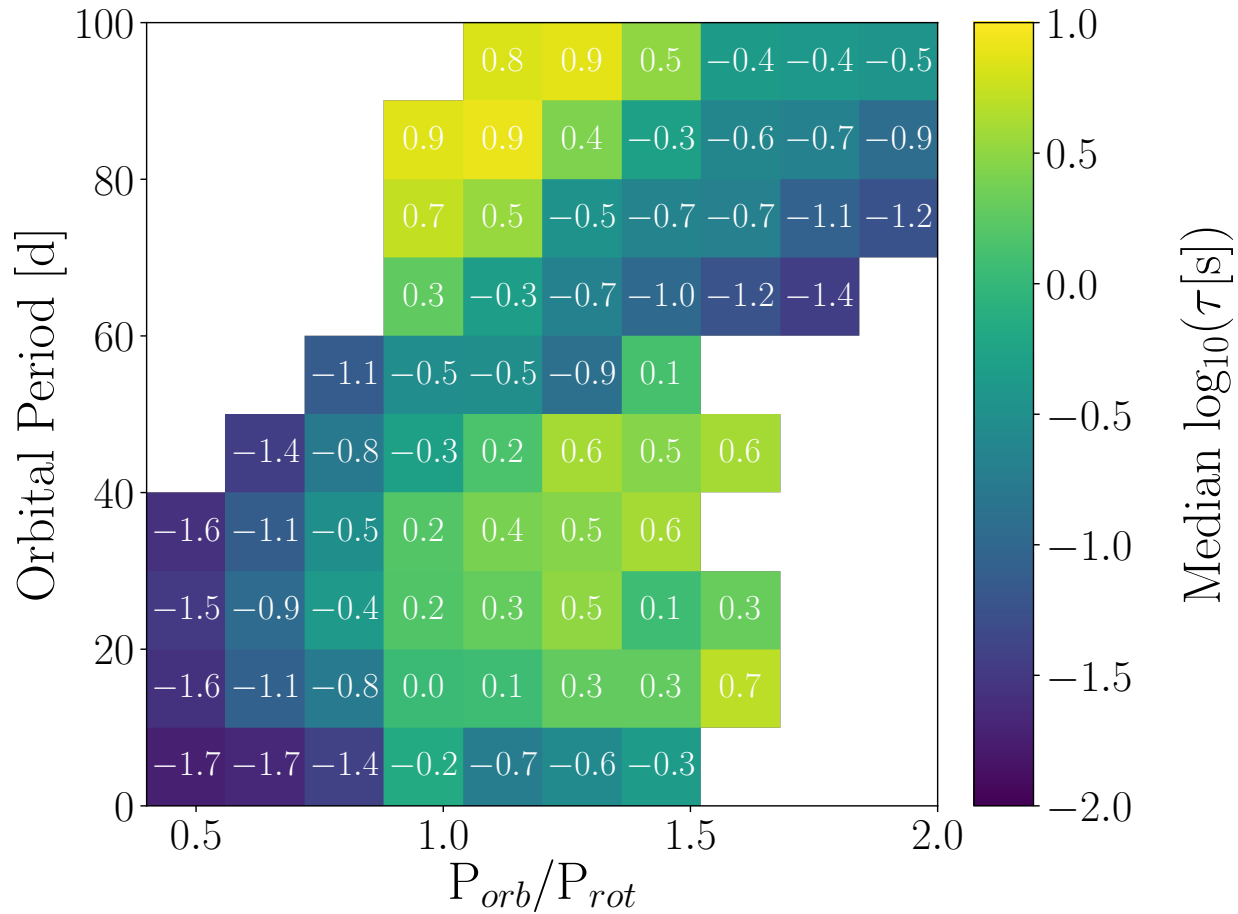


Figure 4.7: Same format as Fig. 4.6, but for $\log_{10}(\tau[\text{s}])$ under the CTL model.

Subynchronous Rotation at Short P_{orb}

As seen in Fig. 4.5, subsynchronous rotation can even occur for short P_{orb} binaries, where tidal-locking is the expectation, if the tidal torques are sufficiently weak. In Fig. 4.8, we examine subsynchronous rotation in short P_{orb} binaries by displaying the P_{rot} evolution for a $P_{orb} = 7.5$ d binary for various tidal dissipation parameters. Subsynchronous rotation occurs in general for weak tidal torques, $Q > 10^7$ or $\tau < 0.1$ s in these cases, and is not restricted to long P_{orb} binaries. Previous theoretical studies have also predicted subsynchronous rotation in short P_{orb} binaries arising from the balance between tidal torques and magnetic braking (e.g. Habets and Zwaan, 1989; Zahn, 1994; Keppens, 1997) suggesting that this behavior is not an artifact of our choice of tidal or magnetic braking models, but rather a general outcome of the competition between magnetic braking and tidal evolution in low-mass binaries. Short P_{orb} subsynchronous rotators can eventually tidally lock after several Gyrs, e.g. the $Q = 10^8$ case in Fig. 4.8, via the mechanism described above where tidal torques gradually strengthen relative to magnetic braking.

Short P_{orb} subsynchronous binaries exist in nature, such as many *Kepler* EBs (Lurie et al. (2017), see § 4.4.5 for further discussion), Kepler-47 (Orosz et al., 2012), EPIC 219394517 (Torres et al., 2018), and in “Binary 6211” observed by Meibom et al. (2006), suggesting that this theoretical observation is real and borne out in nature. Spin-orbit synchronization should therefore not be assumed for short P_{orb} binaries and sunsynchronous rotation should be expected in many tidally interacting binaries. We explore these effect further and compare our theory to observations of *Kepler* EBs in § 4.4.5.

4.4.3 P_{rot} Distribution of a Synthetic Population of Stellar Binaries

Here we examine how the competition between tidal torques and magnetic braking shape the P_{rot} distribution of low-mass stellar binaries. We consider two cases where tidal torques dominate: “Locked”, where $P_{rot} = P_{eq}$, and “Interacting”, where P_{rot} is within 10% of P_{eq} as in this regime, tides are likely shepherding P_{rot} towards the tidally locked state as we demonstrated in § 4.4.1. We refer to the remaining binaries as “not locked” as magnetic braking and stellar evolution likely

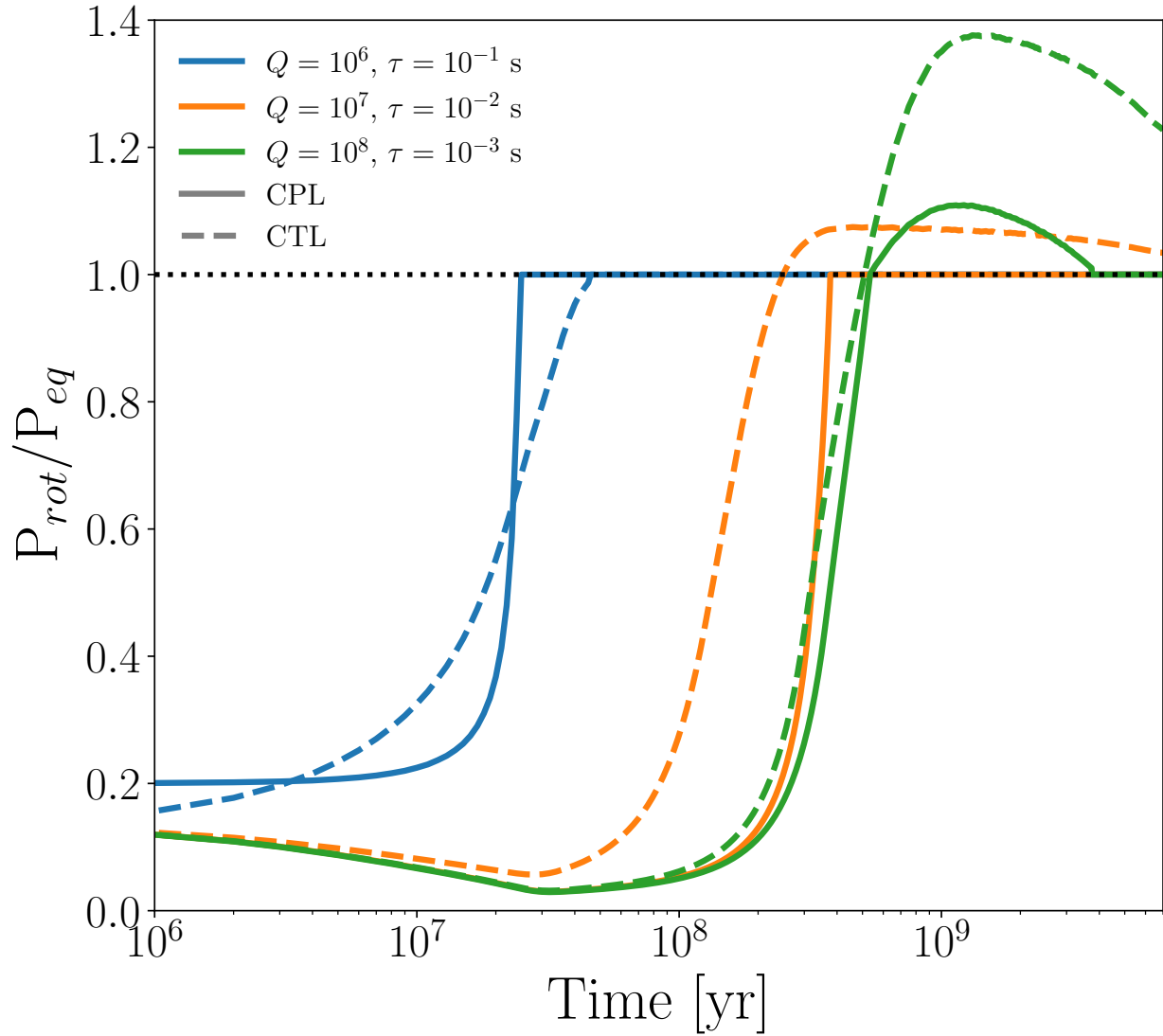


Figure 4.8: Evolution of stellar P_{rot} , normalized by P_{eq} (see Eqn. (4.20) and Eqn. (4.22)), for initial circular binary orbits with initial $P_{orb} = 7.5$ d according to the CPL (solid) and CTL (dashed) models for several values of Q and τ , respectively, using the Matt et al. (2015) magnetic braking model. Systems with strong tidal torques tidally lock, whereas in systems with weaker tidal torques (larger Q and smaller τ , respectively), magnetic braking initially overpowers tidal torques, spinning down the stars past the tidally locked state, resulting in subsynchronous rotation.

dominate their angular momentum evolution. In Fig. 4.9 and Fig. 4.10, we plot P_{rot} as a function of mass for the primary stars in stellar binaries for both the CPL and CTL model, respectively, integrated to system ages uniformly sampled over 1 – 7 Gyr, consistent with ages of stars in the *Kepler* field (Chaplin et al., 2014).

Both models predict a substantial population of tidally locked fast rotators with $P_{rot} \lesssim 20$ d, with tidally locked stars systematically rotating faster (median CPL, CTL $P_{rot} = 22.6$ d and 8.8 d) than not locked (median CPL, CTL both $P_{rot} = 32.4$ d) binaries. The CTL model predicts that the majority of tidally locked binaries, 83%, lock into rapid rotation with $P_{rot} \lesssim 20$ d, typically in short P_{orb} binaries where tidal torques are strongest. The CPL model, however predicts that binaries can tidally lock into a wide range of rotation states as only 46% of locked binaries have $P_{rot} < 20$ d, while the rest can lock out to $P_{rot} \approx 100$ d in long P_{orb} binaries. More massive stars are more likely to tidally lock compared to less massive stars as tidal torques scale with the stellar masses and as R^5 , with R increasing with stellar mass. This feature is seen in the enhanced density of locked systems at larger masses for both tidal models, but in particular for the CPL model. We highlight this enhanced density of locked binaries in systems with more massive primaries in the marginalized mass distributions in the top panels of Fig. 4.9 and Fig. 4.10.

The interacting population tends to rotate more slowly than the not locked population as at short P_{orb} , and hence P_{rot} , binaries preferentially tidally lock due to stronger tidal torques. At longer P_{orb} , weaker tidal torques allow magnetic braking to spin down the stars past P_{eq} , with tidal torques eventually strengthening enough to shepherd P_{rot} towards P_{eq} via the mechanism discussed in § 4.4.1. The CPL and CTL models predict that 31% and 24% of stars, respectively, are either tidally locked or interacting, demonstrating that tidal torques play a pivotal role in shaping the angular momentum evolution in stellar binaries across a wide range of parameters. The P_{rot} - mass distribution for not locked binaries resembles the single star sequence as magnetic braking and stellar evolution dictate their angular momentum evolution.

Tidal locking is not limited to $P_{orb} \lesssim 20$ d, however, as we find stellar binaries can tidally lock over a wide range of P_{rot} up to $P_{rot} = P_{orb} \approx 100$ d according to the CPL model, producing a slow-rotating population above the P_{rot} distribution envelop of solar-mass single stars. This

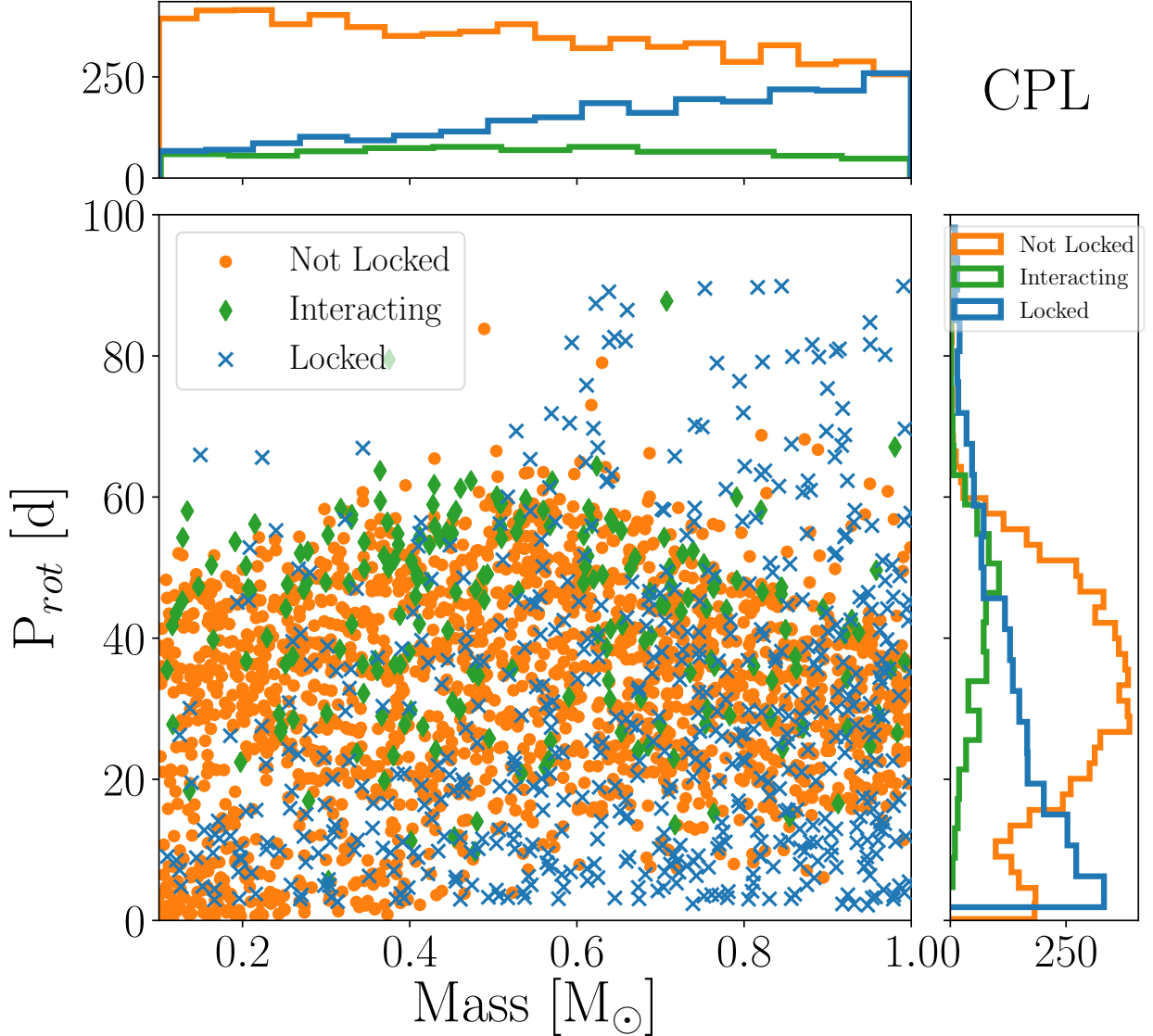


Figure 4.9: Rotation state for tidally locked (blue, $P_{rot} = P_{eq}$), interacting (green, P_{rot} within 10% of P_{eq} and not locked), and not locked (orange, remainder of binaries) stellar binaries. Left: P_{rot} as a function of stellar mass and age according to our CPL simulations integrated to system ages uniformly sampled over 1 – 7 Gyr. Right: Marginalized P_{rot} distribution for each case. Top: Marginalized mass distributions.

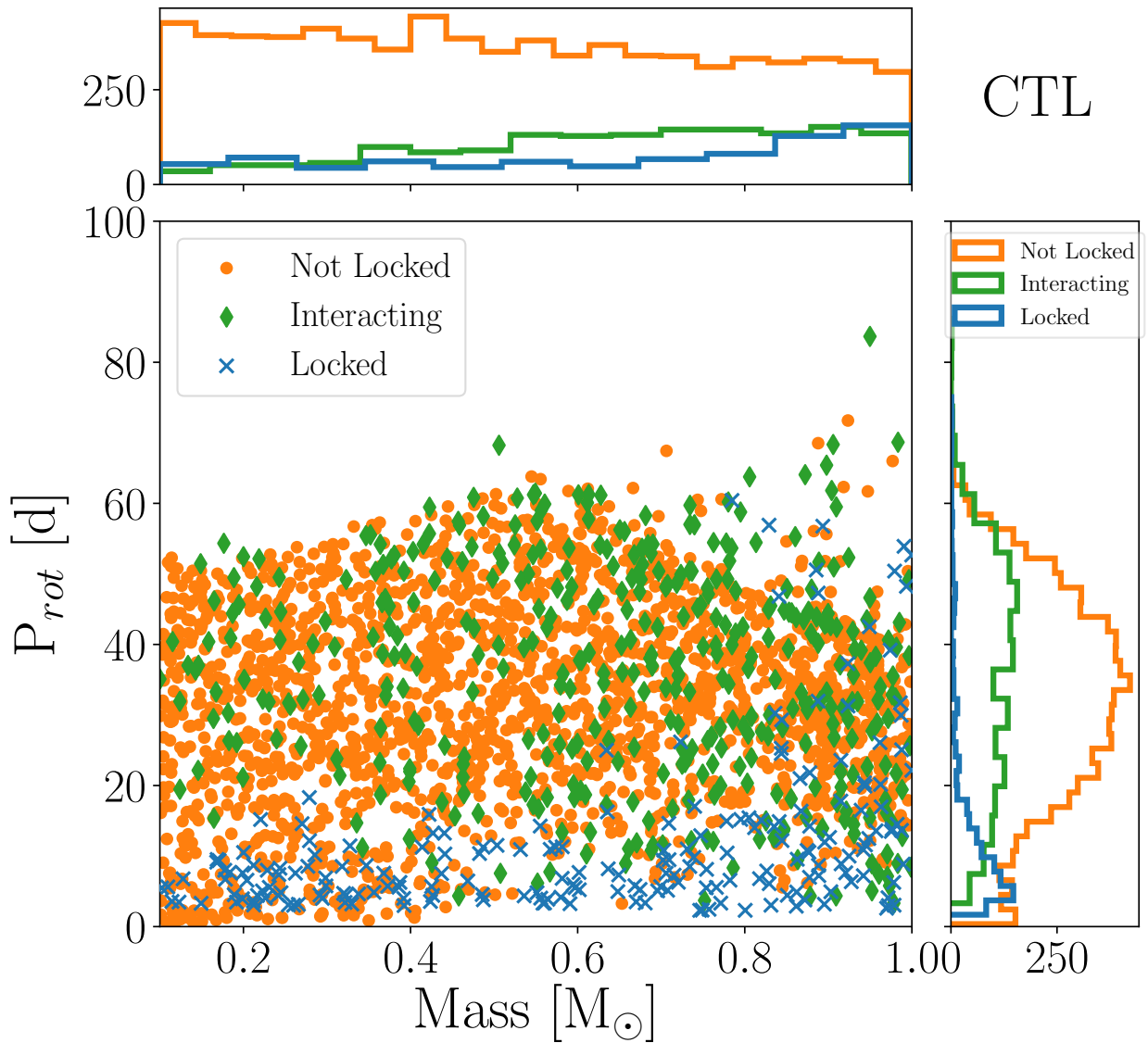


Figure 4.10: Same format as Fig. 4.9, but for the CTL simulations.

behavior is consistent with observations of P_{rot} in *Kepler* eclipsing binaries by Lurie et al. (2017) who find tentative evidence that binaries can tidally lock up to their detection limit of $P_{orb} = P_{rot} = 45$ d. Under the CTL model, however, binaries predominantly tidally lock out to only $P_{orb} \approx 20$ d, although binaries with more massive primaries can occasionally lock, or at least tidally-interact, out to $P_{orb} \approx 80$ d. We highlight this behavior with a histogram of locked and interacting binaries over P_{rot} for both tidal models in Fig. 4.11. The CTL model predicts fewer tidally locked binaries at longer P_{rot} , concentrating most of the locked CTL distribution's density at short P_{rot} , whereas the CPL distribution has a heavy tail extending towards longer P_{rot} . The CPL model, however, predicts larger tidal-locking rates than the CTL model as seen in the enhanced numbers of tidally locked binaries at low P_{rot} Fig. 4.9 compared with Fig. 4.10. The presence of $P_{orb} > 20$ d locked population, or lack thereof, could be a powerful observational discriminant between which equilibrium tidal model acts in low-mass stellar binaries. We discuss this point further in § 4.4.6.

4.4.4 Deviations From Single Star P_{rot} Evolution: Implications for Gyrochronology

We compare the P_{rot} and age distributions of tidally interacting stellar binaries from our CPL and CTL simulations with that of single stars to gauge the impact of tidal torques on driving P_{rot} distributions away from that of single stars and what implications that may have for estimating stellar ages using gyrochronology. We simulate 10,000 single star systems according to the evolution described in § 4.2.1 with initial conditions sampled from the same mass and P_{rot} distributions used for the binary simulations described § 4.2. In Fig. 4.12, we display P_{rot} as a function of mass and age for binaries simulated using both the CPL and CTL model and for single stars.

In binaries, tidal torques tend to drive the P_{rot} evolution away from that of single stars and towards P_{eq} , either maintaining rapid rotation in tidally locked short P_{orb} systems, or working with magnetic braking to slow P_{rot} beyond that of single stars of the same age. The impact of tidal torques on the binary P_{rot} distribution is clear: strong tidal torques in short P_{orb} binaries produce a substantial population of rapid rotators with $P_{rot} \lesssim 20$ d. Except for stars with ages $\lesssim 1$ Gyr, or young late M-dwarfs who are either contracting along the pre-main sequence or have just reached

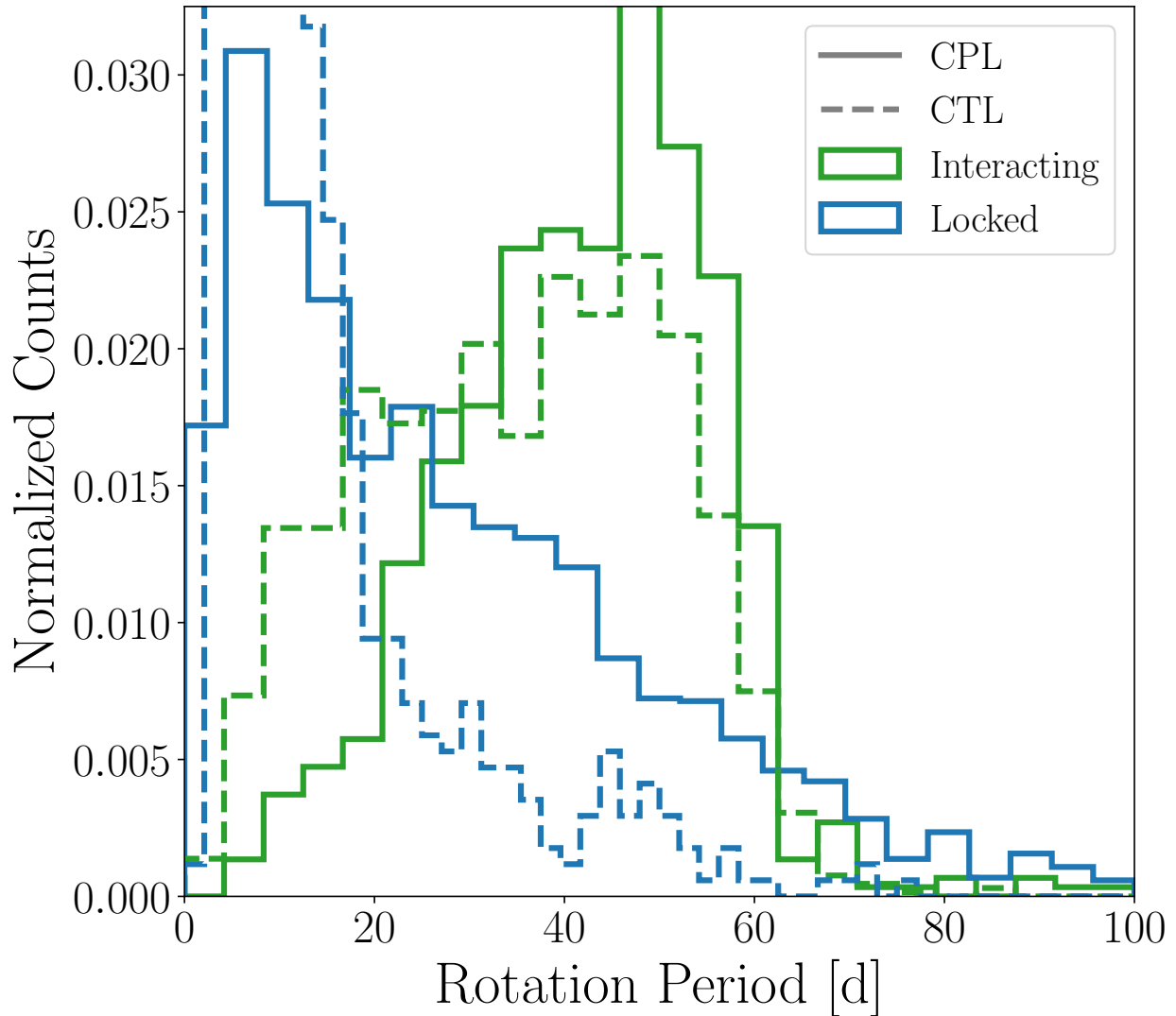


Figure 4.11: P_{rot} distribution for tidally locked (blue) and interacting (green, P_{rot} within 10% of P_{eq} and not locked) binaries according to the CPL (solid line) and CTL (dashed line) models.

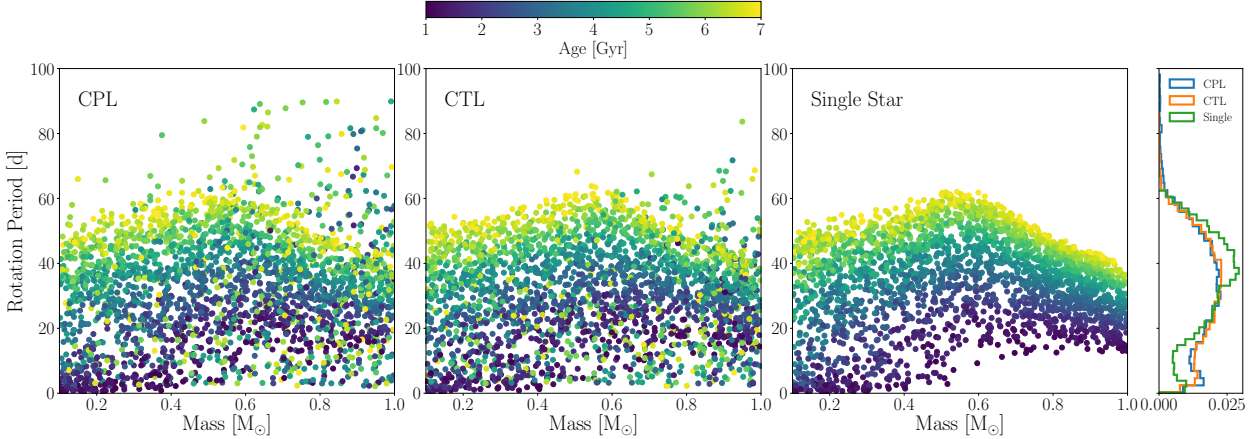


Figure 4.12: P_{rot} as a function of stellar mass and age according to our CPL (left), CTL (left center), and single star (right center) simulations integrated to system ages uniformly sampled over 1 – 7 Gyr using the Matt et al. (2015) magnetic braking model. For each case, we only plot 2,500 systems for clarity but account for all systems when computing the marginalized distributions. Right: The P_{rot} distribution for each case, marginalized over stellar mass.

the main sequence, our single star simulations fail to produce a population of rapid rotators. This theoretical result is consistent with Simonian et al. (2018) who find that the population of *Kepler* stars with $P_{rot} < 7.5$ d is likely dominated by tidally interacting binaries. The influence of tides extends to longer P_{orb} systems producing a slowly-rotating population above the upper envelope of the single star sequence for $M \gtrsim 0.6 M_{\odot}$, e.g. Fig. 4.9 and Fig. 4.10, and is a population that single-star models fail to produce.

In the single star population, there is a clear monotonic relation between P_{rot} and age, with older stars rotating more slowly, a trend that is borne out in nature and is the critical assumption of gyrochronology methods that link P_{rot} to stellar ages via the magnetic braking-driven long-term spin down of low-mass stars (e.g. Skumanich, 1972; Barnes, 2003, 2007; Mamajek and Hillenbrand, 2008; Barnes, 2010; Meibom et al., 2015). This trend is a generic outcome of magnetic braking and is not specific to our choice of magnetic braking model. In stark contrast, both tidal models predict that age does not always strongly correlate with P_{rot} as tidally interacting binaries, at a given primary star mass and P_{rot} , can assume a wide range of ages, especially for $P_{rot} \lesssim 20$ d.

We quantify the impact of binarity on gyrochronology age estimates in Fig. 4.13 by computing

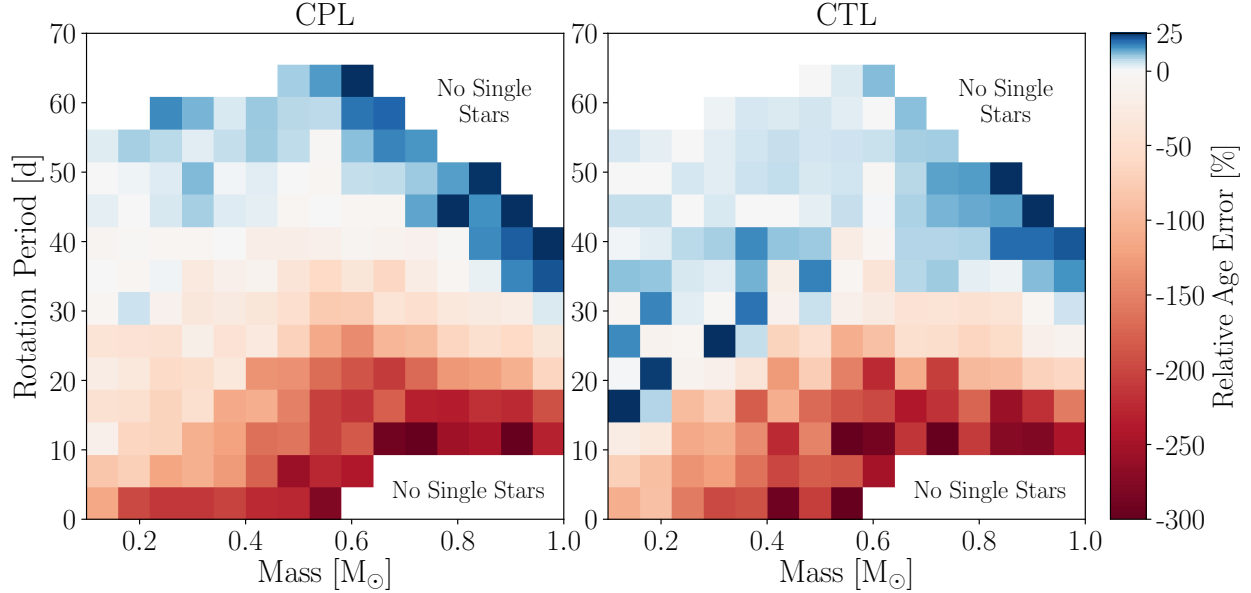


Figure 4.13: Relative age error between single and binary stars for both the CPL (left) and CTL (right) tidal models. The error is computed as the percent difference between the mean ages of single and tidally interacting binary stars in mass and P_{rot} bins.

the percent difference between the mean ages of single and binary stars, for both tidal models, in mass and P_{rot} bins for the populations depicted in Fig. 4.12. This quantity, referred to here as the “Relative Age Error”, represents the systematic error incurred by assigning a tidally interacting binary star the age expected for single stars at a given mass and P_{rot} . For this comparison, we select the subset of tidally locked and tidally interacting binaries as classified in Fig. 4.9 and Fig. 4.10.

For most values of P_{rot} , gyrochronology methods systematically underestimate the ages of tidally interacting binaries, with the relative age error increasing with decreasing P_{rot} and increasing with primary star mass. For binaries with $P_{rot} \lesssim 30$ d, gyrochronology ages are underestimated by 50%, with this error growing to 300% for $P_{rot} \approx 10$ d. For slow rotators with $P_{rot} \gtrsim 40$ d, gyrochronology ages are slightly overestimated by up to 25%, with the largest errors occurring for near solar-mass primary stars where tides and magnetic braking combine to spin down binary stars. The relative age errors would be more pronounced for the most rapidly-rotating stars, e.g. tidally interacting near-solar mass binaries with $P_{rot} \lesssim 10$ d, however, our single star-only models fail to

produce such rotation states.

The age distribution of binaries with $P_{rot} < 20$ d is inconsistent with that of single stars. In this range, the median ages and 68% interval are $2.3^{+2.9}_{-0.9}$ Gyr and $2.4^{+3.0}_{-1.1}$ Gyr according to the CPL and CTL models, respectively, compared to the much younger single stars with ages of $1.6^{+0.8}_{-0.4}$ Gyr. We highlight this dichotomy in Fig. 4.14 by plotting a histogram of system ages from Fig. 4.12 for single or primary stars in binaries with $P_{rot} < 20$ d.

Tidal torques pose a fundamental problem for inferring ages of stars via gyrochronology. Regardless of the choice of equilibrium tidal model or magnetic braking model, stellar binaries readily tidally lock, or at least strongly tidally-interact, across a wide range of P_{orb} and primary star masses, decoupling P_{rot} from age. For example, if one observed a rapidly rotating star with $P_{rot} \lesssim 20$ d, gyrochronology models would predict ages $\lesssim 1.6$ Gyr. If the star is actually an unresolved binary, as could be the case for many *Kepler* rapid rotators (Simonian et al., 2018), it would likely be tidally locked, decoupling P_{rot} from age, causing the predictions of gyrochronology models to fail. This effect is most likely to manifest in rapid rotators ($P_{rot} < 20$ d), but persists across all P_{rot} up to 100 d, producing a contaminating signal, e.g. Fig. 4.12 and Fig. 4.13.

In general, it is difficult to accurately determine if a source is single star or a stellar binary via longterm photometric monitoring, e.g. via *Kepler* or *TESS*, as only a small fraction of stars in binaries will occult one another. Observations of the binarity of field stars by Raghavan et al. (2010) and Duchêne and Kraus (2013) indicate that roughly half of stars are in stellar binaries, with 10% of these binaries having $P_{orb} \lesssim 100$ d, suggesting that unless one accounts for binarity, stellar binaries will produce a contaminating signal in any study of stellar rotation periods and any ages inferred via gyrochronology are potentially subject to systematic errors. Moreover, this problem could be more significant as Simonian et al. (2018) found that most rapid rotators with $P_{rot} \leq 7.5$ d in the *Kepler* field are consistent with tidally-synchronized photometric binaries, suggesting that binary contamination in P_{rot} studies could be widespread. We caution that any application of gyrochronology methods to predict ages for stars, especially those with $P_{rot} \lesssim 20$ d, should rule out or account for stellar binarity, or otherwise risk deriving systematically incorrect ages. Tidal torques do not just produce spin-orbit synchronization at short P_{orb} , but can produce a rich variety

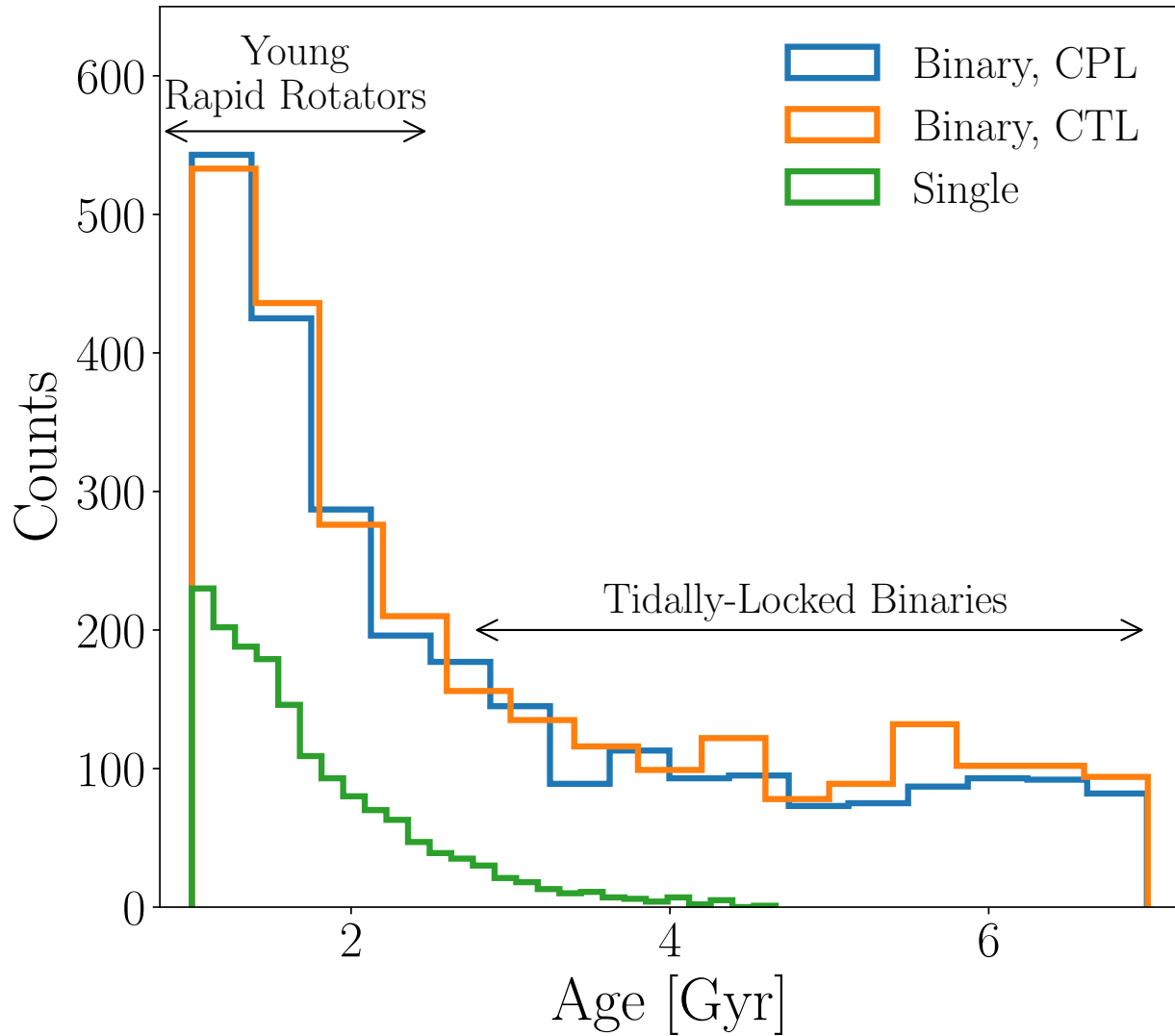


Figure 4.14: Histogram of rapidly-rotating ($P_{rot} < 20$ d) star ages for single and primary stars in binaries from Fig. 4.12. Rapidly-rotating single stars must be young (ages $\lesssim 2$ Gyr), while tidally locked rapidly-rotating binaries exhibit a wide range of ages.

of rotation states that deviate from the expected long-term spin-down experienced by single stars, e.g. Fig. 4.6 and Fig. 4.7. We recommend that the application, or calibration, magnetic braking models to a sample of stellar rotation periods control for binarity.

4.4.5 Comparison to *Kepler*

We compare our simulation results to P_{rot} measurements of primary stars in *Kepler* low-mass eclipsing binaries by Lurie et al. (2017) to gauge if our model predictions, which by design populate a wide, but physically-plausible, region of parameter space, can reproduce features observed in the data. Lurie et al. (2017) measured 816 rotation periods for primary stars in *Kepler* EBs with star spot modulations and visually inspected each light curve to ensure their accuracy. The Lurie et al. (2017) dataset is the largest homogenous set of P_{rot} measurements available for low-mass stellar binaries and represents the state of the art benchmark for studies of the influence of tides on P_{rot} in stellar binaries. We compare our results to the $P_{1,min}$ P_{rot} values reported by Lurie et al. (2017) as the authors demonstrated that these values are likely to be close to the equatorial P_{rot} that we track in our simulations. In Fig. 4.15, we display P_{orb}/P_{rot} as a function of P_{orb} for both the CPL and CTL models where each simulation was integrated to an age uniformly sampled over 1 – 7 Gyr, consistent with ages of *Kepler* field stars (Chaplin et al., 2014).

Qualitatively, the CTL model appears to do a better job of reproducing features seen in the Lurie et al. (2017) data than the CPL model. The CPL model, for example, cannot produce the observed cluster of supersynchronous rotators with $P_{orb}/P_{rot} \lesssim 1.2$ for $P_{orb} < 10$ d whereas the CTL model can. Instead, owing to the its discrete P_{eq} , the CPL model predicts that all tidally locked supersynchronous rotators lie on the line $P_{orb}/P_{rot} = 1.5$. This prediction is inconsistent with the data as no obvious spin-orbit commensurability, aside from 1:1 synchronization, is present in the Lurie et al. (2017) data, likely because stellar convective envelopes lack a fixed shape, making resonant coupling difficult unless it occurs with internal gravity or pressure modes (Burkart et al., 2014; Lurie et al., 2017). Neither model reproduces the very supersynchronous, $P_{orb}/P_{rot} > 1.6$, binaries in the Lurie et al. (2017) data as they typically have orbital eccentricities in excess of 0.3 and are outside of the region of parameter space we consider. The CTL model, however, could in

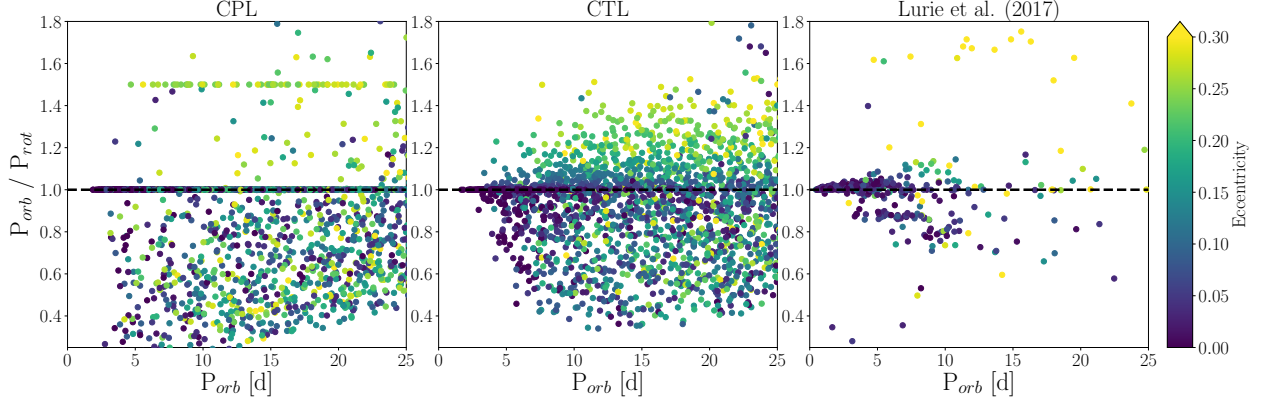


Figure 4.15: P_{orb}/P_{rot} as a function of P_{orb} according to the CPL model (left) and the CTL model (middle), and Lurie et al. (2017) *Kepler* EB observations (right). All points are colored by e . In the right panel, the *Kepler* EBs at low P_{orb} and low P_{orb}/P_{rot} are likely either brown dwarfs or exoplanets (Lurie et al., 2017), and hence are not modeled by our simulations, so we do not consider them, but we display them for completeness.

principle reproduce these points if they are tidally locked binaries as its P_{eq} is a continuous function of e and is applicable for large e , in contrast to the discrete P_{eq} predicted by the CPL model that is valid for smaller e . Both tidal models predict that nearly all binaries with $P_{orb} < 4$ d have circularized orbits and synchronized spins due to strong tidal torques at short stellar separations, in agreement with the Lurie et al. (2017) observations. At very short P_{orb} , in the absence of a perturbing tertiary companion, circularization and synchronization is the inevitable end state for low-mass binaries (Counselman, 1973).

For $P_{orb} \gtrsim 4$ d, our models produce a substantial number of subsynchronous rotators. Although Lurie et al. (2017) argues that differential rotation creates the subsynchronous population, we find that the competition between weak tidal torques and magnetic braking described in § 4.4.1 naturally produces this population. The CPL model, however, struggles to populate the prominent cluster of subsynchronous rotators at $P_{orb}/P_{rot} \approx 0.9$ for $P_{orb} < 10$ d observed by Lurie et al. (2017). Lurie et al. (2017) find that 15% of their sample with $2 < P_{orb} < 10$ days has $P_{orb}/P_{rot} \in [0.84, 0.92]$, compared with 8% of our CTL population and only 2% of the CPL population.

Both models predict a large number of extremely subsynchronous rotators with $P_{orb}/P_{rot} < 0.7$

across all P_{orb} that is not present in the Lurie et al. (2017) data. Magnetic braking creates the lower limit of this subsynchronous population, a line of nearly constant $P_{rot} \approx 60$ d set by how much a star can spin down over 7 Gyr, the longest age considered in our simulations. Our choice of prior distributions for both Q and τ permit very weak tidal interactions that likely gives rise to this population and suggests that our prior does not reflect the underlying distribution of stellar tidal parameters in nature. Alternatively, the data could be incomplete where our models predict slowly-rotating subsynchronous rotators as the photometric amplitude of star spot modulations tends to decrease with increasing P_{rot} , making reliable rotation periods difficult to detect (McQuillan et al., 2014; Lurie et al., 2017; Reinhold et al., 2018).

Although the CTL model seems to better reproduce the Lurie et al. (2017) data, both tidal models can reproduce features observed in the *Kepler* EB distribution, e.g. the synchronized population and subsynchronous rotators, suggesting that our models reasonably approximate the dynamical interactions of tidally-evolving, low-mass stellar binaries. Our comparison between theory and observations is limited, however, because the Lurie et al. (2017) P_{rot} data lack uncertainties and Lurie et al. (2017) approximated the EB orbital e via transit durations and ingress/egress times, potentially leading to inaccurate e determinations. Unconstrained biases in the data, e.g. the lack of long P_{orb} binaries, further inhibit our ability to compare our predictions with the data. Moreover, our prior distributions were chosen to be plausible, but wide, in order to examine our model predictions over parameter space and are not suited for a robust statistical inference to select between which equilibrium tidal model best describes tidal interactions in low-mass binary stars. Below, we offer observational tests that could discriminate between models.

4.4.6 CPL or CTL?

Accurate measurements of P_{rot} and e , especially out to long P_{orb} , can potentially discriminate between which equilibrium tidal model best describes tidal interactions in low-mass stellar binaries. Here, we outline three observational tests that can discriminate between the two models. The first test considers binaries with $P_{orb} < 10$ d that are likely tidally locked on eccentric orbits, but with $e < 0.23$. In this e regime, the CPL model predicts that the majority of systems are tidally locked

into synchronous rotation and does not permit a supersynchronous rotation state, e.g. Eqn. (4.20). The CTL model, however, predicts a continuum of supersynchronous rotators on eccentric orbits, e.g. Eqn. (4.22). Supersynchronous rotation that is not due to tidal interactions can occur in extremely young, rapidly rotating systems that are still contracting along the pre-main sequence, or that have recently reached the main sequence. These young, supersynchronous rotators are unlikely to be tidally locked, usually have $P_{orb}/P_{rot} > 1.5$, and do not stay supersynchronous for long given that solar mass pre-main sequence lifetimes are $\lesssim 100$ Myr, distinguishing them from tidally locked binaries (see Fig. 4.15). If supersynchronous rotation is observed in binaries with $P_{orb} < 10$ d, $P_{orb}/P_{rot} < 1.5$, and $0 < e \lesssim 0.23$, it is evidence in favor of the CTL model over the CPL model.

Second, for tidally locked binaries with $e > 0.23$, the CPL model predicts supersynchronous rotation in the form of a 3:2 spin-orbit comensurability, e.g. the line at $P_{orb}/P_{rot} = 1.5$ seen in the left panel of Fig. 4.15, and no other spin state is permitted, compared to the continuum of supersynchronous rotation states in eccentric tidally locked rotators predicted by the CTL model. If a substantial clustering of stellar binaries with $P_{orb}/P_{rot} = 1.5$ is observed, it would be strong evidence in favor of the CPL model, but there is no obvious clustering of *Kepler* EBs near any spin-orbit resonance. These two tests can fail to discriminate between the CPL and CTL model, however, if the CPL model P_{eq} is a continuous function of e , e.g. Eqn. (4.21), as was argued by Goldreich (1966) and derived by Murray and Dermott (1999). In such a case, one would need a large number of accurate and precise measurements P_{orb} and e , with robust uncertainties, for tidally interacting binaries to discriminate between the CPL and CTL continuous P_{eq} , e.g. Eqn. (4.21) versus Eqn. (4.22). In practice, this is extremely observationally expensive as it requires extensive photometric and spectroscopic observations of many binaries.

A third test, the detection of tidally locked binaries with solar-mass primaries and $P_{rot} \gtrsim 60$ d, would provide strong evidence in favor of the CPL model as the CTL model cannot tidally lock stars beyond $P_{orb} \approx 60$ d, regardless of τ , e.g. Fig. 4.10. The CPL model, however, can tidally lock binaries out to $P_{orb} \gtrsim 90$ d. We recommend observers try to measure P_{rot} and e in binaries out to $P_{orb} = 100$ d to test this hypothesis, but we note that detecting P_{rot} for such slow rotators can be difficult due to small star spot modulation amplitudes (McQuillan et al., 2014; Lurie et al., 2017;

Reinhold et al., 2018). Long term spectroscopic monitoring may be warranted in such cases.

4.5 Discussion

In this work, we probed the long-term angular momentum evolution of low-mass stellar binaries, with a focus on P_{rot} in short and intermediate P_{orb} binaries. We considered the impact of two common equilibrium tidal models, magnetic braking, and stellar evolution. We performed a large suite of simulations for binaries with physically-motivated initial conditions out to $P_{orb} = 100$ and across a wide range of tidal dissipation parameters to examine the competition between tidal torques and magnetic braking for controlling the stellar P_{rot} evolution.

In our simulations, nearly all binaries with $P_{orb} \lesssim 4$ d have tidally-synchronized spins and circularized orbits, in good agreement with observations of *Kepler* EBs and binaries in the field. We showed for $P_{orb} \gtrsim 4$ d, primary stars in stellar binaries can rotate subsynchronously for Gyrs due to the competition between tidal torques and magnetic braking, or supersynchronously if they tidally lock on eccentric orbits. Our predictions are not strongly dependant on the choice of magnetic braking model, but rather are generic outcomes of the interaction between magnetic braking and tidal torques. Both the CPL and CTL equilibrium tidal models predict that binaries tidally-interact at longer P_{orb} than have previously been considered, out to $P_{orb} \approx 60 - 100$ d. Many binaries with $P_{orb} \lesssim 20$ d tidally lock according to both models, in good agreement with previous results, but the CPL model predicts that binaries can readily tidally lock out to $P_{orb} \approx 100$ d. Tidal interactions can cause P_{rot} evolution in stellar binaries to differ from the long-term spin down due to magnetic braking experienced by single stars, decoupling P_{rot} from age. In tidally interacting binaries, gyrochronology, the technique of linking stellar P_{rot} to age, likely fails, potentially underestimating stellar ages by up to 300%. We caution that any application of gyrochronology methods to stars, especially those with $P_{rot} \lesssim 20$ d, should account for the possibility of stellar binarity to prevent deriving incorrect ages.

We compare the predictions of both the CPL and CTL models with observations of P_{rot} and P_{orb} of *Kepler* EBs by Lurie et al. (2017) and find that both can qualitatively reproduce many features seen in the data, validating our approach and suggesting that equilibrium tidal models

can accurately model stellar-tidal evolution in low-mass stellar binaries. The lack of uncertainties on P_{rot} , the approximate orbital eccentricities derived by Lurie et al. (2017), and unconstrained completeness estimates prevent us from discriminating between which tidal model best describes tidal torques in low-mass binaries and from inferring tidal properties of low-mass stars given the *Kepler* EB data.

We described three observational tests that can distinguish between which equilibrium tidal model better describes tidal interactions in low-mass stellar binaries. We primarily suggest that observers measure stellar P_{rot} in binaries with solar-mass primaries for P_{orb} between $60 - 100$ d. If any tidally locked binaries are identified at long P_{orb} , this would be evidence in favor of the CPL model as we found that only binaries tidally interacting via the CPL model could tidally lock at such long P_{orb} . At shorter P_{orb} , precise measurements of P_{rot} and binary e and P_{orb} could distinguish between the CPL and CTL model in tidally locked systems, e.g. identifying if P_{eq} follows Eq. (4.20) vs. Eq. (4.22), especially if the CPL P_{eq} is in fact a discrete function of e . The observations required by these tests, however, are non-trivial. Beyond these tests, our model could be used to infer the tidal properties of binary stars, perhaps in a Markov Chain Monte Carlo framework, by directly comparing simulation results with the observed stellar and orbital properties, given the observational uncertainties and reasonable prior probability distributions for parameters like the initial binary e . This analysis, however, is beyond the scope of this work and we leave it for future endeavors.

Our theoretical predictions outline a critical point: one cannot simply observe a short P_{orb} binary on a circular orbit and assume synchronization, nor can one observe a binary with $P_{orb} \gtrsim 20$ d and assume that tides have not impacted that system's angular momentum evolution. Stellar-tidal interactions can produce synchronous and subsynchronous rotation for short P_{orb} binaries on circular orbits, e.g. Fig. 4.4, depending on the age of the system, e.g. Fig. 4.8, and the strength of tidal dissipation, e.g. Fig. 4.6 and Fig. 4.7. Understanding the long-term angular momentum evolution of stellar binaries out to $P_{orb} = 100$ d requires detailed modeling of its coupled-stellar tidal evolution, and characterizing tidal dissipation parameters. Many new eclipsing stellar binaries will be discovered by TESS (e.g. Sullivan et al., 2015; Matson et al., 2018) and in analysis of K2

data. Obtaining precise orbital and rotational constraints for stellar binaries will permit detailed characterization of tidal interactions between low-mass stars and shed light into the long-term angular momentum evolution in stellar binaries.

4.6 Acknowledgments

We thank the anonymous reviewer for helpful comments that improved the quality of this manuscript. This work was facilitated through the use of advanced computational, storage, and networking infrastructure provided by the Hyak supercomputer system and funded by the Student Technology Fund at the University of Washington. DPF was supported by NASA Headquarters under the NASA Earth and Space Science Fellowship Program - Grant 80NSSC17K0482. RB acknowledges support from the NASA Astrobiology Institute's Virtual Planetary Laboratory under Cooperative Agreement number NNA13AA93A. JRAD acknowledges support from the DIRAC Institute in the Department of Astronomy at the University of Washington. The DIRAC Institute is supported through generous gifts from the Charles and Lisa Simonyi Fund for Arts and Sciences, and the Washington Research Foundation.

Software: matplotlib: Hunter (2007), numpy: van der Walt et al. (2011), pandas: McKinney (2010), VPNet: Barnes et al. (2019)

4.7 Analytic Torque Balance

Here we derive the equation for the stellar P_{rot} at which tidal torques balance magnetic braking discussed in § 4.4.1. As in § 4.4.1, we assume that both stars have $M = 1M_\odot$, 0 obliquity, and we assume a circular binary orbit. We assume that the torque balance occurs while the stars are on the main sequence, where stellar properties change slowly, so the angular momentum evolution is controlled by the balance between tidal torques and magnetic braking, not stellar radius contraction. Under this assumption, we can set $R = 1R_\odot$ and assume constant moments of inertia. For simplicity, we assume that magnetic braking proceeds under the Matt et al. (2015) model and the CTL model describes tidal torques.

As discussed in § 4.4.1, both stars are in the unsaturated rotation regime, so the torque due to magnetic braking is given by Eqn. (4.2), which under the aforementioned assumptions, reduces to

$$\frac{dJ}{dt} \Big|_{MB} = -C_{MB} \left(\frac{P_{rot,\odot}}{P_{rot}} \right)^3 \quad (4.25)$$

where $P_{rot} = 2\pi/\omega$ and $C_{MB} = 6.3 \times 10^{30}$ ergs (Matt et al., 2015, 2019).

Under the CTL model and our assumptions, the change in rotation rate due to tidal torques, Eqn. 4.16, reduces to

$$\frac{d\omega}{dt} \Big|_{tides} = \frac{P_{orb} Z_{CTL}}{2\pi M r_g^2 R^2} \left(1 - \frac{P_{orb}}{P_{rot}} \right) \quad (4.26)$$

where $P_{orb} = 2\pi/n$. For fixed moment of inertia, $dJ/dt = I d\omega/dt$, and after inserting Eqn. 4.18 for Z_{CTL} , the tidal torque on the stellar rotations becomes

$$\frac{dJ}{dt} \Big|_{tides} = \frac{C_{tides} k_2 \tau}{P_{orb}^5} \left(1 - \frac{P_{orb}}{P_{rot}} \right). \quad (4.27)$$

where $C_{tides} = 24\pi^5 R_\odot^5/G$.

The torques due to tides and magnetic braking balance when $\frac{dJ}{dt}|_{tides} + \frac{dJ}{dt}|_{MB} = 0$,

$$\frac{C_{tides} k_2 \tau}{P_{orb}^5} \left(1 - \frac{P_{orb}}{P_{rot}} \right) - C_{MB} \left(\frac{P_{rot,\odot}}{P_{rot}} \right)^3 = 0. \quad (4.28)$$

By specifying P_{orb} and $k_2 \tau$, we can numerically solve Eqn. (4.28) for the P_{rot} at which torques due to magnetic braking and tides balance, often producing subsynchronous rotation as seen in Fig. 4.3 and our simulations in § 4.4.1.

Chapter 5

BAYESIAN INFERENCE WITH SLOW MODELS USING `approxposterior`

Portions of this chapter were originally published in collaboration with Jake VanderPlas in the September 2018 edition of the Journal of Open Source Software (Fleming and VanderPlas 2018, JOSS, Vol. 3, 29, p. 781; 2018, DOI: 10.21105/joss.00781), and are reproduced below with permission of the Journal of Open Source Software. Portions of this chapter were originally published in collaboration with Rory Barnes, Rodrigo Luger, and Jacob VanderPlas in 2020 in the Astrophysical Journal (Fleming et al. 2020, ApJ, accepted, © American Astronomical Society), and are reproduced below with permission of the American Astronomical Society.

In this thesis, I have developed and contributed to numerous theoretical models, all implemented in VPLanet, that simulate the long-term evolution of stars and their planets. In this Chapter, I explore how I can use those models to infer the evolutionary history of exoplanetary systems, in conjunction with observational constraints, using Bayesian statistics. I explain the significant numerical challenges that can make such studies intractable, motivating the development of a software package for rapid, approximate Bayesian inference, `approxposterior` (Fleming and VanderPlas, 2018). I describe the `approxposterior` algorithm and implementation in detail, provide example use cases, and conclude by discussing in-progress and future work with `approxposterior`.

5.1 Bayesian Inference with Computationally-Expensive Models

I can constrain the evolutionary histories of exoplanetary systems using the models implemented in VPLanet by calibrating the simulation initial conditions such that the output agrees with the

observed data, within the observational uncertainties. This task is mathematically codified by the statistical method of Bayesian inference. Generally, Bayesian inference proceeds as follows: One seeks to derive a probability distribution for model parameters, e.g. VPLanet parameters such as a the stellar mass or tidal Q. That distribution should quantify how likely it is that the parameter takes on certain values and capture the inherent uncertainty in the parameter values given data. This distribution is known as the “posterior probability distribution” and accounts for observed data, the data uncertainties, and one’s prior belief about how the parameters are distributed. To compute the posterior distribution of model parameters, \mathbf{x} , given observed data, $Data$, one uses Bayes’ Theorem:

$$P(\mathbf{x}|Data) \propto P(Data|\mathbf{x})P(\mathbf{x}), \quad (5.1)$$

where $P(\mathbf{x}|Data)$ is the posterior probability of \mathbf{x} given $Data$, $P(\mathbf{x})$ is the prior probability assigned to \mathbf{x} , and $P(Data|\mathbf{x})$ is the probability of the data given \mathbf{x} , commonly referred to as the likelihood of $Data$ given \mathbf{x} . This equation neglects the normalization constant, $1/P(Data)$, as this is typically quite difficult to compute because it requires integrating the likelihood over the prior. Through Bayes’ Theorem, the posterior probability can be thought of as using data to update one’s prior belief of how \mathbf{x} is distributed, given a model for the likelihood of the data. Note that in this thesis, I use the natural logarithm of Bayes’ Theorem and refer to $\ln P(\mathbf{x}|Data)$ to as the “Inprobability”. For notational convenience, I define the Inprobability as $f(\mathbf{x})$.

With VPLanet, I must compute the likelihood by running a simulation to compute a prediction, e.g. a planet’s orbital period after Gyrs of tidal evolution, and compare it to the observed value and associated uncertainty. This comparison is typically performed using a χ^2 statistic if the uncertainties are assumed to be Gaussian and uncorrelated, a standard assumption. Since computing the likelihood requires running a VPLanet simulation and hence the posterior is not an analytic function, and since I cannot compute $P(Data)$, I must use a Monte Carlo sampling technique to estimate the posterior distribution. This procedure is usually done using Markov Chain Monte Carlo (MCMC) methods such as the affine-invariant MCMC code, emcee, whose usage is ubiquitous in astronomy (Foreman-Mackey et al., 2013). MCMC methods are incredibly powerful as they just

require computing a function that is proportional to the posterior probability, e.g. the likelihood times the prior for a given \mathbf{x} , allowing them to neglect the normalization term and directly sample from the posterior distribution. How the sampling proceeds depends on the MCMC algorithm, but generally given long enough MCMC chains, the derived distributions are asymptotically guaranteed to converge to the correct distribution. Standard MCMC runs can therefore require upwards of 10^6 likelihood calculations, likely more depending on the dimensionality of the problem, to draw a suitable number of samples from the posterior distribution and build up statistical power.

Consider an experiment in which I want to infer the stellar and tidal evolution of an exoplanetary system given some observed data. `VPLanet` has reasonable physical models for both phenomena, so I could use `VPLanet` within an MCMC chain to constrain the evolution. Each `VPLanet` simulation with these models, however, takes one minute to run. If the MCMC chain required 10^6 likelihood calculations, the MCMC run would expend about 2 years of core-hours. This extreme computational expense renders MCMC sampling with `VPLanet` computationally intractable at scale, especially for model comparison studies that require multiple MCMC runs. Furthermore, because of the “Curse of Dimensionality”, the number of samples required to resolve the posterior distribution grows exponentially with the dimensionality of the problem (Bellman and Corporation, 1957), exacerbating this issue for more complex simulations. Clearly, for Bayesian inference to become feasible for models like `VPLanet` with runtimes ≥ 10 seconds, a method to compute the posterior distribution while minimizing the number of forward model evaluations is required. I address this issue and enable Bayesian parameter inference with `VPLanet` by developing `approxposterior` (Fleming and VanderPlas, 2018).

5.1.1 Fast and Accurate Approximate Bayesian Inference with `approxposterior`

`approxposterior` is a Python package for efficient approximate Bayesian inference and Bayesian optimization of computationally-expensive probabilistic models (Fleming and VanderPlas, 2018). `approxposterior` implements both the “Bayesian Active Learning for Posterior Estimation” (BAPE, Kandasamy et al. (2017)) and “Adaptive Gaussian process approximation for Bayesian inference with expensive likelihood functions” (AGP, Wang and Li (2018)) approximate Bayesian

inference algorithms. `approxposterior` generalizes these algorithms by including several modifications to improve the accuracy and afford the user more control over the inference. To perform the inference, `approxposterior` uses machine learning by training a Gaussian process (GP, Rasmussen and Williams, 2006) surrogate, or emulator, for the computationally-expensive model. That is, the GP learns to predict the Inprobability used in Bayes' Theorem, $f(\mathbf{x})$, by regressing on a small initial subset of forward model runs, a process referred to as “training” in the machine learning literature. `approxposterior`'s GP therefore approximates the true Inprobability, $f(\mathbf{x})$, as $\hat{f}(\mathbf{x})$ as where the latter quantity is the mean of the GP conditional predictive distribution evaluated at \mathbf{x} . Because the GP predictions are cheap, it can be used within an MCMC sampling method, e.g. `emcee`, to obtain an approximation to the posterior probability distribution for the forward model parameters instead of running the forward model each likelihood evaluation, dramatically reducing the computational expense.

Moreover, `approxposterior` employs an active learning approach to iteratively improve the GP's predictive performance while minimizing the number of calls to the expensive model required to generate the GP's training set as an additional means of reducing the computational cost. Both algorithms implemented by `approxposterior`, BAPE and AGP, include a similar active learning approach to intelligently expand the GP's training set. Both methods leverage the fact that each evaluation of the GP conditional predictive distribution, or each GP prediction of $f(\mathbf{x})$, is a one-dimensional Gaussian distribution. `approxposterior` can then identify high-likelihood, and hence high posterior probability, regions in parameter space where the GP's predictions are uncertain, i.e. a wide Gaussian distribution at that point. `approxposterior` then runs the forward model in these regions to supplement its training set and improve the GP's predictive ability in regions of parameter space that are relevant to the inference, reducing the computational cost to estimate posterior probability distributions. Below, I qualitatively describe the `approxposterior` algorithm, include the training set augmentation procedure, in more detail

5.2 approxposterior Algorithm

Qualitatively, the `approxposterior` algorithm is as follows. First, assume a forward model with d input parameters that is designed to reproduce some set of observations, i.e. the *Data*. For the research problem in Chapter 6, for example, d is five. The model parameters have an input domain, D , that is defined by the user. The parameters are further described by a prior probability distribution based on the user’s prior belief for how the model parameters are distributed. Next, the user generates a training set, T , consisting of m_0 forward model simulations distributed across the parameter space. The user chooses how the m_0 samples are distributed throughout parameter space according to their preferred experimental design. `approxposterior` then trains a GP on T to construct a non-parametric model (sometimes called a “surrogate model” or “emulator”) that represents the outcomes of the forward model over the parameter space. Crucially, GPs also generate an uncertainty for the surrogate model at every point in parameter space.

`approxposterior` then identifies m more locations in parameter space to apply the forward model and add to T . The new locations are selected by determining the regions that the GP has identified as having both a high lnprobability, i.e. high posterior density, and a high predictive uncertainty. This selection is accomplished by maximizing a utility function (u , described below) that quantifies where the GP predicts high posterior density and high uncertainty in parameter space, focusing resources on parameter combinations that are likely to be consistent with the observations. `approxposterior` re-trains the GP with the augmented T . The GP is then passed to an MCMC algorithm, e.g. `emcee`, that samples the parameter space to obtain the approximate posterior distributions of the model parameters.

At the end of each iteration, `approxposterior` checks if a convergence condition (described in § 5.3.2) has been met. If the algorithm has not yet converged, `approxposterior` selects an additional m new points to add to T , re-trains the GP, and again estimates the posterior distribution. This process repeats until convergence or until `approxposterior` has run the maximum number of iterations, n_{max} , set by the user. In Algorithm 1, I list the aforementioned steps that comprise this algorithm. As defined above, $f(\mathbf{x}) = \ln\mathcal{L}(\mathbf{x}) + \ln\text{Prior}(\mathbf{x})$, i.e. the lnprobabil-

ity function used for MCMC sampling with `emcee`. For my application, for example, evaluating $f(\mathbf{x})$ requires running a VPLanet simulation to compute $\ln \mathcal{L}(\mathbf{x})$ (see § 6.2.4 in Chapter 6). In Algorithm 1, \mathbf{x}^+ is the point in parameter space selected by maximizing u .

Algorithm 1: `approxposterior` Approximate Inference Pseudo Code

```

Assume an input domain  $D$ , GP prior on  $f(\mathbf{x})$ 
Generate a training set,  $T$ , consisting of  $m_0$  pairs of  $(\mathbf{x}, f(\mathbf{x}))$ 
for  $t = 0, 1, \dots, n_{\max}$  do
    for  $i = 0, 1, \dots, m$  do
        Find  $\mathbf{x}^+ = \operatorname{argmax}_{\mathbf{x} \in D} u(\mathbf{x})$ 
        Compute  $f(\mathbf{x}^+)$ 
        Append  $(\mathbf{x}^+, f(\mathbf{x}^+))$  to  $T$ 
        Re-train GP, optimize GP hyperparameters given augmented  $T$ 
    end
    Use MCMC to obtain approximate posterior distribution with GP surrogate for  $f(\mathbf{x})$ 
    if converged then
        break
    end
end

```

GPs require a kernel function to model the covariance between points in parameter space. By default, `approxposterior` assumes a squared exponential kernel. By placing a GP prior with a squared exponential kernel on $f(\mathbf{x})$, for example, I assume that the function is smooth and continuous, both reasonable assumptions for modeling the posterior density. For inference problems that are liable to violate these assumptions, other kernels, e.g. the Ornstein-Uhlenbeck kernel, may be more appropriate. I refer the reader to Rasmussen and Williams (2006) for detailed descriptions of common GP kernels and their mathematical properties. `approxposterior` uses `george` (Ambikasaran et al., 2014) for all GP calculations and hence users can apply any combination of kernels implemented in that software package for their inference problems.

`approxposterior` has several free parameters that can be set by the user: m_0 , the size of the initial training set, n_{\max} , the maximum number of iterations, m , the number of new points to select each iteration where the forward model will be evaluated, and ε , the convergence threshold. Typically, I find that $n_{\max} = 2 - 3 \times d$, $m, m_0 = 10 - 20 \times d$, and $\varepsilon = 0.1$ work well in practice, although

performance may vary depending on the use case. For a complete list of `approxposterior` parameters, I refer the reader to the online documentation¹ (see also § 5.3.4).

Note that `approxposterior` does not linearly transform the parameter space to the unit hypercube as did Kandasamy et al. (2017). Moreover, `approxposterior` does not fix the covariance scale lengths, instead opting to estimate all GP kernel hyperparameters by maximizing the marginal likelihood of the GP, given its training set, at a user-specified cadence. In Algorithm 1, I optimize the GP hyperparameters each time a new point is added to the training set, but in practice I found this is unnecessary, especially at later iterations when the GP has developed a reasonable approximation of the posterior. I prefer to optimize the GP hyperparameters twice per iteration, once after half of the m new points have been selected, and again after all m points have been selected.

5.3 `approxposterior`: Theory and Practical Usage

In this section, I further describe `approxposterior`'s training set augmentation procedure and how to check for convergence in § 5.3.1 and § 5.3.2, respectively. I examine how these procedures work in practice for the science case explored in Chapter 6. I then provide a simple example of an `approxposterior` Python script that reproduces the Wang and Li (2018) test to both validate `approxposterior` and show its practical usage in § 5.3.3. Finally in § 5.3.4, I comment on `approxposterior`'s extensive online examples and documentation.

5.3.1 Augmenting the Training Set

Each iteration, `approxposterior` selects m new points to add to the GP's training set by maximizing the utility function, u . To motivate the choice of u , consider the following argument based on Kandasamy et al. (2017): `approxposterior` assumes that the forward model the GP learns on, here `VPLanet` via `lnL`, is computationally-expensive to run, and hence `approxposterior` seeks to minimize the number of forward model evaluations required to build its training set. For

¹ <https://dflemin3.github.io/approxposterior/>

inference problems, it is natural to select high-lnpprobability regions in parameter space to augment the GP training set as this is where the posterior density is large. Furthermore, selecting regions in parameter space where the GP’s predictive uncertainty is already small offers little value, compared to regions where its predictions are more uncertain, as additional points in low-uncertainty regions are unlikely to alter the GP’s predictions.

With these considerations in mind, Kandasamy et al. (2017) leverage the analytic properties of GPs to derive the “exponentiated variance” utility function, given by their Eqn. (5),

$$u_{EV}(\mathbf{x}) = \exp(2\mu_t(\mathbf{x}) + \sigma_t^2(\mathbf{x}))(\exp(\sigma_t^2(\mathbf{x})) - 1), \quad (5.2)$$

where $\mu_t(\mathbf{x})$ and $\sigma_t^2(\mathbf{x})$ are the mean and variance of the GP’s predictive conditional distribution evaluated at \mathbf{x} , respectively, for the t^{th} approxposterior iteration. Using the same parameters, Wang and Li (2018) derive a similar entropy-based utility function given by their Eqn. (7),

$$u_{AGP}(\mathbf{x}) = \mu_t(\mathbf{x}) + \frac{1}{2} \ln(2\pi e \sigma_t^2(\mathbf{x})). \quad (5.3)$$

approxposterior defaults to using Eqn. 5.2. To select each new point to add to the training set, approxposterior maximizes the utility function specified by the user with the Nelder-Mead method (Nelder and Mead, 1965). Note that this optimization is rather cheap since it only requires evaluating the GP’s predictive conditional distribution, so this task is not a significant computational bottleneck. I typically restart this optimization 5 times to reduce the influence of local extrema, but the number of restarts is a free parameter that can be tuned by the user. Note that in practice, approxposterior optimizes the natural logarithm of the utility function to ensure numerical stability.

As demonstrated in Kandasamy et al. (2017), Eqn. (5.2) identifies high-likelihood points where the GP’s predictions are uncertain, significantly reducing the cost of training an accurate GP surrogate model. I found that Eqn. (5.3) behaves similarly in practice. In Fig. 5.1, I display the approximate joint and marginal posterior distribution derived by approxposterior from Fleming

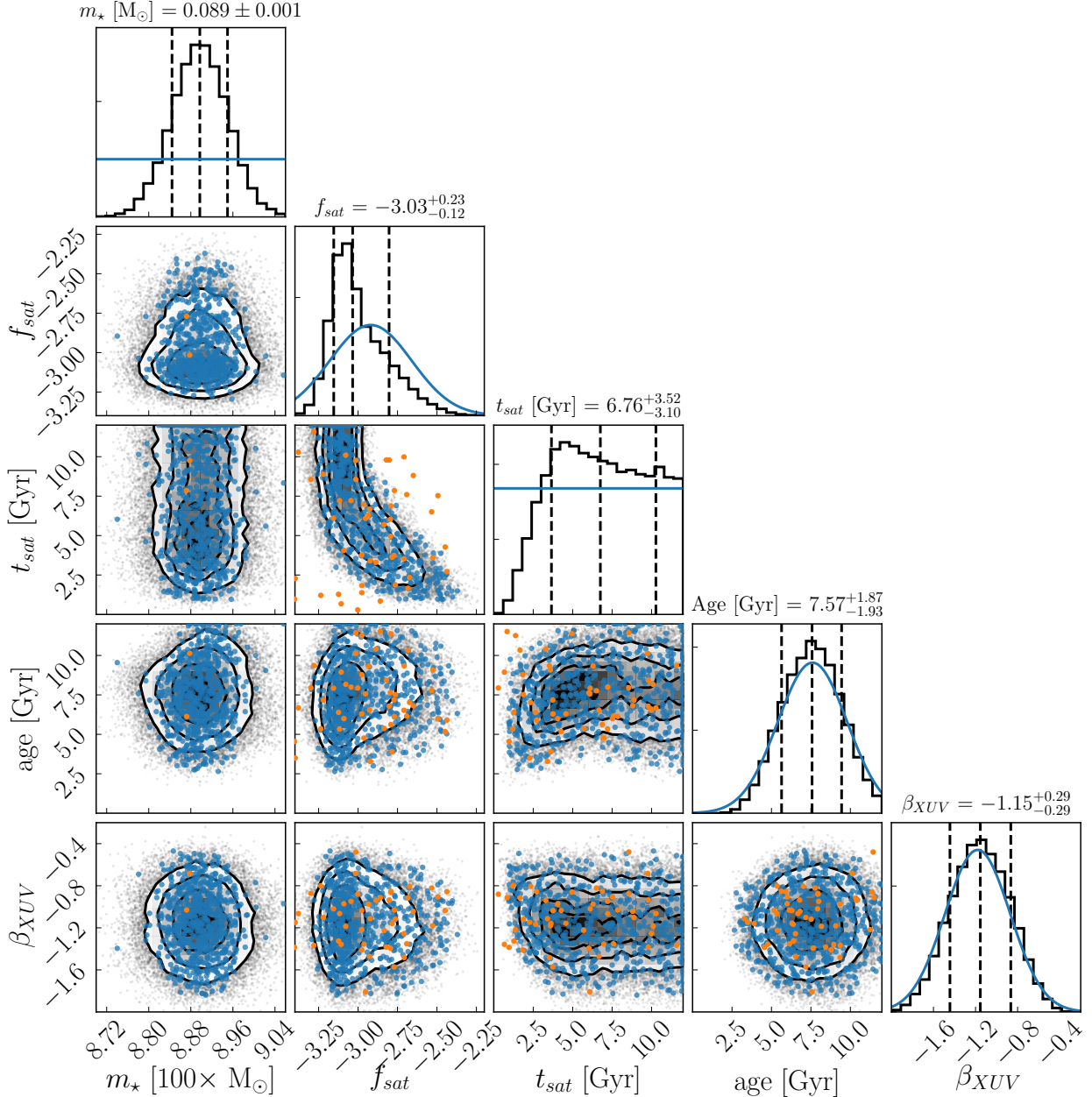


Figure 5.1: Same as Fig. 6.2, but overplotted with the training set for `approxposterior`'s GP. The orange points display the initial training points whereas the blue points display the points iteratively selected by maximizing the Kandasamy et al. (2017) utility function, Eqn. (5.2). By design, `approxposterior` selected points to expand its training set in regions of high posterior density, improving its GP's predictive accuracy in the most relevant regions of parameter space while seldom wasting computational resources in the low likelihood regions.

et al. (2020) overplotted with the initial training set in orange and the points selected by sequentially maximizing Eqn. (5.2) in blue. See Chapter 6 for additional information on the science underlying this application. Given the small initial training set, `approxposterior` successfully selects high-posterior density points in parameter space to augment the GP’s training set. Some points are selected in low-likelihood regions early on, typically near the edges of parameter space where the GP’s uncertainty was initially large.

5.3.2 Convergence

I assess the convergence of the `approxposterior` algorithm by comparing the means of the approximate marginal posterior distributions over successive iterations. I consider an `approxposterior` run “converged” if the differences between the marginal posterior means, relative to the widths of the marginal posteriors, are less than a tolerance parameter, ε , for k_{max} consecutive iterations. Effectively, this criterion checks if the expected value of each model parameter over the posterior distribution varies by $\leq \varepsilon$ standard deviations from the previous iteration’s expected values. That is, I require the `approxposterior` convergence diagnostic $z_{t,j} \leq \varepsilon$ for all j , where

$$z_{t,j} = |\mu_{t,j} - \mu_{t-1,j}| / \sigma_{t-1,j}, \quad (5.4)$$

and $\mu_{t,j}$ and $\sigma_{t,j}$ are the mean and standard deviation of the approximate marginal posterior distribution for the t^{th} iteration and the j^{th} parameter. This quantity is analogous to the “z-score” commonly used in many statistical tests. Following Wang and Li (2018), I require this condition to be satisfied for k_{max} consecutive iterations to ensure `approxposterior` is producing a consistent result. With this scheme, `approxposterior` tolerates deviations from the previous estimate that are less than, or at least consistent with, the previous values, given the inherent uncertainty implied by the width of the posterior distribution. For my application explored in Chapter 6, for example, I adopted conservative choices of $\varepsilon = 0.1$ and $k_{max} = 5$. Each `approxposterior` iteration, I also visually inspected the estimated posterior distribution to ensure convergence.

In Fig. 5.2, I display the convergence diagnostic quantity, z_t , as a function of iteration for

each model parameter for the `approxposterior` run presented in the Chapter 6 for illustrative purposes. In this case, `approxposterior` quickly finds a consistent result as z_t decreases below the convergence threshold within the first few iterations. For each parameter, z_t continues to decrease until iteration 3 before stabilizing. The evolution of z_t is not monotonic, however, owing to the stochastic nature of GPs, the hyperparameter optimization scheme, and MCMC sampling that can cause these values to occasionally be slightly worse than previous iterations. Requiring convergence over k_{max} consecutive iterations mitigates the impact of this stochasticity.

5.3.3 A Simple Example

Here, I demonstrate how to use `approxposterior` in practice to reproduce the 2-dimensional (2D) Rosenbrock function inference test examined by Wang and Li (2018). The 2D Rosenbrock function is a classic optimization test function with a global minimum of 0 at (1,1). The Rosenbrock function exhibits non-linear, banana-like correlations making it a suitable challenge for `approxposterior`. Wang and Li (2018) define the 2D Rosenbrock function likelihood as

$$l(\mathbf{x}) = \exp\left(-\frac{1}{100}(x_1 - 1)^2 - (x_1^2 - x_2)^2\right) \quad (5.5)$$

where $\mathbf{x} = \{x_1, x_2\}$. In practice, `approxposterior` works with the natural logarithm of Eqn. (5.5). I follow Wang and Li (2018) and adopt a uniform prior distribution for both x_1 and x_2 over [-5, 5].

Below, I include a simple Python script for applying `approxposterior` to the 2D Rosenbrock inference problem.² In the first section, I define algorithm parameters that set the size of the initial training set, m_0 , and control how `approxposterior` operates, e.g. I only run two iterations by setting $n_{max} = 2$. As demonstrated below, this number of iterations is sufficient to reproduce the Wang and Li (2018) result. I also define the hard parameter bounds equal to the prior bounds to prevent the GP from blowing up by trying to learn in forbidden regions of parameter space, e.g. $x_1 > 5$. Next, I create the training set, $T = \{\theta, y\}$, where the model parameters $\theta = \mathbf{x}$. Note how y is the sum of the lnlikelihood and lnprior distribution, that is, the unnormalized

²The script is available at <https://github.com/dflemin3/approxposterior/blob/master/examples/inference/example.py>

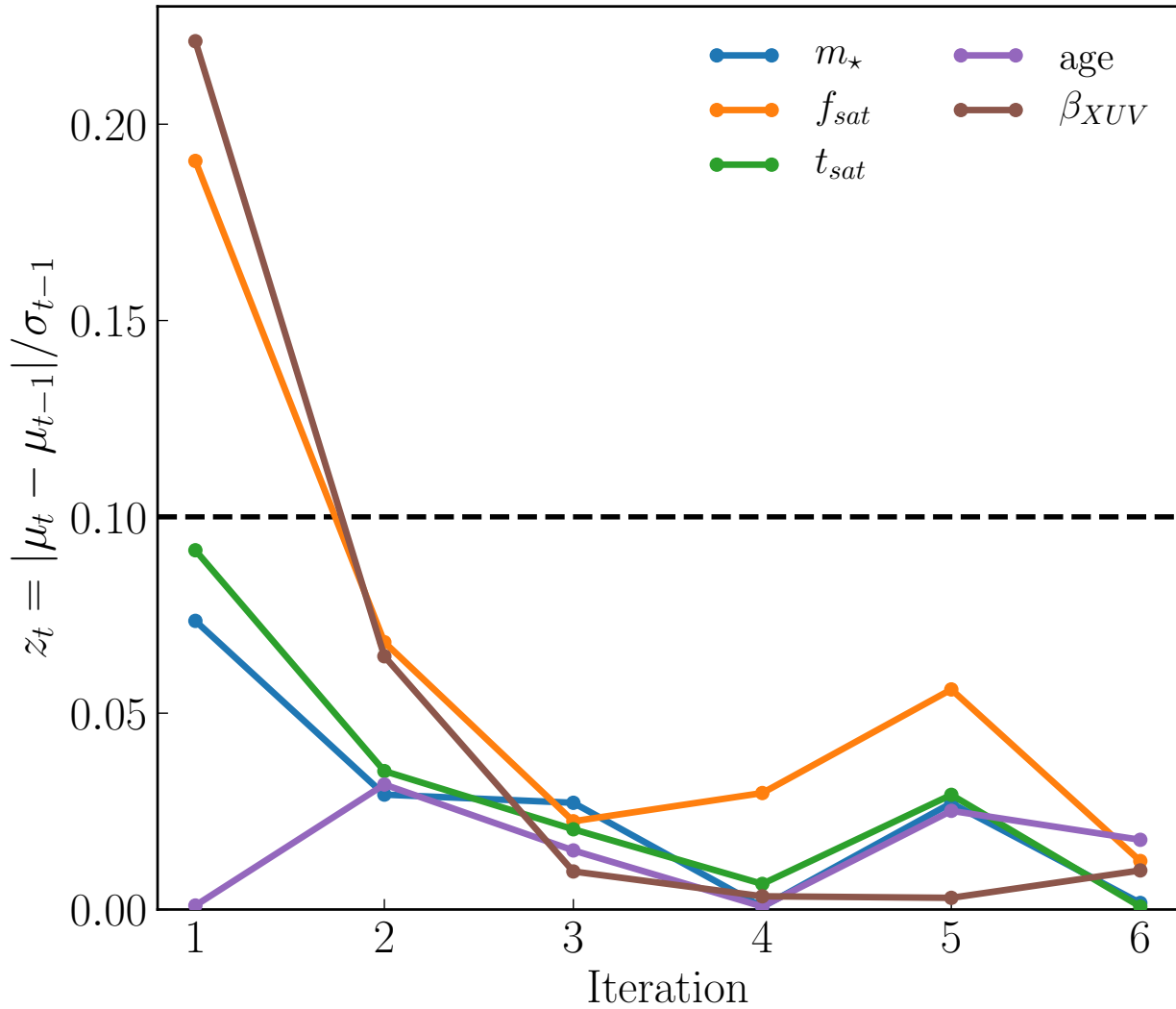


Figure 5.2: The approxposterior convergence diagnostic, z_t , as a function of iteration for the run presented in the Chapter 6. Note that in approxposterior, the initial iteration is iteration 0. The black dashed line indicates the adopted convergence threshold of $\varepsilon = 0.1$. approxposterior quickly converges to a consistent and accurate result.

posterior probability. In approxposterior notation, the GP iteratively learns $\hat{y} = \hat{f}(\mathbf{x})$ as an approximation of $y = f(\mathbf{x})$.

As explained above, approxposterior requires a GP. approxposterior has a handy convenience function for initializing GPs, *defaultGP*, that creates a GP with a squared exponential kernel and takes care of various bookkeeping tasks for the user behind-the-scenes. In the script, I use this function to initialize the GP and pass it, along with functions that describe the lnlikelihood, lnprior, and how to sample from the prior to the ApproxPosterior object used to perform inference. Finally, I call the approxposterior run method with the parameters described above and after a few minutes, the inference is complete. I finally extract the posterior samples using an emcee utility function and visualize the joint posterior probability distribution estimated by approxposterior. I display this distribution in Fig. 5.3.

```
#!/usr/bin/env python
# -*- coding: utf-8 -*-

from approxposterior import approx, gpUtils, likelihood as lh, utility as ut
import numpy as np
import corner

# Define algorithm parameters
m0 = 50                                # Initial size of training set
m = 20                                    # Num points to find each iteration
nmax = 2                                   # Maximum number of iterations
bounds = [(-5,5), (-5,5)]                 # Prior bounds
algorithm = "bape"                         # Use the Kandasamy et al. (2017) formalism
np.random.seed(57)

samplerKwargs = {"nwalkers" : 20}           # emcee.EnsembleSampler
mcmcKwargs = {"iterations" : int(2.0e4)}    # emcee.EnsembleSampler.run_mcmc

# Evaluate model lnlikelihood + lnprior for each theta sampled from prior
theta = lh.rosenbrockSample(m0)
y = np.zeros(len(theta))
for ii in range(len(theta)):
```

```

y[ii] = lh.rosenbrockLnlike(theta[ii]) + lh.rosenbrockLnprior(theta[ii])

# Use default GP with squared exponential kernel
gp = gpUtils.defaultGP(theta, y, white_noise=-12)

# Initialize object using the Wang & Li (2018) Rosenbrock function example
ap = approx.ApproxPosterior(theta=theta, y=y, gp=gp,
                             lnprior=lh.rosenbrockLnprior,
                             lnlike=lh.rosenbrockLnlike,
                             priorSample=lh.rosenbrockSample,
                             bounds=bounds, algorithm=algorithm)

# Run!
ap.run(m=m, nmax=nmax, estBurnin=True, nGPRestarts=3,
       mcmcKwargs=mcmcKwargs, ache=False, samplerKwargs=samplerKwargs,
       verbose=True, thinChains=False, onlyLastMCMC=True)

# Load in MCMC chain, plot the corner plot and where AP selected points
samples = ap.sampler.get_chain(discard=ap.iburns[-1], flat=True,
                               thin=ap.ithins[-1])
fig = corner.corner(samples, quantiles=[0.16, 0.5, 0.84], show_titles=True,
                     scale_hist=True, plot_contours=True)
fig.axes[2].scatter(ap.theta[m0:,0], ap.theta[m0:,1], s=10,
                    color="red", zorder=20)
fig.savefig("finalPosterior.png", bbox_inches="tight")

```

Compare the posterior distribution in Fig. 5.3 to Figures 1 and 3 from Wang and Li (2018). The agreement is excellent, validating my implementation in `approxposterior`. I also display the points selected by `approxposterior`'s training set augmentation procedure in red. As expected, the points `approxposterior` selected preferentially cluster in regions of high posterior density, improving the accuracy of `approxposterior`'s GP surrogate model in the relevant regions of parameter space.

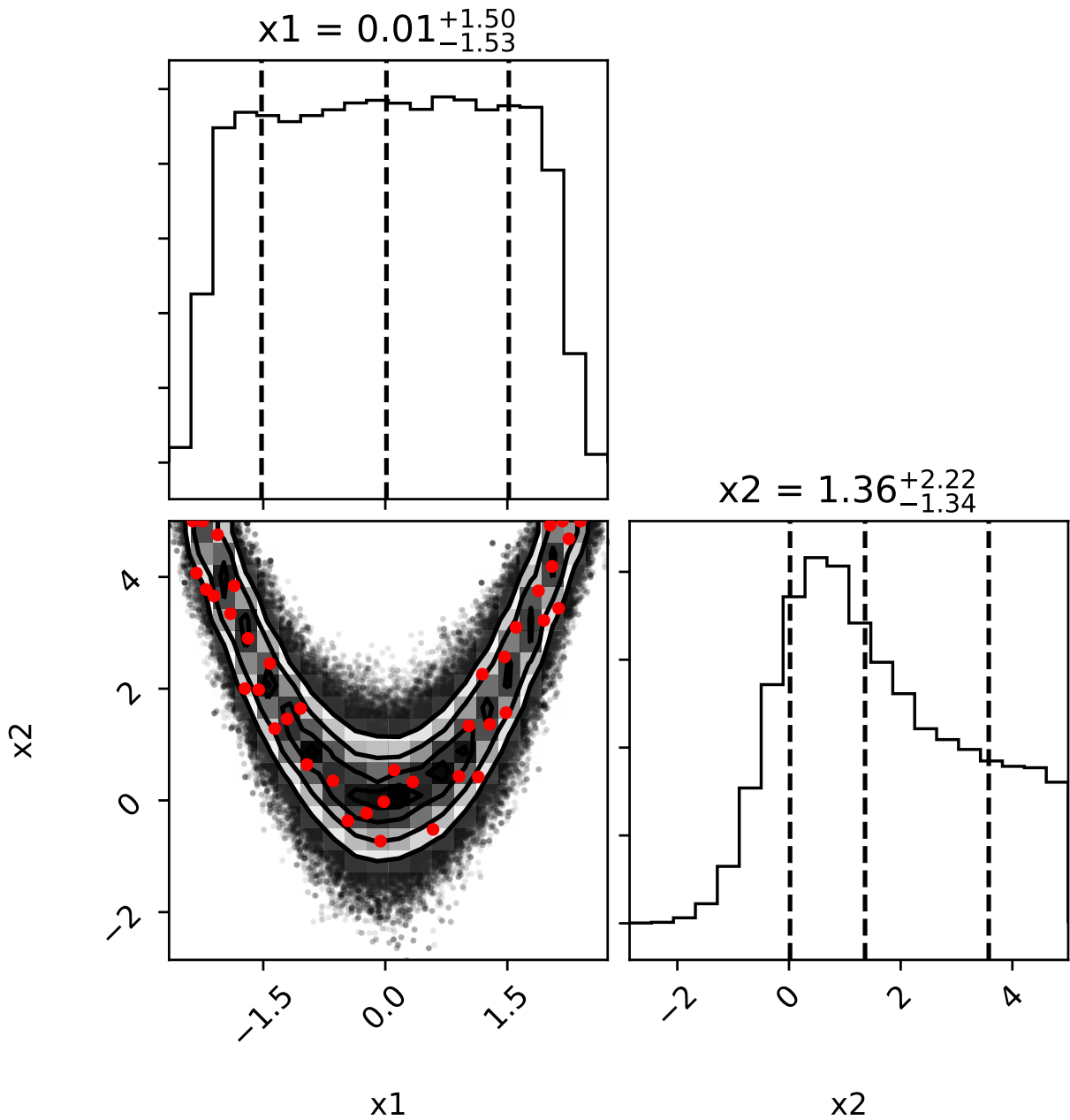


Figure 5.3: The posterior probability distribution for the 2D Rosenbrock example from Wang and Li (2018) estimated by approxposterior. The red points denote points selected by approxposterior's training set augmentation scheme using the BAPE algorithm. As explained above, approxposterior preferentially selects points in regions of high posterior density. The posterior distribution estimated by approxposterior is in good agreement with the results of Wang and Li (2018), their Figures 1 and 3.

5.3.4 *Online Documentation*

I wrote extensive online documentation for `approxposterior` that is located on both its main GitHub page³ and on an additional public documentation website⁴. The online examples comprise both annotated Jupyter Lab notebooks and commented Python scripts, like the one shown above, to allow new users understand how `approxposterior` is called and used in practice. Moreover, the online documentation includes the full `approxposterior` API; each parameter in every `approxposterior` class and function is fully described, including a definition for each parameter and reasonable default values. The online documentation serves to help new users employ `approxposterior` in their own research. As the primary author of `approxposterior`, I encourage new users to both fully read the online documentation and run all examples before developing scripts for their own application.

5.4 *Applying approxposterior to Terrestrial Exoplanet Atmospheric Retrieval*

`approxposterior` is agnostic to the forward model it learns and is therefore not restricted to working with VPLanet-based Inprobabilities. `approxposterior` is applicable for a wide array of Bayesian inference problems, particularly those that involve computationally-expensive models as demonstrated in this Chapter and in Chapter 6. Here, I discuss an additional application of `approxposterior` to the inference, or retrieval, of chemical abundances from synthetic transmission spectra of terrestrial exoplanet atmospheres (Lustig-Yaeger et al., in prep).

With future facilities like JWST eventually coming online, astronomers will likely be able to detect and characterize the first terrestrial exoplanet atmospheres. The most likely targets for this effort are the TRAPPIST-1 planets owing to the system’s proximity to Earth, the relatively large planetary transit depths, and the small star-planet separations (Gillon et al., 2016, 2017; Morley et al., 2017; Lustig-Yaeger et al., 2019). Since the TRAPPIST-1 planets all transit, JWST will be able to measure the absorption of stellar light passing through any atmosphere the planets possess

³<https://github.com/dflemin3/approxposterior>

⁴<https://dflemin3.github.io/approxposterior/>

as a function of wavelength, a technique known as transmission spectroscopy. Given suitable theoretical models for an exoplanet’s transmission spectra, e.g. Lincowski et al. (2018), modelers can solve the inference problem of inferring, or retrieving, the abundance of chemical species like O₂ in an exoplanet’s atmosphere by matching theoretical models of transmission spectra with the observed spectra and uncertainties (e.g. Krissansen-Totton et al., 2018; Tremblay et al., 2020). Retrievals are another application of Bayesian inference, analogous to the case of matching VPlanet outputs with observational constraints discussed in this thesis.

Retrievals, however, are inherently computationally-expensive tasks because simulating transmission spectra requires not only simulating a physically-plausible exoplanet climate and atmospheric temperature structure (Lincowski et al., 2018), but also requires performing complex radiative transfer simulations (e.g. with SMART, Meadows and Crisp, 1996; Crisp, 1997). To mitigate this computational expense, numerous groups have turned to machine learning to bypass this modeling in favor of training a model that maps atmospheric chemical abundances to transmission spectra using neural networks (Waldmann, 2016; Márquez-Neila et al., 2018; Zingales and Waldmann, 2018; Cobb et al., 2019; Fisher et al., 2019; Himes et al., 2020). In this paradigm, the neural network is trained on a large ($\geq 10^4 - 10^5$) grid of pre-computed transmission spectra with known atmospheric chemical abundances and planetary properties. The neural network learns an approximate mapping between input planetary physical and atmospheric properties and the transmission spectra, bypassing complex climate and radiative transfer simulations to significantly reduce the computational expense of retrievals.

Although promising, neural network-based approaches suffer two related critical limitations. First, neural networks have a large number of parameters and hence require massive grids of pre-computed spectra for training whose size scales exponentially with the dimensionality of the inference. Simulating this initial grid is of course computationally-expensive. Second, if the theoretical model for the transmission spectra changes, say new line lists are developed or climate models are refined, the neural network’s initial training grid must be recomputed as a previously-trained neural network would have been tuned to out-dated, or at worst, incorrect physics, biasing any retrieved abundances.

Here, I present work-in-progress from Lustig-Yaeger et al, in prep, to demonstrate that `approxposterior` is well-suited to retrievals, providing comparable accuracy as direct inference methods but requiring about 800 times fewer computational resources. I consider the case of inferring the isothermal atmospheric temperature and mixing ratios of H₂O and CO₂ from a synthetic transmission spectra of TRAPPIST-1e with noise levels comparable to what astronomers expect from JWST (Lincowski et al., 2018). In this case, I consider two retrieval methods (see Lustig-Yaeger et al, in prep. for a complete description). For the first method, I run SMART radiative transfer simulations each `x` evaluation within an `emcee` sampler to derive the posterior distribution. I refer to this method as the “fiducial” inference method. For the second, I use `approxposterior` within `emcee` to replace the `x` evaluation and estimate the posterior distribution. Each method’s MCMC chain were ran with identical parameters.

I display the posterior distributions inferred by both methods in Fig. 5.4. The fiducial posterior distribution is purple and the `approxposterior`-derived distribution is orange. Both the joint and marginal posterior distributions derived by `approxposterior` are in excellent with the distributions derived by the fiducial method, demonstrating `approxposterior`’s ability to accurately replace the complex radiative transfer simulations for computing the lnprobability. Note the how the marginal constraints, both the best fit value and the uncertainties, derived by both methods listed in Fig. 5.4 are in nearly perfect agreement. Furthermore, `approxposterior` required about 4,000 SMART simulations total to train its GP whereas `emcee` required about 3,000,000 to evaluate the MCMC. In this case, `approxposterior` is about ~ 800 times more efficient than the fiducial method, a dramatic reduction in computational cost without appreciably reducing the accuracy on the inference. Clearly, `approxposterior` offers a promising method to enable rapid and accurate Bayesian inference for computationally-expensive models.

5.5 Conclusions

In this Chapter, I introduced `approxposterior`, an open-source Python machine learning package that uses GP regression for rapid and accurate approximate Bayesian inference. I outlined the mathematics and algorithm underpinning `approxposterior` and examined its practical appli-

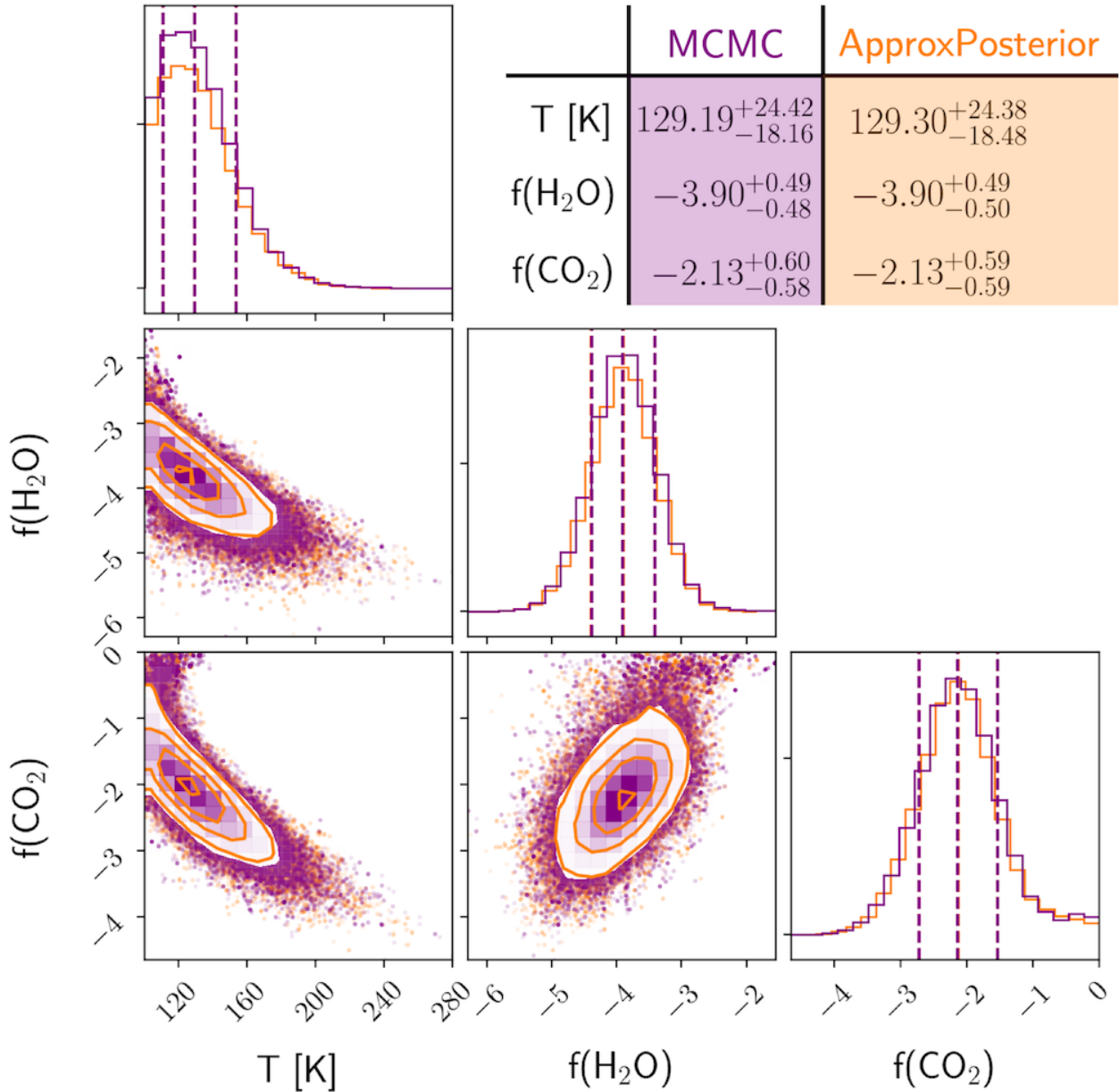


Figure 5.4: Joint and marginal posterior probability distributions derived by `emcee` (purple) and `approxposterior` (orange) from an atmospheric retrieval of a simulated noised JWST transmission spectrum of TRAPPIST-1e (used with permission from Lustig-Yaeger et al., in prep). This retrieval experiment attempts to infer the isothermal atmospheric temperature, T , and the mixing ratios of H_2O and CO_2 . `approxposterior` accurately recovers both the nontrivial correlations between model parameters and marginal parameter constraints as did `emcee`, within Monte Carlo error, but requiring about 800 times fewer computational resources.

cation. After explaining the `approxposterior` algorithm and convergence scheme, I sketched an in-progress research project using `approxposterior` and demonstrated that it was as accurate as direct inference methods using `emcee`, but required 800 times fewer computational resources.

Chapter 6

INFERRING THE XUV HISTORY OF THE TRAPPIST-1 PLANETARY SYSTEM

*Portions of this chapter were originally published in collaboration with Rory Barnes, Rodrigo Luger, and Jacob VanderPlas in 2020 in the *Astrophysical Journal* (Fleming et al. 2020, *ApJ*, accepted, © American Astronomical Society), and are reproduced below with permission of the American Astronomical Society.*

6.1 Introduction

The James Webb Space Telescope (JWST) is poised to detect and characterize the first terrestrial exoplanet atmospheres via transmission spectroscopy. This search will likely focus on planets orbiting nearby M dwarfs given their favorable relative transit depths, the potential buildup of biosignature gases due to UV-driven photochemistry (Segura et al., 2005), and the large occurrence rates of M dwarf planets (Dressing and Charbonneau, 2015). The correct interpretation of those observations, however, is predicated on understanding the system’s long-term evolution, most importantly processes that could impact the planet’s atmospheric state and habitability, such as atmospheric escape, water loss, and the potential buildup of an abiotic O₂ atmosphere (Watson et al., 1981; Lammer et al., 2003; Murray-Clay et al., 2009; Luger and Barnes, 2015). These volatile escape mechanisms are partially driven by the host star’s XUV luminosity (X-ray and EUV emission ranging over approximately 1-1000Å), and therefore characterizing the long-term stellar XUV evolution of late M-dwarfs is critical to assessing the present state of their planets, including habitability.

High-energy stellar radiation originates from the corona via the heating of magnetically-confined plasma (Vaiana et al., 1981). The stellar magnetic field is likely generated via differential rotation

within the stellar convective envelope (Parker, 1955), linking rotation to stellar activity and XUV emission. Stellar rotation rates slow over time due to magnetic braking (Skumanich, 1972), causing XUV emission to decline with time. The X-ray luminosity (L_X) of FGK stars, for example, has been empirically shown to monotonically decrease with age (Jackson et al., 2012). This trend has also been observed for commonly-used proxies for stellar age, rotation period and Rossby number ($\text{Ro} = P_{\text{rot}} / \tau$ for convective turnover timescale τ , Pizzolato et al., 2003; Wright et al., 2011).

Stellar activity evolution is characterized by two distinct phases. First, in the saturated phase, young, rapidly-rotating stars ($\text{Ro} \lesssim 0.1$) maintain a constant $L_X / L_{\text{bol}} \approx 10^{-3}$ (Wright et al., 2011; Jackson et al., 2012). Then, at longer rotation periods and larger Ro, stars transition to the unsaturated phase in which L_X / L_{bol} exponentially decays over time (Pizzolato et al., 2003; Ribas et al., 2005). Recent work has shown that the stellar dynamo processes that generate magnetic fields and drive XUV emission in fully-convective M dwarfs follow the same evolution with Ro as described above for solar-type stars (Wright and Drake, 2016; Wright et al., 2018). We can therefore apply this model to examine the XUV evolution of individual fully-convective stars.

TRAPPIST-1 (Gillon et al., 2016, 2017), an ultracool dwarf located 12 pc from Earth, harbors 7 approximately Earth-sized transiting planets that are prime targets for JWST transmission spectroscopy observations (Morley et al., 2017; Lincowski et al., 2018; Lustig-Yaeger et al., 2019). TRAPPIST-1's high observed L_X (Wheatley et al., 2017), short photometric rotation period (3.3 d, Luger et al., 2017), and low Rossby number ($\text{Ro} \approx 0.01$, Roettenbacher and Kane, 2017) suggest that TRAPPIST-1 is still saturated today (Pizzolato et al., 2003; Wright et al., 2011, 2018). Both Roettenbacher and Kane (2017) and Morris et al. (2018) suggest that the photometrically-determined rotation period is inaccurate, with the latter study proposing that the 3.3 d period corresponds to a characteristic timescale for active regions on the stellar surface. TRAPPIST-1's $v \sin i = 6 \text{ km s}^{-1}$ (Barnes et al., 2014), however, implies a rotation period of ~ 1 d for $i = 90^\circ$, providing evidence that TRAPPIST-1's rapid rotation is physical and consistent with saturation ($P_{\text{rot}} \lesssim 20$ d, Wright et al., 2018).

The TRAPPIST-1 planetary system currently receives significant high-energy fluxes (Bourrier et al., 2017b; Wheatley et al., 2017; Peacock et al., 2019), possibly a consequence of TRAPPIST-1

remaining in the saturated regime. These fluxes were likely more extreme during the pre-main sequence, driving significant water loss and potentially rendering the planets uninhabitable (Bolmont et al., 2017; Bourrier et al., 2017a). Here, we model the long-term stellar and XUV evolution of TRAPPIST-1 to characterize the evolving XUV environment of its planetary system. We use MCMC to derive probability distributions for our model parameters that describe the XUV evolution that are consistent with TRAPPIST-1’s observed properties and their uncertainties.

TRAPPIST-1 is not the only system that merits this modelling, however, as the Transiting Exoplanet Survey Satellite will likely discover additional transiting planets orbiting in the habitable zone of nearby M dwarfs (Barclay et al., 2018), some of which may be suitable targets for atmospheric characterization with JWST. In this work, we show that stellar XUV histories can be accurately inferred using machine learning (`approxposterior`, Fleming and VanderPlas, 2018), but using $980\times$ less computational resources than traditional MCMC methods. This speed-up enables our methods to scale to additional stars that host potential targets for atmospheric characterization and is generalizable to a large number of applications, potentially enabling Bayesian statistical analyses that are otherwise intractable with traditional MCMC approaches, e.g. `emcee` (Foreman-Mackey et al., 2013).

We describe our model and statistical methods in § 6.2. We present our results and demonstrate the ability of machine learning to reproduce our analysis in § 6.3, and discuss the implications of our results in § 6.4. In § 5.2, we describe the `approxposterior` algorithm and discuss its convergence properties.

6.2 Methods

6.2.1 Simulating XUV Evolution with `VPLanet`

We simulate TRAPPIST-1’s stellar evolution using the STELLAR module in `VPLanet`¹ (Barnes et al., 2019), which performs a bicubic interpolation over mass and age of the Baraffe et al. (2015) stellar evolution tracks. The Baraffe et al. (2015) models (also employed by both Burgasser and

¹`VPLanet` is publicly available at <https://github.com/VirtualPlanetaryLaboratory/vplanet>.

Mamajek (2017) and Van Grootel et al. (2018) to constrain TRAPPIST-1’s stellar properties) were computed for solar metallicity stars and hence are suitable for TRAPPIST-1 whose [Fe/H] is consistent with solar (Gillon et al., 2016, see also Burgasser and Mamajek (2017)).

We assume TRAPPIST-1’s L_{XUV} evolution traces that of L_X and use the Ribas et al. (2005) model,

$$\frac{L_{XUV}}{L_{bol}} = \begin{cases} f_{sat} & t \leq t_{sat} \\ f_{sat} \left(\frac{t}{t_{sat}} \right)^{-\beta_{XUV}} & t > t_{sat} \end{cases}, \quad (6.1)$$

where f_{sat} is the constant ratio of stellar XUV to bolometric luminosity during the saturated phase, t_{sat} is the duration of the saturated phase, and β_{XUV} is the exponent that controls how steeply L_{XUV} decays after saturation. In practice, we define $f_{sat} = \log_{10}(L_{XUV}/L_{bol})$ and transform Eqn. (6.1) accordingly.

Note that each `VPLanet` simulation (and hence likelihood calculation, see § 6.2.4) in principle only requires interpolating the Baraffe et al. (2015) L_{bol} tracks and evaluating an explicit function of time to compute L_{XUV} , both computationally-cheap tasks. `VPLanet`, however, is a general purpose code designed to simulate the evolution of an exoplanetary system and its host star by simultaneously integrating coupled ordinary differential equations and explicit functions of time that describe the evolution. This generalized structure requires numerous steps to facilitate physical couplings, such as validation steps and a host of intermediate calculations (for more details, see Barnes et al., 2019). Moreover, `STELLAR` simultaneously evolves a star’s radius, effective temperature, radius of gyration, L_{XUV} , and rotation rate in addition to L_{bol} , adding computational overhead. Each `VPLanet` simulation using `STELLAR` therefore lasts about 10s.

6.2.2 Markov Chain Monte Carlo Analysis

We use `emcee`, a Python implementation of the affine-invariant Metropolis-Hastings MCMC sampling algorithm (Foreman-Mackey et al., 2013), to infer posterior probability distributions for our model parameters that describe the evolution of TRAPPIST-1. These distributions are conditioned

on observations of TRAPPIST-1, the activity evolution of late-type stars, and account for both observational uncertainties and correlations between parameters. Our model parameters that we fit for via MCMC comprise the state vector

$$\mathbf{x} = \{m_\star, f_{sat}, t_{sat}, \text{age}, \beta_{XUV}\}, \quad (6.2)$$

where m_\star and age are the stellar mass and age, respectively, and the other parameters are defined by Eqn. (6.1). All of the code used to perform the simulations and analysis in this work is publicly available online.²

6.2.3 Prior Probability Distributions

Since we have few available observable properties of TRAPPIST-1 to use to condition our analysis (L_{bol} and L_{XUV}/L_{bol} , see § 6.2.4), our prior probability distributions will strongly impact our results. We use previous studies and empirical data of late M dwarfs to assemble the best available constraints to serve as priors for our MCMC analysis. We list our adopted prior probability distributions in Table 6.1.

Following Van Grootel et al. (2018), we rely on TRAPPIST-1’s luminosity and age to constrain its mass. We therefore adopt a simple uniform prior of $m_\star \sim \mathcal{U}(0.07, 0.11) \text{ M}_\odot$. For the age, we use the empirical estimate for TRAPPIST-1 derived by Burgasser and Mamajek (2017), age $\sim \mathcal{N}(7.6, 2.2^2) \text{ Gyr}$, as their thorough analysis considered both observations of TRAPPIST-1 and a host of empirical age indicators for ultracool dwarfs. This age distribution is consistent with Gonzales et al. (2019) who conclude that TRAPPIST-1 is a field-age dwarf based on their spectral energy distribution modeling. We cap the maximum age we consider at 12 Gyr. Younger ages have been suggested based on TRAPPIST-1’s activity (e.g. $\gtrsim 500 \text{ Myr}$, Bourrier et al., 2017b), but here we argue that behavior is consistent with an extended saturation timescale.

We construct an empirical $f_{sat} = \log_{10}(L_{XUV}/L_{bol})$ distribution from the sample of fully-convective, saturated M dwarfs with observed L_X from Wright et al. (2011). For each star in

² <https://github.com/dflemin3/trappist>

the Wright et al. (2011) sample, we follow Wheatley et al. (2017) and estimate L_{XUV} as a function of L_X using Eqn. (2) from Chadney et al. (2015). We find that the distribution is well-approximated by a normal distribution, $f_{sat} \sim \mathcal{N}(-2.92, 0.26^2)$, and we adopt it as our prior.

The duration of the saturated phase is estimated to be $t_{sat} \approx 100$ Myr for FGK stars (Jackson et al., 2012). Studies of stellar activity of late type stars as a function of stellar age, or its proxy, rotation period, indicate that the activity lifetime, and hence duration of the saturated phase, is likely longer for later-type stars (Shkolnik and Barman, 2014; Wright et al., 2011; West et al., 2015), with fully-convective M dwarfs potentially remaining active throughout their lifetimes ($t_{sat} \gtrsim 7$ Gyr, West et al., 2008; Schneider and Shkolnik, 2018). Furthermore, the spin-down timescales of late M dwarfs increases with decreasing stellar mass (Delfosse et al., 1998), with late M dwarfs retaining rapid rotation longer than earlier-type stars and hence remaining active for up to $P_{rot} \approx 86$ d (West et al., 2015), much longer than TRAPPIST-1’s estimated rotation period. Given these constraints, we adopt a broad uniform t_{sat} prior distribution capped by the maximum age we consider, $t_{sat} \sim \mathcal{U}(0.1, 12)$ Gyr.

In the unsaturated phase, L_X , and hence L_{XUV} , decay exponentially with power law slope β_{XUV} (Ribas et al., 2005). Jackson et al. (2012) find that β_{XUV} does not significantly vary with stellar mass in their sample of FGK stars. Since Wright and Drake (2016) found that the X-ray evolution of fully-convective stars is qualitatively similar to that of partially-convective FGK stars, we adopt the β_{XUV} distribution of late K dwarfs from the Jackson et al. (2012) sample as our prior, $\beta_{XUV} \sim \mathcal{N}(-1.18, 0.31^2)$.

6.2.4 Likelihood Function and Convergence

We further condition our analysis on TRAPPIST-1’s observed bolometric luminosity, $L_{bol} = 5.22 \pm 0.19 \times 10^{-4} L_\odot$ (Van Grootel et al., 2018, but see also Gonzales et al. (2019)), and $L_{XUV}/L_{bol} = 7.5 \pm 1.5 \times 10^{-4}$ (Wheatley et al., 2017). In other words, we require that our forward models (VPLanet simulations) yield results that are consistent with the observations of TRAPPIST-1 and their uncertainties.

Table 6.1. Prior Distributions

| Parameter [units] | Prior | Notes |
|---------------------|------------------------------|------------------------------|
| $m_\star [M_\odot]$ | $\mathcal{U}(0.07, 0.11)$ | – |
| f_{sat} | $\mathcal{N}(-2.92, 0.26^2)$ | Wright et al. (2011) |
| t_{sat} [Gyr] | $\mathcal{U}(0.1, 12)$ | – |
| age [Gyr] | $\mathcal{N}(7.6, 2.2^2)$ | Burgasser and Mamajek (2017) |
| β_{XUV} | $\mathcal{N}(-1.18, 0.31^2)$ | Jackson et al. (2012) |

For a given state vector \mathbf{x} , we define the natural logarithm of our likelihood function, $\ln \mathcal{L}$, as

$$\ln \mathcal{L} \propto -\frac{1}{2} \left[\frac{(L_{bol} - L_{bol}(\mathbf{x}))^2}{\sigma_{L_{bol}}^2} + \frac{(L_{XUV}/L_{bol} - L_{XUV}/L_{bol}(\mathbf{x}))^2}{\sigma_{L_{XUV}/L_{bol}}^2} \right] \quad (6.3)$$

where L_{bol} , L_{XUV}/L_{bol} and $L_{bol}(\mathbf{x})$, $L_{XUV}/L_{bol}(\mathbf{x})$ are the observed values and `VPLanet` outputs given \mathbf{x} , respectively, and $\sigma_{L_{bol}}$ and $\sigma_{L_{XUV}/L_{bol}}$ are the observational uncertainties. For each \mathbf{x} , we compute the natural logarithm of the posterior probability at \mathbf{x} , $\ln p(\mathbf{x})$, required for ensemble MCMC sampling as $f(\mathbf{x}) = \ln \mathcal{L}(\mathbf{x}) + \ln p(\mathbf{x})$. We use the distributions described in § 6.2.3 to calculate the natural logarithm of the prior probability of \mathbf{x} , $\ln p(\mathbf{x})$.

We run our MCMC with 100 parallel chains for 10,000 iterations, initializing each chain by randomly sampling each element of \mathbf{x} from their respective prior distributions. During each step of the MCMC chain, `VPLanet` takes \mathbf{x} as input and simulates TRAPPIST-1’s evolution up to the age in \mathbf{x} , predicting L_{bol} and L_{XUV}/L_{bol} to evaluate $\ln \mathcal{L}$. We discard the first 500 iterations as burn-in and assess the convergence of our MCMC chains by computing the integrated autocorrelation length and acceptance fraction for each chain. We find a mean acceptance fraction of 0.48 and a minimum and mean number of iterations per integrated autocorrelation length of 93 and 132, respectively, indicating that our chains have converged (Foreman-Mackey et al., 2013). Given our integrated autocorrelation lengths, our MCMC chain yielded about 10,000 effective samples from the posterior distribution.

6.2.5 Inference with approxposterior

The methods presented above can be applied to any late-type star to constrain its L_{XUV} history, given suitable priors and observational constraints. Our MCMC analysis, however, required 4,070 core hours on the University of Washington’s Hyak supercomputer to converge. The main computational cost is incurred by running a \sim 10s VPLanet simulation each MCMC step to evaluate $\ln \mathcal{L}$, requiring \sim 1,000,000 simulations in total for the full MCMC analysis. Assuming similar convergence properties, repeating this analysis for even a modest sample of 30 stars would require \sim 122,000 core-hours, a significant computational expense. Moreover, performing a similar analysis with a more computationally-expensive model would only exacerbate this issue.

To mitigate the computational cost, we apply `approxposterior`³, an open source Python machine learning package (Fleming and VanderPlas, 2018), to compute an accurate approximation to the true MCMC-derived posterior distribution for TRAPPIST-1’s XUV evolution. `approxposterior`, a modified implementation of the “Bayesian Active Learning for Posterior Estimation” (BAPE) algorithm of Kandasamy et al. (2017), trains a Gaussian process (GP, see Rasmussen and Williams (2006)) replacement for the Inprobability evaluation, learning on the results of VPLanet simulations. The GP is then used within an MCMC sampling algorithm, e.g. `emcee`, to quickly obtain the posterior distribution. In our case, predicting the Inprobability using the GP (\sim 130 μ s) is 80,000 \times faster than running VPLanet (10s) each Inprobability evaluation, yielding a massive reduction in computational cost.

Following Kandasamy et al. (2017), `approxposterior` iteratively improves the GP’s predictive ability by identifying high-likelihood regions in parameter space, and hence high posterior density regions, where the GP predictions are uncertain. `approxposterior` then evaluates VPLanet in those regions to supplement the training set, improving the GP’s predictive ability in the relevant regions of parameter space, while minimizing the number of forward model evaluations required for suitable predictive accuracy. Similar techniques using a GP surrogate model have been shown to rapidly and accurately infer Bayesian posterior distributions for computationally-

³`approxposterior` is publicly available at <https://github.com/dflemin3/approxposterior>.

expensive cosmology studies (e.g. Bird et al., 2019; McClintock and Rozo, 2019).

To model the covariance between points in the GP training set, we use a squared exponential kernel,

$$k(x_i, x_j) = \exp\left(-\frac{(x_i - x_j)^2}{2l^2}\right), \quad (6.4)$$

where x_i and x_j are two arbitrary points in parameter space and l is a hyperparameter that controls the scale length of the correlations. We assume correlations in each dimension have different scale lengths and fit for each l by optimizing the GP’s marginal likelihood of the training set data using Powell’s method (Powell, 1964), randomly restarting this optimization 10 times to mitigate the influence of local extrema. To ensure our solution is numerically stable, we add a small white noise term of $\ln(\sigma_w) = -15$ to the diagonal of the GP covariance matrix.

We initially trained the GP on a set of 50 VPLanet simulations with initial conditions sampled from our prior distributions. We then ran `approxposterior` until it converged after 7 iterations. Each iteration, `approxposterior` selected 100 new training points according to the Kandasamy et al. (2017) point selection criterion. `approxposterior` ran VPLanet at each point for a total of 750 training samples. The trained GP was then used within `emcee` to quickly obtain the approximate posterior distribution following the same MCMC sampling procedure described above. In § 5.2, we provide additional information about the `approxposterior` algorithm and its convergence properties.

6.3 Results

6.3.1 The Evolution of TRAPPIST-1

In Fig. 6.1, we display the posterior probability distributions for our model parameters derived using MCMC with VPLanet and `emcee`. We adopt the median values of the marginal distributions as our best-fit solutions and derive the lower and upper uncertainties using the 16th and 84th percentiles, respectively. We list these values in Table 6.2.

TRAPPIST-1 likely maintained a large L_{XUV} throughout its lifetime as we find $f_{sat} = -3.03^{+0.23}_{-0.12}$ and $t_{sat} = 6.64^{+3.53}_{-3.13}$ Gyr, consistent with observed L_{XUV}/L_{bol} and long activity lifetimes of late M

dwarfs (West et al., 2008; Wright et al., 2018). The long upper-tail in the marginal f_{sat} distribution arises from the combination of the degeneracy between f_{sat} and t_{sat} and from our strong empirical f_{sat} prior that disfavors $f_{sat} \gtrsim -2.5$. The degeneracy stems from our model attempting to match TRAPPIST-1’s observed L_{XUV}/L_{bol} . For example, larger values of f_{sat} produce high initial L_{XUV}/L_{bol} , requiring shorter t_{sat} , and hence an earlier transition to unsaturated L_{XUV}/L_{bol} decay, to decrease L_{XUV}/L_{bol} to its observed value, and vice versa.

Although our t_{sat} prior distribution, based on empirical measurements of late M-dwarfs (see § 6.2.3), equally favors both short and long saturation timescales, the marginal posterior density for t_{sat} steeply declines for $t_{sat} \lesssim 4$ Gyr. This decline implies that ultracool dwarfs like TRAPPIST-1 likely remain saturated for many Gyrs. Our analysis strongly disfavors short saturation timescales, with only a 0.5% chance that $t_{sat} \leq 1$ Gyr, the saturation timescale adopted by Luger and Barnes (2015) in their analysis of water loss from exoplanets orbiting in the habitable zone of late M dwarfs and in Lincowski et al. (2018). From the posterior distribution, we infer that there is a 40% chance that TRAPPIST-1 is still in the high- L_{XUV}/L_{bol} saturated phase today, suggesting that the TRAPPIST-1 planets could have undergone prolonged volatile loss.

The marginal age and β_{XUV} posterior distributions reflect their prior distributions as for the former, L_{bol} is not sufficient to constrain TRAPPIST-1’s age beyond our adopted prior because the luminosities of ultracool dwarfs do not significantly change during the main sequence (Baraffe et al., 2015). The marginal posterior for β_{XUV} does not vary from the prior because our XUV model is over-parameterized with 3 parameters to fit 2 observations, although all are motivated by empirical data and hence merit inclusion. Our model prefers to exploit the degeneracy between f_{sat} and t_{sat} to match TRAPPIST-1’s observed L_{XUV} in our MCMC instead of varying the slope of the unsaturated L_{XUV} decay. Even though our model is over-parameterized, the observations of TRAPPIST-1 used to condition our probabilistic model do in fact influence the posterior distribution as the reduction in posterior variance relative to the prior can be seen in the joint posterior and marginal distributions of Fig. 6.1 for m_* , f_{sat} , and t_{sat} .

In the joint posterior distribution, age and β_{XUV} weakly correlate with f_{sat} , requiring a narrow spread of $f_{sat} \approx -3.05$ for young ages and steeper β_{XUV} , respectively. β_{XUV} and t_{sat} are uncorre-

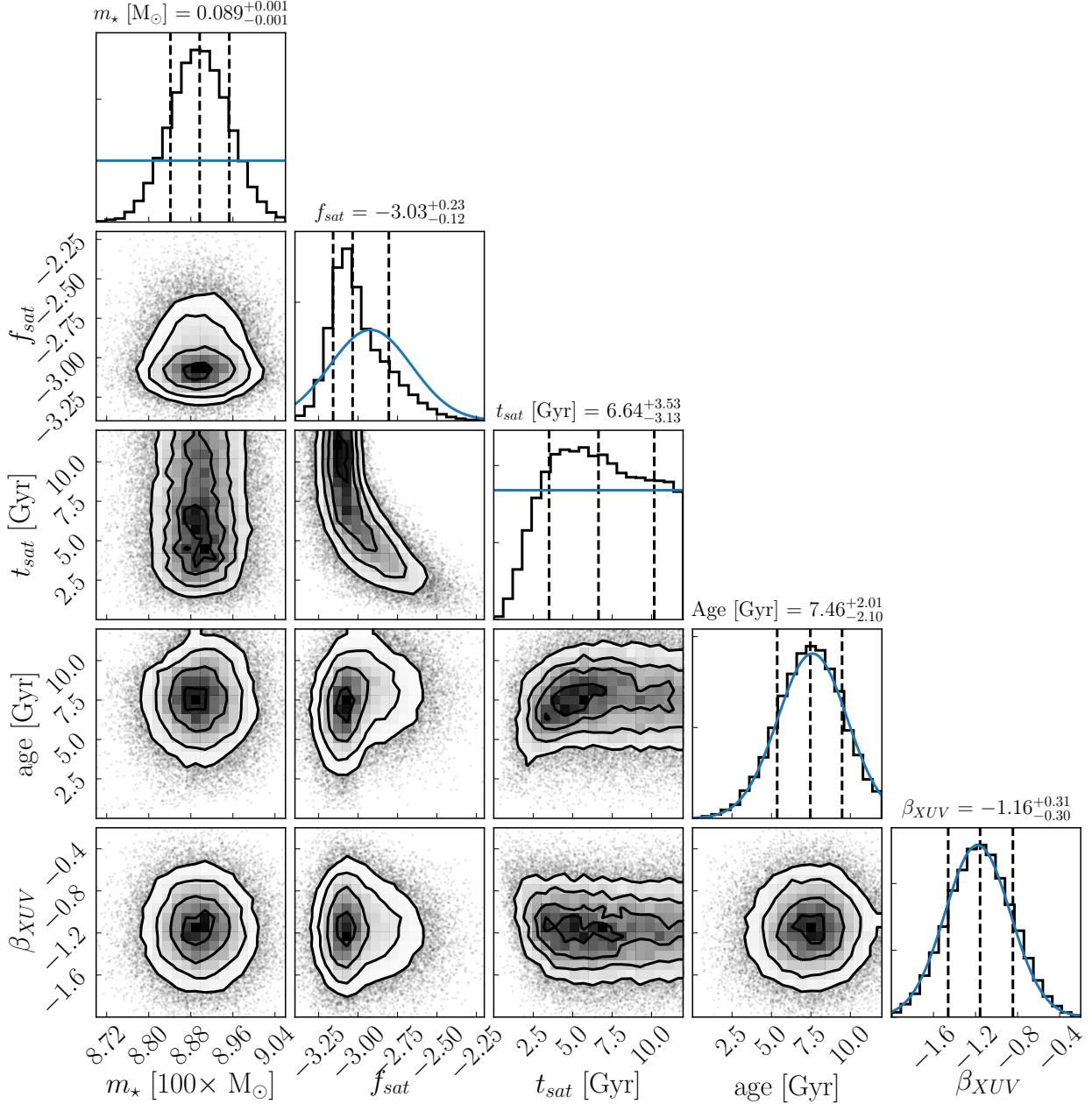


Figure 6.1: Joint and marginal posterior probability distributions for the TRAPPIST-1 stellar parameters given in Eqn. (6.2) made using `corner` (Foreman-Mackey, 2016). The black vertical dashed lines on the marginal distributions indicate the median values and lower and upper uncertainties from the 16th and 84th percentiles, respectively. The blue curves superimposed on the marginal distributions display the adopted prior probability distribution for each parameter. From the posterior, we infer that there is a 40% chance that TRAPPIST-1 is still in the saturated phase today.

lated, except at short t_{sat} where steep β_{XUV} are disfavored as this evolution would underpredict the observed L_{XUV} . We constrain TRAPPIST-1’s mass to $m_\star = 0.089 \pm 0.001 M_\odot$, in a good agreement with and 6× more precise than the value derived by Van Grootel et al. (2018). In § 6.3.3, we consider how this mass constrain impacts TRAPPIST-1’s predicted radius.

Finally, we estimate the Monte Carlo standard error (MCSE) for each model parameter. The MCSE does not reflect the inherent probabilistic uncertainty in our model that arises from conditioning on data with uncertainties, but rather it approximates the error incurred by estimating parameters using an ensemble of MCMC chains of finite length. Using the batch means method (Flegal et al., 2008; Flegal and Jones, 2010), we find MCSEs for m_\star , f_{sat} , t_{sat} , age, and β_{XUV} of 3.41×10^{-6} , 1.23×10^{-3} , 2.0×10^{-2} , 1.30×10^{-2} , and 2.12×10^{-3} , respectively. These errors are much less than the posterior uncertainty and can be safely ignored.

6.3.2 Comparison with `approxposterior`

We compare the approximate posterior distribution derived using `approxposterior` with our previous results (referred to as the fiducial MCMC). We display the approximate joint and marginal posterior distributions in Fig. 6.2 and list the marginal constraints derived by both methods in Table 6.2.

As seen in Fig. 6.2, `approxposterior` recovers the non-trivial correlations between model parameters seen in the fiducial MCMC posterior distribution. We emphasize this good agreement by overplotting the `approxposterior` estimated posterior distribution (blue) on top of the fiducial MCMC results (black) in Fig. 6.3.

Our parameter constraints derived using `approxposterior` are in good agreement with those inferred using `emcee`. We find average errors in parameter medians and 1σ uncertainties of 0.61% and 5.5%, respectively, relative to the constraints deriving using `emcee`. These differences are larger than the MCSEs because the GP employed by `approxposterior` is an accurate, yet imperfect, surrogate for the lnprobability calculation. `approxposterior` tends to underestimate parameter uncertainties by a few percent because its algorithm preferentially selects high-likelihood points to expand its training set (see § 5.3.1). This concentration of high-likelihood

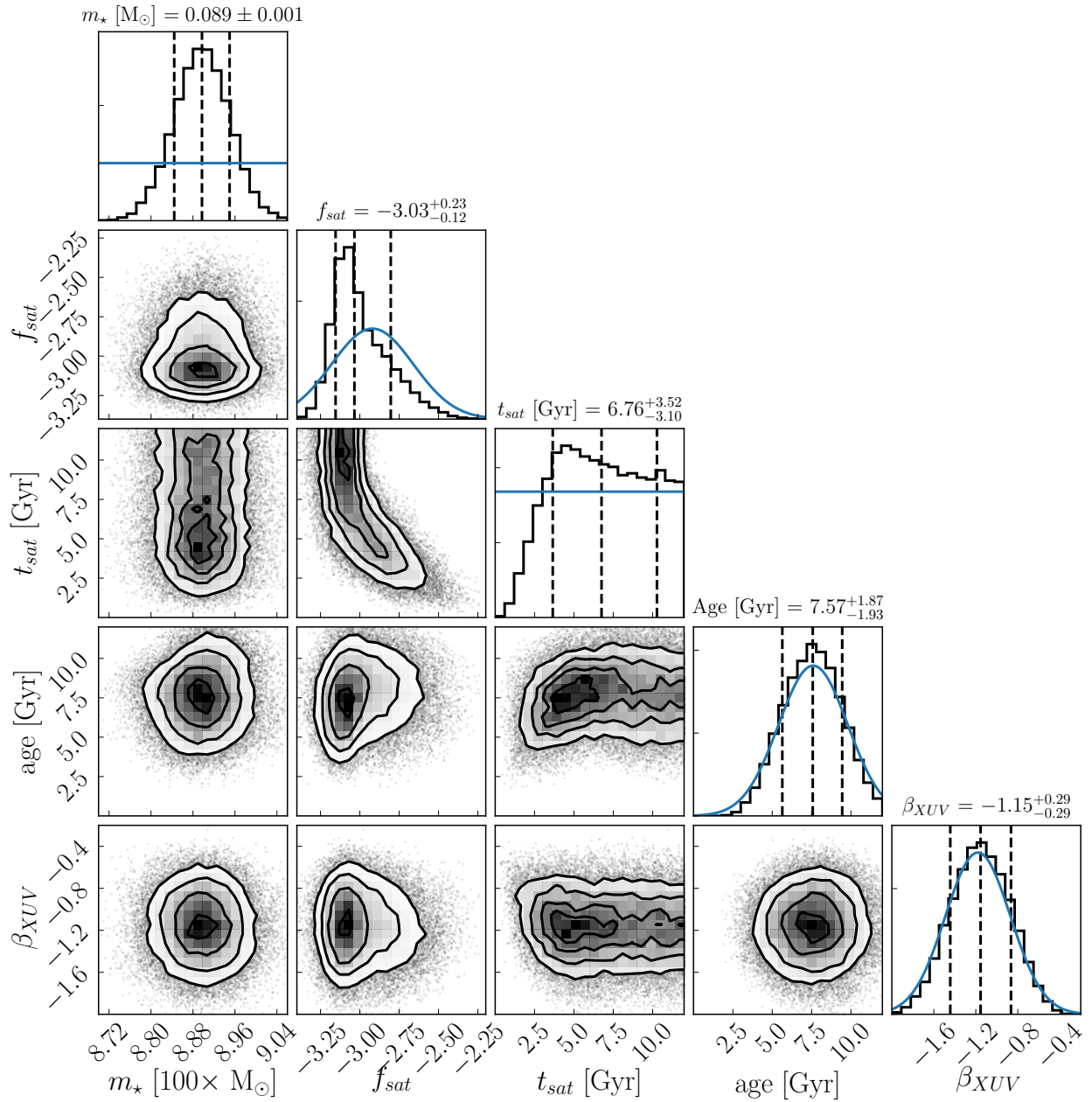


Figure 6.2: Same format as Fig. 6.1, but derived by `approxposterior`. `approxposterior` recovered constraints and parameter correlations that are in good agreement with the emcee MCMC, but requiring $980\times$ less computational resources.

points slightly biases the inferred GP scale lengths, l , towards smaller values, effectively overfitting. The smaller values of l shrink the estimated posterior distribution, producing the underestimated parameter uncertainties. We mitigate this effect by adding a small white noise term to the diagonal of the GP covariance matrix.

Not only can `approxposterior` accurately recover Bayesian parameter constraints and correlations, it does so extremely quickly. `approxposterior` requires only about 4 core hours to estimate the approximate posterior distribution, a factor of $980\times$ faster than our fiducial MCMC. Moreover, `approxposterior` used $1330\times$ fewer `VPLanet` simulations to build its training set than the $\sim 10^6$ simulations ran by the fiducial MCMC for likelihood evaluations. This reduction in computational expense arises from a combination of `approxposterior`'s GP-based Inprobability predictions only taking $\sim 130\mu\text{s}$, compared to the much longer 10s per `VPLanet` simulation, and its intelligent iterative training set augmentation algorithm. `approxposterior`'s efficient selection of the GP's training set focuses on high-likelihood regions to improve the GP's predictive ability in relevant regions of parameter space while minimizing the training set size.

Our findings demonstrate that `approxposterior` can be used to estimate accurate approximations to the posterior probability distributions of the parameters that control stellar XUV evolution in late M dwarfs, but significantly faster than traditional MCMC methods. Note that `approxposterior` is agnostic to the underlying forward model it learns on, enabling Bayesian parameter inference with other computationally-expensive forward models.

6.3.3 TRAPPIST-1's Evolutionary History and Its Planets' XUV Environment

Here we consider plausible stellar evolutionary histories for TRAPPIST-1 by simulating 100 samples from the posterior distribution. We plot the evolution of TRAPPIST-1's L_{bol} , L_{XUV} , and radius in Fig. 6.4 and compare our models to the measured values.

TRAPPIST-1 remains saturated throughout its 1 Gyr-long pre-main sequence, with both L_{XUV} and L_{bol} decreasing by a factor of ~ 40 before stabilizing on the main sequence. TRAPPIST-1's radius likely shrank by roughly a factor of 4 along the pre-main sequence. We derive a present-day radius $R_\star = 0.112 \pm 0.001 R_\odot$ from the posterior distribution, a value that is $\sim 7\%$ smaller

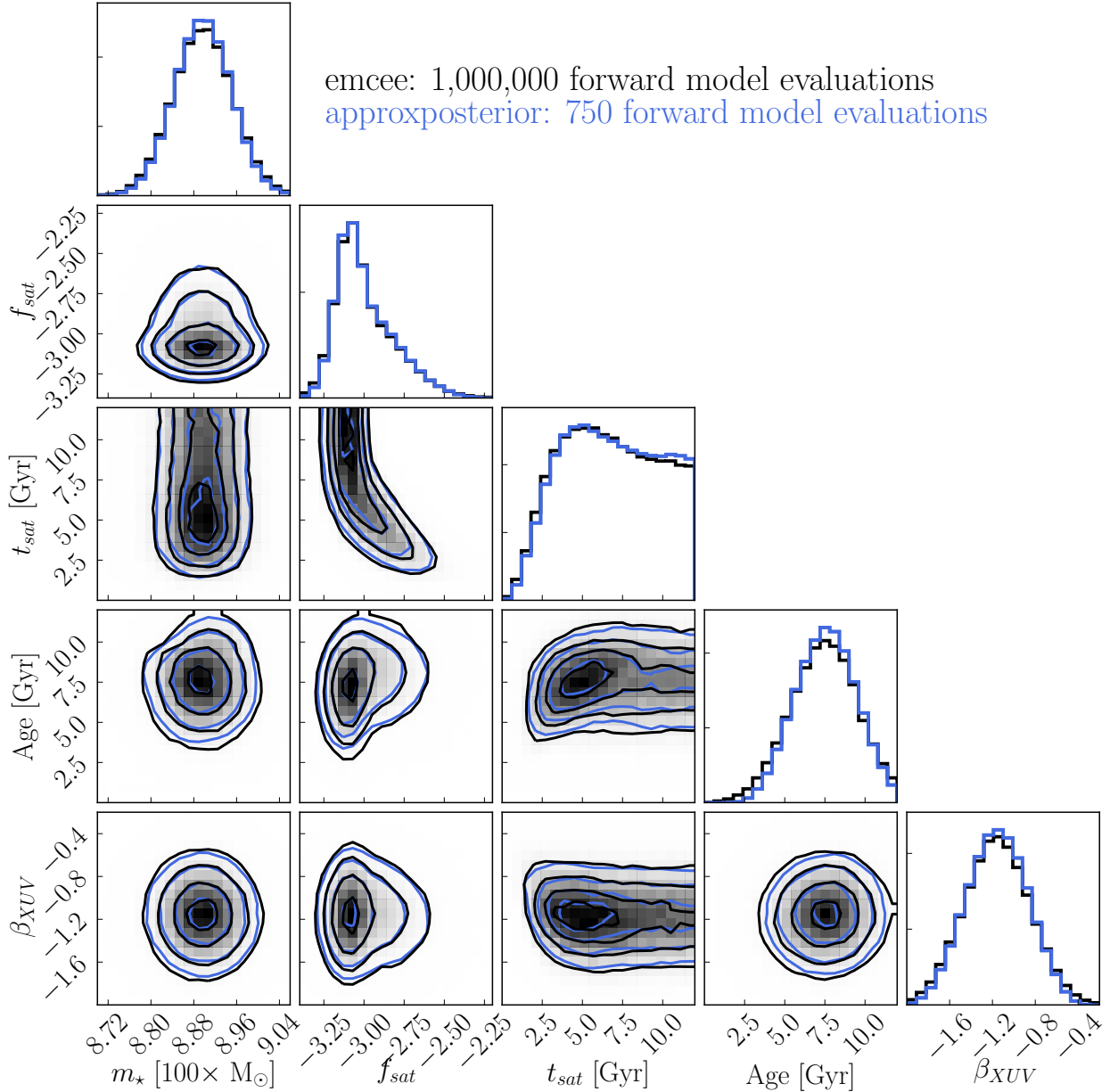


Figure 6.3: Same format as Fig. 6.1, but with the fiducial posterior distribution in black and the approxposterior-derived posterior distribution in blue. The joint and marginal posterior distributions estimated by approxposterior are in excellent agreement with our fiducial emcee-derived results.

Table 6.2. Parameter Constraints and Errors

| Parameter [units] | VPLanet-emcee MCMC | AP MCMC | AP Relative Error | Monte Carlo Error |
|---------------------|---------------------------|---------------------------|-------------------|-----------------------|
| m_* [M_\odot] | $0.089^{+0.001}_{-0.001}$ | $0.089^{+0.001}_{-0.001}$ | <0.1% | 3.41×10^{-6} |
| f_{sat} | $-3.03^{+0.23}_{-0.12}$ | $-3.03^{+0.23}_{-0.12}$ | <0.1% | 1.23×10^{-3} |
| t_{sat} [Gyr] | $6.64^{+3.53}_{-3.13}$ | $6.76^{+3.52}_{-3.10}$ | 1.81% | 2.0×10^{-2} |
| age [Gyr] | $7.46^{+2.01}_{-2.10}$ | $7.57^{+1.87}_{-1.93}$ | 1.47% | 1.30×10^{-3} |
| β_{XUV} | $-1.16^{+0.31}_{-0.30}$ | $-1.15^{+0.29}_{-0.29}$ | 0.86% | 2.12×10^{-3} |
| P(saturated) | 0.40 | 0.39 | 2.5% | 3.30×10^{-3} |

Note. — Best fit values and uncertainties are derived using the medians, 16th, and 84th percentiles from the marginal posterior distributions, respectively. Here, AP is shorthand for approxposterior. P(saturated) indicates the posterior probability that TRAPPIST-1 is still in the saturated regime today. The relative errors are computed as the absolute percent difference between the best fit values derived by emcee and approxposterior. The approxposterior-derived results are in good agreement with the fiducial emcee MCMC.

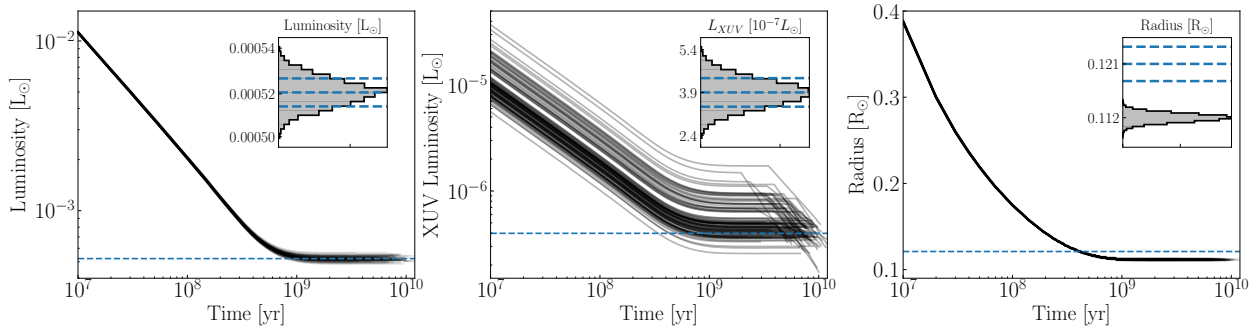


Figure 6.4: Plausible evolutionary histories of TRAPPIST-1’s L_{bol} (left), L_{XUV} (center), and radius (right) using 100 samples drawn from the posterior distribution and simulated with VPLanet. In each panel, the blue shaded regions display the 1, 2, and 3 σ uncertainties. The insets display the marginal distributions (black) evaluated at the age of the system, with the blue dashed lines indicating the observed value and $\pm 1 \sigma$ uncertainties. The radius, L_{bol} , and L_{XUV} constraints are adopted from Van Grootel et al. (2018) and Wheatley et al. (2017), respectively, by convolving the Van Grootel et al. (2018) L_{bol} measurement with the L_{XUV}/L_{bol} constraints from Wheatley et al. (2017).

than the Van Grootel et al. (2018) constraint, $R_\star = 0.121 \pm 0.003 R_\odot$, that was computed from their inferred mass and TRAPPIST-1’s density (Delrez et al., 2018). This difference arises from the likely underprediction of TRAPPIST-1’s radius by the Baraffe et al. (2015) models, consistent with stellar evolution models often underestimating the radii of late M dwarfs (Reid and Hawley, 2005; Spada et al., 2013).

An alternate explanation to account for its inflated radius is that TRAPPIST-1 has super-solar metallicity (Burgasser and Mamajek, 2017; Van Grootel et al., 2018), but Van Grootel et al. (2018) found in their modeling that TRAPPIST-1 required a metallicity of $[Fe/H] = 0.4$ to reproduce its density and radius. Van Grootel et al. (2018) show that as this result is 4.5σ off from the best fit value from Gillon et al. (2016), who found $[Fe/H] = 0.04 \pm 0.08$. The super-solar hypothesis is therefore strongly disfavored by the observational data. If we instead compute the radius from our marginal stellar mass posterior distribution and the observed density (Delrez et al., 2018), we obtain $R_\star = 0.120 \pm 0.002 R_\odot$, in agreement with Van Grootel et al. (2018) who used the same procedure.

Since TRAPPIST-1 could still be saturated today, its planetary system has likely experienced a persistent extreme XUV environment. In Fig. 6.5, we probe the distribution of XUV fluxes, F_{XUV} , derived from our posterior distributions for each TRAPPIST-1 planet when the system was 0.01, 0.1, and 1 Gyr old. We normalize these values by the F_{XUV} received by Earth during the mean solar cycle ($F_{XUV,\oplus} = 3.88 \text{ erg s}^{-1}\text{cm}^{-2}$, Ribas et al., 2005) and assume the planets remained near their current semi-major axes after migration in the natal protoplanetary disk halted (Luger et al., 2017).

We infer that TRAPPIST-1b likely received extreme $F_{XUV}/F_{XUV,\oplus} \gtrsim 10^4$ during the early pre-main sequence before decaying to the present-day $F_{XUV}/F_{XUV,\oplus} \approx 10^3$, consistent with estimates from Wheatley et al. (2017). The extended upper-tail of the F_{XUV} distributions corresponds to the large f_{sat} values permitted by the posterior distributions. The likely habitable zone planets, e, f, and g, similarly experienced severe XUV fluxes ranging from $F_{XUV}/F_{XUV,\oplus} \approx 10^2 - 10^{3.5}$ throughout the pre-main sequence. Even today, e, f, and g receive $F_{XUV}/F_{XUV,\oplus} \approx 10^2$, far in excess of the modern Earth, due to TRAPPIST-1’s large present L_{XUV} , its extended saturated phase, and the close

proximity of M dwarf HZ planets to their host star. These significant high energy fluxes likely drove an extended epoch of substantial atmospheric escape and water loss from the TRAPPIST-1 planets, potentially producing substantial abiotic O₂ atmospheres (Luger and Barnes, 2015; Bolmont et al., 2017; Bourrier et al., 2017a).

6.4 Discussion and Conclusions

Here, we used MCMC to derive probabilistic constraints for TRAPPIST-1’s stellar and L_{XUV} evolution to characterize the evolving XUV environment of its planetary system. We inferred that TRAPPIST-1 likely maintained high $L_{XUV}/L_{bol} \approx 10^{-3}$ throughout its lifetime, with a 40% chance that TRAPPIST-1 is still in the saturated regime today. Our results indicate that at least some ultracool dwarfs can sustain large L_{XUV} in the saturated regime for Gyrs, consistent with activity lifetimes of late M dwarfs (West et al., 2008). We suggest that studies of volatile loss from planets orbiting ultracool dwarfs model the long-term L_{XUV} evolution of the host star, or at least assume saturation timescales of $t_{sat} \gtrsim 4$ Gyrs. Our choice of prior distributions strongly impacts our results as our inference hinges on only two measured properties of TRAPPIST-1, L_{XUV} and L_{bol} . To mitigate this effect, we consulted previous studies and empirical observations of the activity evolution of late M dwarfs to construct realistic prior distributions.

The TRAPPIST-1 planets likely experienced significant XUV fluxes during the pre-main sequence, potentially driving extreme atmospheric erosion and water loss (Bolmont et al., 2017; Bourrier et al., 2017a). The high-energy fluxes incident on the inner-most planets throughout this phase were probably large enough for atmospheric mass loss to be recombination-limited ($F_{UV} \gtrsim 10^4 \text{ g s}^{-1} \text{ cm}^{-2}$) and scale as $\dot{m} \sim F_{XUV}^{0.6}$ (Murray-Clay et al., 2009), as opposed to the oft-assumed energy-limited escape ($\dot{m} \sim F_{XUV}$, Watson et al., 1981; Lammer et al., 2003), potentially inhibiting volatile loss. If the TRAPPIST-1 planets did lose significant amounts of water as our estimates suggest, they must have formed with a large initial volatile inventory to account for their observed low densities (Grimm et al., 2018).

We demonstrated that the open source Python machine learning package, `approxposterior` (Fleming and VanderPlas, 2018), can efficiently compute an accurate approximation to the poste-

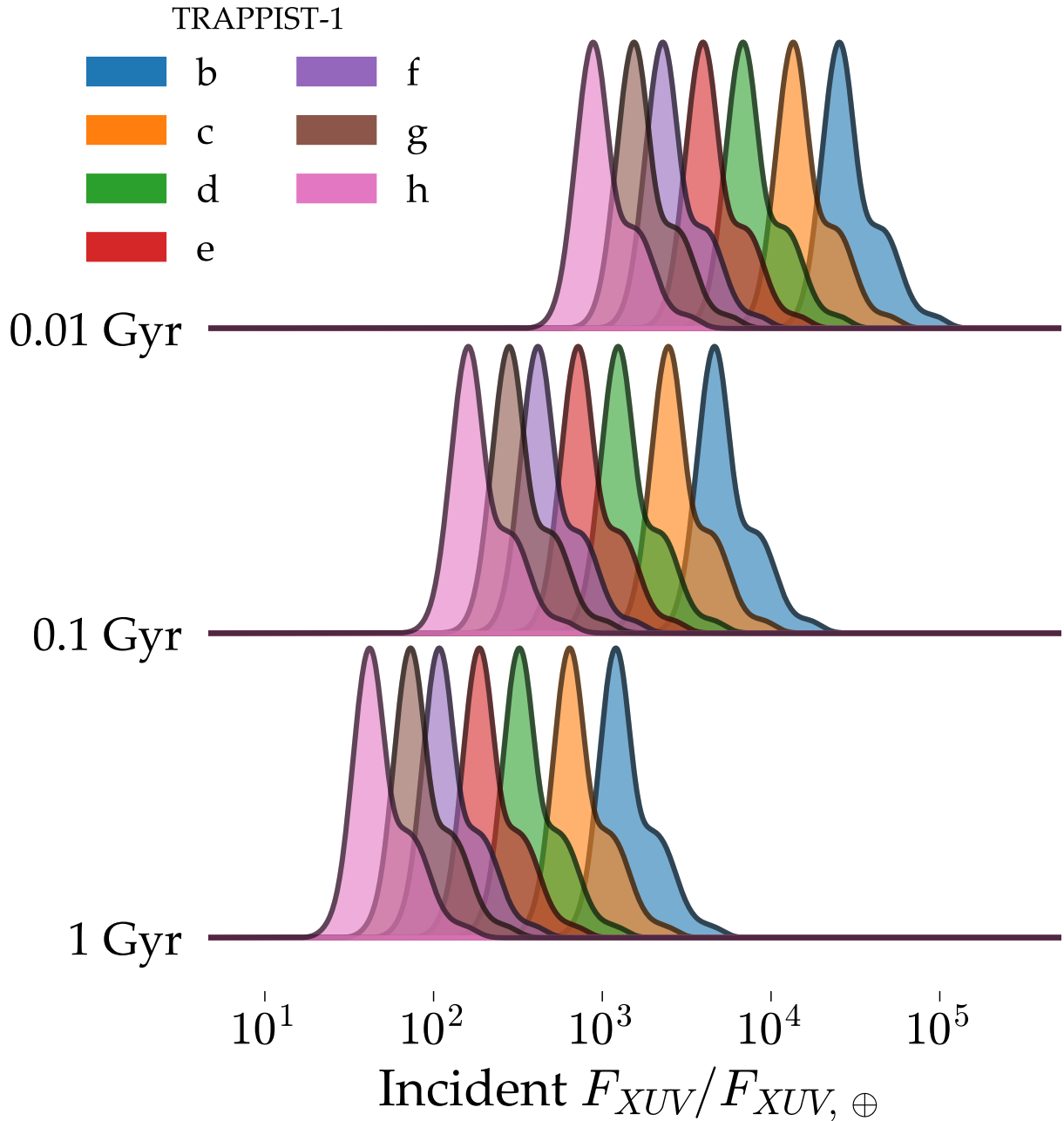


Figure 6.5: $F_{XUV}/F_{XUV,\oplus}$ for each TRAPPIST-1 planet derived from samples drawn from the posterior distribution and simulated using VPPlanet when the system was 0.01, 0.1, and 1 Gyr old. The latter age corresponds to the approximate age at which TRAPPIST-1 entered the main sequence. The TRAPPIST-1 planetary system has likely endured a long-lasting extreme XUV environment.

rior distribution using an adaptive learning GP-based method, requiring $1330 \times$ fewer VP_{lanet} simulations and a factor of $980 \times$ less core hours than traditional MCMC approaches. The posterior distributions derived by `approxposterior` reproduced the non-trivial parameter correlations and best-fit values uncovered by our fiducial MCMC analysis. We find that `approxposterior` recovers the best-fit values and 1σ uncertainties of our model parameters with an average error of 0.61% and 5.5%, respectively, relative to our constraints derived using `emcee`. If future observations of TRAPPIST-1 refine its fundamental parameters, and possibly L_{XUV}/L_{bol} , `approxposterior` can be used to rapidly and accurately replicate our analysis to update our constraints.

Finally, we note that our methodology constrains parameters that describe the long-term XUV evolution of TRAPPIST-1, conditioned on measurements. In principle, this approach can be extended to obtain evolutionary histories of planetary systems in general. For example, in Figures 6.4 and 6.5, we examined the long-term evolution of TRAPPIST-1 and the evolving XUV fluxes received by its planetary system, respectively, with samples drawn from the posterior distribution. Future research can combine those results with additional physical effects, e.g. water loss or tidal dissipation, to build a probabilistic model for the long-term evolution of the planetary system, given our model for the underlying physics, to characterize its present state. In other words we could infer the evolutionary history of a planet or planetary system given suitable observational constraints. While simulating additional physical effects will inevitably increase the computational expense, we have demonstrated that `approxposterior` can enable such efforts and provide insight into the histories of stars and their planets.

6.5 Acknowledgments

We thank the anonymous referee for their careful reading of our manuscript and insightful comments. This work was facilitated through the use of advanced computational, storage, and networking infrastructure provided by the Hyak supercomputer system and funded by the Student Technology Fund at the University of Washington. DPF was supported by NASA Headquarters under the NASA Earth and Space Science Fellowship Program - Grant 80NSSC17K0482. This

work was supported by the NASA Astrobiology Program Grant Number 80NSSC18K0829 and benefited from participation in the NASA Nexus for Exoplanet Systems Science research coordination network. Software: `approxposterior`: Fleming and VanderPlas (2018), `corner`: Foreman-Mackey (2016), `emcee`: Foreman-Mackey et al. (2013), `george`: Ambikasaran et al. (2014), `VPLanet`: Barnes et al. (2019)

Chapter 7

CONCLUSIONS

In Chapter 1, I... XXX The recent discoveries of circumbinary planets by *Kepler* raise questions for contemporary planet formation models. Understanding how these planets form requires characterizing their formation environment, the circumbinary protoplanetary disc, and how the disc and binary interact and change as a result. The central binary excites resonances in the surrounding protoplanetary disc that drive evolution in both the binary orbital elements and in the disc. To probe how these interactions impact binary eccentricity and disk structure evolution, N-body smooth particle hydrodynamics (SPH) simulations of gaseous protoplanetary disks surrounding binaries based on Kepler 38 were run for 10^4 binary periods for several initial binary eccentricities. We find that nearly circular binaries weakly couple to the disc via a parametric instability and excite disc eccentricity growth. Eccentric binaries strongly couple to the disc causing eccentricity growth for both the disc and binary. Disks around sufficiently eccentric binaries that strongly couple to the disc develop an $m = 1$ spiral wave launched from the 1:3 eccentric outer Lindblad resonance (EOLR) that corresponds to an alignment of gas particle longitude of periastrons. All systems display binary semi-major axis decay due to dissipation from the viscous disc.

In Chapter 2, I... XXX We outline a mechanism that explains the observed lack of circumbinary planets (CBPs) via coupled stellar-tidal evolution of isolated binary stars. Tidal forces between low-mass, short-period binary stars on the pre-main sequence slow the stellar rotations, transferring rotational angular momentum to the orbit as the stars approach the tidally locked state. This transfer increases the binary orbital period, expanding the region of dynamical instability around the binary, and destabilizing CBPs that tend to preferentially orbit just beyond the initial dynamical stability limit. After the stars tidally lock, we find that angular momentum loss due to magnetic braking can significantly shrink the binary orbit, and hence the region of dynamical stability, over time

impacting where surviving CBPs are observed relative to the boundary. We perform simulations over a wide range of parameter space and find that the expansion of the instability region occurs for most plausible initial conditions and that in some cases, the stability semi-major axis doubles from its initial value. We examine the dynamical and observable consequences of a CBP falling within the dynamical instability limit by running N-body simulations of circumbinary planetary systems and find that typically, at least one planet is ejected from the system. We apply our theory to the shortest period *Kepler* binary that possesses a CBP, Kepler-47, and find that its existence is consistent with our model. Under conservative assumptions, we find that coupled stellar-tidal evolution of pre-main sequence binary stars removes at least one close-in CBP in 87% of multi-planet circumbinary systems.

In Chapter 3, I examine how tides, stellar evolution, and magnetic braking shape the P_{rot} evolution of low-mass stellar binaries up to P_{orb} of 100 d across a wide range tidal dissipation parameters using two common equilibrium tidal models. I find that many binaries with $P_{orb} \lesssim 20$ d tidally lock, and most with $P_{orb} \lesssim 4$ d tidally lock into synchronous rotation on circularized orbits. At short P_{orb} , tidal torques produce a population of fast rotators that single-star only models of magnetic braking fail to produce. In many cases, I show that the competition between magnetic braking and tides produces a population of subsynchronous rotators that persists for Gyrs, even in short P_{orb} binaries, qualitatively reproducing the subsynchronous eclipsing binaries (EBs) discovered in the *Kepler* field by Lurie et al. (2017). Both equilibrium tidal models predict that binaries can tidally-interact out to $P_{orb} \approx 80$ d, while the Constant Phase Lag tidal model predicts that binaries can tidally lock out to $P_{orb} \approx 100$ d. Tidal torques often force the P_{rot} evolution of stellar binaries to depart from the long-term magnetic braking-driven spin down experienced by single stars, revealing that P_{rot} is not be a valid proxy for age in all cases, i.e. gyrochronology can underpredict ages by up to 300% unless one accounts for binarity. I conclude this Chapter by suggesting how accurate determinations of orbital eccentricities and P_{rot} can be used to discriminate between which equilibrium tidal models best describes tidal interactions in low-mass binary stars.

In Chapter 4, I introduce `approxposterior`, an open source Python machine learning package for approximate Bayesian inference using Gaussian process regression. XXX

Finally, in Chapter 5, I model the long-term XUV luminosity of TRAPPIST-1 to constrain the evolving high-energy radiation environment experienced by its planetary system. Using Markov Chain Monte Carlo (MCMC), I derive probabilistic constraints for TRAPPIST-1’s stellar and XUV evolution that account for observational uncertainties, degeneracies between model parameters, and empirical data of low-mass stars. I constrain TRAPPIST-1’s mass to $m_* = 0.089 \pm 0.001 M_\odot$ and find that its early XUV luminosity likely saturated at $\log_{10}(L_{XUV}/L_{bol}) = -3.03^{+0.23}_{-0.12}$. From the posterior distribution, I infer that there is a $\sim 40\%$ chance that TRAPPIST-1 is still in the saturated phase today, suggesting that TRAPPIST-1 has maintained high activity and $L_{XUV}/L_{bol} \approx 10^{-3}$ for several Gyrs. TRAPPIST-1’s planetary system therefore likely experienced a persistent and extreme XUV flux environment, potentially driving significant atmospheric erosion and volatile loss. The inner planets likely received XUV fluxes $\sim 10^3 - 10^4 \times$ that of the modern Earth during TRAPPIST-1’s ~ 1 Gyr-long pre-main sequence phase. Deriving these constraints via MCMC is computationally non-trivial, so scaling my methods to constrain the XUV evolution of a larger number of M dwarfs that harbor terrestrial exoplanets would incur significant computational expenses. I demonstrate that `approxposterior` accurately and efficiently replicates my analysis using 980 times less computational time and 1330 times fewer simulations than MCMC sampling using `emcee`. I find that `approxposterior` derives constraints with mean errors on the best fit values and 1σ uncertainties of 0.61% and 5.5%, respectively, relative to `emcee`.

BIBLIOGRAPHY

- Agüeros, M. A., Covey, K. R., Lemonias, J. J., Law, N. M., Kraus, A., Batalha, N., Bloom, J. S., Cenko, S. B., Kasliwal, M. M., Kulkarni, S. R., Nugent, P. E., Ofek, E. O., Poznanski, D., and Quimby, R. M. (2011). The Factory and the Beehive. I. Rotation Periods for Low-mass Stars in Praesepe. *ApJ*, 740:110.
- Alexander, R. (2012). The Dispersal of Protoplanetary Disks around Binary Stars. *ApJ*, 757:L29.
- Allain, S. (1998). Modelling the angular momentum evolution of low-mass stars with core-envelope decoupling. *A&A*, 333:629–643.
- Aly, H., Dehnen, W., Nixon, C., and King, A. (2015). Misaligned gas discs around eccentric black hole binaries and implications for the final-parsec problem. *MNRAS*, 449(1):65–76.
- Ambikasaran, S., Foreman-Mackey, D., Greengard, L., Hogg, D. W., and O’Neil, M. (2014). Fast Direct Methods for Gaussian Processes.
- Andronov, N., Pinsonneault, M. H., and Terndrup, D. M. (2006). Mergers of Close Primordial Binaries. *ApJ*, 646:1160–1178.
- Armitage, P. J. and Natarajan, P. (2005). Eccentricity of Supermassive Black Hole Binaries Coalescing from Gas-rich Mergers. *ApJ*, 634:921–927.
- Armstrong, D. J., Osborn, H. P., Brown, D. J. A., Faedi, F., Gómez Maqueo Chew, Y., Martin, D. V., Pollacco, D., and Udry, S. (2014). On the abundance of circumbinary planets. *MNRAS*, 444:1873–1883.
- Artymowicz, P. (1992). Dynamics of Binary and Planetary System Interaction with Disks: Eccentricity Changes. *PASP*, 104:769.

- Artymowicz, P., Clarke, C. J., Lubow, S. H., and Pringle, J. E. (1991). The effect of an external disk on the orbital elements of a central binary. *ApJ*, 370:L35–L38.
- Artymowicz, P. and Lubow, S. H. (1994). Dynamics of binary-disk interaction. 1: Resonances and disk gap sizes. *ApJ*, 421:651–667.
- Artymowicz, P. and Lubow, S. H. (1996). Mass Flow through Gaps in Circumbinary Disks. *ApJ*, 467:L77.
- Backus, I. and Quinn, T. (2016). Fragmentation of protoplanetary discs around M-dwarfs. *MNRAS*, 463(3):2480–2493.
- Balsara, D. S. (1995). von Neumann stability analysis of smooth particle hydrodynamics—suggestions for optimal algorithms. *Journal of Computational Physics*, 121(2):357–372.
- Baraffe, I., Homeier, D., Allard, F., and Chabrier, G. (2015). New evolutionary models for pre-main sequence and main sequence low-mass stars down to the hydrogen-burning limit. *A&A*, 577:A42.
- Barclay, T., Pepper, J., and Quintana, E. V. (2018). A Revised Exoplanet Yield from the Transiting Exoplanet Survey Satellite (TESS). *ApJS*, 239:2.
- Barker, A. J. and Ogilvie, G. I. (2009). On the tidal evolution of Hot Jupiters on inclined orbits. *MNRAS*, 395:2268–2287.
- Barnes, J. R., Jenkins, J. S., Jones, H. R. A., Jeffers, S. V., Rojo, P., Arriagada, P., Jordán, A., Minniti, D., Tuomi, M., Pinfield, D., and Anglada-Escudé, G. (2014). Precision radial velocities of 15 M5-M9 dwarfs. *MNRAS*, 439:3094–3113.
- Barnes, R. (2017). Tidal Locking of Habitable Exoplanets. *ArXiv e-prints*.
- Barnes, R., Deitrick, R., Luger, R., Driscoll, P. E., Quinn, T. R., Fleming, D. P., Guyer, B., McDonald, D. V., Meadows, V. S., Arney, G., Crisp, D., Domagal-Goldman, S. D., Lincowski,

- A., Lustig-Yaeger, J., and Schwieterman, E. (2016). The Habitability of Proxima Centauri b I: Evolutionary Scenarios. *ArXiv e-prints*.
- Barnes, R., Luger, R., Deitrick, R., Driscoll, P., Quinn, T. R., Fleming, D. P., Smotherman, H., McDonald, D. V., Wilhelm, C., Garcia, R., Barth, P., Guyer, B., Meadows, V. S., Bitz, C. M., Gupta, P., Domagal-Goldman, S. D., and Armstrong, J. (2019). VPPlanet: The Virtual Planet Simulator. *arXiv e-prints*.
- Barnes, R., Mullins, K., Goldblatt, C., Meadows, V. S., Kasting, J. F., and Heller, R. (2013). Tidal Venuses: Triggering a Climate Catastrophe via Tidal Heating. *Astrobiology*, 13:225–250.
- Barnes, S. A. (2003). On the Rotational Evolution of Solar- and Late-Type Stars, Its Magnetic Origins, and the Possibility of Stellar Gyrochronology. *ApJ*, 586:464–479.
- Barnes, S. A. (2007). Ages for Illustrative Field Stars Using Gyrochronology: Viability, Limitations, and Errors. *ApJ*, 669:1167–1189.
- Barnes, S. A. (2010). A Simple Nonlinear Model for the Rotation of Main-sequence Cool Stars. I. Introduction, Implications for Gyrochronology, and Color-Period Diagrams. *ApJ*, 722:222–234.
- Bate, M. R. (2000). Predicting the properties of binary stellar systems: the evolution of accreting protobinary systems. *MNRAS*, 314:33–53.
- Bate, M. R., Bonnell, I. A., and Bromm, V. (2002). The formation of close binary systems by dynamical interactions and orbital decay. *MNRAS*, 336:705–713.
- Bellman, R. and Corporation, R. (1957). *Dynamic Programming*. Rand Corporation research study.
- Bennett, D. P., Rhie, S. H., Udalski, A., Gould, A., Tsapras, Y., Kubas, D., Bond, I. A., Greenhill, J., Cassan, A., Rattenbury, N. J., Boyajian, T. S., Luhn, J., Penny, M. T., Anderson, J., Abe, F., Bhattacharya, A., Botzler, C. S., Donachie, M., Freeman, M., Fukui, A., Hirao, Y., Itow, Y., Koshimoto, N., Li, M. C. A., Ling, C. H., Masuda, K., Matsubara, Y., Muraki, Y., Nagakane,

- M., Ohnishi, K., Oyokawa, H., Perrott, Y. C., Saito, T., Sharan, A., Sullivan, D. J., Sumi, T., Suzuki, D., Tristram, P. J., Yonehara, A., Yock, P. C. M., MOA Collaboration, Szymański, M. K., Soszyński, I., Ulaczyk, K., Wyrzykowski, Ł., OGLE Collaboration, Allen, W., DePoy, D., Gal-Yam, A., Gaudi, B. S., Han, C., Monard, I. A. G., Ofek, E., Pogge, R. W., μ FUN Collaboration, Street, R. A., Bramich, D. M., Dominik, M., Horne, K., Snodgrass, C., Steele, I. A., Robonet Collaboration, Albrow, M. D., Bachelet, E., Batista, V., Beaulieu, J.-P., Brillant, S., Caldwell, J. A. R., Cole, A., Coutures, C., Dieters, S., Dominis Prester, D., Donatowicz, J., Fouqué, P., Hundertmark, M., Jørgensen, U. G., Kains, N., Kane, S. R., Marquette, J.-B., Menzies, J., Pollard, K. R., Ranc, C., Sahu, K. C., Wambsganss, J., Williams, A., Zub, M., and PLANET Collaboration (2016). The First Circumbinary Planet Found by Microlensing: OGLE-2007-BLG-349L(AB)c. *AJ*, 152:125.
- Bird, S., Rogers, K. K., Peiris, H. V., Verde, L., Font-Ribera, A., and Pontzen, A. (2019). An emulator for the Lyman- α forest. *J. Cosmology Astropart. Phys.*, 2:050.
- Bodenheimer, P. and Lissauer, J. J. (2014). Accretion and Evolution of $\sim 2.5 M_{\oplus}$ Planets with Voluminous H/He Envelopes. *ApJ*, 791:103.
- Bolmont, E., Gallet, F., Mathis, S., Charbonnel, C., Amard, L., and Alibert, Y. (2017). Tidal dissipation in rotating low-mass stars and implications for the orbital evolution of close-in massive planets. II. Effect of stellar metallicity. *A&A*, 604:A113.
- Bolmont, E. and Mathis, S. (2016). Effect of the rotation and tidal dissipation history of stars on the evolution of close-in planets. *Celestial Mechanics and Dynamical Astronomy*, 126:275–296.
- Bonnell, I. A. and Bate, M. R. (1994). The Formation of Close Binary Systems. *MNRAS*, 271.
- Bourrier, V., de Wit, J., Bolmont, E., Stamenković, V., Wheatley, P. J., Burgasser, A. J., Delrez, L., Demory, B.-O., Ehrenreich, D., Gillon, M., Jehin, E., Leconte, J., Lederer, S. M., Lewis, N., Triaud, A. H. M. J., and Van Grootel, V. (2017a). Temporal Evolution of the High-energy Irradiation and Water Content of TRAPPIST-1 Exoplanets. *AJ*, 154:121.

- Bourrier, V., Ehrenreich, D., Wheatley, P. J., Bolmont, E., Gillon, M., de Wit, J., Burgasser, A. J., Jehin, E., Queloz, D., and Triaud, A. H. M. J. (2017b). Reconnaissance of the TRAPPIST-1 exoplanet system in the Lyman- α line. *A&A*, 599:L3.
- Bouvier, J. (2008). Lithium depletion and the rotational history of exoplanet host stars. *A&A*, 489:L53–L56.
- Bouvier, J., Forestini, M., and Allain, S. (1997). The angular momentum evolution of low-mass stars. *A&A*, 326:1023–1043.
- Bromley, B. C. and Kenyon, S. J. (2015). Planet Formation around Binary Stars: Tatooine Made Easy. *ApJ*, 806:98.
- Burgasser, A. J. and Mamajek, E. E. (2017). On the Age of the TRAPPIST-1 System. *ApJ*, 845:110.
- Burkart, J., Quataert, E., and Arras, P. (2014). Dynamical resonance locking in tidally interacting binary systems. *MNRAS*, 443:2957–2973.
- Chadney, J. M., Galand, M., Unruh, Y. C., Koskinen, T. T., and Sanz-Forcada, J. (2015). XUV-driven mass loss from extrasolar giant planets orbiting active stars. *Icarus*, 250:357–367.
- Chambers, J. E., Wetherill, G. W., and Boss, A. P. (1996). The Stability of Multi-Planet Systems. *Icarus*, 119:261–268.
- Chaplin, W. J., Basu, S., Huber, D., Serenelli, A., Casagrande, L., Silva Aguirre, V., Ball, W. H., Creevey, O. L., Gizon, L., Handberg, R., Karoff, C., Lutz, R., Marques, J. P., Miglio, A., Stello, D., Suran, M. D., Pricopi, D., Metcalfe, T. S., Monteiro, M. J. P. F. G., Molenda-Żakowicz, J., Appourchaux, T., Christensen-Dalsgaard, J., Elsworth, Y., García, R. A., Houdek, G., Kjeldsen, H., Bonanno, A., Campante, T. L., Corsaro, E., Gaulme, P., Hekker, S., Mathur, S., Mosser, B., Régulo, C., and Salabert, D. (2014). Asteroseismic Fundamental Properties of Solar-type Stars Observed by the NASA Kepler Mission. *ApJS*, 210:1.

- Chatterjee, S., Ford, E. B., Matsumura, S., and Rasio, F. A. (2008). Dynamical Outcomes of Planet-Planet Scattering. *ApJ*, 686:580–602.
- Chavez, C. E., Georgakarakos, N., Prodan, S., Reyes-Ruiz, M., Aceves, H., Betancourt, F., and Perez-Tijerina, E. (2015). A dynamical stability study of Kepler Circumbinary planetary systems with one planet. *MNRAS*, 446(2):1283–1292.
- Claret, A., Gimenez, A., and Cunha, N. C. S. (1995). Circularization and synchronization times in the main sequence of detached eclipsing binaries.I. Using the formalism by Tassoul. *A&A*, 299:724.
- Cobb, A. D., Himes, M. D., Soboczenski, F., Zorzan, S., O’Beirne, M. D., Güneş Baydin, A., Gal, Y., Domagal-Goldman, S. D., Arney, G. N., Angerhausen, D., and 2018 NASA FDL Astrobiology Team, I. (2019). An Ensemble of Bayesian Neural Networks for Exoplanetary Atmospheric Retrieval. *AJ*, 158(1):33.
- Counselman, III, C. C. (1973). Outcomes of Tidal Evolution. *ApJ*, 180:307–316.
- Cranmer, S. R. and Saar, S. H. (2011). Testing a Predictive Theoretical Model for the Mass Loss Rates of Cool Stars. *ApJ*, 741:54.
- Crisp, D. (1997). Absorption of sunlight by water vapor in cloudy conditions: A partial explanation for the cloud absorption anomaly. *Geophys. Res. Lett.*, 24:571–574.
- Cuadra, J., Armitage, P. J., Alexander, R. D., and Begelman, M. C. (2009). Massive black hole binary mergers within subparsec scale gas discs. *MNRAS*, 393(4):1423–1432.
- Darwin, G. H. (1880). On the Secular Changes in the Elements of the Orbit of a Satellite Revolving about a Tidally Distorted Planet. *Philosophical Transactions of the Royal Society of London Series I*, 171:713–891.
- Delfosse, X., Forveille, T., Perrier, C., and Mayor, M. (1998). Rotation and chromospheric activity in field m dwarfs. *Astronomy and Astrophysics*, 331:581–595.

- Delrez, L., Gillon, M., Triaud, A. H. M. J., Demory, B.-O., de Wit, J., Ingalls, J. G., Agol, E., Bolmont, E., Burdanov, A., Burgasser, A. J., Carey, S. J., Jehin, E., Leconte, J., Lederer, S., Queloz, D., Selsis, F., and Van Grootel, V. (2018). Early 2017 observations of TRAPPIST-1 with Spitzer. *MNRAS*, 475:3577–3597.
- Dermine, T., Izzard, R. G., Jorissen, A., and Van Winckel, H. (2013). Eccentricity-pumping in post-AGB stars with circumbinary discs. *A&A*, 551:A50.
- Dobbs-Dixon, I., Lin, D. N. C., and Mardling, R. A. (2004). Spin-Orbit Evolution of Short-Period Planets. *ApJ*, 610:464–476.
- D’Orazio, D. J., Haiman, Z., Duffell, P., MacFadyen, A., and Farris, B. (2016). A transition in circumbinary accretion discs at a binary mass ratio of 1:25. *MNRAS*, 459(3):2379–2393.
- D’Orazio, D. J., Haiman, Z., and MacFadyen, A. (2013). Accretion into the central cavity of a circumbinary disc. *MNRAS*, 436(4):2997–3020.
- Douglas, S. T., Agüeros, M. A., Covey, K. R., and Kraus, A. (2017). Poking the Beehive from Space: K2 Rotation Periods for Praesepe. *ApJ*, 842:83.
- Dressing, C. D. and Charbonneau, D. (2015). The Occurrence of Potentially Habitable Planets Orbiting M Dwarfs Estimated from the Full Kepler Dataset and an Empirical Measurement of the Detection Sensitivity. *ApJ*, 807:45.
- Duchêne, G. and Kraus, A. (2013). Stellar Multiplicity. *ARA&A*, 51:269–310.
- Dunhill, A. C. and Alexander, R. D. (2013). The curiously circular orbit of Kepler-16b. *MNRAS*, 435:2328–2334.
- Dunhill, A. C., Cuadra, J., and Dougados, C. (2015). Precession and accretion in circumbinary discs: the case of HD 104237. *MNRAS*, 448(4):3545–3554.
- Dvorak, R. (1986). Critical orbits in the elliptic restricted three-body problem. *A&A*, 167:379–386.

- Dvorak, R., Froeschle, C., and Froeschle, C. (1989). Stability of outer planetary orbits (P-types) in binaries. *A&A*, 226:335–342.
- Escala, A., Larson, R. B., Coppi, P. S., and Mardones, D. (2005). The Role of Gas in the Merging of Massive Black Holes in Galactic Nuclei. II. Black Hole Merging in a Nuclear Gas Disk. *ApJ*, 630(1):152–166.
- Essick, R. and Weinberg, N. N. (2016). Orbital Decay of Hot Jupiters Due to Nonlinear Tidal Dissipation within Solar-type Hosts. *ApJ*, 816:18.
- Fabrycky, D. and Tremaine, S. (2007). Shrinking Binary and Planetary Orbits by Kozai Cycles with Tidal Friction. *ApJ*, 669:1298–1315.
- Farris, B. D., Duffell, P., MacFadyen, A. I., and Haiman, Z. (2014). Binary Black Hole Accretion from a Circumbinary Disk: Gas Dynamics inside the Central Cavity. *ApJ*, 783(2):134.
- Ferraz-Mello, S., Rodríguez, A., and Hussmann, H. (2008). Tidal friction in close-in satellites and exoplanets: The Darwin theory re-visited. *Celestial Mechanics and Dynamical Astronomy*, 101:171–201.
- Fisher, C., Hoeijmakers, H. J., Kitzmann, D., Márquez-Neila, P., Grimm, S. L., Sznitman, R., and Heng, K. (2019). Interpreting High-Resolution Spectroscopy of Exoplanets Using Cross-Correlations and Supervised Machine Learning. *arXiv e-prints*, page arXiv:1910.11627.
- Flegal, J. M., Haran, M., and Jones, G. L. (2008). Markov chain monte carlo: Can we trust the third significant figure? *Statist. Sci.*, 23(2):250–260.
- Flegal, J. M. and Jones, G. L. (2010). Batch means and spectral variance estimators in markov chain monte carlo. *Ann. Statist.*, 38(2):1034–1070.
- Fleming, D. P., Barnes, R., Graham, D. E., Luger, R., and Quinn, T. R. (2018). On the Lack of Circumbinary Planets Orbiting Isolated Binary Stars. *ApJ*, 858:86.

- Fleming, D. P., Barnes, R., Luger, R., and VanderPlas, J. (2020). On the XUV Luminosity Evolution of TRAPPIST-1. *ApJ, accepted.*
- Fleming, D. P. and Quinn, T. R. (2017). Coevolution of binaries and circumbinary gaseous discs. *MNRAS*, 464:3343–3356.
- Fleming, D. P. and VanderPlas, J. (2018). approxposterior: Approximate Posterior Distributions in Python. *The Journal of Open Source Software*, 3:781.
- Foreman-Mackey, D. (2016). corner.py: Scatterplot matrices in Python. *The Journal of Open Source Software*, 1.
- Foreman-Mackey, D., Hogg, D. W., Lang, D., and Goodman, J. (2013). emcee: The MCMC Hammer. *PASP*, 125:306.
- Forgan, D. (2014). Assessing circumbinary habitable zones using latitudinal energy balance modelling. *MNRAS*, 437:1352–1361.
- Foucart, F. and Lai, D. (2013). Assembly of Protoplanetary Disks and Inclinations of Circumbinary Planets. *ApJ*, 764:106.
- Gaia Collaboration, Prusti, T., de Bruijne, J. H. J., Brown, A. G. A., Vallenari, A., Babusiaux, C., Bailer-Jones, C. A. L., Bastian, U., Biermann, M., Evans, D. W., and et al. (2016). The Gaia mission. *A&A*, 595:A1.
- Gallet, F., Bolmont, E., Mathis, S., Charbonnel, C., and Amard, L. (2017). Tidal dissipation in rotating low-mass stars and implications for the orbital evolution of close-in planets. I. From the PMS to the RGB at solar metallicity. *A&A*, 604:A112.
- Gallet, F. and Bouvier, J. (2013). Improved angular momentum evolution model for solar-like stars. *A&A*, 556:A36.
- Gallet, F. and Bouvier, J. (2015). Improved angular momentum evolution model for solar-like stars. II. Exploring the mass dependence. *A&A*, 577:A98.

- Gillon, M., Jehin, E., Lederer, S. M., Delrez, L., de Wit, J., Burdanov, A., Van Grootel, V., Burgasser, A. J., Triaud, A. H. M. J., Opitom, C., Demory, B.-O., Sahu, D. K., Bardalez Gagliuffi, D., Magain, P., and Queloz, D. (2016). Temperate Earth-sized planets transiting a nearby ultracool dwarf star. *Nature*, 533:221–224.
- Gillon, M., Triaud, A. H. M. J., Demory, B.-O., Jehin, E., Agol, E., Deck, K. M., Lederer, S. M., de Wit, J., Burdanov, A., Ingalls, J. G., Bolmont, E., Leconte, J., Raymond, S. N., Selsis, F., Turbet, M., Barkaoui, K., Burgasser, A., Burleigh, M. R., Carey, S. J., Chaushev, A., Copperwheat, C. M., Delrez, L., Fernandes, C. S., Holdsworth, D. L., Kotze, E. J., Van Grootel, V., Almleaky, Y., Benkhaldoun, Z., Magain, P., and Queloz, D. (2017). Seven temperate terrestrial planets around the nearby ultracool dwarf star TRAPPIST-1. *Nature*, 542:456–460.
- Goldreich, P. (1966). Final spin states of planets and satellites. *AJ*, 71:1.
- Goldreich, P. and Peale, S. (1966). Spin-orbit coupling in the solar system. *AJ*, 71:425.
- Goldreich, P. and Soter, S. (1966). Q in the Solar System. *Icarus*, 5:375–389.
- Goldreich, P. and Tremaine, S. (1979). The excitation of density waves at the Lindblad and corotation resonances by an external potential. *ApJ*, 233:857–871.
- Goldreich, P. and Tremaine, S. (1980). Disk-satellite interactions. *ApJ*, 241:425–441.
- Gong, Y.-X. (2017). P-type Planet-Planet Scattering: Kepler Close Binary Configurations. *ApJ*, 834:55.
- Gong, Y.-X. and Ji, J. (2017). The Scattering Outcomes of Kepler Circumbinary Planets: Planet Mass Ratio. *AJ*, 154:179.
- Gonzales, E. C., Faherty, J. K., Gagné, J., Teske, J., McWilliam, A., and Cruz, K. (2019). A Reanalysis of the Fundamental Parameters and Age of TRAPPIST-1. *ApJ*, 886(2):131.
- Greenberg, R. (2009). Frequency Dependence of Tidal q. *ApJ*, 698:L42–L45.

- Grimm, S. L., Demory, B.-O., Gillon, M., Dorn, C., Agol, E., Burdanov, A., Delrez, L., Sestovic, M., Triaud, A. H. M. J., Turbet, M., Bolmont, É., Caldas, A., de Wit, J., Jehin, E., Leconte, J., Raymond, S. N., Van Grootel, V., Burgasser, A. J., Carey, S., Fabrycky, D., Heng, K., Hernandez, D. M., Ingalls, J. G., Lederer, S., Selsis, F., and Queloz, D. (2018). The nature of the TRAPPIST-1 exoplanets. *A&A*, 613:A68.
- Habets, G. M. H. J. and Zwaan, C. (1989). Asynchronous rotation in close binary systems with circular orbits. *A&A*, 211:56–70.
- Haisch, Jr., K. E., Lada, E. A., and Lada, C. J. (2001). Disk Frequencies and Lifetimes in Young Clusters. *ApJ*, 553:L153–L156.
- Hamers, A. S., Perets, H. B., and Portegies Zwart, S. F. (2016). A triple origin for the lack of tight coplanar circumbinary planets around short-period binaries. *MNRAS*, 455:3180–3200.
- Heller, R., Leconte, J., and Barnes, R. (2011). Tidal obliquity evolution of potentially habitable planets. *A&A*, 528:A27.
- Herbst, W., Bailer-Jones, C. A. L., and Mundt, R. (2001). The Mass Dependence of Stellar Rotation in the Orion Nebula Cluster. *ApJ*, 554:L197–L200.
- Herbst, W., Bailer-Jones, C. A. L., Mundt, R., Meisenheimer, K., and Wackermann, R. (2002). Stellar rotation and variability in the Orion Nebula Cluster. *A&A*, 396:513–532.
- Himes, M. D., Harrington, J., Cobb, A. D., Gunes Baydin, A., Soboczenski, F., O’Beirne, M. D., Zorzan, S., Wright, D. C., Scheffer, Z., Domagal-Goldman, S. D., and Arney, G. N. (2020). Accurate Machine Learning Atmospheric Retrieval via a Neural Network Surrogate Model for Radiative Transfer. *arXiv e-prints*, page arXiv:2003.02430.
- Holman, M. J. and Wiegert, P. A. (1999). Long-Term Stability of Planets in Binary Systems. *AJ*, 117:621–628.

- Howell, S. B., Sobeck, C., Haas, M., Still, M., Barclay, T., Mullally, F., Troeltzsch, J., Aigrain, S., Bryson, S. T., Caldwell, D., Chaplin, W. J., Cochran, W. D., Huber, D., Marcy, G. W., Miglio, A., Najita, J. R., Smith, M., Twicken, J. D., and Fortney, J. J. (2014). The K2 Mission: Characterization and Early Results. *PASP*, 126:398.
- Huang, S.-S. (1966). A theory of the origin and evolution of contact binaries. *Annales d'Astrophysique*, 29:331.
- Hunter, J. D. (2007). Matplotlib: A 2d graphics environment. *Computing In Science & Engineering*, 9(3):90–95.
- Hurley, J. R., Tout, C. A., and Pols, O. R. (2002). Evolution of binary stars and the effect of tides on binary populations. *MNRAS*, 329:897–928.
- Hut, P. (1981). Tidal evolution in close binary systems. *A&A*, 99:126–140.
- Irwin, J. and Bouvier, J. (2009). The rotational evolution of low-mass stars. In Mamajek, E. E., Soderblom, D. R., and Wyse, R. F. G., editors, *The Ages of Stars*, volume 258 of *IAU Symposium*, pages 363–374.
- Ivanova, N., Belczynski, K., Fregeau, J. M., and Rasio, F. A. (2005). The evolution of binary fractions in globular clusters. *MNRAS*, 358:572–584.
- Ivanova, N. and Taam, R. E. (2003). Magnetic Braking Revisited. *ApJ*, 599:516–521.
- Jackson, A. P., Davis, T. A., and Wheatley, P. J. (2012). The coronal X-ray-age relation and its implications for the evaporation of exoplanets. *MNRAS*, 422:2024–2043.
- Jackson, B., Barnes, R., and Greenberg, R. (2009). Observational Evidence for Tidal Destruction of Exoplanets. *ApJ*, 698:1357–1366.
- Jackson, B., Greenberg, R., and Barnes, R. (2008). Tidal Evolution of Close-in Extrasolar Planets. *ApJ*, 678:1396–1406.

- Jetley, P., Gioachin, F., Mendes, C., Kale, L. V., and Quinn, T. (2008). Massively parallel cosmological simulations with changa. In *2008 IEEE International Symposium on Parallel and Distributed Processing*, pages 1–12.
- Kale, L. V. and Krishnan, S. (1996). Charm++: Parallel programming with message-driven objects. *Parallel programming using C+*, pages 175–213.
- Kandasamy, K., Schneider, J., and Pczos, B. (2017). Query efficient posterior estimation in scientific experiments via bayesian active learning. *Artificial Intelligence*, 243:45 – 56.
- Kane, S. R. and Hinkel, N. R. (2013). On the Habitable Zones of Circumbinary Planetary Systems. *ApJ*, 762:7.
- Keppens, R. (1997). Spin and orbital angular momentum exchange in binary star systems. *A&A*, 318:275–288.
- Khaliullin, K. F. and Khaliullina, A. I. (2011). Orbital circularization of close binary stars on the pre-main sequence. *MNRAS*, 411:2804–2816.
- Kirk, B., Conroy, K., Prša, A., Abdul-Masih, M., Kochoska, A., Matijević, G., Hambleton, K., Barclay, T., Bloemen, S., Boyajian, T., Doyle, L. R., Fulton, B. J., Hoekstra, A. J., Jek, K., Kane, S. R., Kostov, V., Latham, D., Mazeh, T., Orosz, J. A., Pepper, J., Quarles, B., Ragozzine, D., Shporer, A., Southworth, J., Stassun, K., Thompson, S. E., Welsh, W. F., Agol, E., Derekas, A., Devor, J., Fischer, D., Green, G., Groppi, J., Jacobs, T., Johnston, C., LaCourse, D. M., Saetre, K., Schwengeler, H., Toczyński, J., Werner, G., Garrett, M., Gore, J., Martinez, A. O., Spitzer, I., Stevick, J., Thomadis, P. C., Vrijmoet, E. H., Yenawine, M., Batalha, N., and Borucki, W. (2016). Kepler Eclipsing Binary Stars. VII. The Catalog of Eclipsing Binaries Found in the Entire Kepler Data Set. *AJ*, 151:68.
- Kley, W. and Haghighipour, N. (2014). Modeling circumbinary planets: The case of Kepler-38. *A&A*, 564:A72.

- Kley, W. and Haghighipour, N. (2015). Evolution of circumbinary planets around eccentric binaries: The case of Kepler-34. *A&A*, 581:A20.
- Kley, W., Papaloizou, J. C. B., and Ogilvie, G. I. (2008). Simulations of eccentric disks in close binary systems. *A&A*, 487(2):671–687.
- Kostov, V. B., Orosz, J. A., Welsh, W. F., Doyle, L. R., Fabrycky, D. C., Haghighipour, N., Quarles, B., Short, D. R., Cochran, W. D., Endl, M., Ford, E. B., Gregorio, J., Hinse, T. C., Isaacson, H., Jenkins, J. M., Jensen, E. L. N., Kane, S., Kull, I., Latham, D. W., Lissauer, J. J., Marcy, G. W., Mazeh, T., Müller, T. W. A., Pepper, J., Quinn, S. N., Ragozzine, D., Shporer, A., Steffen, J. H., Torres, G., Windmiller, G., and Borucki, W. J. (2016). Kepler-1647b: The Largest and Longest-period Kepler Transiting Circumbinary Planet. *ApJ*, 827(1):86.
- Kozai, Y. (1962). Secular perturbations of asteroids with high inclination and eccentricity. *AJ*, 67:591–598.
- Kratter, K. M. and Shannon, A. (2014). Planet packing in circumbinary systems. *MNRAS*, 437:3727–3735.
- Krissansen-Totton, J., Garland, R., Irwin, P., and Catling, D. C. (2018). Detectability of Biosignatures in Anoxic Atmospheres with the James Webb Space Telescope: A TRAPPIST-1e Case Study. *AJ*, 156(3):114.
- Lam, C. and Kipping, D. (2018). A machine learns to predict the stability of circumbinary planets. *ArXiv e-prints*.
- Lammer, H., Selsis, F., Ribas, I., Guinan, E. F., Bauer, S. J., and Weiss, W. W. (2003). Atmospheric Loss of Exoplanets Resulting from Stellar X-Ray and Extreme-Ultraviolet Heating. *ApJ*, 598:L121–L124.
- Lanza, A. F. and Mathis, S. (2016). Tides and angular momentum redistribution inside low-mass stars hosting planets: a first dynamical model. *Celestial Mechanics and Dynamical Astronomy*, 126:249–274.

- Leconte, J., Chabrier, G., Baraffe, I., and Levrard, B. (2010). Is tidal heating sufficient to explain bloated exoplanets? Consistent calculations accounting for finite initial eccentricity. *A&A*, 516:A64.
- Leung, G. C. K. and Lee, M. H. (2013). An Analytic Theory for the Orbits of Circumbinary Planets. *ApJ*, 763(2):107.
- Levato, H. (1974). Rotation in binary stars. *A&A*, 35:259–265.
- Li, G., Holman, M. J., and Tao, M. (2016). Uncovering Circumbinary Planetary Architectural Properties from Selection Biases. *ApJ*, 831:96.
- Li, J. and Wickramasinghe, D. T. (1998). Magnetic braking in magnetic binary stars. *MNRAS*, 300:718–732.
- Lidov, M. L. (1962). The evolution of orbits of artificial satellites of planets under the action of gravitational perturbations of external bodies. *Planet. Space Sci.*, 9(10):719–759.
- Lin, D. N. C., Bodenheimer, P., and Richardson, D. C. (1996). Orbital migration of the planetary companion of 51 Pegasi to its present location. *Nature*, 380:606–607.
- Lincowski, A. P., Meadows, V. S., Crisp, D., Robinson, T. D., Luger, R., Lustig-Yaeger, J., and Arney, G. N. (2018). Evolved Climates and Observational Discriminants for the TRAPPIST-1 Planetary System. *ApJ*, 867:76.
- Lines, S., Leinhardt, Z. M., Baruteau, C., Paardekooper, S. J., and Carter, P. J. (2015). Modelling circumbinary protoplanetary disks. I. Fluid simulations of the Kepler-16 and 34 systems. *A&A*, 582:A5.
- Lines, S., Leinhardt, Z. M., Baruteau, C., Paardekooper, S. J., and Carter, P. J. (2016). Modelling circumbinary protoplanetary disks. II. Gas disk feedback on planetesimal dynamical and collisional evolution in the circumbinary systems Kepler-16 and 34. *A&A*, 590:A62.

- Lodato, G. and Price, D. J. (2010). On the diffusive propagation of warps in thin accretion discs. *MNRAS*, 405(2):1212–1226.
- Lubow, S. H. (1991). Simulations of Tidally Driven Eccentric Instabilities with Application to Superhumps. *ApJ*, 381:268.
- Lubow, S. H. and Artymowicz, P. (1996). Young Binary Star/Disk Interactions. In Wijers, R. A. M. J., Davies, M. B., and Tout, C. A., editors, *NATO Advanced Science Institutes (ASI) Series C*, volume 477 of *NATO Advanced Science Institutes (ASI) Series C*, page 53.
- Lubow, S. H. and Artymowicz, P. (2000). Interactions of Young Binaries with Disks. In Mannings, V., Boss, A. P., and Russell, S. S., editors, *Protostars and Planets IV*, page 731.
- Lubow, S. H., Martin, R. G., and Nixon, C. (2015). Tidal Torques on Misaligned Disks in Binary Systems. *ApJ*, 800(2):96.
- Luger, R. and Barnes, R. (2015). Extreme Water Loss and Abiotic O₂Buildup on Planets Throughout the Habitable Zones of M Dwarfs. *Astrobiology*, 15:119–143.
- Luger, R., Sestovic, M., Kruse, E., Grimm, S. L., Demory, B.-O., Agol, E., Bolmont, E., Fabrycky, D., Fernandes, C. S., Van Grootel, V., Burgasser, A., Gillon, M., Ingalls, J. G., Jehin, E., Raymond, S. N., Selsis, F., Triaud, A. H. M. J., Barclay, T., Barentsen, G., Howell, S. B., Delrez, L., de Wit, J., Foreman-Mackey, D., Holdsworth, D. L., Leconte, J., Lederer, S., Turbet, M., Almleaky, Y., Benkhaldoun, Z., Magain, P., Morris, B. M., Heng, K., and Queloz, D. (2017). A seven-planet resonant chain in TRAPPIST-1. *Nature Astronomy*, 1:0129.
- Lurie, J. C., Vyhmeister, K., Hawley, S. L., Adilia, J., Chen, A., Davenport, J. R. A., Jurić, M., Puig-Holzman, M., and Weisenburger, K. L. (2017). Tidal Synchronization and Differential Rotation of Kepler Eclipsing Binaries. *AJ*, 154:250.
- Lustig-Yaeger, J., Meadows, V. S., and Lincowski, A. P. (2019). The Detectability and Characterization of the TRAPPIST-1 Exoplanet Atmospheres with JWST. *arXiv e-prints*.

- MacFadyen, A. I. and Milosavljević, M. (2008). An Eccentric Circumbinary Accretion Disk and the Detection of Binary Massive Black Holes. *ApJ*, 672(1):83–93.
- MacGregor, K. B. and Brenner, M. (1991). Rotational evolution of solar-type stars. I - Main-sequence evolution. *ApJ*, 376:204–213.
- Mamajek, E. E. and Hillenbrand, L. A. (2008). Improved Age Estimation for Solar-Type Dwarfs Using Activity-Rotation Diagnostics. *ApJ*, 687:1264–1293.
- Mardling, R. A. and Aarseth, S. J. (2001). Tidal interactions in star cluster simulations. *MNRAS*, 321:398–420.
- Marilli, E., Frasca, A., Covino, E., Alcalá, J. M., Catalano, S., Fernández, M., Arellano Ferro, A., Rubio-Herrera, E., and Spezzi, L. (2007). Rotational periods of solar-mass young stars in Orion. *A&A*, 463:1081–1091.
- Márquez-Neila, P., Fisher, C., Sznitman, R., and Heng, K. (2018). Supervised machine learning for analysing spectra of exoplanetary atmospheres. *Nature Astronomy*, 2:719–724.
- Martin, D. V. (2017). Circumbinary planets - II. When transits come and go. *MNRAS*, 465:3235–3253.
- Martin, D. V., Mazeh, T., and Fabrycky, D. C. (2015). No circumbinary planets transiting the tightest Kepler binaries - a possible fingerprint of a third star. *MNRAS*, 453:3554–3567.
- Martin, D. V. and Triaud, A. H. M. J. (2014). Planets transiting non-eclipsing binaries. *A&A*, 570:A91.
- Martin, D. V. and Triaud, A. H. M. J. (2015). Circumbinary planets - why they are so likely to transit. *MNRAS*, 449:781–793.
- Martin, R. G., Nixon, C., Lubow, S. H., Armitage, P. J., Price, D. J., Doğan, S., and King, A. (2014). The Kozai-Lidov Mechanism in Hydrodynamical Disks. *ApJ*, 792(2):L33.

- Mathis, S. (2015). Variation of tidal dissipation in the convective envelope of low-mass stars along their evolution. *A&A*, 580:L3.
- Matson, R. A., Howell, S. B., and Ciardi, D. (2018). Detecting Unresolved Binaries in TESS Data with Speckle Imaging. *arXiv e-prints*.
- Matt, S. P., Brun, A. S., Baraffe, I., Bouvier, J., and Chabrier, G. (2015). The Mass-dependence of Angular Momentum Evolution in Sun-like Stars. *ApJ*, 799:L23.
- Matt, S. P., Brun, A. S., Baraffe, I., Bouvier, J., and Chabrier, G. (2019). Erratum: The Mass-dependence of Angular Momentum Evolution in Sun-like Stars. *ApJ*, 870:L27.
- Mayer, L., Kazantzidis, S., Madau, P., Colpi, M., Quinn, T., and Wadsley, J. (2007). Rapid Formation of Supermassive Black Hole Binaries in Galaxy Mergers with Gas. *Science*, 316(5833):1874.
- Mazeh, T. (2008). Observational Evidence for Tidal Interaction in Close Binary Systems. In Goupil, M.-J. and Zahn, J.-P., editors, *EAS Publications Series*, volume 29 of *EAS Publications Series*, pages 1–65.
- McClintock, T. and Rozo, E. (2019). Reconstructing Probability Distributions with Gaussian Processes. *arXiv e-prints*.
- McKinney, W. (2010). Data structures for statistical computing in python. In van der Walt, S. and Millman, J., editors, *Proceedings of the 9th Python in Science Conference*, pages 51 – 56.
- McQuillan, A., Mazeh, T., and Aigrain, S. (2014). Rotation Periods of 34,030 Kepler Main-sequence Stars: The Full Autocorrelation Sample. *ApJS*, 211:24.
- Meadows, V. S. and Crisp, D. (1996). Ground-based near-infrared observations of the Venus night-side: The thermal structure and water abundance near the surface. *J. Geophys. Res.*, 101:4595–4622.

- Meibom, S., Barnes, S. A., Platais, I., Gilliland, R. L., Latham, D. W., and Mathieu, R. D. (2015). A spin-down clock for cool stars from observations of a 2.5-billion-year-old cluster. *Nature*, 517:589–591.
- Meibom, S. and Mathieu, R. D. (2005). A Robust Measure of Tidal Circularization in Coeval Binary Populations: The Solar-Type Spectroscopic Binary Population in the Open Cluster M35. *ApJ*, 620:970–983.
- Meibom, S., Mathieu, R. D., and Stassun, K. G. (2006). An Observational Study of Tidal Synchronization in Solar-Type Binary Stars in the Open Clusters M35 and M34. *ApJ*, 653:621–635.
- Meibom, S., Mathieu, R. D., and Stassun, K. G. (2007). The Effect of Binarity on Stellar Rotation: Beyond the Reach of Tides. *ApJ*, 665:L155–L158.
- Meibom, S., Mathieu, R. D., and Stassun, K. G. (2009). Stellar Rotation in M35: Mass-Period Relations, Spin-Down Rates, and Gyrochronology. *ApJ*, 695:679–694.
- Meibom, S., Mathieu, R. D., Stassun, K. G., Liebesny, P., and Saar, S. H. (2011). The Color-period Diagram and Stellar Rotational Evolution - New Rotation Period Measurements in the Open Cluster M34. *ApJ*, 733:115.
- Menon, H., Wesolowski, L., Zheng, G., Jetley, P., Kale, L., Quinn, T., and Governato, F. (2015). Adaptive techniques for clustered N-body cosmological simulations. *Computational Astrophysics and Cosmology*, 2:1.
- Meru, F. and Bate, M. R. (2012). On the convergence of the critical cooling time-scale for the fragmentation of self-gravitating discs. *MNRAS*, 427(3):2022–2046.
- Meschiari, S. (2012a). Circumbinary Planet Formation in the Kepler-16 System. I. N-body Simulations. *ApJ*, 752:71.
- Meschiari, S. (2012b). Planet Formation in Circumbinary Configurations: Turbulence Inhibits Planetesimal Accretion. *ApJ*, 761:L7.

- Mestel, L. (1968). Magnetic braking by a stellar wind-I. MNRAS, 138:359.
- Moe, M. and Kratter, K. M. (2018). Dynamical Formation of Close Binaries during the Pre-main-sequence Phase. ApJ, 854:44.
- Monaghan, J. J. and Gingold, R. A. (1983). Shock Simulation by the Particle Method SPH. *Journal of Computational Physics*, 52(2):374–389.
- Morley, C. V., Kreidberg, L., Rustamkulov, Z., Robinson, T., and Fortney, J. J. (2017). Observing the Atmospheres of Known Temperate Earth-sized Planets with JWST. ApJ, 850:121.
- Morris, B. M., Agol, E., Davenport, J. R. A., and Hawley, S. L. (2018). Possible Bright Starspots on TRAPPIST-1. ApJ, 857:39.
- Muñoz, D. J. and Lai, D. (2015). Survival of planets around shrinking stellar binaries. *Proceedings of the National Academy of Science*, 112:9264–9269.
- Murray, C. D. and Dermott, S. F. (1999). *Solar system dynamics*.
- Murray, J. R. (1996). SPH simulations of tidally unstable accretion discs in cataclysmic variables. MNRAS, 279:402–414.
- Murray-Clay, R. A., Chiang, E. I., and Murray, N. (2009). Atmospheric Escape From Hot Jupiters. ApJ, 693:23–42.
- Nelder, J. A. and Mead, R. (1965). A Simplex Method for Function Minimization. *The Computer Journal*, 7(4):308–313.
- Nelson, R. P. and Papaloizou, J. C. B. (2003). The interaction of a giant planet with a disc with MHD turbulence - II. The interaction of the planet with the disc. MNRAS, 339(4):993–1005.
- Nelson, R. P., Papaloizou, J. C. B., Masset, F., and Kley, W. (2000). The migration and growth of protoplanets in protostellar discs. MNRAS, 318:18–36.

- Nixon, C., King, A., and Price, D. (2013). Tearing up the disc: misaligned accretion on to a binary. *MNRAS*, 434(3):1946–1954.
- Ogilvie, G. I. (2013). Tides in rotating barotropic fluid bodies: the contribution of inertial waves and the role of internal structure. *MNRAS*, 429:613–632.
- Ogilvie, G. I. and Lin, D. N. C. (2007). Tidal Dissipation in Rotating Solar-Type Stars. *ApJ*, 661:1180–1191.
- Orosz, J. A., Welsh, W. F., Carter, J. A., Fabrycky, D. C., Cochran, W. D., Endl, M., Ford, E. B., Haghjipour, N., MacQueen, P. J., Mazeh, T., Sanchis-Ojeda, R., Short, D. R., Torres, G., Agol, E., Buchhave, L. A., Doyle, L. R., Isaacson, H., Lissauer, J. J., Marcy, G. W., Shporer, A., Windmiller, G., Barclay, T., Boss, A. P., Clarke, B. D., Fortney, J., Geary, J. C., Holman, M. J., Huber, D., Jenkins, J. M., Kinemuchi, K., Kruse, E., Ragozzine, D., Sasselov, D., Still, M., Tenenbaum, P., Uddin, K., Winn, J. N., Koch, D. G., and Borucki, W. J. (2012). Kepler-47: A Transiting Circumbinary Multiplanet System. *Science*, 337:1511.
- Paardekooper, S.-J., Leinhardt, Z. M., Thébault, P., and Baruteau, C. (2012). How Not to Build Tatooine: The Difficulty of In Situ Formation of Circumbinary Planets Kepler 16b, Kepler 34b, and Kepler 35b. *ApJ*, 754:L16.
- Papaloizou, J. C. B., Nelson, R. P., and Masset, F. (2001). Orbital eccentricity growth through disc-companion tidal interaction. *A&A*, 366:263–275.
- Papaloizou, J. C. B. and Terquem, C. (2006). Planet formation and migration. *Reports on Progress in Physics*, 69:119–180.
- Parker, E. N. (1955). Hydromagnetic Dynamo Models. *ApJ*, 122:293.
- Parker, E. N. (1958). Dynamics of the Interplanetary Gas and Magnetic Fields. *ApJ*, 128:664.
- Patra, K. C., Winn, J. N., Holman, M. J., Yu, L., Deming, D., and Dai, F. (2017). The Apparently Decaying Orbit of WASP-12b. *AJ*, 154:4.

- Peacock, S., Barman, T., Shkolnik, E. L., Hauschildt, P. H., and Baron, E. (2019). Predicting the Extreme Ultraviolet Radiation Environment of Exoplanets around Low-mass Stars: The TRAPPIST-1 System. *ApJ*, 871:235.
- Pelupessy, F. I. and Portegies Zwart, S. (2013). The formation of planets in circumbinary discs. *MNRAS*, 429:895–902.
- Pierens, A. and Nelson, R. P. (2007). On the migration of protoplanets embedded in circumbinary disks. *A&A*, 472:993–1001.
- Pierens, A. and Nelson, R. P. (2013). Migration and gas accretion scenarios for the Kepler 16, 34, and 35 circumbinary planets. *A&A*, 556:A134.
- Pizzolato, N., Maggio, A., Micela, G., Sciortino, S., and Ventura, P. (2003). The stellar activity-rotation relationship revisited: Dependence of saturated and non-saturated X-ray emission regimes on stellar mass for late-type dwarfs. *A&A*, 397:147–157.
- Popova, E. A. and Shevchenko, I. I. (2013). Kepler-16b: Safe in a Resonance Cell. *ApJ*, 769(2):152.
- Popp, M. and Eggl, S. (2017). Climate variations on Earth-like circumbinary planets. *Nature Communications*, 8:14957.
- Powell, M. J. D. (1964). An efficient method for finding the minimum of a function of several variables without calculating derivatives. *The Computer Journal*, 7(2):155–162.
- Pringle, J. E. (1991). The properties of external accretion discs. *MNRAS*, 248:754.
- Quarles, B., Satyal, S., Kostov, V., Kaib, N., and Haghighipour, N. (2018). Stability Limits of Circumbinary Planets: Is There a Pile-up in the Kepler CBPs? *ArXiv e-prints*.
- Quinn, T., Katz, N., Stadel, J., and Lake, G. (1997). Time stepping N-body simulations. *arXiv e-prints*, pages astro-ph/9710043.

- Raghavan, D., McAlister, H. A., Henry, T. J., Latham, D. W., Marcy, G. W., Mason, B. D., Gies, D. R., White, R. J., and ten Brummelaar, T. A. (2010). A Survey of Stellar Families: Multiplicity of Solar-type Stars. *ApJS*, 190:1–42.
- Ragusa, E., Lodato, G., and Price, D. J. (2016). Suppression of the accretion rate in thin discs around binary black holes. *MNRAS*, 460(2):1243–1253.
- Rasmussen, C. E. and Williams, C. K. I. (2006). *Gaussian Processes for Machine Learning*.
- Rauer, H., Catala, C., Aerts, C., Appourchaux, T., Benz, W., Brandeker, A., Christensen-Dalsgaard, J., Deleuil, M., Gizon, L., Goupil, M.-J., Güdel, M., Janot-Pacheco, E., Mas-Hesse, M., Pagano, I., Piotto, G., Pollacco, D., Santos, Č., Smith, A., Suárez, J.-C., Szabó, R., Udry, S., Adibekyan, V., Alibert, Y., Almenara, J.-M., Amaro-Seoane, P., Eiff, M. A.-v., Asplund, M., Antonello, E., Barnes, S., Baudin, F., Belkacem, K., Bergemann, M., Bihain, G., Birch, A. C., Bonfils, X., Boisse, I., Bonomo, A. S., Borsa, F., Brandão, I. M., Brocato, E., Brun, S., Burleigh, M., Burston, R., Cabrera, J., Cassisi, S., Chaplin, W., Charpinet, S., Chiappini, C., Church, R. P., Csizmadia, S., Cunha, M., Damasso, M., Davies, M. B., Deeg, H. J., Díaz, R. F., Dreizler, S., Dreyer, C., Eggenberger, P., Ehrenreich, D., Eigmüller, P., Erikson, A., Farmer, R., Feltzing, S., de Oliveira Fialho, F., Figueira, P., Forveille, T., Fridlund, M., García, R. A., Giommi, P., Giuffrida, G., Godolt, M., Gomes da Silva, J., Granzer, T., Grenfell, J. L., Grottsch-Noels, A., Günther, E., Haswell, C. A., Hatzes, A. P., Hébrard, G., Hekker, S., Helled, R., Heng, K., Jenkins, J. M., Johansen, A., Khodachenko, M. L., Kislyakova, K. G., Kley, W., Kolb, U., Krivova, N., Kupka, F., Lammer, H., Lanza, A. F., Lebreton, Y., Magrin, D., Marcos-Arenal, P., Marrese, P. M., Marques, J. P., Martins, J., Mathis, S., Mathur, S., Messina, S., Miglio, A., Montalban, J., Montalto, M., Monteiro, M. J. P. F. G., Moradi, H., Moravveji, E., Mordasini, C., Morel, T., Mortier, A., Nascimbeni, V., Nelson, R. P., Nielsen, M. B., Noack, L., Norton, A. J., Ofir, A., Oshagh, M., Ouazzani, R.-M., Pápics, P., Parro, V. C., Petit, P., Plez, B., Poretti, E., Quirrenbach, A., Ragazzoni, R., Raimondo, G., Rainer, M., Reese, D. R., Redmer, R., Reffert, S., Rojas-Ayala, B., Roxburgh, I. W., Salmon, S., Santerne, A., Schneider, J., Schou, J., Schuh, S., Schunker, H., Silva-Valio, A., Silvotti, R., Skillen, I., Snellen, I., Sohl, F., Sousa, S. G.,

- Sozzetti, A., Stello, D., Strassmeier, K. G., Švanda, M., Szabó, G. M., Tkachenko, A., Valencia, D., Van Grootel, V., Vauclair, S. D., Ventura, P., Wagner, F. W., Walton, N. A., Weingrill, J., Werner, S. C., Wheatley, P. J., and Zwintz, K. (2014). The PLATO 2.0 mission. *Experimental Astronomy*, 38:249–330.
- Rebull, L. M., Stauffer, J. R., Megeath, S. T., Hora, J. L., and Hartmann, L. (2006). A Correlation between Pre-Main-Sequence Stellar Rotation Rates and IRAC Excesses in Orion. *ApJ*, 646:297–303.
- Reid, I. N. and Hawley, S. L. (2005). *New light on dark stars : red dwarfs, low-mass stars, brown dwarfs*.
- Rein, H. and Liu, S.-F. (2012). REBOUND: an open-source multi-purpose N-body code for collisional dynamics. *A&A*, 537:A128.
- Rein, H. and Spiegel, D. S. (2015). IAS15: a fast, adaptive, high-order integrator for gravitational dynamics, accurate to machine precision over a billion orbits. *MNRAS*, 446:1424–1437.
- Reiners, A. and Mohanty, S. (2012). Radius-dependent Angular Momentum Evolution in Low-mass Stars. I. *ApJ*, 746:43.
- Reinhold, T., Bell, K. J., Kuszlewicz, J., Hekker, S., and Shapiro, A. I. (2018). Transition from spot to faculae domination – An alternate explanation for the dearth of intermediate \textit{Kepler} rotation periods. *arXiv e-prints*.
- Reinhold, T., Reiners, A., and Basri, G. (2013). Rotation and differential rotation of active Kepler stars. *A&A*, 560:A4.
- Repetto, S. and Nelemans, G. (2014). The coupled effect of tides and stellar winds on the evolution of compact binaries. *MNRAS*, 444:542–557.
- Ribas, I., Bolmont, E., Selsis, F., Reiners, A., Leconte, J., Raymond, S. N., Engle, S. G., Guinan, E. F., Morin, J., Turbet, M., Forget, F., and Anglada-Escudé, G. (2016). The habitability of

- Proxima Centauri b. I. Irradiation, rotation and volatile inventory from formation to the present. *A&A*, 596:A111.
- Ribas, I., Guinan, E. F., Güdel, M., and Audard, M. (2005). Evolution of the Solar Activity over Time and Effects on Planetary Atmospheres. I. High-Energy Irradiances (1-1700 Å). *ApJ*, 622:680–694.
- Richardson, D. C., Quinn, T., Stadel, J., and Lake, G. (2000). Direct Large-Scale N-Body Simulations of Planetesimal Dynamics. *Icarus*, 143(1):45–59.
- Ricker, G. R., Winn, J. N., Vanderspek, R., Latham, D. W., Bakos, G. Á., Bean, J. L., Berta-Thompson, Z. K., Brown, T. M., Buchhave, L., Butler, N. R., Butler, R. P., Chaplin, W. J., Charbonneau, D., Christensen-Dalsgaard, J., Clampin, M., Deming, D., Doty, J., De Lee, N., Dressing, C., Dunham, E. W., Endl, M., Fressin, F., Ge, J., Henning, T., Holman, M. J., Howard, A. W., Ida, S., Jenkins, J., Jernigan, G., Johnson, J. A., Kaltenegger, L., Kawai, N., Kjeldsen, H., Laughlin, G., Levine, A. M., Lin, D., Lissauer, J. J., MacQueen, P., Marcy, G., McCullough, P. R., Morton, T. D., Narita, N., Paegert, M., Palle, E., Pepe, F., Pepper, J., Quirrenbach, A., Rinehart, S. A., Sasselov, D., Sato, B., Seager, S., Sozzetti, A., Stassun, K. G., Sullivan, P., Szentgyorgyi, A., Torres, G., Udry, S., and Villasenor, J. (2014). Transiting Exoplanet Survey Satellite (TESS). In *Space Telescopes and Instrumentation 2014: Optical, Infrared, and Millimeter Wave*, volume 9143 of Proc. SPIE, page 914320.
- Rodríguez, A., Callegari, N., Michtchenko, T. A., and Hussmann, H. (2012). Spin-orbit coupling for tidally evolving super-Earths. *MNRAS*, 427:2239–2250.
- Rodríguez-Ledesma, M. V., Mundt, R., and Eisloffel, J. (2009). Rotational studies in the Orion Nebula Cluster: from solar mass stars to brown dwarfs. *A&A*, 502:883–904.
- Roedig, C., Dotti, M., Sesana, A., Cuadra, J., and Colpi, M. (2011). Limiting eccentricity of subparsec massive black hole binaries surrounded by self-gravitating gas discs. *MNRAS*, 415(4):3033–3041.

- Roedig, C., Sesana, A., Dotti, M., Cuadra, J., Amaro-Seoane, P., and Haardt, F. (2012). Evolution of binary black holes in self gravitating discs. Dissecting the torques. *A&A*, 545:A127.
- Roettenbacher, R. M. and Kane, S. R. (2017). The Stellar Activity of TRAPPIST-1 and Consequences for the Planetary Atmospheres. *ApJ*, 851:77.
- Rogers, L. A., Bodenheimer, P., Lissauer, J. J., and Seager, S. (2011). Formation and Structure of Low-density exo-Neptunes. *ApJ*, 738:59.
- Roškar, R., Fiacconi, D., Mayer, L., Kazantzidis, S., Quinn, T. R., and Wadsley, J. (2015). Orbital decay of supermassive black hole binaries in clumpy multiphase merger remnants. *MNRAS*, 449(1):494–505.
- Sahlmann, J., Triaud, A. H. M. J., and Martin, D. V. (2015). Gaia’s potential for the discovery of circumbinary planets. *MNRAS*, 447:287–297.
- Schneider, A. C. and Shkolnik, E. L. (2018). HAZMAT. III. The UV Evolution of Mid- to Late-M Stars with GALEX. *AJ*, 155:122.
- Segura, A., Kasting, J. F., Meadows, V., Cohen, M., Scalo, J., Crisp, D., Butler, R. A. H., and Tinetti, G. (2005). Biosignatures from Earth-Like Planets Around M Dwarfs. *Astrobiology*, 5:706–725.
- Shi, J.-M., Krolik, J. H., Lubow, S. H., and Hawley, J. F. (2012). Three-dimensional Magnetohydrodynamic Simulations of Circumbinary Accretion Disks: Disk Structures and Angular Momentum Transport. *ApJ*, 749(2):118.
- Shkolnik, E. L. and Barman, T. S. (2014). HAZMAT. I. The Evolution of Far-UV and Near-UV Emission from Early M Stars. *AJ*, 148:64.
- Silsbee, K. and Rafikov, R. R. (2015). Birth Locations of the Kepler Circumbinary Planets. *ApJ*, 808(1):58.

- Simonian, G. V. A., Pinsonneault, M. H., and Terndrup, D. M. (2018). Rapid Rotation in the Kepler Field: Not a Single Star Phenomenon. *ArXiv e-prints*.
- Skumanich, A. (1972). Time Scales for CA II Emission Decay, Rotational Braking, and Lithium Depletion. *ApJ*, 171:565.
- Smullen, R. A., Kratter, K. M., and Shannon, A. (2016). Planet scattering around binaries: ejections, not collisions. *MNRAS*, 461:1288–1301.
- Spada, F., Demarque, P., Kim, Y.-C., and Sills, A. (2013). The Radius Discrepancy in Low-mass Stars: Single versus Binaries. *ApJ*, 776:87.
- Stassun, K. G., Mathieu, R. D., Mazeh, T., and Vrba, F. J. (1999). The Rotation Period Distribution of Pre-Main-Sequence Stars in and around the Orion Nebula. *AJ*, 117:2941–2979.
- Stauffer, J., Rebull, L., Bouvier, J., Hillenbrand, L. A., Collier-Cameron, A., Pinsonneault, M., Aigrain, S., Barrado, D., Bouy, H., Ciardi, D., Cody, A. M., David, T., Micela, G., Soderblom, D., Somers, G., Stassun, K. G., Valenti, J., and Vrba, F. J. (2016). Rotation in the Pleiades with K2. III. Speculations on Origins and Evolution. *AJ*, 152:115.
- Stepien, K. (1995). Loss of angular momentum of cool close binaries and formation of contact systems. *MNRAS*, 274:1019–1028.
- Sullivan, P. W., Winn, J. N., Berta-Thompson, Z. K., Charbonneau, D., Deming, D., Dressing, C. D., Latham, D. W., Levine, A. M., McCullough, P. R., Morton, T., Ricker, G. R., Vanderspek, R., and Woods, D. (2015). The Transiting Exoplanet Survey Satellite: Simulations of Planet Detections and Astrophysical False Positives. *ApJ*, 809:77.
- Sumi, T., Kamiya, K., Bennett, D. P., Bond, I. A., Abe, F., Botzler, C. S., Fukui, A., Furusawa, K., Hearnshaw, J. B., Itow, Y., Kilmartin, P. M., Korpela, A., Lin, W., Ling, C. H., Masuda, K., Matsubara, Y., Miyake, N., Motomura, M., Muraki, Y., Nagaya, M., Nakamura, S., Ohnishi, K., Okumura, T., Perrott, Y. C., Rattenbury, N., Saito, T., Sako, T., Sullivan, D. J., Sweatman,

- W. L., Tristram, P. J., Udalski, A., Szymański, M. K., Kubiak, M., Pietrzyński, G., Poleski, R., Soszyński, I., Wyrzykowski, Ł., Ulaczyk, K., and Microlensing Observations in Astrophysics (MOA) Collaboration (2011). Unbound or distant planetary mass population detected by gravitational microlensing. *Nature*, 473:349–352.
- Sutherland, A. P. and Fabrycky, D. C. (2016). On the Fate of Unstable Circumbinary Planets: Tatooines: Close Encounters with a Death Star. *ApJ*, 818:6.
- Tarduno, J. A., Blackman, E. G., and Mamajek, E. E. (2014). Detecting the oldest geodynamo and attendant shielding from the solar wind: Implications for habitability. *Physics of the Earth and Planetary Interiors*, 233:68–87.
- Tokovinin, A., Thomas, S., Sterzik, M., and Udry, S. (2006). Tertiary companions to close spectroscopic binaries. *A&A*, 450:681–693.
- Toomre, A. (1964). On the gravitational stability of a disk of stars. *ApJ*, 139:1217–1238.
- Torres, G., Curtis, J. L., Vanderburg, A., Kraus, A. L., and Rizzuto, A. (2018). Eclipsing Binaries in the Open Cluster Ruprecht 147. I. EPIC 219394517. *ApJ*, 866:67.
- Tremblay, L., Line, M. R., Stevenson, K., Katarić, T., Zellem, R. T., Fortney, J. J., and Morley, C. (2020). The Detectability and Constraints of Biosignature Gases in the Near- and Mid-infrared from Transit Transmission Spectroscopy. *AJ*, 159(3):117.
- Vaiana, G. S., Cassinelli, J. P., Fabbiano, G., Giacconi, R., Golub, L., Gorenstein, P., Haisch, B. M., Harnden, Jr., F. R., Johnson, H. M., Linsky, J. L., Maxson, C. W., Mewe, R., Rosner, R., Seward, F., Topka, K., and Zwaan, C. (1981). Results from an extensive Einstein stellar survey. *ApJ*, 245:163–182.
- van der Walt, S., Colbert, S. C., and Varoquaux, G. (2011). The numpy array: A structure for efficient numerical computation. *Computing in Science Engineering*, 13(2):22–30.

- Van Eylen, V., Winn, J. N., and Albrecht, S. (2016). Orbital Circularization of Hot and Cool Kepler Eclipsing Binaries. *ApJ*, 824:15.
- Van Grootel, V., Fernandes, C. S., Gillon, M., Jehin, E., Manfroid, J., Scuflaire, R., Burgasser, A. J., Barkaoui, K., Benkhaldoun, Z., Burdanov, A., Delrez, L., Demory, B.-O., de Wit, J., Queloz, D., and Triaud, A. H. M. J. (2018). Stellar Parameters for Trappist-1. *ApJ*, 853:30.
- van Saders, J. L., Pinsonneault, M. H., and Barbieri, M. (2018). Forward Modeling of the Kepler Stellar Rotation Period Distribution: Interpreting Periods from Mixed and Biased Stellar Populations. *ArXiv e-prints*.
- van't Veer, F. and Maceroni, C. (1988). The angular momentum loss of rapidly rotating late-type main sequence binaries. *A&A*, 199:183–190.
- Vartanyan, D., Garmilla, J. A., and Rafikov, R. R. (2016). Tatooine Nurseries: Structure and Evolution of Circumbinary Protoplanetary Disks. *ApJ*, 816:94.
- Veras, D. and Raymond, S. N. (2012). Planet-planet scattering alone cannot explain the free-floating planet population. *MNRAS*, 421:L117–L121.
- Verbunt, F. and Zwaan, C. (1981). Magnetic braking in low-mass X-ray binaries. *A&A*, 100:L7–L9.
- Wadsley, J. W., Stadel, J., and Quinn, T. (2004). Gasoline: a flexible, parallel implementation of TreeSPH. *New A*, 9(2):137–158.
- Waldmann, I. P. (2016). Dreaming of Atmospheres. *ApJ*, 820(2):107.
- Wang, H. and Li, J. (2018). Adaptive gaussian process approximation for bayesian inference with expensive likelihood functions. *Neural Computation*, 30(11):3072–3094.
- Watson, A. J., Donahue, T. M., and Walker, J. C. G. (1981). The dynamics of a rapidly escaping atmosphere - Applications to the evolution of earth and Venus. *Icarus*, 48:150–166.

- Welsh, W., Orosz, J., Quarles, B., and Haghighipour, N. (2015). Kepler-47: A Three-Planet Circumbinary System. In *AAS/Division for Extreme Solar Systems Abstracts*, volume 3 of *AAS/Division for Extreme Solar Systems Abstracts*, page 402.01.
- Welsh, W. F., Orosz, J. A., Carter, J. A., and Fabrycky, D. C. (2014). Recent Kepler Results On Circumbinary Planets. In Haghighipour, N., editor, *Formation, Detection, and Characterization of Extrasolar Habitable Planets*, volume 293 of *IAU Symposium*, pages 125–132.
- West, A. A., Hawley, S. L., Bochanski, J. J., Covey, K. R., Reid, I. N., Dhital, S., Hilton, E. J., and Masuda, M. (2008). Constraining the Age-Activity Relation for Cool Stars: The Sloan Digital Sky Survey Data Release 5 Low-Mass Star Spectroscopic Sample. *AJ*, 135:785–795.
- West, A. A., Weisenburger, K. L., Irwin, J., Berta-Thompson, Z. K., Charbonneau, D., Dittmann, J., and Pineda, J. S. (2015). An Activity-Rotation Relationship and Kinematic Analysis of Nearby Mid-to-Late-Type M Dwarfs. *ApJ*, 812:3.
- Wheatley, P. J., Louden, T., Bourrier, V., Ehrenreich, D., and Gillon, M. (2017). Strong XUV irradiation of the Earth-sized exoplanets orbiting the ultracool dwarf TRAPPIST-1. *MNRAS*, 465:L74–L78.
- Wilkins, A. N., Delrez, L., Barker, A. J., Deming, D., Hamilton, D., Gillon, M., and Jehin, E. (2017). Searching for Rapid Orbital Decay of WASP-18b. *ApJ*, 836:L24.
- Winn, J. N. and Fabrycky, D. C. (2015). The Occurrence and Architecture of Exoplanetary Systems. *ARA&A*, 53:409–447.
- Wisdom, J. (1980). The resonance overlap criterion and the onset of stochastic behavior in the restricted three-body problem. *AJ*, 85:1122–1133.
- Wisdom, J. (2008). Tidal dissipation at arbitrary eccentricity and obliquity. *Icarus*, 193:637–640.
- Witte, M. G. and Savonije, G. J. (2002). Orbital evolution by dynamical tides in solar type stars. Application to binary stars and planetary orbits. *A&A*, 386:222–236.

- Wright, N. J. and Drake, J. J. (2016). Solar-type dynamo behaviour in fully convective stars without a tachocline. *Nature*, 535:526–528.
- Wright, N. J., Drake, J. J., Mamajek, E. E., and Henry, G. W. (2011). The Stellar-activity-Rotation Relationship and the Evolution of Stellar Dynamos. *ApJ*, 743:48.
- Wright, N. J., Newton, E. R., Williams, P. K. G., Drake, J. J., and Yadav, R. K. (2018). The stellar rotation-activity relationship in fully convective M dwarfs. *MNRAS*, 479:2351–2360.
- Young, M. D. and Clarke, C. J. (2015). Binary accretion rates: dependence on temperature and mass ratio. *MNRAS*, 452(3):3085–3091.
- Zahn, J.-P. (1975). The dynamical tide in close binaries. *A&A*, 41:329–344.
- Zahn, J.-P. (1994). Rotation and lithium depletion in late-type binaries. *A&A*, 288:829–841.
- Zahn, J.-P. (2008). Tidal dissipation in binary systems. In Goupil, M.-J. and Zahn, J.-P., editors, *EAS Publications Series*, volume 29 of *EAS Publications Series*, pages 67–90.
- Zahn, J.-P. and Bouchet, L. (1989). Tidal evolution of close binary stars. II - Orbital circularization of late-type binaries. *A&A*, 223:112–118.
- Zhao, B. and Li, Z.-Y. (2013). Orbital and Mass Ratio Evolution of Protobinaries Driven by Magnetic Braking. *ApJ*, 763:7.
- Zingales, T. and Waldmann, I. P. (2018). ExoGAN: Retrieving Exoplanetary Atmospheres Using Deep Convolutional Generative Adversarial Networks. *AJ*, 156(6):268.